HARNESSING COLLOIDAL PLASMONIC METASURFACES FOR ADVANCED OPTICAL PHENOMENA

Conti Ylli

Universitat Autònoma de Barcelona

Chemistry Department

Doctoral program in Materials Science

Doctoral Thesis

HARNESSING COLLOIDAL PLASMONIC METASURFACES FOR ADVANCED OPTICAL PHENOMENA

Thesis director:

Dr. Leonardo Scarabelli

Tutor:

Prof. Eva Maria Pellicer

Candidate:

Conti Ylli

Academic year: 2021-2022

Barcelona, 2024

ICMAB INSTITUT DE CIÈNCIA DE MATERIALS DE BARCELONA

EXCELENCIA SEVERO OCHOA

CSIC CONSEJO SUPERIOR DE INVESTIGACIONES CIENTÍFICAS

Nanopt

D. Leonardo Scarabelli, "La Caixa" Junior Leader del Instituto de Ciencia de Materiales de Barcelona informa que:

Ms. Ylli Conti, licenciada en Ingeñería de Materiales, ha realizado en el Instituto de Ciencia de Materiales de Barcelona (ICMAB-CSIC) bajo su dirección el trabajo descrito en la presente memoria, que lleva por título "*Harnessing Colloidal Plasmonic Metasurfaces for Advanced Optical Phenomena*", y que presenta para optar al grado de Doctor por la Universidad Autónoma de Barcelona con Mención Internacional.

Bellaterra, 1 de mayo de 2024

Fdo. Leonardo Scarabelli

CONTENTS

LIST OF ABBREVIATIONS 9

SCOPE OF THE THESIS AND PREFACE 11

CHAPTER 1 17

PLASMONICS, METASURFACES, AND NON-LINEAR OPTICS 17

INTRODUCTION 17

1.1 PLASMONIC PROPERTIES OF METAL NANOSTRUCTURES 20

1.1.1 Light-metal film interaction: Surface Plasmon Polaritons 24

1.1.1 Light-nanoparticles interaction 28

1.1.4 Beyond individual nanostructures: plasmon coupling 33

1.1.5 Photonic crystals and Surface Lattice Resonances 35

1.2 FUNDAMENTALS OF NON-LINEAR OPTICS 39

1.2.1 Plasmonics Metasurfaces for NL Optics 43

1.2.2 Colloidal-based plasmonic metasurfaces for NL Optics 45

1.2 PLASMONICS AND EMISSION PHENOMENA 46

1.2.1 Quantum emitters 48

1.3 PLASMONIC ARRAY COUPLING WITH GAIN MEDIA 50

1.3.1 Weak coupling regime Purcell Effect 51

1.3.2 Plasmonic metasurfaces: other applications 53

1.3.3 Strong coupling regime 56

1.4 REFERENCES 60

CHAPTER 2 74

ALTERNATIVE FABRICATION PROCESSES FOR PLASMONIC METASURFACES 74

INTRODUCTION 74

2.1 NANOIMPRINT LITHOGRAPHY (NIL) 77

2.2 TOP-DOWN AND BOTTOM-UP APPROACHES FOR PLASMONIC METASURFACES 82

2.3 COLLOIDAL SELF-ASSEMBLY 85

2.3.1 Interaction between particles 87

2.3.2. Van der Waals interaction (VdW) 90
2.3.3. Depletion forces and steric repulsion 90
2.3.4. Electrostatic interaction 91
2.3.5. Capillary forces 92
2.3.6 Hydrophobic interaction 94
2.4 TEMPLATE-ASSISTED SELF-ASSEMBLY (TASA) 97
2.4.1 Preparation of the plasmonic metasurfaces 101
2.5 CHEMICAL CONTRAST IN SITU GROWTH 109
2.5.1 Fabrication of the HPC stencils 111
2.5.2 Chemical inking step 116
2.5.3 In situ growth 118
2.5.4 In situ growth on spin-coated thin PDMS films 125
2.4 REFERENCES 131

CHAPTER 3 149

OPTICAL CHARACTERIZATIONS AND METASURFACES ENGINEERING 149

3.1 PLASMONIC METASURFACES: THE ROLE OF A HIGH REFRACTIVE INDEX LAYER 150
3.2 OPTICAL CHARACTERIZATION OF PLASMONIC METASURFACES 155
3.2.1 Exploring plasmonic metasurfaces for NL optics 163
3.2.3 Optical characterization of in situ growth plasmonic array 166
3.3 CHIRAL PLASMONIC METASURFACES 168
3.3.1 Optical characterization of chiral plasmonic metasurfaces 170
3.4 PLASMONIC METASURFACES MODIFICATION 175
3.6.2 Pre-assembly modifications: effect of size distribution 177
3.6.3 Pre-assembly modifications: the effect of composition 180
3.6.4 Post-assembly modifications: thermal annealing 183
3.6 REFERENCE 190

CHAPTER 4 198

NANOPTICS APPLICATION: PHOTOLUMINESCENCE AND LASING EMISSION 198

INTRODUCTION 198
4.1 One photon excited stimulated emission in plasmonic metasurfaces 199

4.1.1 LASING EMISSION: THE CASE OF 400 NM LATTICE PERIOD 201
4.1.2 Modeling of the lasing emission for 400 nm lattice period 207
4.1.2 OFF-NORMAL LASING EMISSION: 500, AND 600 NM LATTICE PERIOD CASES 211
4.2 TWO-PHOTON EMISSION MEDIATED BY PLASMONIC METASURFACES 215
4.4 CHIRAL PHOTOLUMINESCENCE 225
4.5 REFERENCES 232

CHAPTER 5 241

CONCLUSION AND PERSPECTIVES 241

5.1 REFERENCES 250

EXPERIMENTAL SECTION 253

1. MATERIALS 253
2. METHODS 256
2.1 Synthesis 256
2.1.1 Seed mediated Au nanoparticles synthesis 256
2.1.2 Synthesis of silver AgNPs 260
2.1.3 Ligand exchange 263
2.2 MOLDS AND MASTER FABRICATION 265
2.2.1 s-PDMs molds 265
2.2.2 h-PDMs stamp for mater replicas and for HPC imprinting for in situ 266
2.2.3 Operative silicon masters 267
2.2.4 OrmoStamp® for operative master replicas fabrication 268
2.3 SAMPLE FABRICATION 269
2.3.1 Glass samples preparation 269
2.3.2 Lasing samples 270
2.3.3 Gammadion samples for chiral fluorescence enhancement 272
2.3.4 Samples for two-photon photoluminescence (2PPL) 272
2.3.5 In situ samples 273
2.4 MORPHOLOGICAL CHARACTERIZATION 277
2.5 OPTICAL CHARACTERIZATIONS 277
2.5.1 Transmittance circular dichroism 278
2.6 LASING EMISSION CHARACTERIZATION 279

2.6.1 Circularly emission characterization 279
2.7 TWO-PHOTON EXCITATED EMISSION 280
2.8 COMPUTATIONAL METHODS 280
ES REFERENCES 282

APPENDIX A 286
A.1 LIST OF PUBLICATIONS 286
A.2 CONTRIBUTION TO SCIENTIFIC EVENTS 287
A.3 HONOURS AND AWARDS 288

ALANCE DE LA TESIS Y PREFACIO 290

ACKNOWLEDGEMENTS 294

LIST OF ABBREVIATIONS

Ag	Silver
Al	Aluminum
Au	Gold
ASE	Amplified Spontaneus Emission
CAPA	Capillary-Assisted Particles Assembly
CD	Circular dichroism
CPL	Chiral Photoluminescence
Cu	Copper
CVD	Chemical Vapor Deposition
DFG	Difference Frequency Generation
EBL	Electron Beam Lithography
EM	Electromagnetic
FIB	Focus Ion Beam
HCP	Hexagonal closed packed
HPC	Hydroxypropyl cellulose
h-PDMS	Hard-poly(dimethylsiloxane)
IR	Infrared
LCP	Left Circularly Polarized
LDOS	Local Density of Optical States
LSPR	Localized Plasmon Resonance
NIL	Nanoimprint Lithography
NIR	Near-infrared
NL	Non-Linear
NP	Nanoparticle
PEG	poly(ethylene) glycol
PL	Photoluminescence
P2P	Plate-to-plate
RCP	Right Circularly Polarized

RhB	Rhodamine B
RT	Room Temperature
R-W	Rayleigh-Wood
R2P	Roll-to-plate
R2R	Roll-to-roll
SEM	Scanning Electron Microscopy
SFG	Sum Frequency Generation
SHG	Second Harmonic Generation
SLR	Surface Lattice Resonance
s-PDMS	Soft-poly(dimethylsiloxane)
SPP	Surface Plasmon Polariton
T_g	Glass Transition
TASA	Template-Assisted Self-Assembly
TE	Transverse electric
TEM	Transmission Electron Microscopy
TM	Transverse magnetic
THG	Third Harmonic Generation
UV	Ultraviolet
UV-O_3	UV-Ozone
Vis	Visible
VdW	Van der Waals
2D	two-dimensional
3D	three-dimensional
2P	Two-photon
1P	One-photon
2PA	Two-Photon Absorption
2PPL	Two-Photon Photoluminescence

SCOPE OF THE THESIS AND PREFACE

This Ph.D. thesis work was carried out within the framework of the Post-doctoral Junior Leader-Incoming fellowship funded by "La Caixa" Foundation (ID 100010434, fellowship code LCF/BQ/PI20/11760028) which aimed at the development of alternative strategies for the construction of nanostructured plasmonic materials for the study of plasmon-molecule dynamics, plasmon-mediated processes, and surface-enhanced chemistry.

Specifically, my work focused on the fabrication of such plasmonic/photonic architectures, including molecular species, the characterization of their optical properties using various experimental techniques, and the practical application of the final optical cavities in the realm of non-linear optics.

Photonic metasurfaces are artificial 2D-structures made with subwavelength components, arranged either periodically or non-periodically, to produce distinctive electromagnetic responses. This design flexibility enables the creation of materials with exceptional macroscopic properties that cannot be found in nature.

Plasmonic nanoparticles also act as building blocks for photonic structures such as ordered arrays, where coupling between plasmons and diffractive states leads to the emergence of surface lattice plasmon resonances, spectrally tunable from the ultraviolet (UV) to the infrared (IR) by varying the lattice parameter of the array (Λ), the refractive index of the surrounding medium and the angle of illumination. Lattice resonances retain the properties of the individual components, such as an enhanced scattering cross section typical of plasmonic resonances, while exhibiting narrow bandwidths, high quality factors (Q-factors) and spatial delocalization typical of diffractive phenomena. As a result, surface lattice resonances can be used to promote nonlinear optical phenomena such as lasing, strong coupling or second harmonic generation.

The creation of finely tuned plasmonic arrays requires scalable fabrication techniques that combines advantages of both top-down and bottom-up approaches. Self-assembly techniques

using colloidal building blocks offer low-cost alternatives to top-down techniques, providing high-throughput all-around approach for implementing colloidal plasmonic metasurfaces on a variety of different materials. The results achieved suggest that self-assembly is now a viable approach for the fabrication of high-quality optical cavities for advanced optical applications such as lasing and enhanced two-photon excited fluorescence.

Besides optimizing the template-assisted self-assembly technique, we had motivated to develop a new strategy to overcome some of the constraint related to approach that use pre-synthetized colloids, such as the excess of reagents and the need of ligand stabilizers. In situ growth, where plasmonic structures form directly on substrates avoids batch synthesis and self-assembly steps, was developed as an exciting alternative to achieve tunable nanometric patterns. The proof-of-concept presented in this thesis demonstrates the possibility to grow plasmonic arrays that behave as optical cavities through direct in situ growth, a result that was never achieved before. Despite these exciting results, further research is necessary to comprehend the mechanistic aspects of in situ growth and control particle morphology and orientation, ultimately enhancing scalability and versatility of this emerging approach.

The experimental work of the thesis was performed mainly in the Institute of Materials Science of Barcelona (ICMAB-CSIC), complemented by one research stay period of four months at the University of Houston (Texas, USA).

Below is presented a brief outline of each chapter.

The introductory **Chapter 1** provides the essential context on plasmonics and nonlinear (NL) optics within the framework of this thesis, with specific focus on elucidating the characteristics of the metal nanoparticles, metal nanoparticles arrays, and nanoparticle-molecular interactions to promote nonlinear optical phenomena.

The purpose of **Chapter 2** is to summaries and categories the principles of plasmonic colloidal assembly, comparing different fabrication methods and highlighting emerging ones. In

particular, the focus is on alternative approaches using soft lithography, including template-assisted self-assembly, and the more recent "in situ growth" strategy for constructing functional nanostructures by integrating nanoimprint lithography (NIL) and chemical contrast techniques. The discussion focuses on the use of metal nanoparticles (NPs) to create so-called "colloidal-based plasmonic metasurfaces".

The **Chapter 3** presents the optical characterization results obtained in the context of this thesis. Some engineering strategies are presented to show how different routes can be taken to design colloidal plasmonic metasurface. These include changing the refractive index of the environment, the morphology of the plasmonic units or the substrate material, in pre- and post-assembly phases. This study showcases the adaptability of templated self-assembly in utilizing various components to fabricate plasmonic arrays of greater complexity allowing to engineer the collective optical response.

In **Chapter 4** our investigation delved into the characteristics of colloidal plasmonic metasurfaces in enhancing various optical phenomena. These included stimulating lasing emission in common dye molecules (Rhodamine B), enhanced two-photon excited emission in core-shell quantum dots, and induced chiral emission in achiral emitter molecules *via* resonant coupling with colloids arranged into chiral shaped arrays.

Forse un giorno, pensando precisamente a quest'ora, a quest'ora malinconica in cui attendo, con le spalle curve, che sia ora di salire sul treno, sentirei il mio cuore battere più in fretta e mi direi: quel giorno a quell'ora è cominciato tutto. E arriverei - al passato, soltanto al passato - ad accettare me stesso.

Sartre - "La Nausea"

Chapter 1

PLASMONICS, METASURFACES, AND NON-LINEAR OPTICS

"The theory of quantum electrodynamics describes Nature as absurd from the point of view of common sense. And it agrees fully with experiment. So, I hope you accept Nature as She is — absurd."

Richard Feynman, QED: The Strange Theory of Light and Matter (1965)

Introduction

The study of light-matter interaction has fascinated researchers since ancient times. Plasmonics lays at the intersection between optics and nanotechnology and to find its roots, it is necessary to go back to the 4th-century during the Roman Empire period.

The first historical example of plasmonic material is represented by the "*Lycurgus cup*", currently conserved in the British Museum of London (**Figure 1.1 a**). Named in honor of the mythical king Lycurgus, this ancient cage-cup crafted from dichroic glass shows remarkable colour-changing properties, passing from green to red depending on the illumination angle. Despite the exact manufactory process used to achieve the dichroic effect remains unclear, modern studies have attributed it to the contamination with trace amounts of finely ground gold and silver dust, coming from gold leaf left by accident in the artisan's workshop, or tools residues then dispersed during the glass processing.

Lycurgus cup's intriguing light-matter interaction foreshadowed plasmonics' huge potential that is now leading to major breakthroughs in sensing, imaging, and other advanced nanotechnologies.

Although early mentions of a red coloring induced in glass by gold are found in ancient Egyptian manuscripts dated back to the Greco-Roman period,[1] the first scientific contribution describing the use of gold for ceramic processing appears in the early 17th century and was ascribed to the alchemist Andrew Cassius. Combining gold and stannic hydroxide, his experiments resulted in

an unusual purple pigment with iridescent properties named "*Purple of Cassius*", as described in the book "*De Auro*" published in 1685,[2] which was later applied throughout Europe by all the most famous glass and porcelain factories of the 19th century (**Figure 1.1 b**).

However, the first milestone posed for the future development of nanotechnology dates back to 1857 on the merits of Sir Michael Faraday, the same English scientist who contributed enormously to the development of both electromagnetism and electrochemistry. In fact, among other revolutionary scientific inventions such as the Faraday cage, the Bunsen burner, and the oxidation numbers' system, Faraday was also credited with the first example of "*colloidal suspension*" as we describe it today in modern colloidal chemistry. While mounting thin sheets of gold leaf onto microscope slides, he observed the accidental formation of a ruby gold suspension. The last of Faraday's gold colloids that survived the Second World War is still preserved in the Faraday Museum of the Royal Institute of London (**Figure 1.1 c**), remaining optically active and stable after more than 150 years.

"I have been occupying myself with gold this summer; I did not feel headstrong enough for stronger things. This work has been of the Mountain and Mouse fashion; and if I ever publish it and it comes to your sight I dare say you will think so." [3]

Clearly fascinated by the world of colloids, he has further investigated various methods to obtain them using aqueous solution with reducing agents such as phosphorous in carbon disulfide, realizing that "*mere variation on the size gave rise to a variety of resultant colors*".

By directing a beam of light through the liquid, Faraday observed a cone effect resulting from the presence of suspended gold particles in the liquid. These tiny particles scattered the light laterally depending on the wavelength, giving rise to what was then recognized as the *Faraday-Tyndall effect.* The observations collected by Michael Faraday and John Tyndall set the basis for Lord John Rayleigh studies of elastic light scattering induced by particles with size (*d*)

much smaller than the wavelength of the incoming radiation ($d << \lambda$), providing a scientific explanation for the sky-hue colors observed at different times of the day.

When sunlight enters the Earth's atmosphere, it induces polarization in atmospheric particles, causing them to form small dipoles that scatter sunlight with intensity $I \propto 1/\lambda^4$. This scattering is more effective for shorter wavelengths, such as blue and violet, than for longer wavelengths, such as red and yellow. As a result, the sky appears blue during the day because shorter wavelengths dominate. At sunrise and sunset, sunlight travels through more of the atmosphere, increasing the scattering of shorter wavelengths and allowing red and yellow to become more prominent, creating warm tones in the sky.

A more comprehensive theoretical framework was provided by Gustav Mie in 1908, when he developed a complete theory on the scattering and absorption of an electromagnetic radiation by a sphere of different size ($d \geq \lambda$). In his theory, particles scattering is described as an interference effect developed through phase changes over the object surface when illuminated. By applying boundary conditions and solving Maxwell's equations, the multiple scattering paths, arising from the spherical waves crossing generated on the surface of the sphere, lead to the formation of interference patterns with high preferential directionality.

Mie theory became increasingly relevant with the advent plasmonics and plasmonic nanoparticles' synthesis and is still applied for the description of several light matter interactions correlated with the collective oscillations of the free electrons of various metallic nanostructures. Over the last century that brings us to modern time, the plasmonic properties of metallic colloids have found applications in an incredible diversity of scientific and technological areas.

The aim of this first chapter is to provide the necessary background on plasmonics and non-linear (NL) optics in the context of this thesis, with particular emphasis on the properties of so-called "*colloidal-based plasmonic metasurface*".

Figure 1.1 Pictures of: (**a**) the Lycurgus cup (IV century AD, British Museum of London): when illuminated from the front, the cup appears green (reflection), while when illuminated from the inside, a red coloration emerges (transmission); (**b**) Cranberry glass or Gold Ruby colored by Purple of Cassius pigment from the treasury chamber of the Wittelsbacher located in the Munich Residenz; (**c**) Faraday's ruby gold suspensions conserved at the Royal Museum of London.

1.1 Plasmonic properties of metal nanostructures

The field of plasmonics explores how to manipulate light-matter interaction along metal-dielectric interfaces in the nanometer scale, when the surface/volume ratio of the objects becomes critical. The distinctive optical properties of noble metal nanoparticles, such as gold (Au), silver (Ag) or copper (Cu), arise from the presence of high number of free conduction electrons that can approximate a "*solid-state plasma*". When these systems interact with an electromagnetic (EM) radiation, the free-electrons resonate with the incident electric field, getting into an excited resonant state that leads to strong EM field confinement and near-field enhancement. This excited collective oscillation, known as "*plasmons resonance*", significantly modifies the scattering and absorption behavior of these materials from ultraviolet (UV) to infrared (IR) regions of the EM spectrum, paving the way for different applications in fields such as photo- and electrocatalysis, biomedicine, photovoltaics, imaging, and sensing.

Understanding the intricate interplay between light and matter is fundamental to explore the fascinating realm of plasmonics. At the base of these interactions lie Maxwell's equations, governing the relationship between electromagnetic fields and the material properties expressed through dielectric permittivity (ε) and magnetic permeability (μ). From this interaction arise the polarization of the macroscopic material (**P**)[1], a vector quantity representing the induced dipole moment per unit volume within a material in response to an applied external electric field (**E**) expressed as:

$$\mathbf{P} = \varepsilon_0 \chi_e \mathbf{E} \qquad \textbf{(1.1)}$$

where ε_0 represents the dielectric permittivity in vacuum and χ_e the electric susceptibility of the material. When an electric field is applied to a metal, the frequency-dependent material response is expressed through its complex dielectric function $\tilde{\varepsilon}(\omega)$.

$$\tilde{\varepsilon}(\omega) = \varepsilon_1(\omega) + i\varepsilon_2(\omega) \qquad \textbf{(1.2)}$$

where $\varepsilon_1(\omega)$ and $\varepsilon_2(\omega)$ represent the real and imaginary parts of the dielectric function, respectively. The real part ($\varepsilon_1(\omega)$) describes the ability of a material to respond to an external field through its polarizability α, hence, how the strength of the polarization, to which the material is subjected, affects the propagation of the electric field through the material. The imaginary part ($\varepsilon_2(\omega)$) is related to how the material absorb the energy from the external source and convert or transfer it, namely the optical losses faced in polarizing a material, giving a quantitative estimation of the electric field attenuation experienced while propagating through the material. This quantity is related to the refractive index of the medium $\tilde{n}(\omega) = n(\omega) + ik(\omega)$ as $\tilde{n} = \sqrt{\tilde{\varepsilon}}$, where the real part ($n$) is related to the EM radiation dispersion in the medium, and the imaginary part (k), also known as the *extinction coefficient*, describes the optical absorption (*i.e.*, the optical losses) of the system. This latter quantity is related to the attenuation

[1] vectorial quantities written in bold.

coefficient κ of the Beer–Lambert law, describing the attenuation of a monochromatic light beam with intensity I_0 (due to absorption, scattering or reflection) when it passes through a medium layer of thickness *l* (optical path):

$$I = I_0 \exp(-\kappa l) \qquad \textbf{(1.3)}$$

The metals response to an external field was firstly elucidated through the *Drude* model, to offer a simplified insightful representation.[4] Suggested in the early 20th century, this free electron gas model was derived by applying the kinetic theory to the conduction band of a metal. In essence, conduction band electrons are represented as a cloud of negatively charged particles, while the positive cores have fixed position. The response of the metal can then be approximated by the influence of the external field, characterized by the harmonic form $E(t) = E_0 \exp(-i\omega t)$, on these freely moving electrons, which drives their damped in-phase oscillation characterized by a relaxation frequency $\gamma = 1/\tau$, assuming non-dissipative collisions (τ is the relaxation time of the free electron gas). Ultimately, the dielectric function takes the form:

$$\tilde{\varepsilon}(\omega) = 1 - \frac{\omega_p^2}{\omega^2 + i\gamma\omega} \qquad \textbf{(1.4)}$$

where $\omega_p = \sqrt{\frac{Ne^2}{m\varepsilon_0}}$ represents the *plasmon frequency* of N electrons with mass *m*, associated to the collective oscillation of the free electrons of a material.

However, this model presents several limitations and does not fully capture the complexity of electron behavior in real materials, not considering the presence of a band structure, the energy dissipation, the temperature-dependency of the dielectric function, and electron-electron interactions.

Further investigation led to an extension of the model that includes the contribution of inter-band transitions, due to the electrons of the valence band, and the polarization residues contribution due to the ion cores with the so-called background dielectric constant (ε_∞).[4]

$$\tilde{\varepsilon}(\omega) = \varepsilon_{\infty}(\omega) - \frac{\omega_p^2}{\omega^2 + i\gamma\omega} \qquad \textbf{(1.5)}$$

where typically $1 \leq \varepsilon_{\infty}(\omega) \leq 10$, depending on the strength of the core electrons contribution to the external electric field response. Since the response of the material interacting with EM radiation is frequency-dependent, it is possible to identify three regimes:

1. $\boldsymbol{\omega > \omega_p}$ in the high frequency regime, the external frequency surpasses the one of the natural oscillations of the electrons which are not able to effectively follow the propagating electric field. As such, the EM waves can penetrate the metal more deeply without being immediately reflected by the electron collective oscillations. The material in this regime exhibits what is known as "*transparency window*".
2. $\boldsymbol{\omega < \omega_p}$ in the low frequency regime, the response of the free electrons become more pronounced, and the metals tend to exhibit strong reflection and absorption of light, converting most of the energy into heat. In this regime, the imaginary part of the dielectric function is dominating over the real part.
3. $\boldsymbol{\omega = \omega_p}$ in the resonance regime, the external electric field $\mathbf{E}$ induces a proportional dipole moment ($\mathbf{p}$) depending on the object polarizability (α), by dragging the electrons in a collective oscillation with maximized amplitude and exciting the plasmon resonance. For metals this regime falls mostly in the Vis-NIR part of the EM spectrum, where the real part of the dielectric permittivity is negative while the imaginary part approach to zero, suggesting the strong confinement of the EM field over the volume of the nanoscale object with greater EM enhancements due to the lower optical losses.

In essence, in response to the presence of an oscillating EM field, the free electrons in the metal can establish a coherent oscillation with respect to the fixed lattice positions, where the positive nuclei reside. Such processes resonate at certain frequencies of the incident radiation, enabling

the emergence of "*surface plasmonic polaritons*" (SPPs), in the case propagating waves onto planar metal surface, or "*localized surface plasmonic resonances*" (LSPRs), when there is the confinement of a photon over a nanometric object, which will be discussed in more details in the following paragraphs.

Some of the energy involved in this light-matter interaction can be dissipated as heat (ohmic losses) promoted by non-radiative electron decays after absorption process, or re-radiated *via* scattering process into the surrounding free space.[5]

Among noble metals, *Gold* (Au) is the most chemically stable, but *Silver* (Ag) stands out for its superior performance in generating strong plasmonic resonances in the Vis spectral region, showing the smallest ohmic losses due to shorter relaxation frequencies (γ) of the inter-band transitions, generated from the core electrons and falling in the UV part of the EM spectrum.

Copper (Cu) is an interesting Earth-abundant alternative plasmonic candidate for Vis-NIR applications, showing inter-band transitions below 600 nm. However, its poor chemical stability makes it less suitable for being widely used.

Finally, *Aluminum* (Al) exhibits a great plasmonic response in the UV range, with inter-band transitions falling in the visible part, but is highly susceptible to oxidation, forming Al_2O_3 when exposed to air, which limits its plasmonic performance.

1.1.1 Light-metal film interaction: Surface Plasmon Polaritons

Surface plasmon polaritons (SPP) are an attractive and versatile class of two-dimensional EM waves propagating along a metal/dielectric flat interface and decaying evanescently in both perpendicular directions to the surface (**Figure 1.2 a**).

The wave formed on the plane (x,z) must have the electric field component parallel to the normal of the same surface, in TM configuration.

Considering a system involving a dielectric (ε_d or ε_1) and metal (ε_m or ε_2) medium forming an interface, the condition for SPP to exist is that the magnetic field in both media assumes the shape of:

$$H_{jy} = H_j e^{ik_x\hat{x}} e^{-k_{jz}\hat{z}} \qquad \textbf{(1.6)}$$

where j represents d (1) or m (2) respect to the assumption of the surface wave component exists in the dielectric or metal media, $e^{ik_x\hat{x}}$ is the plane wave component propagating along $\hat{x}$, and $e^{-k_{jz}\hat{z}}$ is the evanescent wave component propagating along $\hat{z}$. Thus, since the free space wavevector has components $k_x^2 + k_{jz}^2 = k_0^2\varepsilon_j = \frac{\omega^2}{c^2}n^2$ the propagation constant can be written as:

$$k_{jz} = \sqrt{(k_x^2 - k_0^2\varepsilon_j)} \qquad \textbf{(1.7)}$$

Combing the expression of H_{jy} for both media $H_{1y}$and H_{2y} (or H_{dy} and H_{my}) with Maxwell's equations, two solutions of the electric field in the dielectric E_1 and metal E_2can be derived:

$$E_1 = \frac{H_{1y}}{\varepsilon_1\omega}(ik_{1z}\hat{x} - k_x\hat{z}) \text{ and } E_2 = \frac{H_{2y}}{\varepsilon_2\omega}(-ik_{2z}\hat{x} - k_x\hat{z}) \qquad \textbf{(1.8)}$$

These waves are represented by an electric field propagating along the $\hat{x}, \hat{z}$ and the magnetic field in $\hat{y}$ direction (TM configuration). For the electric field to be continuous at the interface, the so-called "condition of existence" of the surface wave emerges:

$$\frac{k_{1z}}{\varepsilon_1} = -\frac{k_{2z}}{\varepsilon_2} \quad \textit{i.e.} \quad \frac{k_{1z}}{k_{2z}} = -\frac{\varepsilon_2}{\varepsilon_1} \qquad \textbf{(1.9)}$$

And since k_{1z} and k_{2z} are both positive, the condition implies that ε_1 and ε_2 must have opposite sign. For example, if we assume that $k_x > k_0$ and the dielectric medium is air (ε_d =1), thus, ε_m =-1 and thus $k_{1z} < k_{2z}$ which means that the wave decay faster in the metal. By expressing **Eq 9** for j = 1 (dielectric) and j= 2 (metal) and combining the expressions, it is

possible to derive the dispersion relation of the surface plasmon modes (**Figure 1.2 b**), which describes how wavevector (k_x) of these waves changes as the light frequency (ω) varies, influencing the mode confinement and propagation length, and the rate at which SPPs propagate along the interface:[6]

$$k_x(\omega) = k_0\sqrt{\frac{\varepsilon_d\varepsilon_m}{\varepsilon_d+\varepsilon_m}} \qquad \textbf{(1.10)}$$

where c is the speed of light in vacuum and $k_0 = n\frac{\omega}{c}$ represents the magnitude of the light wave vector in free space, ε_d is the dielectric permittivity of the dielectric medium (1), and ε_m is the dielectric permittivity of the metal (2).

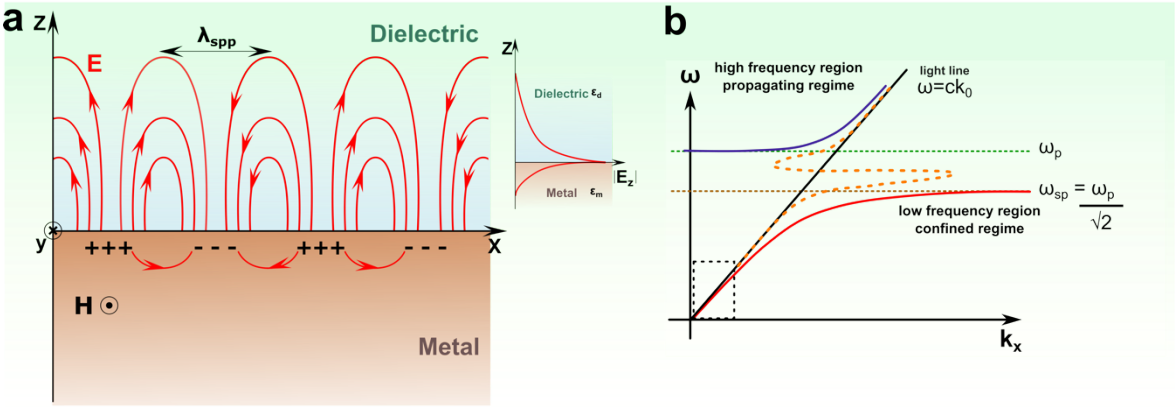

Figure 1.2 **Dispersion relation diagram of surface plasmon resonances**. (**a**) Scheme of the SPP at dielectric/metal interface (considering air as dielectric layer) showing the electric field distribution of the surface wave depending on the frequency ω and wavevector k_x along the propagation direction. (**b**) Dispersion relation of surface plasmon polaritons highlighting the damping mechanism due to the absorption in the metal ($\varepsilon_2(\omega)>0$). The upper branch (**purple** curve) corresponds to waves propagating in the free space at high frequency ($\omega > \omega_p$). The lower branch (**red** curve) represents the low frequency regime where with increasing k_x the wave approach asymptotically to ω_{sp} assuming stationery behavior. The **dashed black** rectangle highlights the region where $\omega << \omega_p$ and the mode.

The dispersion curve diagram provides information about the conditions under which SPPs can be excited. As for free space wave the propagation constant is related to the wavelength as $\lambda_0 = \frac{2\pi}{k_0}$, similarly for plasmon polaritons $\lambda_{SPP} = \frac{2\pi}{k_x}$.

Analyzing the region on the right of the light line, for large k_x the quantity $\varepsilon_d + \varepsilon_m = 0$ ($\varepsilon_d = -\varepsilon_m$), and the $\lambda_{SPP} = \frac{2\pi}{k_x}$ results smaller than λ_0. k_x becomes pure imaginary and the wave assumes evanescent nature, *i.e.* it exhibits a more confined nature (not propagate as an electromagnetic wave), and whose energy is spatially concentrated in the vicinity of the source. For air/metal interface where $\varepsilon_d = 1$, Drude model (**Eq 1.4**) implies that $\varepsilon_2 = 1 - \frac{\omega_p^2}{\omega^2}$, $\varepsilon_m = -1$, *i.e.* is negative when $\omega = \frac{\omega_p}{\sqrt{2}} = \omega_{spp}$. Since the frequency converges to ω_{spp} for $k_x \to \infty$, the wave assumes a stationary behavior with group velocity ($v_g = d\omega/dk$) approaching zero; consequently, the mode is identified as the "surface plasmon polariton" and results strongly confined to the interface, as it cannot penetrate the metal. It is worth mentioning that if the geometry of the systems involves more layers such as air/metal/glass, all the interfaces can generate surface plasmon resonances but will do so at different frequencies. In fact, since $n = \sqrt{\varepsilon}$, if the refractive index of the dielectric media increases the resonance of the SPP would emerge at lower frequencies. A last consideration concerns the propagation length of the SPP. Since ε_m presents an imaginary part, the propagation constant can be written as $\tilde{k}_x(\omega) = k_x'(\omega) + ik_x''(\omega)$, and is related to the propagation length L_p as:

$$L_P = \frac{1}{\mathrm{Im}\, k_x(\omega)} = \frac{1}{k_x''} \qquad \textbf{(1.11)}$$

At higher frequencies where k_x'' increases, the penetration length decreases. For example, in the case of silver in the visible region of the electromagnetic spectrum, $L_p \sim 200$ μm.[7]

Thus, no transverse electromagnetic wave with frequency smaller than the ω_p can travel through the medium. This means that the light impinging on the system is reflected into free space at the dielectric-metal interface, but as the frequencies approximate ω_p, the optical losses due to the absorption cannot be neglected and a discontinuity is observed due to the creation of the evanescent wave which reduce the reflection. Thus, the wave assumes Lorentzian line shape (**dashed orange** line in **Figure 1.2 b**).

For the low frequencies region were $\omega << \omega_p$, the term $\varepsilon_m = 1 - \frac{\omega_p^2}{\omega^2}$ from Drude model becomes negative and $k_x \approx k_0\sqrt{\varepsilon_d}$. Here, the dispersion curve closely follows the light line (**red** trace in the **dashed black** square of **Figure 1.2 b**), indicating that the electromagnetic field penetrates deeper into the dielectric medium compared to the metal, resulting in a weaker localization of surface plasmon polaritons.

At high frequencies where $\omega >> \omega_p$, ε_m become real and positive and the metal assumes a dielectric behavior. The result is the formation of the upper branch in the dispersion diagram (**purple** trace in **Figure 1.2 b**).

In a practical scenario where a dielectric medium exhibits negligible absorption and a noble metal counterpart possesses a substantially negative real part of the dielectric constant, it is possible to assume that the system supports long-lived surface plasmon polaritons (SPPs) at optical wavelengths. Since SPP show a wave vector larger than the wave vector of photons in air, the resulting momentum mismatch requires specialized phase-matching techniques to excite these plasmon modes, including grating or prism coupling (using Kretschmann and Otto configurations).[8] The manipulation of the dispersion properties made it possible to tailor the behavior of SPPs to suit specific needs, leading to advancements in fields such as plasmonic waveguides, sensors, and integrated optics.

1.1.1 Light-nanoparticles interaction

The interaction between electromagnetic radiation and nanoscale metallic objects gives rise to a fascinating phenomenon known as Localized Surface Plasmon Resonances (LSPRs). The induced in-phase oscillation of free conduction electrons leads to an excitation of the plasmon, when the resonance condition $\omega = \omega_p$ is reached, ensuring an efficient energy transfer between the external field and the collective electron oscillations over the metal surface, leading to observe a remarkably confined EM wave within the nanoscale volume. The spectral position of

the plasmon band depends on size, shape, composition, and refractive index of the environment.[9]

The optical properties for spherical nanoparticles with dimensions *d* below 30 nm are described adequately by the *quasi-static approximation*, and *d* results much smaller than the wavelength of the incident light ($d << \lambda$).

When an electric field of magnitude $|\mathbf{E}_0|$ interacts with a spherical NP of radius *r*, it influences the electron sea cloud surrounding the metal atoms by inducing a dipole moment **p** proportional to the polarizability of the object (α), given by the *Clausius- Mossotti* relation:

$$\alpha = 4\pi r^3 \frac{\varepsilon - \varepsilon_m}{\varepsilon + 2\varepsilon_m} \qquad \textbf{(1.12)}$$

Where ε_0 and ε_m represents respectively the dielectric constant of vacuum and the dielectric constant for non-absorbing isotropic medium (*e.g.* in air the value is 1), and giving the relationship:

$$\mathbf{p} = \varepsilon_0 \varepsilon_m \alpha \mathbf{E}_0 = \varepsilon_0 \varepsilon_m 4\pi r^3 \frac{\varepsilon - \varepsilon_m}{\varepsilon + 2\varepsilon_m} \mathbf{E}_0 \qquad \textbf{(1.13)}$$

Hence, the polarizability experiences a resonant enhancement when the denominator $|\varepsilon + 2\varepsilon_m|$ is close to zero, implying that the real part of $\varepsilon(\omega)$, $\varepsilon_1(\omega) = -2\varepsilon_m$,. As such, the resonance frequency strongly depends on the dielectric environment, shifting towards lower frequencies when ε_m increase. Metal nanoparticles are therefore ideal platforms for optical sensing of refractive index changes.

Under the *quasi-static* approximation, a small particle can be represented as an ideal electric dipole, able to radiate an electromagnetic field once excited at its plasmon resonance. The dipole radiation leads to the scattering of an incident wave ($\mathbf{E}(\mathbf{r},t) = \mathbf{E}_0 e^{-i\omega t}$) by the sphere, which can therefore be represented as a point dipole radiation.[4]

When resonantly polarized, the polarizability (α) of a metal nanoparticle is resonantly enhanced leading to an increase of both the scattering and absorption efficiency, due to a more effective interaction with the incoming electromagnetic wave.

The combined effect of absorption and scattering from a plasmonic system contributes to the overall intensity reduction of an incident light, resulting in a quantity known as *extinction cross-section*, which express the probability of a photon to be either efficiently absorbed or scattered by the system ($C_{ex} = C_{scat} + C_{abs}$). The efficiency of absorption increases with increasing particle size, but at a slower rate compared to scattering as it scales as the cube of particles radius (r^3). In contrast, scattering decreases rapidly with increasing particle size, as it follows a sixth-power dependence on the particle diameter (r^6). As particle size increases, the efficiency of absorption eventually exceeds that of scattering, although at a slower rate.[10]

As the particle size increases ($r \geq \lambda$), the *quasi-static* approximation does not hold, since significant phase changes of the driving electric field occur over the particle volume. Here, *Mie theory* provides a better electrodynamic approach to accurately characterize the changes in nanoparticles scattering behavior,[11] by decomposing the internal and scattered fields into a series of normal modes described by vector harmonics and performing a power series expansion of the absorption and scattering coefficients. The polarizability α of a sphere of volume V is expanded and a *size parameter* $x = \frac{\pi r}{\lambda_0}$, relating the sphere radius to the free-space wavelength, comes into play. Consequently, a retardation effect of the exciting field over the volume of a nanosphere is observed, and it leads to a red shift of the plasmon resonance. Moreover, this approach and generalized numerical methods allow to investigate scattering and absorption processes for particles with arbitrary shapes and sizes. This enables the study of higher-order modes, such as quadrupolar, and more accurately describe the scattering and absorption properties of particles. For noble metals, the dipole resonance spectral position experiences a red shift as the particle size increases, ascribed to the increase of the distance between charges at opposite interfaces, lowering the resonance frequency. The observed red shift underlines the influence of inter-band transitions, characterized by an increase of $\varepsilon_2(\omega)$ and not considered in Drude model, diminishing as the plasmon resonance shifts away from the inter-band transition

edge. An increase of the polarization magnitude means an inherently reduction of the absorption, due to the imaginary part of $\varepsilon(\omega)$.

However, an increase in volume also leads to a broadening of the plasmon resonance due to radiation damping.[12] In conclusion, the particle plasmon resonance can be damped by two competing processes: radiative decay (emission of photons) and non-radiative decay (creation of electron-hole pairs *via* intra-band or inter-band transitions from *d*-level to the *sp*-level of conduction band).[4]

One of the key aspect of LSPRs is their strong dependence on the geometry of the nanoparticle, which has a significant effect on the spectral location of the plasmon resonance, thereby establishing different resonance conditions (**Figure 1.3 a**, **b**).

edge. An increase of the polarization magnitude means an inherently reduction of the absorption, due to the imaginary part of $\varepsilon(\omega)$.

However, an increase in volume also leads to a broadening of the plasmon resonance due to radiation damping.[12] In conclusion, the particle plasmon resonance can be damped by two competing processes: radiative decay (emission of photons) and non-radiative decay (creation of electron-hole pairs *via* intra-band or inter-band transitions from *d*-level to the *sp*-level of conduction band).[4]

One of the key aspects of LSPRs is their strong dependence on the geometry of the nanoparticle, which has a significant effect on the spectral location of the plasmon resonance, thereby establishing different resonance conditions (**Figure 1.3 a**, **b**).

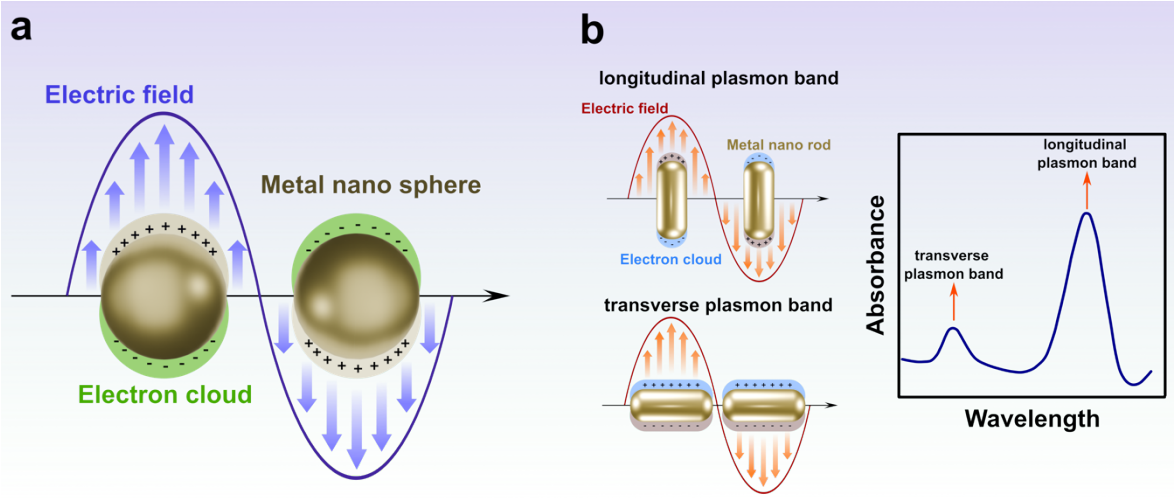

Figure 1.3 Schematic of the Localized Plasmon Resonances (LSPRs) for metal (**a**) nanosphere and (**b**) nanorod.

Commonly, the modification of the plasmonic response of individual nanoparticles is achieved in colloidal suspensions through *bottom-up* synthesis.[13]

Spherically shaped nanoparticles with high symmetry exhibit a single dipolar resonance, while particles characterized by shape anisotropy such as nanorods or nanotriangles, multipolar resonances can emerge, adding versatility and complexity to the tunability of the optical response.[14] Metal nanorods, for example, manifest both *transverse* and *longitudinal* surface plasmon resonances due to the electrons oscillation along different symmetry axis, and resulting in two distinct plasmon band positioned at different wavelengths on EM spectrum (**Figure 1.3 b**).[15]

Nanoparticles exhibit inherent variability in size, shape, and composition, each resulting in different optical properties. In ensemble measurements, this heterogeneity of nanoparticles manifests as scattering spectra characterized by broader and asymmetric Lorentzian peaks, instead of the narrower and symmetric Gaussian peaks that would be expected if all nanoparticles were identical. However, techniques such as dark-field and near-field microscopy offer a solution to this challenge. In contrast to traditional far-field extinction microscopy techniques, far-field dark field optical microscopy and near-field optical extinction microscopy are capable of observing plasmon resonances at the level of individual particles. In the case of dark field optical microscopy, the approach is to selectively collect only the scattered light

emitted by the structure under investigation. This is achieved by the strategic use of a dark field condenser to block the ballistic transmitted light. By isolating the scattered light, researchers can improve the contrast and visibility of features associated with plasmon resonances, providing a clearer and more specific insight into the behavior of individual particles.[16] Near-field optical extinction microscopy, on the other hand, operates in the close vicinity of the sample surface (few nm) by using special probes, e.g. tips with holes capable of generating evanescent waves at the apex, enables the probing of nanoscale interactions between light and matter with high resolution.[17]

1.1.4 Beyond individual nanostructures: plasmon coupling

When more than one particle is present within the same system, additional spectral shifts are expected from electromagnetic interactions between localized modes of the single nanoparticles. In quasi static approximation, these interactions have a predominantly dipolar nature, allowing to consider the particle assembly as a collection of interacting dipoles (the so called coupled-dipole approximation).

When two or more nanoparticles are brought in close proximity, their plasmon modes engage in interactions that can be explained by a model similar to molecular orbital hybridization.

The simplest representation of this interaction involves the coupling of two nearby dipoles oscillators with magnitude of their dipole moment p_1 and p_2, for which the interaction energy V is proportional to $p_1 p_2 / d^3$ where d is the interparticle center-to-center distance. This interaction energy is strong enough to induce shifts in their resonant frequencies, giving rise to a complex combined plasmon mode split in low energy *bonding* and high energy *antibonding* LSPRs (**Figure 1.4**).[18,19]

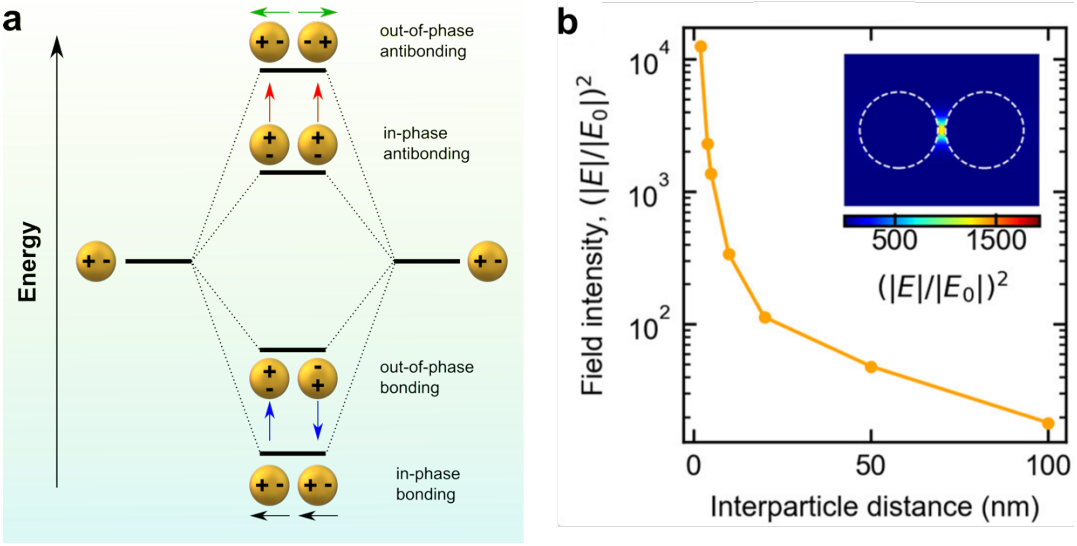

Figure 1.4 (**a**) Schematic representation of plasmon hybridization model applied to a symmetric dimer configuration, depicting the in-phase/out-of-phase bonding/antibonding combinations of dipole moments. Arrows within the diagram denote the direction of the individual particle's dipole moments. (**b**) Effect of gap size between two plasmonic nanoparticles on the electromagnetic field enhancement. Inset: Illustration of a hotspot of the electromagnetic field generated in the nanogap of a plasmonic dimer. **Panel b**: Copyright 2022, Chem Rev. Adapted with permission.[20]

Since the interaction between the particles is subjected to the mutual orientation of their respective dipoles, the lower-energy mode is characterized by longitudinally aligned dipoles, resulting in radiative modes with a induced large dipole and a strong coupling to the far-field, known as "*bright*" plasmon modes. On the other hand, the antibonding configuration is characterized by the dipoles of individual nanoparticles in *antialignment* configuration, resulting in a resonance with essentially a zero net dipole moment that does not interact with incident light and does not appear in the optical absorption of the particle pair.[21] These are known as "*dark*" or "*cavity-like*" modes.

The hybridization of plasmon modes not only alters the energy landscape of the coupled nanoparticles but also influences their optical and electronic properties, providing a nuanced understanding of the dynamic interactions within closely packed nanoparticles. The size of the nanoparticles and the distance between them can determine the involvement of higher order multipoles in these interactions. In the case of large or close packed nanoparticles, the scenario becomes significantly more complicated. However, the fundamental optical properties and the

consequent spectral shift and enhanced intensity can still be described by dipole-dipole interaction. When the system is excited by an appropriate polarized incident light, an intensified and highly localized electric field enhancements is observed in the nanogaps between coupled particles. These near-field regions are often referred to as "*hot spots*" and have been widely exploited to enhance optical effects that occur at such small scales, like in the case of surface enhanced Raman spectroscopy (SERS). The presence of a hot spot within the gap between the nanoparticles is tangible evidence of the pronounced interaction between LSPRs.[22]

1.1.5 Photonic crystals and Surface Lattice Resonances

Photonic crystals are materials presenting a dielectric constant that varies periodically in space within the material itself. This property can be exploited to generate constructive and destructive interference patterns within the material, leading to the formation of optical bandgap, which is essentially a range of frequencies where the transmission of light is restricted.[23]

For these interactions to take place, the lattice periodicity needs to be comparable to the wavelength of the incident light, and photonic crystals consequently require an artificial fabrication capable of nanometric precision.

Similar to photonic crystals, the term "*metasurface*" (from Greek "μετά" [meta] meaning "*beyond*") refers to a class of 2D materials whose unique optical properties derive from the arrangement of the nanosized component or building blocks, or "*meta-atoms"*, presenting specific shape and geometries. The rational design of increasingly complex plasmonic architectures allows to tailor and integrate advanced plasmonic and photonic optical properties. Since these properties are distinctively structure-dependent, metamaterial engineering opens unprecedented opportunities in several research fields, paving the way for practical application such as photocatalysis, biosensing, energy harvesting and photonics.

In this introduction, we will focus our attention to metamaterials constituted by plasmonic building blocks. As described in the previous paragraph, for small particles with size *a* separated

by a quantity $d << \lambda_{inc}$, within a range >10 nm, the interaction among them dominates in the near-field region, where a broadening of the resonance and an extreme light confinement with decay rate $\propto d^3$ occurs.

An improvement of the localized plasmon resonances can be achieved by significant boost through the inclusion of far-field coupling of these resonances mediated *via* their scattered radiation fields. In scenarios where particles are randomly distributed, the scattered fields reaching a given particle do not have a specific phase relation, resulting in relatively negligeable effects. Conversely, when metal nanoparticles are arranged in a periodic array with a period Λ comparable to the wavelength of the incident light (λ_{inc}), act as "nanoantennas". Therefore, the particle array can be described as an array of interacting point dipoles. The scattered fields corresponding to diffraction of the incident light on the plane of the array, under appropriate conditions, will arrive in phase with the incident light while impinging on a given particle. Thus, the quality factor (figure of merit expressed as $Q_f = \omega/\Delta\omega$) of the resonance can be significantly increased by appropriate tuning of the array period. Typically, colloidal nanoparticles exhibit Q_f <10 of the LSPR, but values >100 when arranged into arrays.

When nanoparticles are arranged into periodic arrays with lattice pitch (Λ) comparable to the wavelength (λ_{inc}) of the incident electromagnetic radiation, unique collective plasmon resonances arise. Considering the *coupled-dipole approximation* (CDA), this phenomenon is observed when the in-plane scattered field of N plasmonic units arrives in phase with the scattered field of neighboring particles in the array. The LSPR of each nanoparticle in the array can then couple with the diffractive orders of the incident light generated on a patterned surface acting as a plasmonic grating, at wavelengths close to the *Rayleigh-Wood anomalies*. Thus, the collective response induced by the incident EM field, results from the generation of oscillating electric dipoles within the particles, which can re-radiate the field along the orthogonal direction

and couple with the wave vector of the diffraction orders.[24] This coupling leads to the formation of collective optical responses known as *surface lattice resonances* (SLRs).[24–29]

For an array of N particles with polarizability α_n and positions r_n, the induced dipole can be written as:

$$\mathbf{P}_n = \alpha_n \mathbf{E}_{loc,n} \qquad \textbf{(1.14)}$$

where $\mathbf{E}_{loc,n} = \mathbf{E}_{inc,n} + \sum_i \mathbf{E}_{dipole,n}$ is the local field at the nanoparticle at r_n position and represents the sum of the incident field $\mathbf{E}_{inc,i}$, and the retarded fields $\mathbf{E}_{dipole,n}$ produced by N-1 dipoles. In this context a straightforward analytical solution can be derived by assuming the same induced polarization within each particle. Thus, the resulting expression for the induced dipole in each individual plasmonic unit can be written as follows:

$$\mathbf{P} = \frac{\mathbf{E_0}}{1/\alpha_s - \mathbf{S}} \qquad \textbf{(1.15)}$$

where E_0 is the amplitude of the incident plane wave with wavenumber $k = 2\pi/\lambda$, and S is the dipole sum obtained considering the dependence over the angle θ between r_n and the polarization direction induced by the incident field. The dipoles sum S depends on array parameters such as particle size and array period (Λ), providing additional degree of freedom to improve the quality of the SLRs. The excitation of these resonances is triggered when $\mathrm{Re}(1/\alpha s) = \mathrm{Re}(S)$ and then $\mathrm{Re}(1/\alpha s - S)$ approach to zero, leading to a substantial increase in the polarization of individual particles within the array and a resonance effect particularly pronounced. The width of the plasmonic surface lattice resonances is intricately linked to the term $\mathrm{Im}(1/\alpha s - S)$ and can be minimized by compensating the term $\mathrm{Im}(1/\alpha s)$ with $\mathrm{Im}(S)$. Computational analyses suggests that the dipole sum S is significantly large and comparable to α_s when certain diffracted waves propagate along the surface of the array.[24]

This insight supports the characterization of plasmonic SLRs as "diffraction-coupled", emphasizing the role of diffracted waves in shaping the resonance properties of the array. The

dispersion relation of the diffraction orders, which describes these lattice modes on the base of the empty lattice approximation, can be written as: [30,31]

$$|\boldsymbol{k}_0^{\parallel} + \mathbf{G}| = n_{eff}\frac{\omega}{c} \qquad \textbf{(1.16)}$$

where $\boldsymbol{k}_0^{\parallel}$ is the in-plane component of the incident light wave vector $\boldsymbol{k}_0$, and $\mathbf{G} = m_1\mathbf{b_1}+m_2\mathbf{b_2}$ is the reciprocal lattice vector along the same direction as $\boldsymbol{k}_0^{\parallel}$, given by the primitive vectors $\mathbf{b_1}$ and $\mathbf{b_2}$. The spectral position of the Rayleigh-Wood anomalies (λ_{RW}) for an array with lattice period $\Lambda_{x,y}$ can be estimated approximately using the following simplified equation:

$$\lambda_{RW} = \frac{\Lambda_{x,y}}{q}(n_m \pm \sin(\theta)) \qquad \textbf{(1.17)}$$

where n_m represents the refractive index of the array environment, θ is the illumination angle and $q = \sqrt{(m^2 + l^2)}$ is the diffraction order (with m and l integers associated with the lattice vectors of the periodic structure). When only the first order is considered (⟨0, ±1⟩, with m=0, l =±1, and ⟨±1,0⟩, with m =±1, l =0) then q = 1.

In 2D squared arrays the lattice vectors possess identical magnitudes in each direction of the plane (xy), and at $\boldsymbol{k}_0^{\parallel} = 0$ (*i.e.* considering the illumination at normal incidence) the diffractive orders become degenerate, with origin in the same Γ point within the Brillouin's first zone.

As can be evinced from **Eq. 19**, a unique characteristic of SLRs (especially when compared to LSPRs) is their spectral tunability upon varying geometrical parameters such as the lattice pitch, and illumination angle.[29] The resulting surface lattice resonances preserve both their plasmonic and photonic nature, exhibiting strong electromagnetic confinements, intense extinction cross-sections, and high spatial delocalization, longer lifetimes, and narrow spectral features with great quality factors, which increases proportionally to the number of NPs composing the array.[32] For arrays extending in both the x and y directions, this can be understood as the addition of dipoles to the far-field interaction, which scales slowly as $1/d$, due to the reduction of the optical losses, compared to the characteristic $1/d^3$ decay length of near-field interactions, dominating for

closely packed nanoparticles. In **Chapter 3**, we will discuss how the optical properties of SLRs can be engineered using different strategies, making SLRs suitable for applications such as sensing, photonics, and catalysis.

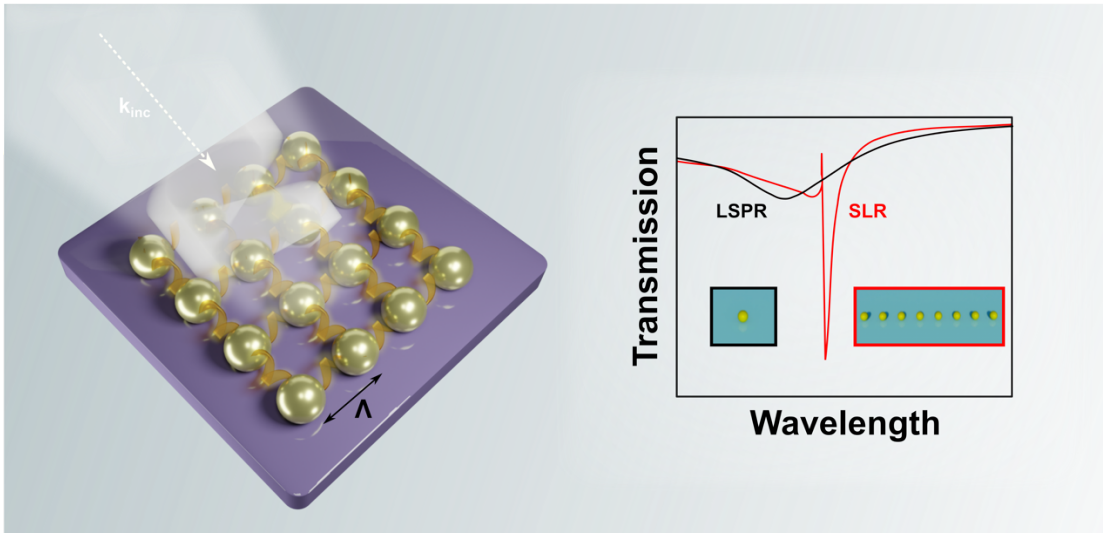

Figure 1.5 Schematic of plasmonic surface lattice resonances (SLRs) in plasmonic array with periodicity Λ. The transmission spectrum on the right shows the narrow bandwidth resonances typically associated with SLRs compared to the broad band LSPRs. Spectrum: Copyright 2018, ACS. Adapted with permission.[24]

1.2 Fundamentals of Non-Linear Optics

When an intense coherent light source interacts with a material, the collective displacement of the charges that generate the resulting outgoing electromagnetic fields undergoes a gradual and asymmetric distortion that affects the overall optical response of the system.[33] This distortion is results in a non-linear (NL) increase in the intensity of the scattered light, typically exhibiting a square or cube dependence on the intensity of the incident optical field. The mathematical description of the NL electromagnetic response is once again based on the study of the polarization vector (**P**), which in this case includes both linear ($\mathbf{P}^{(1)}$) and non-linear ($\mathbf{P}^{(n)}$) polarization vector components. Consequently, there is no longer a linear dependence on the strength of the applied electric field (**E**). Assuming an input field polarized along the *x*-direction,

the expression of **P** of **Eq. 1** can be expanded in power series to include the non-linear terms as:[2]

$$\mathbf{P}_i = \varepsilon_0 \left[\chi_{ij}^{(1)}\mathbf{E}_j + \chi_{ijk}^{(2)}\mathbf{E}_j\mathbf{E}_k + \chi_{jkl}^{(3)}\mathbf{E}_j\mathbf{E}_k\mathbf{E}_l + \cdots\right] = \mathbf{P}_i^l + \mathbf{P}_i^{nl} \qquad \textbf{(1.18)}$$

$$\mathbf{P}_i^{nl} = \varepsilon_0 \left[\chi_{ijk}^{(2)}\mathbf{E}_j\mathbf{E}_k + \chi_{jkl}^{(3)}\mathbf{E}_j\mathbf{E}_k\mathbf{E}_l + \cdots\right] = \mathbf{P}_i^{(2)} + \mathbf{P}_i^{(3)} + \cdots \qquad \textbf{(1.19)}$$

where ε_0 represents the vacuum permittivity, and $\chi^{(1)}$ denotes the first order linear susceptibility of the medium, describing processes like absorption and emission in light-matter interactions discussed in the previous sections of this Chapter. Additionally, $\chi^{(2)}$ and $\chi^{(3)}$ correspond to the second- and third-order non-linear susceptibilities respectively, characterizing higher-order non-linear phenomena. For example, when **Eq. 19** is applied to an incident monochromatic electromagnetic field $\mathbf{E}(\mathbf{r},t) = E_0 e^{j(\mathbf{k}\cdot\mathbf{r}-\omega t)}$, the non-linear terms of polarization ($\mathbf{P}_i^{(2)}$, and $\mathbf{P}_i^{(3)}$) can oscillate at distinct frequencies without contravening the conservation of energy, leading to phenomena such as second (2ω) and third (3ω) harmonic generation, denoted as SHG and THG, respectively. In other example, when the incident field is composed of a superposition of two plane waves $\mathbf{E}(\mathbf{r},t) = \mathbf{E}_1 e^{j(\boldsymbol{k}_1\cdot\mathbf{r}-\omega_1 t)} + \mathbf{E}_2 e^{j(\boldsymbol{k}_2\cdot\mathbf{r}-\omega_2 t)} + cc$, where $\boldsymbol{k}_1$ and $\boldsymbol{k}_2$ are the wave vectors, ω_1 and ω_2 represent the corresponding frequencies of the two interacting tones, and *cc* is the complex conjugation, the NL terms can oscillate at frequencies ($\omega_1 \pm \omega_2$) giving rise to sum (SFG) and difference frequency generation(DFG).[34] The exploration of frequency conversion processes involving the second-order susceptibility $\chi^{(2)}$ has gained considerable attention in the past two decades. These processes have found applications in various fields, including photonics, holography, and invisible cloaking technology.

Similarly to first-order light-matter interactions, higher-order phenomena are also restricted by symmetry rules stemming from the electronic structures of materials. If the structure presents

[2] Einstein notation used for these equations. The order of the tensor is indicated by the upper index (1), (2), (3), while the lower index i, j, k indicate the vector components implicitly summed.

an inversion symmetry center, and an imaginary line is thought to pass through that center, an inversion operation for each point with coordinates (x, y, z) to the corresponding point (-x, -y, -z) will result in the same structure. Consequently, when an electric field with opposite sign is applied (–**E**), the second-order polarization yields $-\mathbf{P}_i^{(2)} = \mathbf{P}_i^{(2)}$, indicating that $\chi^{(2)}$ (or higher-orders susceptibility) must be zero.

In other terms, this implies that centrosymmetric structures retain their properties unaltered under external influences and do not manifest any NL responses. To induce non-linear effects, a symmetry-breaking perturbation in the system becomes crucial, enabling the emergence of non-linear phenomena.

Examples of this symmetry-breaking include surface asymmetries resulting from a slight deviation from a perfect spherical shape,[35,36] as observed in metals displaying second-order effects originating from non-linear dipoles at surfaces,[37] or the presence of multipolar plasmonic resonances, driven by retardation effects associated with nanoparticle size and morphology.[38–40]

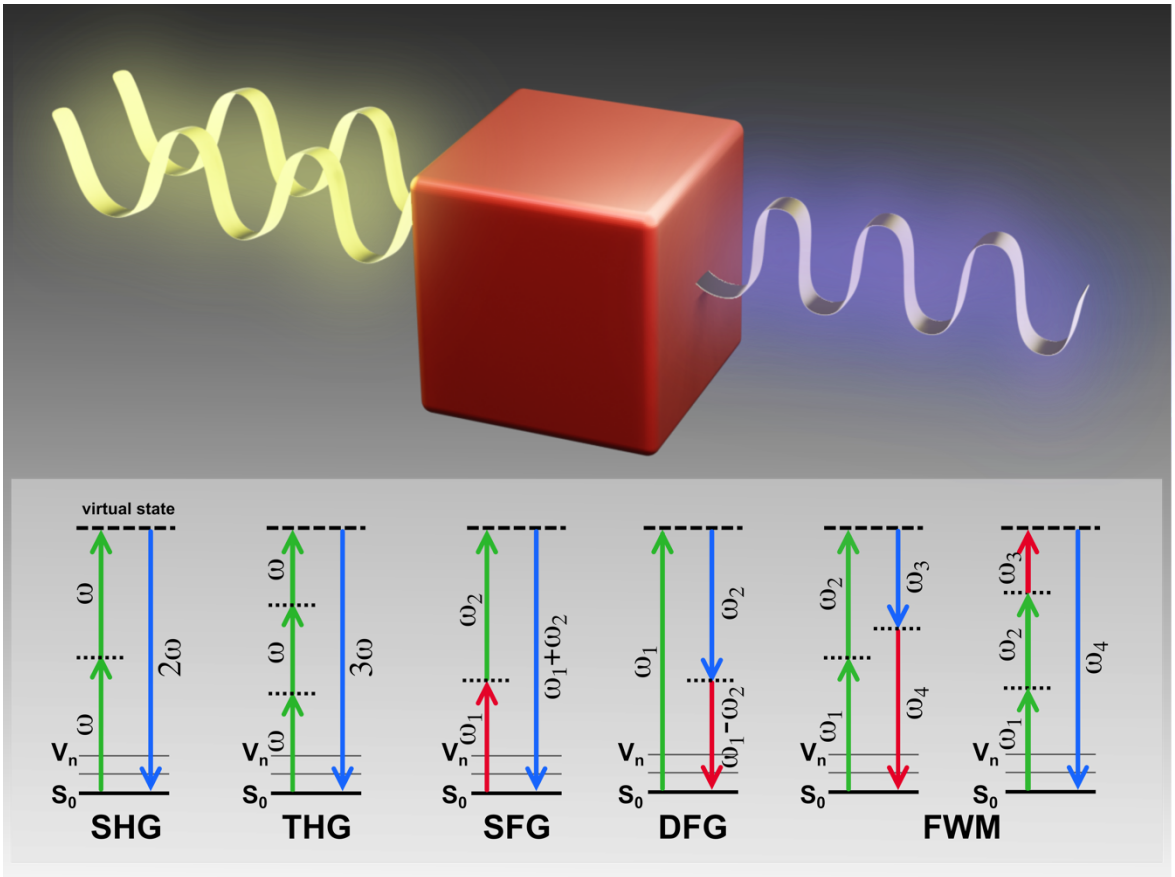

Figure 1.6 **Jablonski diagrams of common NL optical processes.** (**a**) From left to right: second harmonic generation (SHG), third harmonic generation (THG), sum frequency generation (SFG), difference frequency generation (DFG), and four-wave mixing (FWM, non-degenerate case). The virtual excited energy states are represented with **dashed** lines, and the vibrational energy levels with **solid grey** lines. The ground singlet (electronic) energy state is S_0, while the n^{th} singlet (electronic) excited level is S_n, and V_n represents the n^{th} vibrational energy level of the singlet ground energy state (S_0).

All the aforementioned NL optical processes (SHG, THG, SFG, DFG) are categorized as *parametric* processes, for systems that maintain identical initial and final quantum-mechanical states. In these processes, conservation of energy and momentum between interacting photons is facilitated through the nonlinear medium, enabling the ground-level population transition through virtual energetic levels.[34]

On the other hand, processes involving the transfer of population from one real quantum-mechanical state to another are known as *non-parametric* processes. In these cases, the energy of the interacting EM radiation can be transferred to or from the medium. These processes include two-photon absorption (2PA), and two-photon excited photoluminescence (2PPL).

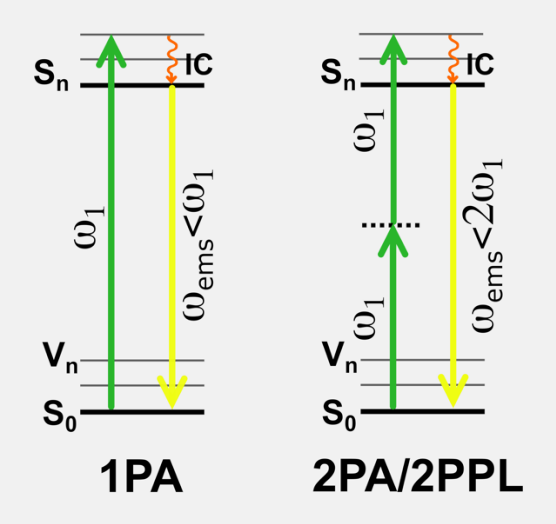

Figure 1.7 Jablonski diagrams of 1PA and 2PA/2PPL processes. From left to right: the one- and two-photon absorption/ photoluminescence processes, respectively represented as one-photon absorption (1PA) and two-photon absorption (2PA). These two processes involve the emission of a photon after the internal conversion process (IC) of the excited electron to the lowest vibrational state of S_n (Kasha's rule).

In both scenarios, the transition from the ground state to an excited state occurs through the simultaneous absorption of two photons with sufficient energy to promote an electron from one level to another. For example, these phenomena have significantly influenced the advancement of two-photon microscopy, enabling deeper tissue penetration with reduced photodamage compared to traditional single-photon bio-imaging techniques.[41]

1.2.1 Plasmonics Metasurfaces for NL Optics

Nowadays, metasurfaces exhibit wide library of shapes and compositions, including nanoholes,[42–45] nanoparticles,[46–48] pillars,[49,50] chiral configurations,[51–56] and antennas systems.[57–60] These almost limitless possibilities translate into an extraordinary versatility in their optical response acting on both the localized plasmonic response of each repeating unit and the geometrical parameters of the array. These parameters determine the quality and spectral position of all localized and collective resonances, thereby enhancing the quantum efficiency of various NL optical processes,[58,61,62] giving an extraordinary ability to shape the wavefront of light with sub-wavelength resolution.[63] **Figure 1.8** reports some interesting examples of this flexibility.

This capability proves essential in fulfilling phase matching condition requirements, crucial aspect in nonlinear optics for frequency conversion,[39,64,65] where incoming light of one frequency (input frequency) generates light at a different frequency (converted frequency). Phase matching is needed to ensure that these different frequencies constructively interfere, maximizing the efficiency of the conversion process. Thus, the mismatch between input and output $\Delta k = k_{out} - nk_{in} = 0$, where k_{out} is the wavevector of the converted frequency, k_{in} represent the wavevector of the input frequencies, and n is an integer. In presence of a periodic structure, the periodicity (Λ) ensures momentum conservation and the equation become $\Delta k\ (\Lambda) = k_{out} - nk_{in} - G(\Lambda) = 0$, where $G(\Lambda)$ is the wavevector associated with the grating). By satisfying this condition, the periodic structure ensures that the sum of the wavevectors of the input and converted waves, along with the wavevector associated with the structure remains unchanged, allowing the efficient NL conversion over extended interaction length.

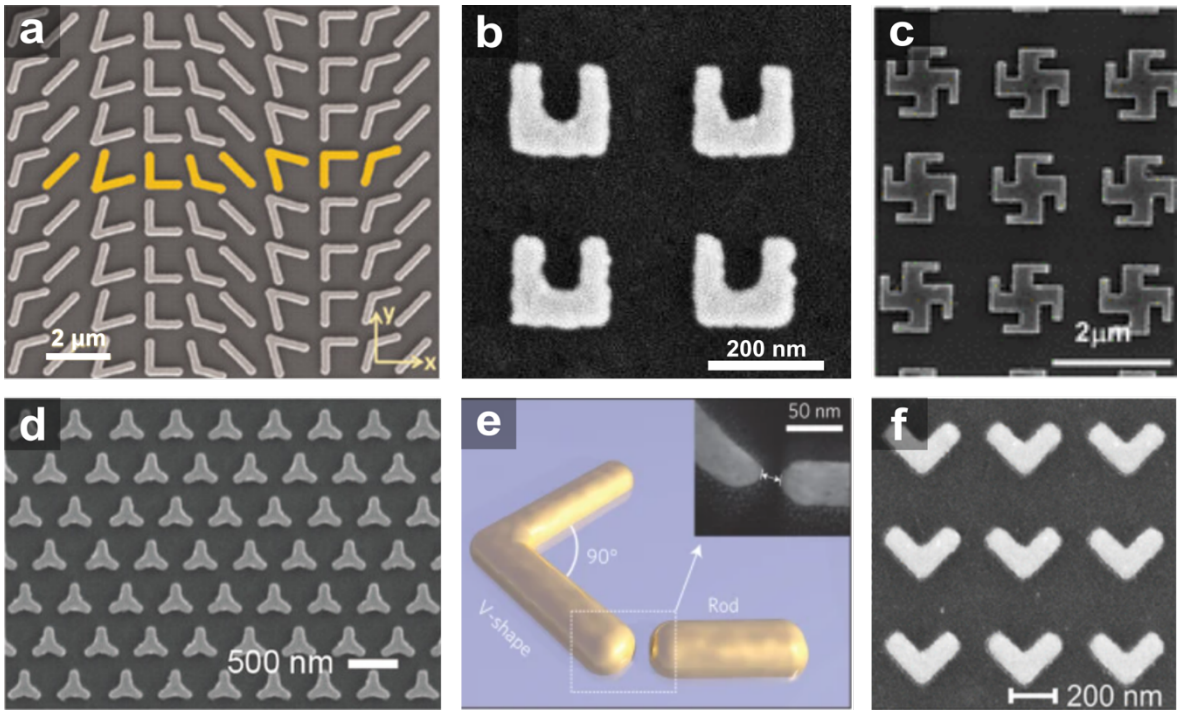

Figure 1.8 **Plasmonic metasurfaces for NL optics**. Scanning Electron Microscopy images of (**a**) phase-gradient metasurface; (**b**) gold split-ring resonator square arrays; (**c**) Gammadion-type geometry third non-linear response respectively, displaying near-unity circular dichroism; (**d**) hybrid plasmonic-Epsilon-Near-Zero metasurface; (**e**) multiresonant antennas for SHG response; (**f**) non-centrosymmetric V-shaped gold nanoparticles. **Panel a**: Copyright 2011, Science. Adapted with permission.[66] **Panel b**: Copyright 2012, APS. Adapted with permission.[67] **Panel c**: Copyright 2020, ACS. Adapted with permission.[52] **Panel d**: Copyright 2020, ACS. Adapted

with permission.[68] **Panel e**: Copyright 2018, ACS. Adapted with permission.[69] **Panel f**: Copyright 2015, Springer Nature. Adapted with permission.[61]

1.2.2 Colloidal-based plasmonic metasurfaces for NL Optics

The exploration of NL optical phenomena through experimentation is centered on the advancement of sophisticated nanofabrication techniques to create high-quality plasmonic metasurfaces, as mentioned above. These technological advances, aimed to enhance the confinement of the associated electromagnetic field, have ultimately elevated the optical non-linearity in material responses under low pump intensities, avoiding the need of intricate phase matching techniques.[70,71]

A detailed discussion on alterative fabrication strategies will be discussed in **Chapter 2**. Here, the discussion is limited to the potential prospective and advancements of the use of colloidal metasurfaces in the fields of NL optics.

The growing scientific interest in metamaterials has given rise to a new phase of development called the "chemistry of metamaterials". The attention is drawn onto the development of engineered properties that can be dynamically modified or that enable interaction with the surrounding chemical environment, generating materials capable of responding chemically, catalytically or undergo a phase change. It also involves the molecular functionalization of unit cells to enable responses based on receptors, pH or electrochemistry.[72–75] In this context, nonlinear optical phenomena offer a unique avenue for progress. Spectroscopic techniques that rely on second- or third-order susceptibilities encode intricate molecular details, allowing information about the surrounding chemical environment to be extracted directly from their optical responses.[34]

The successful fabrication of metamaterials tailored to interact with the chemical environment presents both scientific and technological hurdles. Originally designed for microelectronics, these materials pose challenges to standard nanofabrication processes such as metal evaporation and hard lithography techniques. These conventional methods provide limited control over

crystallography and surface chemistry, requiring innovative approaches for effective metamaterial fabrication in chemical applications. Consequently, the pursuit of chemically active metasurfaces has prompted the scientific community to explore alternative fabrication strategies. In this context, colloidal self-assembly has emerged as a promising candidate. On the one hand, colloidal synthesis offers unprecedented precision in controlling nanoparticle morphology, crystallography, composition, and surface chemistry. On the other hand, self-assembly strategies have advanced to the point where high-quality periodic and hierarchical arrangements can be produced on a large scale.

1.2 Plasmonics and Emission phenomena

"***Photoluminescence***" is a phenomenon consisting in the emission of light by materials when an external source of energy provides to the system sufficient energy to trigger that emission. In particular, energy is provided by the absorption of electromagnetic radiation in the range of the spectrum between UV and IR. Fluorophores or chromophore, utilized for their fluorescent properties, are molecules characterized by their ability to emit light. The efficiency of a fluorophore as a fluorescent compound and the specific wavelengths of absorption and emission are determined by the outermost electron orbitals within the molecule.

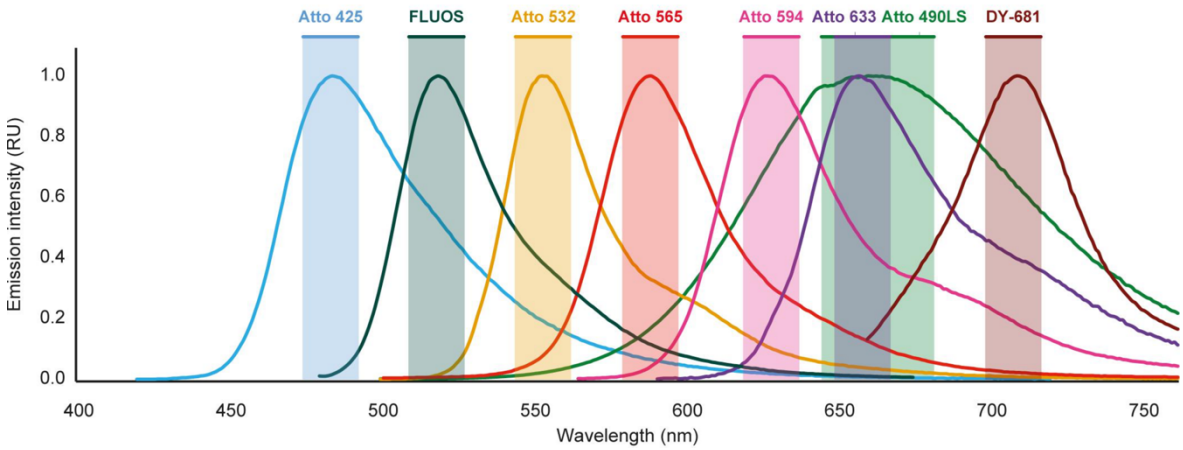

Figure 1.9 Emission Spectra of some common dyes used for investigating fluorescence in situ hybridization with rRNA-targeted oligonucleotide probes. Copyright 2019, Front. Microbiol. Adapted with permission.[76]

Atoms and molecules exhibit quantized energy levels, wherein electrons occupy successively higher energy states while subjected to the Pauli exclusion principle. The absorbed energy can propel an electron from the "*ground state*" to a different orbital, leading to a rapid transition (in femtoseconds timescale) to an "*excited state*". The absorbed energy is released through processes such as vibrational relaxation and emission of a photon emission energy E=hν, where ν is the frequency associated with the energy difference between the two levels involved, which are the main mechanisms by which a fluorophore returns to its low-energy ground state.[77]

This relaxation transition is regulated by selection rules, and various allowed and forbidden decay channels exist through which the energy can be released. Radiative mechanisms, such as fluorescence or spontaneous emission, release energy in the form of photons. Conversely, non-radiative decay mechanisms involve the transfer of thermal or acoustic energy to the surrounding medium. The decay rate between the two energy levels follows an exponential law. By exciting a fluorophore sample with a narrow enough pulse of light monochromatic light, capable of instantaneously generating a population in an excited state the time evolution of the population N in the excited state can be evaluated as:[78]

$$\frac{dN(t)}{dt} = -k \cdot N(t) \qquad \textbf{(1.20)}$$

k is the decay constant given by the sum of the constants for the radiative (Γ) and non-radiative (k_{nr}) decays, both mechanisms are dictated energy levels structure of the active medium.

Integrating **Eq. 1.20**, the result is a time distribution of the emitted photons, which composes an exponential decay profile of the population of the excited state N(t) as:

$$\int_{N_0}^{N} \frac{dN(t)}{dt} = -k \cdot \int_0^t N(t) \qquad \textbf{(1.21)}$$

$$N(t) = N_0 e^{-(\Gamma + k_{nr})t} = N_0 e^{-t/\tau} \qquad \textbf{(1.22)}$$

The emission of fluorescence by fluorophore molecules is a random event and is by nature incoherent [13]. Out of a relatively large number of excited fluorophores, only few molecules manage to emit in a time comparable to the lifetime (τ) of fluorescence, while the others emit

in longer times.[79] In a fluorescence experiment, it is not the number of excited fluorophores that is observed, but a fluorescence intensity fluorescence I(t), which is proportional to the population of the excited state at time t:

$$N(t) \propto I(t) = I_0 e^{-t/\tau} \quad \textbf{(1.23)}$$

The fluorescence efficiency, quantified by the quantum yield (QY) given as the ratio between the radiative (Γ_{rad}) and non-radiative (k_{nr}) emissive events, tends to increase with the number of π-bonds in the molecule. This quantity dependents on the lifetime (τ) of a molecule, *i.e.* the time taken from the molecule to relax to the first vibrational state of the excited state, from which it then emits a photon of light.

The emission of fluorescence is an inherently spontaneous process, and the relaxation rate is dictated by the electromagnetic surroundings. For example, the fluorophores spectral profile is strongly influenced by the polarity and proticity of its environment, which can cause an emission shift. Once electromagnetic radiation is absorbed, fluorophores instantaneously populate the excited states and for the time they reside in these levels, they can interact with their surroundings. The property that measures the probability of light absorption in a solution containing the fluorophore is known as *molar extinction coefficient* (ε, $M^{-1}cm^{-1}$). A larger cross-section means a greater probability of capturing a photon. Therefore, a dye with a higher extinction coefficient will produce a stronger signal for the same level of light-induced background than one with a lower extinction coefficient.

1.2.1 Quantum emitters

Quantum dots (QDs) are different from most particles/molecules and their unique optical and electrical properties, mainly due to quantum mechanical phenomena, make them excellent candidates for different applications including photocatalysis,[80] sensors,[81] and fluorescent chiral nanoprobes.[82] These entities consist of nanometer-scale semiconductor crystals displaying opto-electronic properties dependent on their size.[83,84]

Typically ranging from 1 to 100 nm, these nanocrystals bridge the gap between small molecules and macroscopic crystals. They can be made from either single-component or multi-component materials and formed in a variety of shapes configurations such as dots, rods, trimers and tetramers, all determined by the arrangement of the underlying crystal lattice.[37] The crystalline nature of these particles gives them a high density of electronic states, resulting in huge extinction coefficients and broad absorption spectra, not available in organic chromophores. Thus, the optoelectronic properties strongly dependent from sizes as denoted by absorption and fluorescence spectra in **Figure 1.10**, displaying discrete electronic transitions. The unicity of these systems rely on the possibility to precisely engineering size and composition to control this energy difference, allowing for tunable emission across a wide range of wavelengths.[85]Heterostructures such as core-shell quantum dots (QDs) are particularly well suited for nanophotonic applications. A passivate surface core of semiconductor material with a coating or a shell, typically made by higher bandgap semiconductor material,[86] serves to protect the QDs against degradation due to aggregation and photooxidation. Consequently, this contributes to the enhancement of the photoluminescence quantum efficiency and stability, respectively 20 and 100 times higher than typical organic dye molecules.[87]

By selecting specific materials for core and shell, it is possible to achieve greater control over the confinement of charge carriers wave functions, which allows to tune absorption and emission spectral overlap and thus optimize matching requirements for the desired device, while mitigating reabsorption losses.

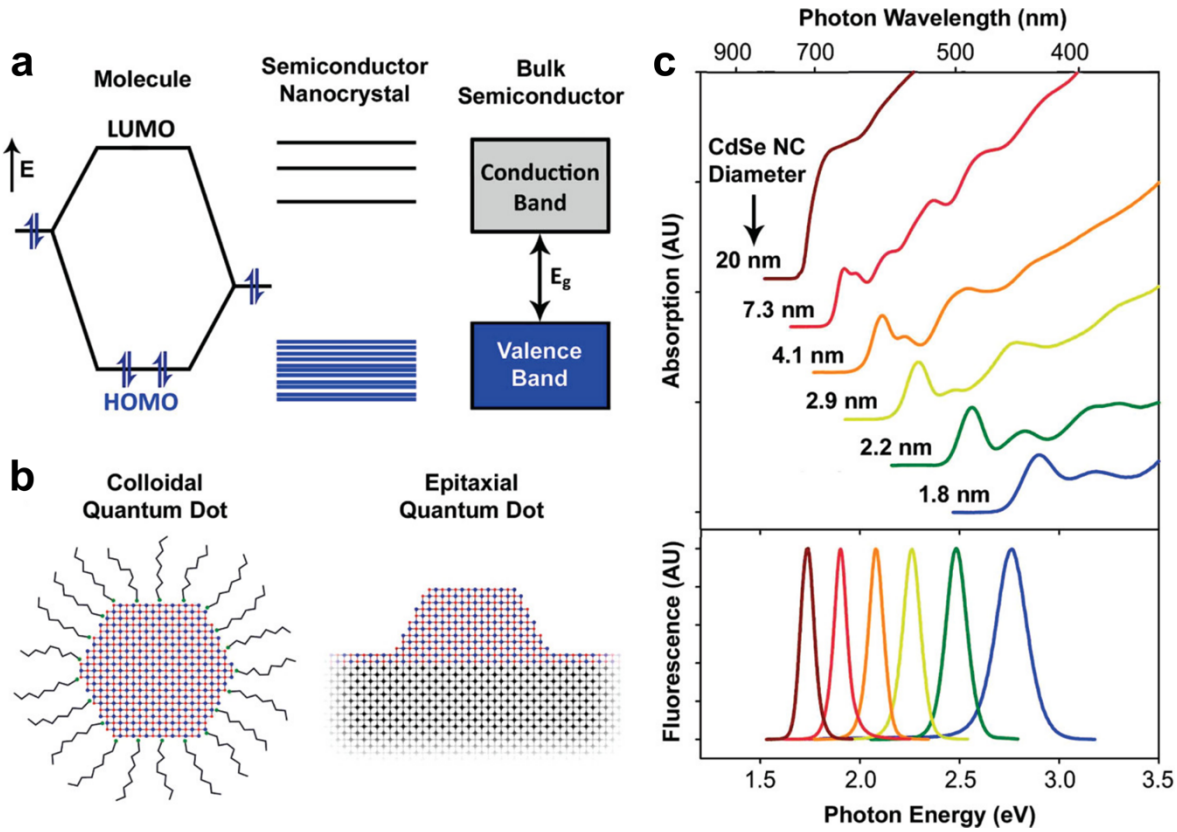

Figure 1.10 (**a**) Schematic of the electronic energy states of a semiconductor passing from discrete molecules to semiconductor nanosized and bulk crystals. The ground state electron occupation is depicted in blue shading. The band gap energy denoted as E_g denotes the minimum energy required to excite an electron from the ground state valence band to the vacant conduction energy band. (**b**) Comparison between two common fabrication methods: colloidal quantum dot suspension, which provide great control over the morphology and monodispersity, and a self-assembled quantum dot (island-like) epitaxially deposited on a crystalline substrate. **c**) Spectra displaying absorption (**upper**) and fluorescence (**lower**) of CdSe semiconductor nanocrystals, highlighting quantum confinement and size tunability. AU denotes arbitrary units. **Panel a**, **b**, **c**: Copyright 2010, ACS. Adapted with permission.[88]

1.3 Plasmonic array coupling with gain media

As we have discussed in this introduction, the collective oscillations of electrons of a metal structure are associated with unique electromagnetic properties. These properties can be exploited to strongly influence nearby gain media emission behavior, and when plasmons and dye molecules are brought into proximity their interaction leads to a range of fascinating phenomena. Tailored nanostructures exert a deep influence on the kinetics of light emission of luminescent materials, and these effects become versatile toolbox, allowing control over

emission efficiency, spatial localization, directional angular distribution, anisotropic polarization, and spectral linewidth for improved quality.

The modification of light-matter interactions mediated by a plasmonic cavity can take place under two possible regimes: the *weak* and the *strong* coupling regimes.

1.3.1 Weak coupling regime Purcell Effect

When an emitter interacts with a photonic crystal, its PL can be significantly modified, including spectrum reshaping and shifts, polarization changes, intensity enhancement or quenching, modulation of both radiative and non-radiative decay rates.[89–92]

Plasmon-enhanced fluorescence was first explored alongside investigations into surface-enhanced Raman spectroscopy during the 1970s and 1980s.[93–95] In recent times, there has been a resurgence of interest in studying in surface enhanced fluorescence, driven by advancements in the precise manipulation of different aspects of this phenomenon.

One of the most extensively studied phenomena in the weak coupling regime involves the alteration of the spontaneous emission rate of an emitter. First proposed by Purcell for the case of a single mode cavity,[96] the enhance in spontaneous emission of a quantum emitter within a cavity was attributed to the increase local density of states compared to free space, whit the emission rate of a quantum emitter directly proportional to the LDOS The Purcell factor (F_P) can therefore be defined as the ratio of the spontaneous emission rate in a cavity (Γ_c) to the emission rate in free space (Γ_0):[97]

$$F_P = \frac{\Gamma_c}{\Gamma_0} = \frac{6\pi c^3 n^3 \omega_c}{Q_f V_{eff}} \qquad \textbf{(1.24)}$$

where *n* represents the refractive index within the cavity, and c is the speed of light. Compared to dielectric cavities typically characterized by high Q_f, but with large mode volumes that limit experimentally the F_P,[98] photonic crystals support strong field enhancements and a significantly altered LDOS, thereby offering a versatile means to control the spontaneous emission rate.

Under weak-coupling conditions, for an emitter positioned in proximity to or within a photonic crystal both the excitation rate and emission rate can be altered. The overlap of the absorption spectrum of the emitter with the plasmon band is essential to induce the enhancement of local field and elevate its excitation rate Γ_{exc}, that heavily depends on the orientation of the emitter dipole relative to the electric field polarization direction of the photonic crystal.

During the emission process, the presence of the plasmonic cavity modifies the direct radiation channel of the emitter, which requires a spectral overlap between the emitter emission and the plasmon resonance. Additionally, the excited-state energy of the emitter can be transferred to the metal, through Förster resonance energy transfer,[99] and then dissipated in the metal (ohmic losses) or emitted by the metal with a very low quantum efficiency. The coupling between dipole emitters and plasmon resonances may also alter the emission direction and polarization,[90] thus, by employing anisotropic plasmonic nanostructures and multicomponent plasmonic nanostructures it is possible to control the spatial direction and angular distribution of the emission.[100,101]

Overall, by rationally design a plasmonic Researchers have been integrated plasmonic metasurfaces with a variety of emissive materials (**Figure 1.11**) such as dye solutions, lanthanide complexes and chelated transition metals, carbon nanotubes (CNTs), semiconducting quantum dots (QDs), 2D materials and perovskites, leading to an enhance of spontaneous emission and even the generation of stimulated emission, due to the overlap of surface lattice resonance modes with the emission bandwidth.[31,102–110]

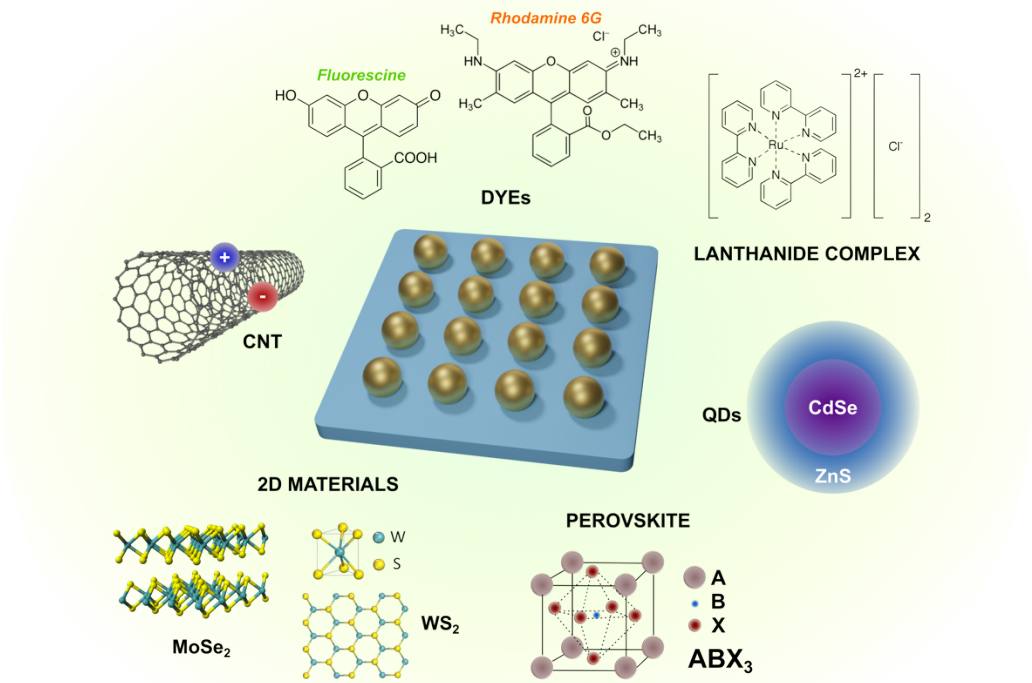

Figure 1.11 Illustration of plasmonic metasurfaces (e.g. Au, Ag, Cu, Al, Ni nanoparticles) and emitter species (dyes molecules, carbon nanotubes (CNTs), lanthanide complexes, quantum dots (QDs), 2D and 3D materials such as Molybdenum diselenide, Tungsten disulfide, perovskites etc.).

1.3.2 Plasmonic metasurfaces: other applications

Nanostructured metasurfaces have been explored as effective toolbox for the manipulation of light-matter interactions at the nanoscale. These effects open up new avenues for plasmonic metasurfaces to impact several scientific and technological fields. For example, efficient light trapping could have significant impact in the context of photovoltaics, where efficient light absorption in the active layer is crucial for subsequent conversion into electrical current. While a thin active layer is preferred for better charge separation, it often leads to a significant drop in light harvesting efficiency, and surface roughness poses a significant challenge to carrier recombination in surface and junction regions. The utilization of nanostructured surfaces offers a solution to overcome these challenges by reducing the physical thickness of the solar cell while retaining the desired scattering effect that enhances the effective path length of incoming light.[111]

To obtain this effect, nanoparticles can act as subwavelength resonant scatterers,[112] effectively trapping incident light and redirecting propagating plane waves from the sun into a thin absorber layer, or they can function as electrodes to collect photocurrent.[113] Alternatively, nanoparticles can be used as nanoantennas to couple the plasmonic near-field to the surrounding semiconductor material, thereby increasing the absorption cross-section of the material.[114,115] The application of metallic plasmonic structures in solar cells has developed rapidly, allowing the active layer to be reduced (>100 nm), resulting in physically thin but optically efficient absorbers.[111] However, challenges such as finding optimal geometries using low-cost metals and overcoming large-scale manufacturing issues hinder potential commercial applications.

The impact of plasmonics goes far beyond the field of photovoltaics, and sensing and phototherapy fields have experienced exponential growth in recent decades by exploiting the combination of plasmonics with chemistry, biology, and medicine, opening new avenues for innovative applications and research. In fact, surface lattice resonances exhibit exceptional spectral sensitivity attributed to the periodicity of their structures and remarkably high phase sensitivity. These distinctive features make plasmonic SLRs excellent candidates for the label-free characterization of biomolecular interactions, facilitating the study of interactions between target analytes (such as antigens, DNA) and their corresponding receptors (e.g., antibodies, DNA capture, proteins).[75,116–119]

For example, Kravets *et al.* exploited the potential of SLRs of gold nano-resonator arrays to enable refractive index monitoring and demonstrate an order of magnitude higher phase sensitivity than SPP sensors based on the Kretschmann configuration.[120] In a follow-up investigation, it was proposed the use of gold double dot arrays on glass coated with a weakly hydrogenated graphene crystal as plasmonic resonators. This innovative approach showed a significant variation in reflected light intensity together with rapid phase changes, suggesting the viability of these plasmonic devices for molecular recognition with enhanced sensitivity at the single molecule level.[121]

Recently, metamaterials have emerged as a key advancement in harnessing the potential of plasmonic nanostructures even for practical and scalable photocatalytic applications. This development represents a crucial step forward in leveraging plasmonic effects on a larger, more usable scale.[122,123]

Narang and collaborators, for example, have explored the field of plasmon-enhanced chemistry in various configurations and reactions.[124–126] Metasurfaces play a key role in increasing the solar light absorption capacity, thereby promoting the generation of hot carriers. Their distinctive feature lies in the large surface area they provide, which creates an abundance of catalytic active sites that are favorable to surface reactions.

Deng *et al.* presented a notable example using a two-dimensional array of bimetallic Cu–Pt core–shell nanoparticle lattices, combination of highly catalytically active Pt sites with the robust plasmonic effects of Cu, where the most substantial photocurrent densities were observed under near-IR illumination.[127] The SLRs emerged as the major contributors to the observed photocurrent enhancement under white light illumination, surpassing the excitations from localized surface plasmon resonances. As result, a twofold improvement in hydrogen evolution reaction (HER) catalytic activity was observed, due to the superior light absorption efficiency and highly confined electromagnetic fields exhibited by the lattice modes. The proper design of a metasurface, showing enhancements in the efficiency of catalytic nanostructures for driving hydrogen evolution reactions, can demonstrates the high potential of these systems in advancing catalysis through plasmonic effects.

Over the years, metasurface research was extended to the integration of non-classical light sources including Second Harmonic Generation (SHG) and single-quantum emitters, opening new possibilities to enhance the overall capability of light-emitting systems.[128] This innovative approach not only addresses the challenges posed by conventional optical components but also explores novel avenues for creating advanced and efficient light-emitting devices. In the realm of conventional Light-Emitting Diodes (LEDs), for example, a significant challenge lies in their

low light extraction efficiencies attributed to total internal reflection at the encapsulation layers, where the critical angle is set at 30°. While total internal reflection (TIR) serves as the basis for various applications, particularly in the realm of fiber optics that has transformed the communication technology, it poses challenges in other applications like light-emitting diodes (LEDs), hindering the photons extraction from the high-index materials constituting the LED device and thus the energy-efficient lighting.

A recent work conducted in LED technology involved the cost-effective integration of index-matching layers with disordered Ag nanoparticles, specifically designed for commercial Gallium Nitride (GaN) LEDs. The innovative fabrication method employs a single-step process using gas-phase cluster beam deposition to create the Ag nanoparticles. The efficiency improvement, reaching a factor of 1.65, was achieved by effectively extracting photons at incident angles beyond 60°.[129]

1.3.3 Strong coupling regime

Conversely to the weak coupling regime, in the strong coupling regime the resonant interaction between excitons and plasmons alter the exciton wave functions and plasmon modes, resulting in significant changes in the spontaneous emission rate and the energy levels of the system. Within this regime, excitation energy is reversibly exchanged before any losses occurs between the plasmonic and excitonic systems, manifesting as Rabi oscillations and typically exhibiting anticrossing and splitting of energy levels at the resonance frequency in the cavity's spectrum (**Figure 1.12**).[89]

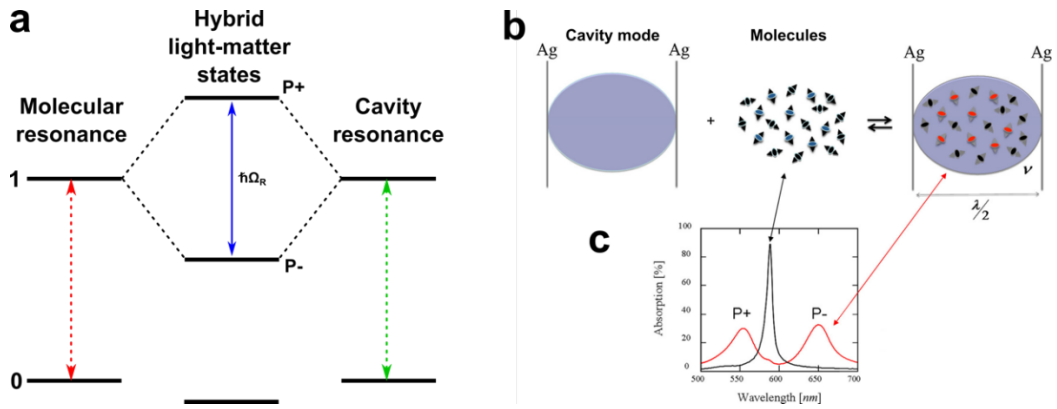

Figure 1.12 Diagram of (**a**) molecular transition and a cavity resonance coupling, which leads to form two hybrid light–matter states upper polariton (P+) and lower polariton (P–) are separated by the so-called Rabi splitting energy $\hbar\Omega_R$. (**b**) Schematic of the λ/2 mode formed in a Fabry–Perot cavity (two parallel Ag mirrors) resonant with the absorption of molecules (represented as little dipoles). Once placed inside the cavity interact strongly with the mode, the coupling leads to the formation of light–matter hybrid states. (**c**) Absorption spectrum of a cyanine dye molecule before (**black** curve) and after (**red** curve) undergoing strong coupling with a cavity resonance. Panel b, c: Copyright 2016, ACS. Adapted with permission.[130]

The new energy levels of this hybrid system differ significantly from those of the individual quantum emitter and electric field. Strong coupling mediated phenomena has been successfully demonstrated between plasmonic nanoparticle lattices and various entities, including dye molecules, organic linkers in metal–organic frameworks (MOFs), ideal platform to organize organic emitters with specific orientations and in a denser volumes, single-walled carbon nanotubes (CNTs), and 2D materials.[131–137]

In general, an emitter can be considered as a two-level system characterized by a ground state $|g\rangle$ and an excited state $|e\rangle$) with transition frequency ω_{eg} (of the emitted light). The transition dipole moment $\vec{\mu}_{eg}$ quantifies the electron's distribution changes during the transition between the two energy states, occurring with a spontaneous emission rate (Γ). On the other side, the cavity where the emitter is placed is characterized by a resonance frequency ω_c and a damping rate γ, associated to the quality factor of the cavity as $Q_f = \omega_c/\gamma$.

Thus, the coupling strength between the emitter and the cavity (g) is related to the rate of energy transferred and it can be expressed as follows:[97]

$$g = \vec{\mu}_{eg} \cdot E = \vec{\mu}_{eg} \cdot \sqrt{\frac{\hbar\omega_c}{2\varepsilon_0\varepsilon_r V_{eff}}} \quad \textbf{(1.25)}$$

where, E is the electric field within the cavity, ε_0, and ε_r represent the vacuum and relative permittivity respectively, and V_{eff} is the effective mode volume within which the electromagnetic field associated with a particular mode of a cavity is concentrated and interacts with the surrounding environment. This term includes the spatial extent of the localized density of states (LDOS), for which small mode volumes lead to larger LDOS values and stronger cavity-emitter coupling strengths. For N emitters in the cavity, the coupling strength becomes √N larger.[89]

Transitioning from weak to strong coupling can be achieved by either enhancing the coupling strength g or reducing the decay rates of both the cavity (γ) and the emitter (Γ).

For the cavity, this can occur when the quality factor is increased and the effective mode volume is reduced, implying a mitigation of optical losses and amplification the electric field within the cavity. This explains the interest in the construction of plasmonic cavity characterized by a high Q_F, representing one of the driving motivations of this thesis work.

Looking at the emitter, the associated emission rate Γ can be improved by lowering the temperature of the system (mitigating non-radiative phenomena such as…), or by increasing the number of emitters coupled to the same optical cavity, generating a larger effective dipole moment that boosts the strength of the coupling towards the establishment of a strong coupling regime.[97] The development of dynamic functional devices operating in the strong coupling regime would open completely new directions towards a new type of chemistry, the so called strong coupling chemistry, where the reactivity and kinetics of molecular system could be manipulated by their interaction with an optical (plasmonic) cavity. Despite this is an exciting and rapidly evolving research direction, this thesis will focus on the fabrication and characterization of colloidal plasmonic metasurfaces operating exclusively in the strong coupling regime.

1.4 References

(1) Thompson, D. Michael Faraday's Recognition of Ruby Gold: The Birth of Modern Nanotechnology. *Gold Bull.* **2007**, *40* (4), 267–269. https://doi.org/10.1007/BF03215598.

(2) Chari, C. S.; Taylor, Z. W.; Bezur, A.; Xie, S.; Faber, K. T. Nanoscale Engineering of Gold Particles in 18th Century Böttger Lusters and Glazes. *Proc. Natl. Acad. Sci.* **2022**, *119* (18), e2120753119. https://doi.org/10.1073/pnas.2120753119.

(3) Mogerman, W. D. Faraday's Lecture on Gold. *Gold Bull.* **1974**, *7* (1), 22–24. https://doi.org/10.1007/BF03215030.

(4) Maier, S. A. *Plasmonics: Fundamentals and Applications*; Springer: New York, 2007.

(5) Jain, P. K.; Huang, X.; El-Sayed, I. H.; El-Sayed, M. A. Noble Metals on the Nanoscale: Optical and Photothermal Properties and Some Applications in Imaging, Sensing, Biology, and Medicine. *Acc. Chem. Res.* **2008**, *41* (12), 1578–1586. https://doi.org/10.1021/ar7002804.

(6) Pitarke, J. M.; Silkin, V. M.; Chulkov, E. V.; Echenique, P. M. Theory of Surface Plasmons and Surface-Plasmon Polaritons. *Rep. Prog. Phys.* **2007**, *70* (1), 1–87. https://doi.org/10.1088/0034-4885/70/1/R01.

(7) Baburin, A. S.; Kalmykov, A. S.; Kirtaev, R. V.; Negrov, D. V.; Moskalev, D. O.; Ryzhikov, I. A.; Melentiev, P. N.; Rodionov, I. A.; Balykin, V. I. Toward a Theoretically Limited SPP Propagation Length above Two Hundred Microns on an Ultra-Smooth Silver Surface [Invited]. *Opt. Mater. Express* **2018**, *8* (11), 3254–3261. https://doi.org/10.1364/OME.8.003254.

(8) Zhang, J.; Zhang, L.; Xu, W. Surface Plasmon Polaritons: Physics and Applications. *J. Phys. Appl. Phys.* **2012**, *45* (11), 113001. https://doi.org/10.1088/0022-3727/45/11/113001.

(9) Kelly, K. L.; Coronado, E.; Zhao, L. L.; Schatz, G. C. The Optical Properties of Metal Nanoparticles: The Influence of Size, Shape, and Dielectric Environment. *J. Phys. Chem. B* **2003**, *107* (3), 668–677. https://doi.org/10.1021/jp026731y.

(10) Cognet, L.; Tardin, C.; Boyer, D.; Choquet, D.; Tamarat, P.; Lounis, B. Single Metallic Nanoparticle Imaging for Protein Detection in Cells. *Proc. Natl. Acad. Sci.* **2003**, *100* (20), 11350–11355. https://doi.org/10.1073/pnas.1534635100.

(11) Mie, G. Beiträge Zur Optik Trüber Medien, Speziell Kolloidaler Metallösungen. *Ann. Phys.* **1908**, *330* (3), 377–445. https://doi.org/10.1002/andp.19083300302.

(12) Meier, M.; Wokaun, A. Enhanced Fields on Large Metal Particles: Dynamic Depolarization. *Opt. Lett.* **1983**, *8* (11), 581–583. https://doi.org/10.1364/ol.8.000581.

(13) Liz-Marzán, L. *Colloidal Synthesis of Plasmonic Nanometals*; CRC Press, 2020.

(14) Wang, W.; Ramezani, M.; Väkeväinen, A. I.; Törmä, P.; Rivas, J. G.; Odom, T. W. The Rich Photonic World of Plasmonic Nanoparticle Arrays. *Mater. Today* **2018**, *21* (3), 303–314. https://doi.org/10.1016/j.mattod.2017.09.002.

(15) Jin, R.; Charles Cao, Y.; Hao, E.; Métraux, G. S.; Schatz, G. C.; Mirkin, C. A. Controlling Anisotropic Nanoparticle Growth through Plasmon Excitation. *Nature* **2003**, *425* (6957), 487–490. https://doi.org/10.1038/nature02020.

(16) Gao, P. F.; Lei, G.; Huang, C. Z. Dark-Field Microscopy: Recent Advances in Accurate Analysis and Emerging Applications. *Anal. Chem.* **2021**, *93* (11), 4707–4726. https://doi.org/10.1021/acs.analchem.0c04390.

(17) Roy, D.; Knight, A. E. Scanning Near-Field Optical Microscopy and Related Techniques. In *Encyclopedia of Spectroscopy and Spectrometry (Third Edition)*; Lindon, J. C., Tranter, G. E., Koppenaal, D. W., Eds.; Academic Press: Oxford, 2017; pp 1–6. https://doi.org/10.1016/B978-0-12-803224-4.00011-X.

(18) Nordlander, P.; Oubre, C.; Prodan, E.; Li, K.; Stockman, M. I. Plasmon Hybridization in Nanoparticle Dimers. *Nano Lett.* **2004**, *4* (5), 899–903. https://doi.org/10.1021/nl049681c.

(19) Brandl, D. W.; Oubre, C.; Nordlander, P. Plasmon Hybridization in Nanoshell Dimers. *J. Chem. Phys.* **2005**, *123* (2), 024701. https://doi.org/10.1063/1.1949169.

(20) Cortés, E.; Wendisch, F. J.; Sortino, L.; Mancini, A.; Ezendam, S.; Saris, S.; de S. Menezes, L.; Tittl, A.; Ren, H.; Maier, S. A. Optical Metasurfaces for Energy Conversion. *Chem. Rev.* **2022**. https://doi.org/10.1021/acs.chemrev.2c00078.

(21) Halas, N. J.; Lal, S.; Chang, W.-S.; Link, S.; Nordlander, P. Plasmons in Strongly Coupled Metallic Nanostructures. *Chem. Rev.* **2011**, *111* (6), 3913–3961. https://doi.org/10.1021/cr200061k.

(22) Le, K. Q.; Alù, A.; Bai, J. Multiple Fano Interferences in a Plasmonic Metamolecule Consisting of Asymmetric Metallic Nanodimers. *J. Appl. Phys.* **2015**, *117* (2), 023118. https://doi.org/10.1063/1.4905619.

(23) Novotny, L.; Hecht, B. *Principles of Nano-Optics*; Cambridge University Press: Cambridge, 2006. https://doi.org/10.1017/CBO9780511813535.

(24) Kravets, V. G.; Kabashin, A. V.; Barnes, W. L.; Grigorenko, A. N. Plasmonic Surface Lattice Resonances: A Review of Properties and Applications. *Chem. Rev.* **2018**, *118* (12),

5912–5951. https://doi.org/10.1021/acs.chemrev.8b00243.

(25) Kravets, V. G.; Schedin, F.; Grigorenko, A. N. Extremely Narrow Plasmon Resonances Based on Diffraction Coupling of Localized Plasmons in Arrays of Metallic Nanoparticles. *Phys. Rev. Lett.* **2008**, *101* (8), 087403. https://doi.org/10.1103/PhysRevLett.101.087403.

(26) Rodriguez, S. R. K.; Schaafsma, M. C.; Berrier, A.; Gómez Rivas, J. Collective Resonances in Plasmonic Crystals: Size Matters. *Phys. B Condens. Matter* **2012**, *407* (20), 4081–4085. https://doi.org/10.1016/j.physb.2012.03.053.

(27) Zhao, L.; Kelly, K. L.; Schatz, G. C. The Extinction Spectra of Silver Nanoparticle Arrays: Influence of Array Structure on Plasmon Resonance Wavelength and Width. *J. Phys. Chem. B* **2003**, *107* (30), 7343–7350. https://doi.org/10.1021/jp034235j.

(28) Humphrey, A. D.; Meinzer, N.; Starkey, T. A.; Barnes, W. L. Surface Lattice Resonances in Plasmonic Arrays of Asymmetric Disc Dimers. *ACS Photonics* **2016**, *3* (4), 634–639. https://doi.org/10.1021/acsphotonics.5b00727.

(29) Zou, S.; Schatz, G. C. Narrow Plasmonic/Photonic Extinction and Scattering Line Shapes for One and Two Dimensional Silver Nanoparticle Arrays. *J. Chem. Phys.* **2004**, *121* (24), 12606. https://doi.org/10.1063/1.1826036.

(30) Guo, R.; Hakala, T. K.; Törmä, P. Geometry Dependence of Surface Lattice Resonances in Plasmonic Nanoparticle Arrays. *Phys. Rev. B* **2017**, *95* (15), 155423. https://doi.org/10.1103/PhysRevB.95.155423.

(31) Guan, J.; Sagar, L. K.; Li, R.; Wang, D.; Bappi, G.; Watkins, N. E.; Bourgeois, M. R.; Levina, L.; Fan, F.; Hoogland, S.; Voznyy, O.; Martins de Pina, J.; Schaller, R. D.; Schatz, G. C.; Sargent, E. H.; Odom, T. W. Engineering Directionality in Quantum Dot Shell Lasing Using Plasmonic Lattices. *Nano Lett.* **2020**, *20* (2), 1468–1474. https://doi.org/10.1021/acs.nanolett.9b05342.

(32) Manjavacas, A.; Zundel, L.; Sanders, S. Analysis of the Limits of the Near-Field Produced by Nanoparticle Arrays. *ACS Nano* **2019**, *13* (9), 10682–10693. https://doi.org/10.1021/acsnano.9b05031.

(33) Krasnok, A.; Tymchenko, M.; Alù, A. Nonlinear Metasurfaces: A Paradigm Shift in Nonlinear Optics. *Mater. Today* **2018**, *21* (1), 8–21. https://doi.org/10.1016/j.mattod.2017.06.007.

(34) Boyd, R. W. *Nonlinear Optics (Third Edition)*; Academic Press: Burlington, 2008; https://doi.org/10.1016/B978-0-12-369470-6.00001-0.

(35) Russier-Antoine, I.; Benichou, E.; Bachelier, G.; Jonin, C.; Brevet, P. F. Multipolar

Contributions of the Second Harmonic Generation from Silver and Gold Nanoparticles. *J. Phys. Chem. C* **2007**, *111* (26), 9044–9048. https://doi.org/10.1021/jp0675025.

(36) Bachelier, G.; Russier-Antoine, I.; Benichou, E.; Jonin, C.; Brevet, P.-F. Multipolar Second-Harmonic Generation in Noble Metal Nanoparticles. *JOSA B* **2008**, *25* (6), 955–960. https://doi.org/10.1364/JOSAB.25.000955.

(37) Panoiu, N. C.; Sha, W. E. I.; Lei, D. Y.; Li, G.-C. Nonlinear Optics in Plasmonic Nanostructures. *J. Opt.* **2018**, *20* (8), 083001. https://doi.org/10.1088/2040-8986/aac8ed.

(38) Nappa, J.; Revillod, G.; Russier-Antoine, I.; Benichou, E.; Jonin, C.; Brevet, P. F. Electric Dipole Origin of the Second Harmonic Generation of Small Metallic Particles. *Phys. Rev. B* **2005**, *71* (16), 165407. https://doi.org/10.1103/PhysRevB.71.165407.

(39) Butet, J.; Duboisset, J.; Bachelier, G.; Russier-Antoine, I.; Benichou, E.; Jonin, C.; Brevet, P.-F. Optical Second Harmonic Generation of Single Metallic Nanoparticles Embedded in a Homogeneous Medium. *Nano Lett.* **2010**, *10* (5), 1717–1721. https://doi.org/10.1021/nl1000949.

(40) Capretti, A.; Walsh, G. F.; Minissale, S.; Trevino, J.; Forestiere, C.; Miano, G.; Negro, L. D. Multipolar Second Harmonic Generation from Planar Arrays of Au Nanoparticles. *Opt. Express* **2012**, *20* (14), 15797–15806. https://doi.org/10.1364/OE.20.015797.

(41) Conti, Y.; Chiang, N.; Scarabelli, L. Colloidal Plasmonic Metasurfaces for the Enhancement of Non-Linear Optical Processes and Molecular Spectroscopies. *ChemNanoMat* **2024**, *10* (4), e202300566. https://doi.org/10.1002/cnma.202300566.

(42) Konstantinova, T. V.; Melent'ev, P. N.; Afanas'ev, A. E.; Kuzin, A. A.; Starikov, P. A.; Baturin, A. S.; Tausenev, A. V.; Konyashchenko, A. V.; Balykin, V. I. A Nanohole in a Thin Metal Film as an Efficient Nonlinear Optical Element. *J. Exp. Theor. Phys.* **2013**, *117* (1), 21–31. https://doi.org/10.1134/S1063776113080165.

(43) Konishi, K.; Higuchi, T.; Li, J.; Larsson, J.; Ishii, S.; Kuwata-Gonokami, M. Polarization-Controlled Circular Second-Harmonic Generation from Metal Hole Arrays with Threefold Rotational Symmetry. *Phys. Rev. Lett.* **2014**, *112* (13), 135502. https://doi.org/10.1103/PhysRevLett.112.135502.

(44) Guo, W.; Liu, B.; He, Y.; You, E.; Zhang, Y.; Huang, S.; Wang, J.; Wang, Z. Plasmonic Gold Nanohole Arrays for Surface-Enhanced Sum Frequency Generation Detection. *Nanomaterials* **2020**, *10* (12), 2557. https://doi.org/10.3390/nano10122557.

(45) Palermo, G.; Rippa, M.; Conti, Y.; Vestri, A.; Castagna, R.; Fusco, G.; Suffredini, E.; Zhou, J.; Zyss, J.; De Luca, A.; Petti, L. Plasmonic Metasurfaces Based on Pyramidal

Nanoholes for High-Efficiency SERS Biosensing. *ACS Appl. Mater. Interfaces* **2021**, *13* (36), 43715–43725. https://doi.org/10.1021/acsami.1c12525.

(46) Pu, Y.; Grange, R.; Hsieh, C.-L.; Psaltis, D. Nonlinear Optical Properties of Core-Shell Nanocavities for Enhanced Second-Harmonic Generation. *Phys. Rev. Lett.* **2010**, *104* (20), 207402. https://doi.org/10.1103/PhysRevLett.104.207402.

(47) Butet, J.; Bachelier, G.; Russier-Antoine, I.; Jonin, C.; Benichou, E.; Brevet, P.-F. Interference between Selected Dipoles and Octupoles in the Optical Second-Harmonic Generation from Spherical Gold Nanoparticles. *Phys. Rev. Lett.* **2010**, *105* (7), 077401. https://doi.org/10.1103/PhysRevLett.105.077401.

(48) McMahon, M. D.; Ferrara, D.; Bowie, C. T.; Lopez, R.; Haglund Jr., R. F. Second Harmonic Generation from Resonantly Excited Arrays of Gold Nanoparticles. *Appl. Phys. B* **2007**, *87* (2), 259–265. https://doi.org/10.1007/s00340-006-2569-3.

(49) Lis, D.; Caudano, Y.; Henry, M.; Demoustier-Champagne, S.; Ferain, E.; Cecchet, F. Selective Plasmonic Platforms Based on Nanopillars to Enhance Vibrational Sum-Frequency Generation Spectroscopy. *Adv. Opt. Mater.* **2013**, *1* (3), 244–255. https://doi.org/10.1002/adom.201200034.

(50) Carletti, L.; Rocco, D.; Locatelli, A.; Angelis, C. D.; Gili, V. F.; Ravaro, M.; Favero, I.; Leo, G.; Finazzi, M.; Ghirardini, L.; Celebrano, M.; Marino, G.; Zayats, A. V. Controlling Second-Harmonic Generation at the Nanoscale with Monolithic AlGaAs-on-AlOx Antennas. *Nanotechnology* **2017**, *28* (11), 114005. https://doi.org/10.1088/1361-6528/aa5645.

(51) Huttunen, M. J.; Bautista, G.; Decker, M.; Linden, S.; Wegener, M.; Kauranen, M. Nonlinear Chiral Imaging of Subwavelength-Sized Twisted-Cross Gold Nanodimers [Invited]. *Opt. Mater. Express* **2011**, *1* (1), 46–56. https://doi.org/10.1364/OME.1.000046.

(52) Kim, D.; Yu, J.; Hwang, I.; Park, S.; Demmerle, F.; Boehm, G.; Amann, M.-C.; Belkin, M. A.; Lee, J. Giant Nonlinear Circular Dichroism from Intersubband Polaritonic Metasurfaces. *Nano Lett.* **2020**, *20* (11), 8032–8039. https://doi.org/10.1021/acs.nanolett.0c02978.

(53) Li, G.; Chen, S.; Pholchai, N.; Reineke, B.; Wong, P. W. H.; Pun, E. Y. B.; Cheah, K. W.; Zentgraf, T.; Zhang, S. Continuous Control of the Nonlinearity Phase for Harmonic Generations. *Nat. Mater.* **2015**, *14* (6), 607–612. https://doi.org/10.1038/nmat4267.

(54) Spreyer, F.; Mun, J.; Kim, H.; Kim, R. M.; Nam, K. T.; Rho, J.; Zentgraf, T. Second Harmonic Optical Circular Dichroism of Plasmonic Chiral Helicoid-III Nanoparticles. *ACS Photonics* **2022**, *9* (3), 784–792. https://doi.org/10.1021/acsphotonics.1c00882.

(55) Liu, Y.; Ma, L.; Jiang, S.; Han, C.; Tang, P.; Yang, H.; Duan, X.; Liu, N.; Yan, H.; Lan, X. DNA Programmable Self-Assembly of Planar, Thin-Layered Chiral Nanoparticle Superstructures with Complex Two-Dimensional Patterns. *ACS Nano* **2021**, *15* (10), 16664–16672. https://doi.org/10.1021/acsnano.1c06639.

(56) Golze, S. D.; Porcu, S.; Zhu, C.; Sutter, E.; Ricci, P. C.; Kinzel, E. C.; Hughes, R. A.; Neretina, S. Sequential Symmetry-Breaking Events as a Synthetic Pathway for Chiral Gold Nanostructures with Spiral Geometries. *Nano Lett.* **2021**, *21* (7), 2919–2925. https://doi.org/10.1021/acs.nanolett.0c05105.

(57) Berthelot, J.; Bachelier, G.; Song, M.; Rai, P.; Francs, G. C. des; Dereux, A.; Bouhelier, A. Silencing and Enhancement of Second-Harmonic Generation in Optical Gap Antennas. *Opt. Express* **2012**, *20* (10), 10498–10508. https://doi.org/10.1364/OE.20.010498.

(58) Ko, K. D.; Kumar, A.; Fung, K. H.; Ambekar, R.; Liu, G. L.; Fang, N. X.; Toussaint, K. C. Jr. Nonlinear Optical Response from Arrays of Au Bowtie Nanoantennas. *Nano Lett.* **2011**, *11* (1), 61–65. https://doi.org/10.1021/nl102751m.

(59) Noor, A.; Damodaran, A. R.; Lee, I.-H.; Maier, S. A.; Oh, S.-H.; Ciracì, C. Mode-Matching Enhancement of Second-Harmonic Generation with Plasmonic Nanopatch Antennas. *ACS Photonics* **2020**, *7* (12), 3333–3340. https://doi.org/10.1021/acsphotonics.0c01545.

(60) Metzger, B.; Schumacher, T.; Hentschel, M.; Lippitz, M.; Giessen, H. Third Harmonic Mechanism in Complex Plasmonic Fano Structures. *ACS Photonics* **2014**, *1* (6), 471–476. https://doi.org/10.1021/ph5000677.

(61) Czaplicki, R.; Husu, H.; Siikanen, R.; Mäkitalo, J.; Kauranen, M.; Laukkanen, J.; Lehtolahti, J.; Kuittinen, M. Enhancement of Second-Harmonic Generation from Metal Nanoparticles by Passive Elements. *Phys. Rev. Lett.* **2013**, *110* (9), 093902. https://doi.org/10.1103/PhysRevLett.110.093902.

(62) Czaplicki, R.; Kiviniemi, A.; Laukkanen, J.; Lehtolahti, J.; Kuittinen, M.; Kauranen, M. Surface Lattice Resonances in Second-Harmonic Generation from Metasurfaces. *Opt. Lett.* **2016**, *41* (12), 2684–2687. https://doi.org/10.1364/OL.41.002684.

(63) Li, G.; Zhang, S.; Zentgraf, T. Nonlinear Photonic Metasurfaces. *Nat. Rev. Mater.* **2017**, *2* (5), 1–14. https://doi.org/10.1038/natrevmats.2017.10.

(64) Zheludev, N. I.; Emel Yanov, V. I. Phase Matched Second Harmonic Generation from Nanostructured Metallic Surfaces. *J. Opt. Pure Appl. Opt.* **2004**, *6* (1), 26–28. https://doi.org/10.1088/1464-4258/6/1/006.

(65) Accanto, N.; Nieder, J. B.; Piatkowski, L.; Castro-Lopez, M.; Pastorelli, F.; Brinks, D.; van Hulst, N. F. Phase Control of Femtosecond Pulses on the Nanoscale Using Second Harmonic Nanoparticles. *Light Sci. Appl.* **2014**, *3* (1), e143–e143. https://doi.org/10.1038/lsa.2014.24.

(66) Yu, N.; Genevet, P.; Kats, M. A.; Aieta, F.; Tetienne, J.-P.; Capasso, F.; Gaburro, Z. Light Propagation with Phase Discontinuities: Generalized Laws of Reflection and Refraction. *Science* **2011**, *334* (6054), 333–337. https://doi.org/10.1126/science.1210713.

(67) Linden, S.; Niesler, F. B. P.; Förstner, J.; Grynko, Y.; Meier, T.; Wegener, M. Collective Effects in Second-Harmonic Generation from Split-Ring-Resonator Arrays. *Phys. Rev. Lett.* **2012**, *109* (1), 015502. https://doi.org/10.1103/PhysRevLett.109.015502.

(68) Deng, J.; Tang, Y.; Chen, S.; Li, K.; Zayats, A. V.; Li, G. Giant Enhancement of Second-Order Nonlinearity of Epsilon-near- Zero Medium by a Plasmonic Metasurface. *Nano Lett.* **2020**, *20* (7), 5421–5427. https://doi.org/10.1021/acs.nanolett.0c01810.

(69) Celebrano, M.; Wu, X.; Baselli, M.; Großmann, S.; Biagioni, P.; Locatelli, A.; De Angelis, C.; Cerullo, G.; Osellame, R.; Hecht, B.; Duò, L.; Ciccacci, F.; Finazzi, M. Mode Matching in Multiresonant Plasmonic Nanoantennas for Enhanced Second Harmonic Generation. *Nat. Nanotechnol.* **2015**, *10* (5), 412–417. https://doi.org/10.1038/nnano.2015.69.

(70) Zhang, W.; Yu, H.; Wu, H.; Halasyamani, P. S. Phase-Matching in Nonlinear Optical Compounds: A Materials Perspective. *Chem. Mater.* **2017**, *29* (7), 2655–2668. https://doi.org/10.1021/acs.chemmater.7b00243.

(71) Le Xuan, L.; Zhou, C.; Slablab, A.; Chauvat, D.; Tard, C.; Perruchas, S.; Gacoin, T.; Villeval, P.; Roch, J.-F. Photostable Second-Harmonic Generation from a Single KTiOPO4 Nanocrystal for Nonlinear Microscopy. *Small* **2008**, *4* (9), 1332–1336. https://doi.org/10.1002/smll.200701093.

(72) Karawdeniya, B. I.; Damry, A. M.; Murugappan, K.; Manjunath, S.; Bandara, Y. M. N. D. Y.; Jackson, C. J.; Tricoli, A.; Neshev, D. Surface Functionalization and Texturing of Optical Metasurfaces for Sensing Applications. *Chem. Rev.* **2022**, *122* (19), 14990–15030. https://doi.org/10.1021/acs.chemrev.1c00990.

(73) Cortés, E.; Wendisch, F. J.; Sortino, L.; Mancini, A.; Ezendam, S.; Saris, S.; de S. Menezes, L.; Tittl, A.; Ren, H.; Maier, S. A. Optical Metasurfaces for Energy Conversion. *Chem. Rev.* **2022**, *122* (19), 15082–15176. https://doi.org/10.1021/acs.chemrev.2c00078.

(74) Lin, H.; Zhang, Z.; Zhang, H.; Lin, K.-T.; Wen, X.; Liang, Y.; Fu, Y.; Lau, A. K. T.; Ma, T.; Qiu, C.-W.; Jia, B. Engineering van Der Waals Materials for Advanced

Metaphotonics. *Chem. Rev.* **2022**, *122* (19), 15204–15355. https://doi.org/10.1021/acs.chemrev.2c00048.

(75) Wang, P.; Krasavin, A. V.; Liu, L.; Jiang, Y.; Li, Z.; Guo, X.; Tong, L.; Zayats, A. V. Molecular Plasmonics with Metamaterials. *Chem. Rev.* **2022**, *122* (19), 15031–15081. https://doi.org/10.1021/acs.chemrev.2c00333.

(76) Lukumbuzya, M.; Schmid, M.; Pjevac, P.; Daims, H. A Multicolor Fluorescence in Situ Hybridization Approach Using an Extended Set of Fluorophores to Visualize Microorganisms. *Front. Microbiol.* **2019**, *10*. https://doi.org/10.3389/fmicb.2019.01383.

(77) Lichtman, J. W.; Conchello, J.-A. Fluorescence Microscopy. *Nat. Methods* **2005**, *2* (12), 910–919. https://doi.org/10.1038/nmeth817.

(78) Svelto, O. *Principles of Lasers*; Springer US: Boston, MA, 2010. https://doi.org/10.1007/978-1-4419-1302-9.

(79) *Principles of Fluorescence Spectroscopy*; Lakowicz, J. R., Ed.; Springer US: Boston, MA, 2006. https://doi.org/10.1007/978-0-387-46312-4.

(80) Jiang, Y.; Weiss, E. A. Colloidal Quantum Dots as Photocatalysts for Triplet Excited State Reactions of Organic Molecules. *J. Am. Chem. Soc.* **2020**, *142* (36), 15219–15229. https://doi.org/10.1021/jacs.0c07421.

(81) Torsi, L.; Farinola, G. M.; Marinelli, F.; Tanese, M. C.; Omar, O. H.; Valli, L.; Babudri, F.; Palmisano, F.; Zambonin, P. G.; Naso, F. A Sensitivity-Enhanced Field-Effect Chiral Sensor. *Nat. Mater.* **2008**, *7* (5), 412–417. https://doi.org/10.1038/nmat2167.

(82) Bigdeli, A.; Ghasemi, F.; Fahimi-Kashani, N.; Abbasi-Moayed, S.; Orouji, A.; Ivrigh, Z. J.-N.; Shahdost-Fard, F.; Hormozi-Nezhad, M. R. Optical Nanoprobes for Chiral Discrimination. *Analyst* **2020**, *145* (20), 6416–6434. https://doi.org/10.1039/D0AN01211D.

(83) Jacak, L.; Hawrylak, P.; Wojs, A. *Quantum Dots*; Springer Science & Business Media, 2013.

(84) Reed, M. A. Quantum Dots. *Sci. Am.* **1993**, *268* (1), 118–123.

(85) Bera, D.; Qian, L.; Tseng, T.-K.; Holloway, P. H. Quantum Dots and Their Multimodal Applications: A Review. *Materials* **2010**, *3* (4), 2260–2345. https://doi.org/10.3390/ma3042260.

(86) Vasudevan, D.; Gaddam, R. R.; Trinchi, A.; Cole, I. Core–Shell Quantum Dots: Properties and Applications. *J. Alloys Compd.* **2015**, *636*, 395–404. https://doi.org/10.1016/j.jallcom.2015.02.102.

(87) Chan, W. C. W.; Nie, S. Quantum Dot Bioconjugates for Ultrasensitive Nonisotopic Detection. *Science* **1998**, *281* (5385), 2016–2018.

https://doi.org/10.1126/science.281.5385.2016.

(88) Smith, A. M.; Nie, S. Semiconductor Nanocrystals: Structure, Properties, and Band Gap Engineering. *Acc. Chem. Res.* **2010**, *43* (2), 190–200. https://doi.org/10.1021/ar9001069.

(89) Achermann, M. Exciton−Plasmon Interactions in Metal−Semiconductor Nanostructures. *J. Phys. Chem. Lett.* **2010**, *1* (19), 2837–2843. https://doi.org/10.1021/jz101102e.

(90) Ming, T.; Chen, H.; Jiang, R.; Li, Q.; Wang, J. Plasmon-Controlled Fluorescence: Beyond the Intensity Enhancement. *J. Phys. Chem. Lett.* **2012**, *3* (2), 191–202. https://doi.org/10.1021/jz201392k.

(91) Li, Y.; Li, Q.; Zhang, Z.; Liu, H.; Lu, X.; Fang, Y. Time-Resolved Photoluminescence Spectroscopy of Exciton–Plasmon Coupling Dynamics. *Plasmonics* **2015**, *10* (2), 271–280. https://doi.org/10.1007/s11468-014-9805-1.

(92) Park, J.-E.; Kim, J.; Nam, J.-M. Emerging Plasmonic Nanostructures for Controlling and Enhancing Photoluminescence. *Chem. Sci.* **2017**, *8* (7), 4696–4704. https://doi.org/10.1039/C7SC01441D.

(93) Kuhn, H. Classical Aspects of Energy Transfer in Molecular Systems. *J. Chem. Phys.* **1970**, *53* (1), 101–108. https://doi.org/10.1063/1.1673749.

(94) Ruppin, R. Decay of an Excited Molecule near a Small Metal Sphere. *J. Chem. Phys.* **1982**, *76* (4), 1681–1684. https://doi.org/10.1063/1.443196.

(95) Moskovits, M. Surface-Enhanced Spectroscopy. *Rev. Mod. Phys.* **1985**, *57* (3), 783–826. https://doi.org/10.1103/RevModPhys.57.783.

(96) Purcell, E. M. Spontaneous Emission Probabilities at Radio Frequencies. In *Confined Electrons and Photons: New Physics and Applications*; Burstein, E., Weisbuch, C., Eds.; Springer US: Boston, MA, 1995; pp 839–839. https://doi.org/10.1007/978-1-4615-1963-8_40.

(97) Bitton, O.; Gupta, S. N.; Haran, G. Quantum Dot Plasmonics: From Weak to Strong Coupling. *Nanophotonics* **2019**, *8* (4), 559–575. https://doi.org/10.1515/nanoph-2018-0218.

(98) David, A.; Benisty, H.; Weisbuch, C. Photonic Crystal Light-Emitting Sources. *Rep. Prog. Phys.* **2012**, *75* (12), 126501. https://doi.org/10.1088/0034-4885/75/12/126501.

(99) Förster, T. Energy Migration and Fluorescence. *J. Biomed. Opt.* **2012**, *17* (1), 011002. https://doi.org/10.1117/1.JBO.17.1.011002.

(100) Curto, A. G.; Volpe, G.; Taminiau, T. H.; Kreuzer, M. P.; Quidant, R.; van Hulst, N. F. Unidirectional Emission of a Quantum Dot Coupled to a Nanoantenna. *Science* **2010**, *329*

(5994), 930–933. https://doi.org/10.1126/science.1191922.

(101) Kosako, T.; Kadoya, Y.; Hofmann, H. F. Directional Control of Light by a Nano-Optical Yagi–Uda Antenna. *Nat. Photonics* **2010**, *4* (5), 312–315. https://doi.org/10.1038/nphoton.2010.34.

(102) Yang, A.; Hoang, T. B.; Dridi, M.; Deeb, C.; Mikkelsen, M. H.; Schatz, G. C.; Odom, T. W. Real-Time Tunable Lasing from Plasmonic Nanocavity Arrays. *Nat. Commun.* **2015**, *6* (1), 6939. https://doi.org/10.1038/ncomms7939.

(103) Fernandez-Bravo, A.; Wang, D.; Barnard, E. S.; Teitelboim, A.; Tajon, C.; Guan, J.; Schatz, G. C.; Cohen, B. E.; Chan, E. M.; Schuck, P. J.; Odom, T. W. Ultralow-Threshold, Continuous-Wave Upconverting Lasing from Subwavelength Plasmons. *Nat. Mater.* **2019**, *18* (11), 1172–1176. https://doi.org/10.1038/s41563-019-0482-5.

(104) Guan, J.; Li, R.; Juarez, X. G.; Sample, A. D.; Wang, Y.; Schatz, G. C.; Odom, T. W. Plasmonic Nanoparticle Lattice Devices for White-Light Lasing. *Adv. Mater.* **2022**, *n/a* (n/a), 2103262. https://doi.org/10.1002/adma.202103262.

(105) Guan, J.; Sagar, L. K.; Li, R.; Wang, D.; Bappi, G.; Wang, W.; Watkins, N.; Bourgeois, M. R.; Levina, L.; Fan, F.; Hoogland, S.; Voznyy, O.; de Pina, J. M.; Schaller, R. D.; Schatz, G. C.; Sargent, E. H.; Odom, T. W. Quantum Dot-Plasmon Lasing with Controlled Polarization Patterns. *ACS Nano* **2020**, *14* (3), 3426–3433. https://doi.org/10.1021/acsnano.9b09466.

(106) Tan, M. J. H.; Park, J.-E.; Freire-Fernández, F.; Guan, J.; Juarez, X. G.; Odom, T. W. Lasing Action from Quasi-Propagating Modes. *Adv. Mater.* **2022**, *34* (34), 2203999. https://doi.org/10.1002/adma.202203999.

(107) Deng, S.; Park, J.-E.; Kang, G.; Guan, J.; Li, R.; Schatz, G. C.; Odom, T. W. Interfacial Engineering of Plasmonic Nanoparticle Metasurfaces. *Proc. Natl. Acad. Sci.* **2022**, *119* (22), e2202621119. https://doi.org/10.1073/pnas.2202621119.

(108) Wang, D.; Bourgeois, M. R.; Guan, J.; Fumani, A. K.; Schatz, G. C.; Odom, T. W. Lasing from Finite Plasmonic Nanoparticle Lattices. *ACS Photonics* **2020**, *7* (3), 630–636. https://doi.org/10.1021/acsphotonics.0c00231.

(109) Hakala, T. K.; Rekola, H. T.; Väkeväinen, A. I.; Martikainen, J.-P.; Nečada, M.; Moilanen, A. J.; Törmä, P. Lasing in Dark and Bright Modes of a Finite-Sized Plasmonic Lattice. *Nat. Commun.* **2017**, *8* (1), 13687. https://doi.org/10.1038/ncomms13687.

(110) Schokker, A. H.; Koenderink, A. F. Lasing at the Band Edges of Plasmonic Lattices. *Phys. Rev. B* **2014**, *90* (15), 155452. https://doi.org/10.1103/PhysRevB.90.155452.

(111) Atwater, H. A.; Polman, A. Plasmonics for Improved Photovoltaic Devices. *Nat.*

Mater. **2010**, *9* (3), 205–213. https://doi.org/10.1038/nmat2629.

(112) Wang, J.; Jia, S.; Cao, Y.; Wang, W.; Yu, P. Design Principles for Nanoparticle Plasmon-Enhanced Organic Solar Cells. *Nanoscale Res. Lett.* **2018**, *13* (1), 211. https://doi.org/10.1186/s11671-018-2620-4.

(113) García de Arquer, F. P.; Mihi, A.; Konstantatos, G. Large-Area Plasmonic-Crystal–Hot-Electron-Based Photodetectors. *ACS Photonics* **2015**, *2* (7), 950–957. https://doi.org/10.1021/acsphotonics.5b00149.

(114) Leenheer, A. J.; Narang, P.; Lewis, N. S.; Atwater, H. A. Solar Energy Conversion via Hot Electron Internal Photoemission in Metallic Nanostructures: Efficiency Estimates. *J. Appl. Phys.* **2014**, *115* (13), 134301. https://doi.org/10.1063/1.4870040.

(115) Ferry, V. E.; Verschuuren, M. A.; Li, H. B. T.; Verhagen, E.; Walters, R. J.; Schropp, R. E. I.; Atwater, H. A.; Polman, A. Light Trapping in Ultrathin Plasmonic Solar Cells. *Opt. Express* **2010**, *18* (102), A237–A245. https://doi.org/10.1364/OE.18.00A237.

(116) Zheng, Y. B.; Kiraly, B.; Weiss, P. S.; Huang, T. J. Molecular Plasmonics for Biology and Nanomedicine. *Nanomed.* **2012**, *7* (5), 751–770. https://doi.org/10.2217/nnm.12.30.

(117) Danilov, A.; Tselikov, G.; Wu, F.; Kravets, V. G.; Ozerov, I.; Bedu, F.; Grigorenko, A. N.; Kabashin, A. V. Ultra-Narrow Surface Lattice Resonances in Plasmonic Metamaterial Arrays for Biosensing Applications. *Biosens. Bioelectron.* **2018**, *104*, 102–112. https://doi.org/10.1016/j.bios.2017.12.001.

(118) Zhao, C.; Xu, X.; Ferhan, A. R.; Chiang, N.; Jackman, J. A.; Yang, Q.; Liu, W.; Andrews, A. M.; Cho, N.-J.; Weiss, P. S. Scalable Fabrication of Quasi-One-Dimensional Gold Nanoribbons for Plasmonic Sensing. *Nano Lett.* **2020**, *20* (3), 1747–1754. https://doi.org/10.1021/acs.nanolett.9b04963.

(119) Tadesse, L. F.; Ho, C.-S.; Chen, D.-H.; Arami, H.; Banaei, N.; Gambhir, S. S.; Jeffrey, S. S.; Saleh, A. A. E.; Dionne, J. Plasmonic and Electrostatic Interactions Enable Uniformly Enhanced Liquid Bacterial Surface-Enhanced Raman Scattering (SERS). *Nano Lett.* **2020**, *20* (10), 7655–7661. https://doi.org/10.1021/acs.nanolett.0c03189.

(120) Kravets, V. G.; Schedin, F.; Kabashin, A. V.; Grigorenko, A. N. Sensitivity of Collective Plasmon Modes of Gold Nanoresonators to Local Environment. *Opt. Lett.* **2010**, *35* (7), 956. https://doi.org/10.1364/OL.35.000956.

(121) Kravets, V. G.; Schedin, F.; Jalil, R.; Britnell, L.; Gorbachev, R. V.; Ansell, D.; Thackray, B.; Novoselov, K. S.; Geim, A. K.; Kabashin, A. V.; Grigorenko, A. N. Singular Phase Nano-Optics in Plasmonic Metamaterials for Label-Free Single-Molecule Detection. *Nat. Mater.* **2013**, *12* (4), 304–309. https://doi.org/10.1038/nmat3537.

(122) Ezendam, S.; Herran, M.; Nan, L.; Gruber, C.; Kang, Y.; Gröbmeyer, F.; Lin, R.; Gargiulo, J.; Sousa-Castillo, A.; Cortés, E. Hybrid Plasmonic Nanomaterials for Hydrogen Generation and Carbon Dioxide Reduction. *ACS Energy Lett.* **2022**, *7* (2), 778–815. https://doi.org/10.1021/acsenergylett.1c02241.

(123) Hüttenhofer, L.; Golibrzuch, M.; Bienek, O.; Wendisch, F. J.; Lin, R.; Becherer, M.; Sharp, I. D.; Maier, S. A.; Cortés, E. Metasurface Photoelectrodes for Enhanced Solar Fuel Generation. *Adv. Energy Mater.* **2021**, *11* (46), 2102877. https://doi.org/10.1002/aenm.202102877.

(124) Cortés, E.; Xie, W.; Cambiasso, J.; Jermyn, A. S.; Sundararaman, R.; Narang, P.; Schlücker, S.; Maier, S. A. Plasmonic Hot Electron Transport Drives Nano-Localized Chemistry. *Nat. Commun.* **2017**, *8* (1), 14880. https://doi.org/10.1038/ncomms14880.

(125) Sundararaman, R.; Narang, P.; Jermyn, A. S.; Goddard III, W. A.; Atwater, H. A. Theoretical Predictions for Hot-Carrier Generation from Surface Plasmon Decay. *Nat. Commun.* **2014**, *5* (1), 5788. https://doi.org/10.1038/ncomms6788.

(126) Movsesyan, A.; Santiago, E. Y.; Burger, S.; Correa-Duarte, M. A.; Besteiro, L. V.; Wang, Z.; Govorov, A. O. Plasmonic Nanocrystals with Complex Shapes for Photocatalysis and Growth: Contrasting Anisotropic Hot-Electron Generation with the Photothermal Effect. *Adv. Opt. Mater.* **2022**, *10* (10), 2102663. https://doi.org/10.1002/adom.202102663.

(127) Deng, S.; Zhang, B.; Choo, P.; Smeets, P. J. M.; Odom, T. W. Plasmonic Photoelectrocatalysis in Copper–Platinum Core–Shell Nanoparticle Lattices. *Nano Lett.* **2021**, *21* (3), 1523–1529. https://doi.org/10.1021/acs.nanolett.0c05029.

(128) Yang, Y.; Seong, J.; Choi, M.; Park, J.; Kim, G.; Kim, H.; Jeong, J.; Jung, C.; Kim, J.; Jeon, G.; Lee, K.; Yoon, D. H.; Rho, J. Integrated Metasurfaces for Re-Envisioning a near-Future Disruptive Optical Platform. *Light Sci. Appl.* **2023**, *12* (1), 152. https://doi.org/10.1038/s41377-023-01169-4.

(129) Mao, P.; Liu, C.; Li, X.; Liu, M.; Chen, Q.; Han, M.; Maier, S. A.; Sargent, E. H.; Zhang, S. Single-Step-Fabricated Disordered Metasurfaces for Enhanced Light Extraction from LEDs. *Light Sci. Appl.* **2021**, *10* (1), 180. https://doi.org/10.1038/s41377-021-00621-7.

(130) Ebbesen, T. W. Hybrid Light–Matter States in a Molecular and Material Science Perspective. *Acc. Chem. Res.* **2016**, *49* (11), 2403–2412. https://doi.org/10.1021/acs.accounts.6b00295.

(131) Sample, A. D.; Guan, J.; Hu, J.; Reese, T.; Cherqui, C. R.; Park, J.-E.; Freire-Fernández, F.; Schaller, R. D.; Schatz, G. C.; Odom, T. W. Strong Coupling Between

Plasmons and Molecular Excitons in Metal–Organic Frameworks. *Nano Lett.* **2021**, *21* (18), 7775–7780. https://doi.org/10.1021/acs.nanolett.1c02740.

(132) Ramezani, M.; Le-Van, Q.; Halpin, A.; Gómez Rivas, J. Nonlinear Emission of Molecular Ensembles Strongly Coupled to Plasmonic Lattices with Structural Imperfections. *Phys. Rev. Lett.* **2018**, *121* (24), 243904. https://doi.org/10.1103/PhysRevLett.121.243904.

(133) Alvarez-Serrano, J. J.; Deop-Ruano, J. R.; Aglieri, V.; Toma, A.; Manjavacas, A. Normal Incidence Excitation of Out-of-Plane Lattice Resonances in Bipartite Arrays of Metallic Nanostructures. *ACS Photonics* **2024**, *11* (1), 301–309. https://doi.org/10.1021/acsphotonics.3c01535.

(134) Väkeväinen, A. I.; Moerland, R. J.; Rekola, H. T.; Eskelinen, A.-P.; Martikainen, J.-P.; Kim, D.-H.; Törmä, P. Plasmonic Surface Lattice Resonances at the Strong Coupling Regime. *Nano Lett.* **2014**, *14* (4), 1721–1727. https://doi.org/10.1021/nl4035219.

(135) Zakharko, Y.; Graf, A.; Zaumseil, J. Plasmonic Crystals for Strong Light–Matter Coupling in Carbon Nanotubes. *Nano Lett.* **2016**, *16* (10), 6504–6510. https://doi.org/10.1021/acs.nanolett.6b03086.

(136) Liu, W.; Lee, B.; Naylor, C. H.; Ee, H.-S.; Park, J.; Johnson, A. T. C.; Agarwal, R. Strong Exciton–Plasmon Coupling in MoS2 Coupled with Plasmonic Lattice. *Nano Lett.* **2016**, *16* (2), 1262–1269. https://doi.org/10.1021/acs.nanolett.5b04588.

(137) Liu, J.; Wang, W.; Wang, D.; Hu, J.; Ding, W.; Schaller, R. D.; Schatz, G. C.; Odom, T. W. Spatially Defined Molecular Emitters Coupled to Plasmonic Nanoparticle Arrays. *Proc. Natl. Acad. Sci.* **2019**, *116* (13), 5925–5930. https://doi.org/10.1073/pnas.1818902116.

Chapter 2

ALTERNATIVE FABRICATION PROCESSES FOR PLASMONIC METASURFACES

"I do not know what I may appear to the world; but to myself I seem to have been only like a boy playing on the seashore and diverting myself in now and then finding a smoother pebble or a prettier shell than ordinary, whilst the great ocean of truth lay all undiscovered before me."

David Brewster, Memories of the Life, Writings, and Discoveries of Sir Isaac Newton (1855)

Introduction

Advances in semiconductor and flexible electronics applications over the last decades have generated an increasing demand for micro- and nano- fabrication techniques characterized by low costs, enhanced throughput, and higher resolution. This increased demand stems from the constraints of traditional methods like electron beam lithography (EBL), which typically exhibit a low throughput that is incompatible with mass production. Despite the availability of alternatives such as extreme ultraviolet lithography and focused ion beam lithography (FIB), their current high costs restrict their application primarily to large industries and corporations. Moreover, these processes limit the selection of materials and operating conditions, as well as the control over crystallography and surface chemistry of the system. These aspects are particularly important for the next generation of metamaterials, which experts in the field identify in chemically functional metasurfaces capable of exploring the chemical space, or the so called "chemistry of metamaterials".

The search for chemically active metasurfaces has spurred the scientific community to explore alternative fabrication methods, and colloidal self-assembly has emerged as a promising solution. On one side, colloidal synthesis allows researchers to fine-tune nanoparticle morphology, crystallography, composition, and surface chemistry with unprecedented precision. The constant progress in the field of colloidal chemistry has enabled great advances in the synthesis of metal NPs using *bottom-up* approaches,[1] achieving an unprecedented control

of the optical properties by manipulating elemental composition, near-field distribution, and even chirality at the single nanoparticle level.[2–4] On the other, self-assembly can be used to create high-quality periodic and hierarchical arrangements on a large scale, opening exciting possibilities for the development of metamaterials in combination with soft lithography.

Particularly relevant for this thesis work is the example of nanoimprint lithography (NIL). Introduced in 1995 by Prof. S.Y. Chou and his group, NIL has emerged as a versatile, cost-effective and high-throughput top-down alternative to micro- and nanofabrication.[5] Here, a pre-fabricated mold, designed as the inverse of the desired pattern, is pushed into a polymeric resist layer, reproducing the pattern by mechanical deformation.[6] A very important advantage of NIL is that the stamp can be recycled after de-molding, allowing to create multiple replicas from a single pre-fabricated stamp. Unlike conventional *top-down* nanolithography methods, which are limited by light diffraction or beam scattering factors, NIL relies on direct mechanical deformation, enabling a significant resolution improvement (currently < 10 nm).[7]

Since it was introduced, NIL technology has been the subject of extensive investigation and refinement by a number of scientists, leading to the development of several process variations.[8] In one of these developments, NIL has been applied for the development of several colloidal self-assembly techniques, combining significant developments in surface chemistry control, feature miniaturization, and scalability to improve the quality of colloidal-based plasmonic metasurfaces, demonstrating higher control on distribution and orientation down to single nano-objects. This led to target high-quality factor plasmonic optical cavities and achievements on high-throughput large-scale self-assembly up to wafer-scale dimensions, and to the emergence of plasmonic colloidal self-assembly as a promising fabrication approach to produce organized two-dimensional (2D) and three-dimensional (3D).[9]

Colloidal self-assembly involves the spontaneous arrangement of existing components into complex, organized structures driven by the minimization of free energy towards a local equilibrium state. This process can be externally influenced and controlled by using guiding

fields and confinement effects. In direct assembly techniques, patterns, external fields, or specific agents are used to force the particles toward specific areas of the substrate and selectively arrange them. As a variety of NPs with different morphologies, including rods, cubes, plates and polyhedra, have been precisely synthesised,[2,3,10–14] a wider range of structures can be achieved by properly managing the symmetries of individual units (or building blocks) and directing their directional interactions.[15] This includes face-centered cubic (fcc), body-centered cubic (bcc), hexagonal-closed packed (hcp), diamond-like lattice, and lattice structures not existing in nature. For example, anisotropic NPs and their interactions exhibit high performance for engineering the self-assemblies of complicated crystals structures.[16–19]

The collective plasmonic response of these colloidal self-assembled metasurfaces are able to overcome the optical losses associated to the localized plasmons of single colloidal building blocks,[20,21] demonstrating high adaptability to different applications fields such as photonics,[22,23] photocatalysis,[24] energy conversion,[25] and biosensing.[26–28]

The aim of this chapter is to summaries and categorize the principles of plasmonic colloidal assembly for the preparation of colloidal plasmonic metasurfaces, comparing various fabrication methods, and spotlighting new emerging trends. The work presented in this thesis is based on alternative approaches which rely on soft lithography. This includes template-assisted self-assembly (TASA) and a newly developed strategy named chemical contrast *in situ* growth, where functional meatasurfaces are grown *via* the combination of NIL for the creation of a surface chemical contrast.

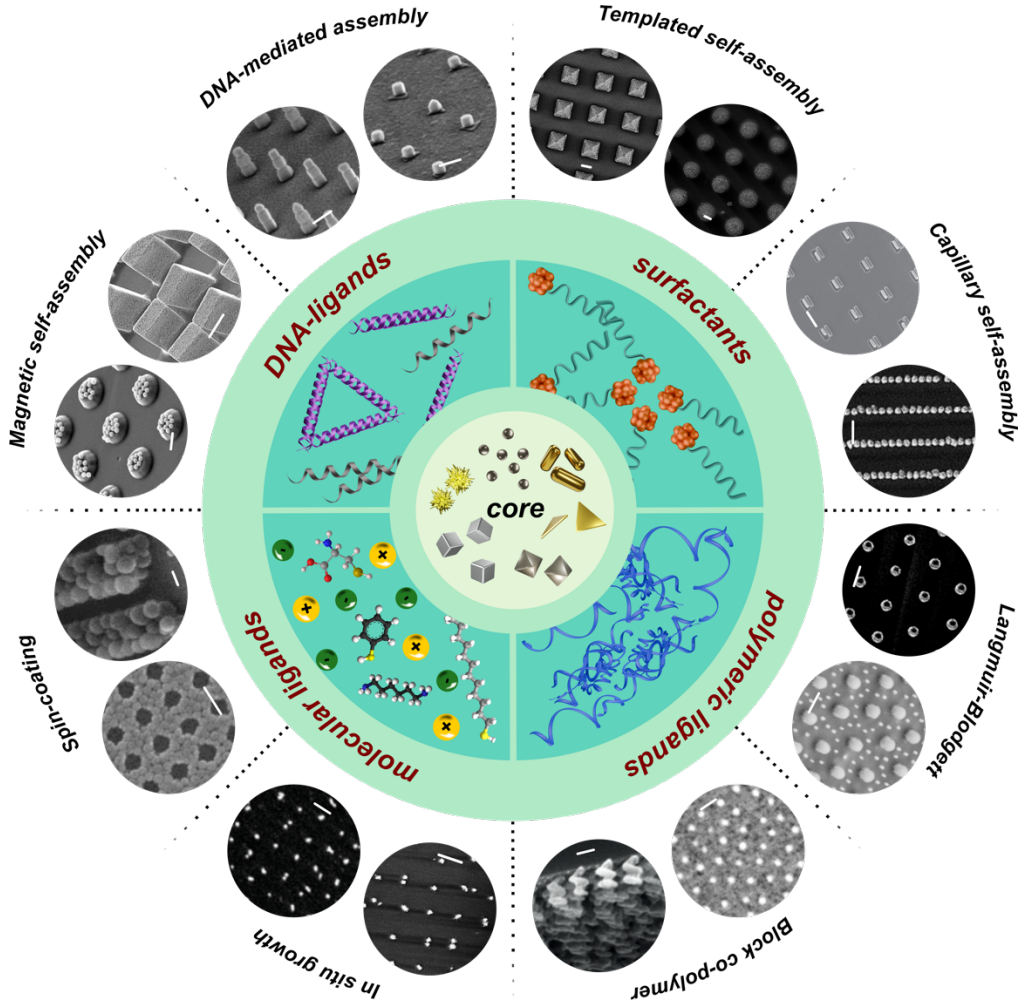

Figure 2.1 **Alternative fabrication strategies for colloidal metasurfaces**. Scanning Electron Microscopy (SEM) images of (clockwise direction): Templated self-assembly (**scale bar** 1µm) Copyright 2017, ACS. Adapted with permission,[29] (**scale bar** 500 nm) Copyright 2023, Wiley-VCH. Adapted with permission;[23] Capillary self-assembly (**scale bar** 500 nm) Copyright 2017, Springer Nature. Adapted with permission,[30] and (**scale bar** 500 nm) Copyright 2014, ACS. Adapted with permission;[31] Langmuir-Blodgett (**scale bar** 1µm) Copyright 2018, RSC. Adapted with permission reprinted with permission,[32] and (**scale bar** 500 nm) Copyright 2020, Wiley-VCH. Adapted with permission;[33] Block co-polymer (**scale bar** 50 nm) Copyright 2013, Springer Nature. Adapted with permission,[34] and (**scale bar** 100 nm) Copyright 2008, Elsevier. Adapted with permission;[35] In situ growth (**scale bar** 500 nm) Copyright 2022, Wiley-VCH. Adapted with permission;[36] Spin-coating (**scale bar** 100, 500 nm) Copyright 2004, ACS. Adapted with permission;[37] Magnetic assembly (**scale bar** 5 µm) Copyright 2013, ACS. Adapted with permission,[38] and (**scale bar** 25 µm) Copyright 2022, ACS. Adapted with permission;[39] *DNA-mediated assembly* (**scale bar** 150 nm) Copyright 2018, Science. Adapted with permission.[40]

2.1 Nanoimprint lithography (NIL)

Nanoimprint lithography has rapidly emerged as a promising alternative to traditional nanolithography processes, driven by its advantages and the increasing demands of the semiconductor and flexible electronics industries. The rapid increase in popularity of NIL can

be found in its compatibility with roll-to-roll (R2R) setups, dramatically increasing its high throughput, and making it one of the most suitable lithography for industrial applications.[41] Considering the NIL based on imprinting contact, it is possible to recognize three processes: plate-to-plate (P2P), roll-to-plate (R2P), and roll-to-roll (R2R) NIL.

- *Plate-to-plate (P2P)*: A rigid flat stamp (patterned wafer) is used to imprint a material deposited onto a flat rigid substrate. This approach is typically unsuitable for large imprint areas, as it requires greater forces (kN) to achieve the necessary imprint pressures.[42] Moreover, this method is typically accompanied by higher defect rates, primarily due to the rigidity of the molds. In our group, we exploited a variant of this technique to fabricate functional masters from the original silicon wafer, minimizing defects and recreating the patterned areas with high-resolution.
- *Roll-to-plate (R2P)*: In roller-based nanoimprint lithography (NIL), the imprinting force is applied to a rigid surface using a roller-press mechanism. Unlike (P2P) NIL, where the entire stamp area is in contact with the substrate, roller-based NIL uses only linear contact along the roller. This significantly reduces the required imprinting force (as low as 200 N) to achieve pressures of approximately 1 bar for a 300 mm imprinting width.[43] Moreover, the line contact feature also significantly improves replication uniformity, by minimizing problems with trapped air bubbles, thickness variations and dust contaminants.[44] Different approaches can be used for this NIL method such as: *i)* using a roller press to imprint a flexible polymer onto a flat patterned mold *via* thermal NIL,[45] or ii) using a flexible mold wrapped around the roller in contact with a rigid plate for the imprinting,[46] or *ii)* using a flexible roller mold coated with the polymer resist, that is then cross-linked and transferred by UV or thermal curing. Using R2P it is possible to reach features size in the range of 20-130 μm in width and 10-100 μm in depth.[47]
- *Roll-to-roll (R2R)*: In this last version, imprinting is achieved by using an imprinting roller with a patterned surface, or one wrapped with a flexible mold, and a flexible substrate

supported by a second roller, rather than a flat plate. This entire approach is based on the roll-to-roll manufacturing concept, and it offers the advantages of continuous processing and high throughput.[48,49] Due to its advantages in industrial applications, several studies have investigated and improved the roll-to-roll nanoimprint lithography (R2R NIL) process.[48,50] In particular, continuous R2R NIL systems, based predominantly on UV NIL, were investigated. Using a resist-coated film pressed against an imprint roller, it results in a reflow of the resist into the cavity of the mold. In this way, 70 nm lines grating have been achieved at speed up to 1,400 mm/min.[48]

Similarly, processes using patterned rollers mold and roll coating mechanisms have been used for thermal R2R NIL, with applications in color filters for flexible displays.[51]

For example, iterative roller imprint mechanisms for multilayer nanostructures can be used to improve the self-alignment. Moreover, R2R NIL was recently extended to rigid substrate such as glass.[52] These advances demonstrate the evolving capabilities and versatility of R2R NIL in different applications.

However, these techniques face a fundamental limitation from both a material and process standpoint, including roller position alignment, uniformity, and large area processing (up to 300 mm).[53] While continuous roll-to-roll nanoimprint lithography offers several advantages for industrial applications, some challenges still hinder its implementation, for example in the need for specialized flexible mold and the selection of a resist material with low viscosity and good coating properties challenge.

In the context of NIL based on resist curing, it is possible to distinguish two type of process (**Figure 2.2 a**, **b**): thermal (*t*-) NIL, and ultraviolet (UV) NIL.

The processes follow four steps:

1. A mold is first heated up to temperature higher than the glass transition (T_g) of the target resist material. The heated mold is put in contact with the resist, inducing its transition to a molten state. An increase in temperature is essential because the elastic modulus

and yield strength of the resin decrease significantly when the temperature exceeds T_g. Nonetheless, excessively high temperatures, beyond T_g, may lead to film damages.[54]

2. The soften resist can efficiently fill the mold cavities, under the appropriate imprinting pressure and time.
3. After imprinting, the temperature is lowered below T_g in order to induce the solidification of the patterned resist.
4. The mold is then lifted-off, leaving the negative image of the pattern/structure imprinted on the resist.

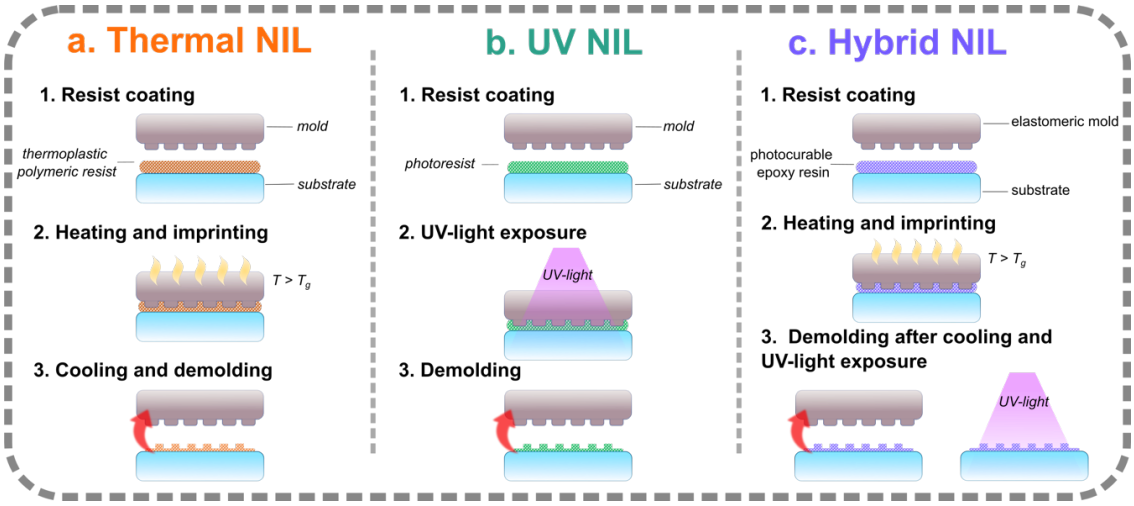

Figure 2.2 Scheme of the principal NIL techniques based on resist curing.

Thermal NIL or "hot embossing" is the process for which thermoplastic polymers, epoxy resins or biomolecules are subjected to imprint after being thermally softened (**Figure 2.2 a**). The softening process relies in a variation of the thermos-mechanical properties of the film.[55]

In the case of *UV NIL* instead (**Figure 2.2 b**), the imprinted structures are cured under UV light exposure, which causes the cross-linking of the photoresist. The resulting pattern is achieved by using transparent template (quartz, glass, or elastomeric stamps). Compared to the thermal nanoimprinting, this approach uses less viscous liquid photoresist which allows the process to be carried out at lower pressures. As a result, the resist fills the mold cavities in

shorter times.[56] Nowadays, depending on the rigidity and transparency of the mold used, *hybrid NIL* techniques have also been developed (**Figure 2.2 c**).

The mold, also known as the template or stamp, stands as a pivotal component in the NIL process., and the resolution of the patterns achieved through NIL fundamentally hinges on the resolution of the features present on the mold's surface.

Choosing the right material for a mold in NIL involves considering various factors beyond just mechanical properties. While harder materials offer superior wear resistance, they can be difficult to deform mechanically, which leads to the creation of fractures and defects. Softer molds simplify stamp creation, but reduce the lifetime of the mold itself..[57] Additionally, optical and chemical properties play crucial roles in material selection for NIL. Key mechanical parameters impacting NIL include hardness and thermal stability (affecting lifetime and wear), thermal expansion coefficients and Poisson's ratio (which can lead to distortions during demolding), roughness (influencing demolding force and potential damage), Young's modulus (impacting bending), and notch resistance (affecting lifetime and handling). Fabrication considerations encompass processability (including etching processes, selectivity, and clean room requirements) and surface quality, which directly impacts resolution.[58] Additional properties beyond mechanical considerations play a crucial role in determining the suitability of a material for use in NIL processes. These include transparency, conductivity, anti-sticking properties (with or without anti-adhesive coatings, such as covalent coatings), availability and cost including standard materials and sizes, tolerances, processing equipment, and time.

Currently, common materials used for hard molds in NIL include Silicon, Quartz, Nickel, and Silicon Nitride (Si_3N_4). For soft UV-NIL templates, various polymeric materials such as polydimethylsiloxane (PDMS), polyurethane acrylate (PUA), polyvinyl alcohol (PVA), and polyvinyl chloride (PVC) are utilized due to their UV transparency, mechanical hardness, and deformability.

Among these, PDMS is widely recognized for its suitability in UV-NIL applications. This material stands out for its exceptional UV transparency and remarkably low Young's modulus, granting it the requisite flexibility for conformal contact. Its minimal reactivity and interfacial energy towards polymeric materials, coupled with its elasticity, allow for clean separation from the polymeric structure without causing damage or distortion. Moreover, a PDMS mold's low surface energy at the polymer interface solves the issue of polymer adhesion during detachment, a significant challenge in NIL. As a result of these advantageous traits —flexibility, UV transparency, and low surface energy— PDMS has become the standard material for soft molds. Despite the limitation of high viscosity and tendency to swell pose, the main advantage of PDMS and other polymeric molds is the possibility to tune their mechanical properties by varying the degree of cross-linking between the siloxane chains within the structure.[58] This tunability introduces the possibility of creating a hybrid stamp where only the patterned region is composed of a hard material, while the backbone remains flexible. Reducing the thickness of the rigid polymer section preserves its high Young's modulus and mechanical strength, while maintaining enough flexibility for NIL.

In the realization of this thesis, two types of molds were used depending on the rigidity of the material (as discussed in the **Experimental Section**): the soft (s-) PDMS was used as mold for performing the self-assembly and hard (h-) PDMS for the imprinting.

2.2 Top-down and bottom-up approaches for plasmonic metasurfaces

Nanofabrication strategies based on both *top-down* and *bottom-up* approaches have been applied for plasmonic metasurfaces engineering.

Top-down techniques, including electron beam lithography (EBL), focused ion beam (FIB) lithography, extreme UV lithography, and thermal evaporation, provide greater control over the particle position producing extremely high-quality substrates.[59] However, while these methods

allow to achieve nanometric features with extraordinary precision, the need of clean-room facilities and expensive specialized equipment pose a significant challenge for cost-effective mass production.

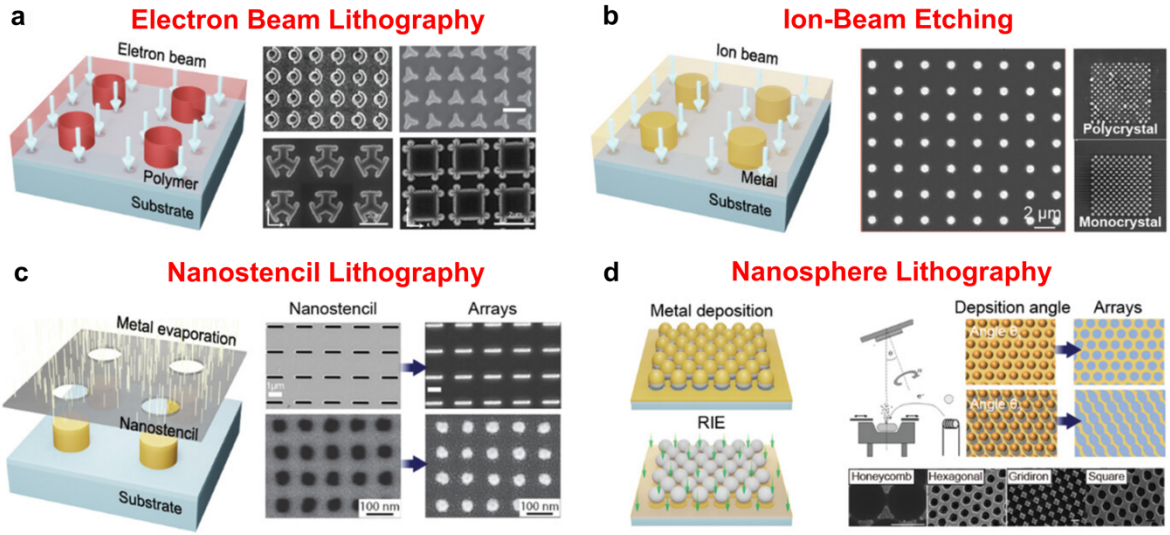

Figure 2.3 **Plasmonic metasurfaces**. Scheme and SEM images of plasmonic arrays fabricated via (**a**) EBL, (**b**) Ion-Beam Etching (IBE), (**c**) nanostencil lithography, (**d**) nanosphere lithography. **Panel a**, **b**, **c**, **d**: Copyright 2023, Wiley-VCH. Adapted with permission.[60]

To address these hurdles, a process named "*PEEL*", which combines **P**hase-shift photolithography, **E**tching, **E**lectron-beam deposition, and **L**ift-off steps, was developed over the years by Prof. Teri Odom. The technique relay on the use of a physical deposition mask of copper to create high-quality plasmonic arrays on-demand with misalignments <5°.[61] Since its development, this technology became widely used, for example, in the fabrication of plasmonic-based lasing architectures, involving the application of a gain medium onto pre-fabricated plasmon cavities.[62,63]

Figure 2.4 **PEEL fabrication process**. (**a**) Scheme showing the use of a metal hole-array film as a deposition mask in the process. (**b**) Scanning electron microscope (SEM) image of partially peeled Au film with

NPs array on substrate. (**c**) Image of Au NP array covering >1 cm^2 area with a red appearance due to the diffraction pattern. (**e**) Au NPs array fabricated via PEEL. **Panel a**, **b**, **c**, **d**: Copyright 2017, Elsevier. Figure adapted with permission.[63]

While PEEL offers several advantages, it also shows some limitations particularly from a scalability and versatility standpoint. Implementing the full PEEL process involves several steps, each requiring specialized equipment and expertise, making it less accessible to low-cost applications. This planar fabrication technique faces also issues such as uniformity across large substrates and incompatibility of all materials with certain steps in the process, which lower its versatility. Moreover, PEEL resolution is limited by the wavelength of the light used in the photolithography, which makes difficult to achieve structures with small features, ultimately limiting the performance of the technique.

This thesis focuses on a particular category of plasmonic metasurfaces, the ones involving the use of pre-synthetized and *in situ* grown plasmonic colloids, known as "*colloidal-based plasmonic metasurfaces*". Colloidal metasurfaces enable the fabrication of structures with nanoscale precision *via* bottom-up alternative methods which will be discussed in the following paragraphs, overcoming some of the challenges associated with top-down approaches. Tackling the fabrication problem from a completely opposite direction, bottom-up chemical synthesis techniques like templated, capillary-assisted, optically printed, and electrophoretic self-assembly provide more accessible and cost-effective alternatives for the fabrication of two- and three-dimensional metasurfaces.

Bottom-up synthesis is driven by the ability to fine-tune particle morphology, crystal structure, and surface chemistry to achieve higher quality plasmon resonances that can be used as optical cavities. The significant advantage lies in the exceptional control over the shape, size, and composition of colloidal building blocks, allowing to create of more complex and exotic geometries such as moiré,[64] chiral,[33,65] and superlattice stractures,[66] and ultimately offering unprecedented control over tunable optical resonances and enhanced light-matter interactions. This breakthrough holds transformative promises for the exploration of a chemistry of

metamaterials, with possible applications in advanced sensing, imaging, and optoelectronics, reshaping the landscape of nanophotonics. The ongoing research for a method that is both simple and scalable, and that can rapidly integrate the precision and uniformity of top-down approaches with the chemical control and cost-effectiveness of bottom-up methods, remains a key objective. This is essential to broaden the access to meticulously tailored plasmonic substrates for specific applications.

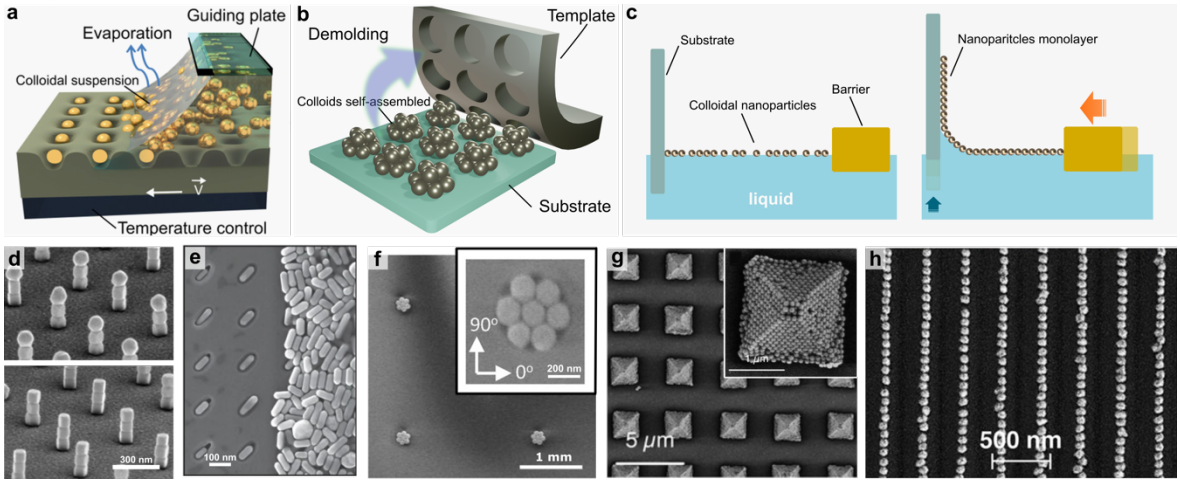

Figure 2.5 **Colloidal-based plasmonic metasurfaces**. Scheme of (**a**) capillary-assisted particle assembly (CAPA), (**b**) template-assisted self-assembly (TASA), and (**c**) Langmuir-Blodgett deposition fabrication techniques. SEM images of: (**d**) Template-DNA-mediated assembly of gold nanoparticles; (**e**) CAPA of gold nanorods; TASA of (**f**) heptamers nanoclusters, and (**g**) pyramidal super-crystals; (**h**) nanoparticles assembled by spin coating on top of a wrinkled polydimethylsiloxane substrate and then transferred onto flat substrates by wet contact printing. Copyright 2020, Wiley-VCH. Adapted with permission.[67]

2.3 Colloidal self-assembly

Thanks to the advancement of colloidal chemistry, plasmonic nanoparticles, can nowadays be synthetized in well-defined sizes and shapes using scalable wet-chemistry processes.[3,14,68–72] As explained in **Chapter 1**, the full versatility of plasmonic nanoparticle systems is realized when these colloids can be organized 3 dimensionally into specific assemblies and patterns, with applications in optoelectronics,[73] biological diagnostics[74] and sensing,[27,75] and energy harvesting.[76] Nanoparticle assemblies are emerging as a distinct class of crystalline materials with collective properties different from bulk crystals or isolated nanocrystals.[77]Various interesting

properties such as vibrational coherence,[78] enhanced conductivity,[79] electronic,[80] mechanical,[81,82] and plasmonic properties[83,84] have been observed in these kinds of structures.

The world of colloidal particles assembly is governed by a complex interplay of factors that can facilitate or hinder the formation of organized structures.[85,86] In fact, self-assembly is driven by non-covalent interactions between particles that forces the colloidal system towards an equilibrium state that results to be energetically favorable.[86,87]

The widespread interest in colloidal assemblies can be attributed to their remarkable versatility across diverse research fields. However, the unique demands of each applications require specific criteria for how the structures are being assembled. For example, in the case of surfaces coating which exhibit a stable liquid repellency, it is crucial to achieve a uniform coverage of colloidal particles on the surface in order to prevent pinning.[88] In the case of applications in photonics, which relying on periodic modulations of refractive index, it is required a high degree of order in the colloidal crystal.[89–91] A direct consequence of the self-assembly versatility is the co-existence of a myriad of self-assembly approaches, where the formulation of generalized guidelines and the identification of the optimal method for colloidal assembly remains difficult. Colloidal self-assembly methods include a range of techniques such as drop casting,[92,93] spin coating,[37,94,95] Langmuir-Blodgett[32,96,97] techniques, capillary-assisted particle assembly (CAPA) and template-assisted self-assembly (TASA)

In order to shed some light over the intricacies of colloidal self-assembly, it is essential to provide an overview of the fundamental characteristics of colloidal particle assembly. The aim of the following sections is to provide a general picture of the interactions between nanoparticles in suspension and at interfaces, as well as their mutual influence during the self-assembly process.

2.3.1 Interaction between particles

Interactions between inorganic nanoparticles involve multiple forces at different temporal and spatial scales, such as Van der Waals (VdW) forces, electrostatic and entropic forces.[89] Dating back to the 1949, Onsager's model of a fluid containing hard rods represents one of the first examples treating a system in which an ordered phase has greater entropy than its disordered counterpart at the same density.[98] In his model, entropy arises from both the translational and orientational freedom of the rods. The transition to order occurs when one aspect of entropy becomes dominant over the other. Onsager's theory focuses on the transition from a disordered isotropic phase to an ordered nematic phase in which the rods are predominantly parallel to each other, albeit with some dispersion in their orientations around the average alignment direction. Relating the entropy per particle to the logarithm of the volume accessible to that particle, for thin and elongated ($D/L \rightarrow 0$) rods aligned on a certain direction, the excluded volume is negligible compared to disordered rods, resembling the behavior of an ideal gas as described by statistical mechanics. This alignment results in a decrease in the excluded volume, leading to a decrease in translational entropy but an increase in orientational order. In these cases, while the alignment of particles may decrease translational entropy (*i.e.* the freedom of moving around), the increase in orientational order compensates for this decrease and leads to a net increase in entropy. Consequently, entropy-driven ordering is consistent with the second law of thermodynamics.

The most common example of entropy-driven ordering is that of the assembled hard spheres. Compared to a dilute fluid phase, for a densely packed solid crystal the free volume per particle, where particles can move without encountering neighboring particles, tends to diminish, approaching zero as spheres occupy approximately 74% of the total volume.[99] However, as fluid density increases, free volume per particle decreases rapidly, ultimately reaching zero at the random-close-packing point, Consequently, denser configurations, such as crystals or highly ordered icosahedral clusters formed by hard colloids, emerge to increase accessible volume and

entropy upon compression.[100] Self-assembly occurs because the system seeks to maximize its entropy, driving particles to organize into ordered structures spontaneously.

Experimentally, entropic interactions can be tuned by synthesizing colloidal particles of different shapes and controlling the size and concentration of the polymers (or other smaller colloidal particles) that induce depletion interactions between the colloids. As a result, we have much more control over colloidal interactions than we do over those between small molecules.

This aspect becomes crucial for the design of complex self-assembling structures. In recent decades, much research into self-assembly has focused on materials with structural complexity to form photonic crystals and quasicrystals by the self-assembly of customized colloidal building blocks, exploiting the increase the entropy of the system. As the entropic cost per colloids (or building block) increases with the number of particles involved, greater specific pair interactions are required to create larger structures of higher complexity.[99]

In such structures, non-specific interactions between particles that shouldn't be close in the desired structure must be weak enough to be easily broken during the self-assembly process allowing the structure to compact. The challenge, however, is that the stronger specific interactions required to overcome entropic costs in larger structures often lead to stronger non-specific interactions. If these non-specific interactions become significantly stronger than the thermal energy at the assembly temperature, the kinetics of self-assembly will be compromised.[101] Currently, experiments aiming to assemble intricate, addressable structures exploit the selective binding characteristics of ligands, surfactants, and DNA linkers. These advancements have propelled research to a stage where nanoscale entities like metal or semiconductor nanoparticles, can self-assemble to form a variety of predetermined, complex three-dimensional arrangements. The rational design of particle-capping organic species, known as soft ligands, is crucial for the production of high-quality ordered assemblies.[102,103]

If the interactions are favorable (lowering the total enthalpy of the system), the self-assembly process is thermodynamically favored, reaching an equilibrium state. In order to control and

program the enthalpic binding interactions between particles, ligands such as DNA-strands can be used to induce nanoparticle superlattices self-assembly.[104] On the other hand, entropy-driven self-assembly, such as drying-mediated processes, leads to kinetically trapped non-equilibrium structure es that can be controlled using micropatterned surfaces or substrates.[105] In these cases, the solvent evaporation leads to rapid changes in the concentration and organization of particles or molecules in the system, driven by the tendency to maximize the system's entropy by adopting a more ordered, but energetically favorable, state. These non-equilibrium structures may have unique properties and arrangements that are thermodynamically meta-stable and can be preserved once the solvent evaporation is completed. Micro- and nano- patterned surfaces provide a tool to control and influence the self-assembly process.[106] The surface topography and chemical functionality can affect the interaction and organization of assembling components. Indeed, the patterned surfaces can act as templates, guiding the self-assembly process into specific patterns or structures, enabling the creation of well-defined and controlled architectures. Moreover, they may influence the kinetics of the assembly process, potentially leading to stable structures or structures with enhanced functionalities. Ligands play a critical role in the fabrication process; through either electrostatic or steric interactions they regulate symmetry and superlattice properties, preventing aggregation, adjusting the interparticle potential, and maintaining the mechanical integrity of the superlattice through strong ligand-ligand interactions.[103] NPs stabilized with highly charged ligands maintain their colloidal stability by exploiting repulsive forces, whereas ligands that occupy significant space stabilize NPs through steric effects.[102] These surface-stabilizing ligands can be added during synthesis, or they can be engineered post-synthesis *via* ligand-exchange to replace existing ligands on the NP surface. The latter represents the case exploited in the context of this work and discussed in the following paragraphs.

2.3.2. Van der Waals interaction (VdW)

Van der Waals attraction interactions rely on short range forces (separation <10nm) and they tend to promote particle aggregation and adhesion to substrates.[107] In non-polar species, these attractive forces can be attributed to fluctuating electron distributions around atoms and molecules which leads to instantaneous dipoles formation. They can be broadly categorized into three types: Keesom forces (orientation force), Debye forces (induction force) and London dispersion forces, all displaying a strength of the interaction dependence from the center-to-center interparticle distance (r^6). In colloidal suspensions, particles may possess permanent dipoles due to the chemical environment of the surface ligands and the crystal structure of self-assemblies. These dipoles interact at various rotational orientations, influencing the arrangement and stability of the colloids. Temperature-dependent attractive forces resulting from these dipoles can inhibit agglomeration or coagulation within the colloidal system.

2.3.3. Depletion forces and steric repulsion

Depletion forces arise in colloidal systems with high concentrated media or with different sized particles, when the particles (with same size) approach each other reducing the effective volume available for the surrounding species ("*depletants*").[108] When particles surface-to-surface distance become smaller than the depletant diameter, the excluded volumes begin to overlap, rendering the area between large colloids inaccessible to depletants.

Consequently, these depletants no longer fit between the particles and they are expelled from interparticle region. The expulsion eliminates any counteracting pressure that was keeping the colloids separated, [109] and the surrounding molecules then start exerting an opposite osmotic pressure (Π) that propels the particles close together. This leads to the aggregation or close-packed self-assembly of colloidal particles, when the effective interaction free energy of the system equals the overlap volume multiplied by the osmotic pressure ($\Delta G = \Pi \Delta V$).[110] Upon ejection, the depletant gains additional degrees of freedom as it is no longer confined between

two particles, resulting in an increase in the translational entropy of the system. Consequently, the system seeks to maximize the space volume in which the depletant can move, leading to increase the confinement of the particles to the smallest possible space, resulting in a closed-packed arrangement. Since the depletion force only arise when the depletant is ejected from the interparticle zone at small interparticle distances (distance smaller than the diameter of the depletant), hence, the depletants size defines the range of the depletion interaction, while the strength of the interaction is affected by the depletant concentration. The unique aspect of the depletion interaction is its ability to induce reversible phase separation without inducing coagulation between the particles.[111] being potentially able to generate quasi-ordered layers on individual surfaces or between two confining surfaces. The depletion force is relatively weak compared to the VdW interaction but can be used as an additional force to destabilize charge or sterically stabilized particles.[109]

To prevent irreversible aggregation, nanoparticles can be protected by either "steric" or "electrostatic" stabilizer (discussed in the **Paragraph 2.3.4**). In the steric case, which typically involves covering the nanoparticles with a tightly bound polymer or surfactant monolayer, the confined nanoparticles come into physical contact with each other and resist to elastic or plastic deformation and rearrangement.[85]

2.3.4. Electrostatic interaction

In almost all assembly processes, electrostatic repulsion plays an important background role, offsetting the perturbing influence of VdW forces to prevent coagulation or adhesion.[112] Electrostatic interactions have the unique feature of being either attractive (between oppositely charged particles) and repulsive (between similarly charged particles). Moreover, they can exhibit directionality, especially in cases involving particles with non-uniform surface charge distributions or permanent electric polarization.[113] Naturally charged particles in aqueous electrolyte solutions, for example, exhibit repulsion through the electric double-layer force.

Those not having natural charge can be modified with ionic or highly hydrated groups to reduce the attractive VdW force and preventing aggregation.

For metal nanoparticles, the assembly behavior is influenced by surface charge and size, as well as their environment. Surface charges on metal nanoparticles influence their interactions with other particles, but also with solvents and ions in solution, affecting their dispersion and stability. Understanding the specific properties of the plasmonic nanoparticles and the environmental conditions is crucial for the valuation of the effect of electrostatic repulsion on their effective volume.[85]

The particles can experience both short- and long- range order repulsive interaction.[114] Short-range electrostatic repulsion (< few nm) often plays a role in particle adsorption at interfaces, preventing the interparticle distance becoming too small thanks to the mutual electrostatic repulsion between their charged surfaces. These forces act typically within the range of the Debye length, the characteristic length scale in colloidal systems determined by the concentration of ions in the particles surrounding medium, as depicted in *DLVO (Derjaguin–Landau–Verwey–Overbeek)* theory.[115,116] Long-range electrostatic repulsion, which is prevalent in highly deionized environments, increases the effective volume per particle. It refers to repulsive forces that act over larger distances, beyond the Debye length.[89] The influence of long-range electrostatic repulsion on metal nanoparticles varies depending on factors such as nanoparticle characteristics (size, and shape can impact the surface charge density and distribution) and the surrounding environment.

2.3.5. Capillary forces

Colloids are commonly dispersed within solutions and organized into structured configurations within their liquid surroundings. When interfaces connect colloidal particles or when the particle-liquid interface is exposed to a vapor phase, the deformation of these interfaces results

in the generation of attractive capillary forces capable of driving particle movements or rearrangement.[117]

Harnessing the topological tailoring of long-range interactions in small particle systems, capillary assisted assembly, guided by the solvent evaporation, emerged as a cost-effective robust protocol used to achieve defined superstructures. [118]

Capillary assembly exploit interaction among particles in solutions, driven by surface tension, extending its influence even at distances of hundreds of micrometers.[119]Capillary attraction is originated at the liquid meniscus bridge between nanoparticles during drying process, also for particles adhered to surfaces, playing a crucial role in self-assembly by enhancing particle adhesion. The shape of the meniscus between the particles, governed by the Laplace equation, gives rise to a long-range attraction that is distinct from the *DLVO* forces.

The fluid dynamics involved in droplet evaporation approaches is typically transient in nature and depends on the Reynolds and Weber numbers, on the angle and interface deformation, on the Marangoni,[120] and coffee ring (CRE) effects,[121] and on the liquid evaporation at the free surface. Convective flows, which affect the distribution of colloids during solvent evaporation strongly influence the drying mechanisms. The most common colloidal drop deposit mechanisms generate a peripheral ring (coffee ring), due to the strong radial flow carrying the particles toward the pinned wetting line where the solvent evaporation is faster for geometrical constrains, and a central bump, due to convection flows due to the local gradient of interfacial tension generated by the presence of foreign species in a liquid (*Marangoni effect*). These strategies employed to counteract these undesired effects include modifying interparticle and particle-surface interactions to reduce the CRE and balancing inward Marangoni flows resulting from surface tension gradients, controlling surfactant concentration, and solution volume. The use of cosolvent and proper ligand selection are also adjusted to effectively manage convective flows.[17,123–125] Therefore, colloidal stability (ligands electro-steric interactions), wettability of the surface, and engineering the templates play a pivotal role to achieve well-controlled colloidal

self-assembly. The interplay between these strategies increases the versatility of the technique based on the use of colloids drop evaporation such as capillary and template assisted self-assembly, allowing it to be tailored to specific colloid-substrate combinations.

Optimized self-assembly protocols facilitate the rapid fabrication of a diverse range of nano- and microarchitectures over large areas enhancing the pattern quality. CAPA is particularly successful in forming metasurfaces with single particle as repeating units, yielding quality factors above 50.[126] Moreover, this method iwas exploited for the organization of anisotropic nanoparticles.[30] The self-assembly is induced by dragging the colloidal suspension droplet meniscus against a templated surface using a doctor-blade-like set up. Evaporation rate and meniscus contact angle become key factors in controlling capillary forces and maintaining colloidal stability. The main disadvantage of this approach is that, since the nanoparticles assemble inside nanocavities of patterned substrates, the fabrication process must involve further transfer printing or dissolution steps.[127–129]

2.3.6 Hydrophobic interaction

These interactions are included in what are collectively known as "*non-DLVO* forces" such as steric and depletion force, polymer bridging interaction, and hydration force. Hydrophobic interactions generally drive aggregation of hydrophobic species in aqueous environments, influencing macromolecular or biomolecular conformation, micelle formation,[130] and oil-water separation.[131] The reorganization of the particles in order to form an interface involves a significant energetic cost, and this free energy of formation needs to be compensated by forces that favor separation of the system into different phases. Since hydrophobic interactions strength increase with increasing temperature, they are often related to an entropic nature. An entropy increase can result from disruption and modification of the hydrogen bonding network at the water-hydrophobic species interface.[132]

Since hydrophobic surfaces tend to repel water molecules and create a low-energy environment, the nanoparticles in the solvent may experience repulsive forces, which help creating organized and stable arrangements. This controlled assembly can result in well-defined structures and patterns, influencing their orientation and organization on the surface.

In the context of this thesis, hydrophobic interactions between hydrophilic NPs and the substrate were exploited to enhance the quality of the plasmonic assemblies.

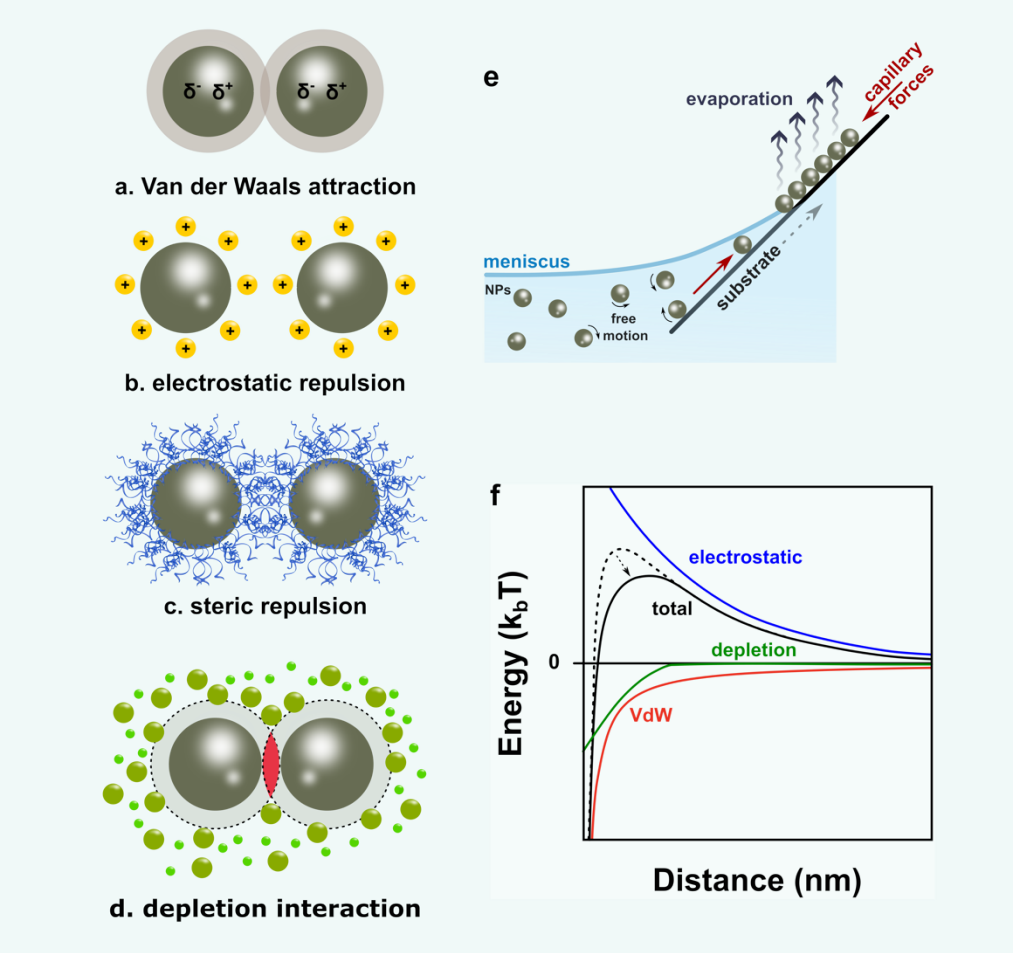

Figure 2.6 **Illustration of the main interaction forces between particles**. (**a**) Van der Waals attraction, (**b**) electrostatic repulsion, (**c**) steric repulsion between particles covered by polymeric ligands, (**d**) depletion forces, where the dashed line represents the excluded volumes surrounding the large colloids, which the center of small depletants cannot occupy and has the same thickness as the depletant radius; when the larger particles come within a distance shorter than the depletant diameter, the depletants are forced out of the interparticle region (**red** area). This expulsion creates an unequal osmotic pressure, causing the colloidal particles to move closer together. (**e**) capillary forces dynamics, where the attractive force arises from the overlap of menisci formed around separate

particles. (**f**) Interaction energy profile of charge-stabilized particles: The **blue** curve represents the repulsion typically attributed to electrostatic interactions; the **red** curve represents the VdW attractive interactions, and the **black** curves represent the total potential energy for a system without (**dashed** line) and with (**solid** line) depletants.

An interesting case-study where hydrophobic interactions are exploited to achieve a dynamic self-assembly was proposed by Baumberg's group in 2016. They proposed a design for a biocompatible colloidal actuating transducer, based on a solution of gold (Au) spherical NPs coated with the amino-terminated polymer poly(N-isopropyl-acrylamide) (p-NIPAM), and showing both high-energy storage (1,000 kBT/cycle) and fast (>MHz) release mechanism.[133] This approach exploits p-NIPAM temperature-responsive coil-to-globule transition at a critical temperature (Tc) of 32 °C. Below Tc, p-NIPAM is a hydrophilic polymer that swells in the presence of water, while above Tc it becomes hydrophobic, expelling water and collapsing to a much smaller volume. In the colloidal suspension, a sparse coating of amino-terminated p-NIPAM displaces some of the charged citrate originally bound to each Au NPs. The solution is then heated above Tc, triggering the p-NIPAM collapsing into hydrophobic spheres, and inducing the piling of more hydrophobic material on top of the nanoparticles, forming a thicker layer and initiating aggregation of weakly charged clusters. Thanks to the established balance between charge and steric interaction, the aggregation process is fully reversible. In fact, when the temperature drops below Tc, the coated AuNPs experience a strong repulsion due to the residual charge, and the p-NIPAM structure is re-inflated, producing single AuNPs coated with p-NIPAM layers 40nm thick. The dynamic nature of this colloidal system expands even further, exploiting the plasmonic photothermal effect to enable the remote and reversible control of the Au NPs via pulsed laser irradiation at 532 nm to bring the system above the Tc. For this system, VdW interactions play a crucial role to provide the necessary attractive force in the collapsed state, while ensuring at the same time a limited interaction strength for efficient separation when the p-NIPAM spheres transit to the inflated state. These colloidal actuators can be repeatedly cycled from inflated (cold, isolated NPs) to deflated (hot, aggregated NPs) state. This system may be of interest for the development of colloidal-based nanomachines in solid systems,

integrating them with the concept of metasurfaces to create, for example, reversible and spatio-temporally controlled active colloidal switchers.

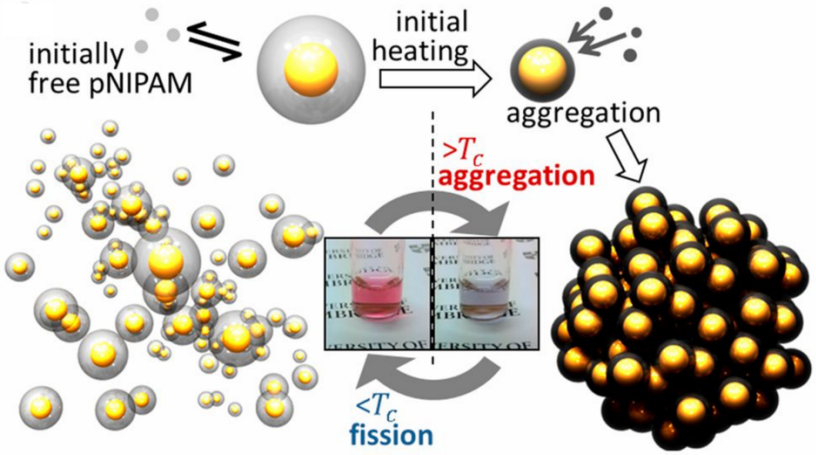

Figure 2.7 Formation of Au nanoparticles coated with p-NIPAM-coated by mixing in solution and heating above 32 °C to attach p-NIPAM onto Au surface. In deflated (hot) state, NPs aggregate closely together (**blue** solution). By cooling down the solution, the particles aggregate into clusters tend to split into individual entities (**red** solution). Fission and aggregation by cooling and heating the particles result reversible process. Copyright 2016, PNAS. Adapted with permission.[133]

2.4 Template-assisted self-assembly (TASA)

In the following part of this chapter, the discussion will focus on the two alternative fabrication strategies that were optimized during this thesis: template-assisted self-assembly (**Paragraph 2.4**) targeting highly homogeneous metasurfaces for the promotion of non-linear optical phenomena, and a new approach named chemical contrast *in situ* growth (**Paragraph 2.5**). Template-assisted self-assembly has emerged as a powerful, scalable, and cost-effective fabrication technique to produce plasmonic metasurfaces with tailored optical properties. This approach relies on the use of pre-patterned elastomeric templates to guide the assembly of metallic nanoparticles or nanostructures into well-defined configurations.

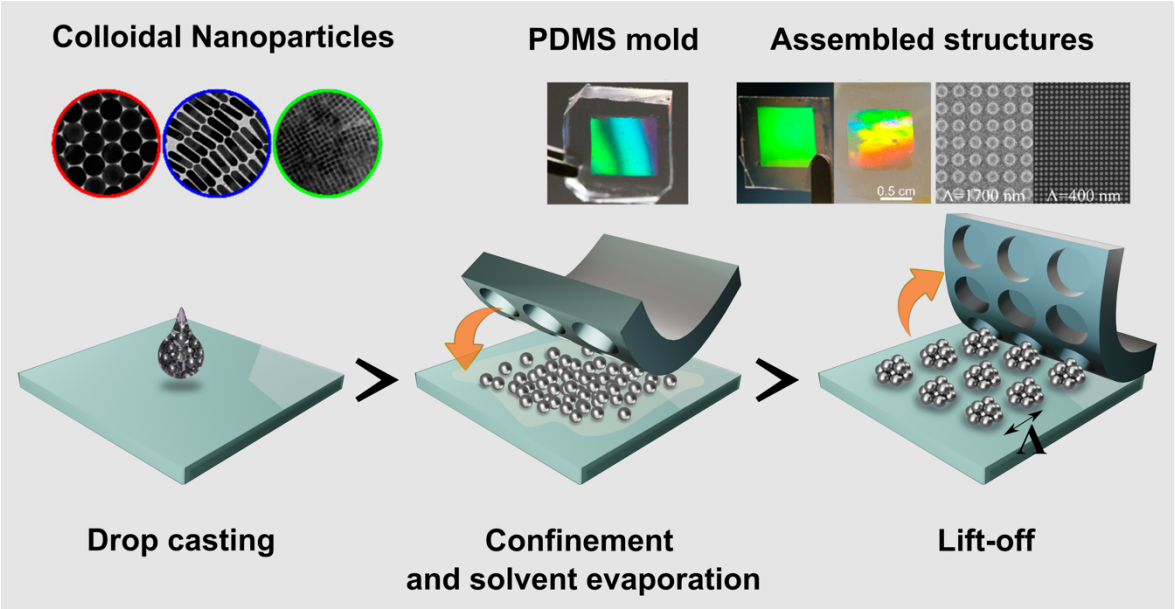

Figure 2.8 Template-assisted self-assembly schematic and representative images of colloidal nanoparticles, patterned templates, and assembled substrates in array with lattice period Λ. Copyright 2021, ACS. Adapted with permission.[134]

By exploiting the interplay between template geometry, surface chemistry and colloidal interactions, template-assisted self-assembly enables the targeting of large assembly areas by confining nanoparticles within cavities of a template through capillary forces at the three-phase contact line of a receding meniscus. This approach has the potential to achieve precise control over the position and orientation at single-particle level through the careful design of the template's topography. The procedure involves drop casting of a small volume (usually a few microliters) of a highly concentrated nanoparticle suspension and the subsequent confinement between a reusable template and a target substrate. During the solvent evaporation, the nanoparticles confined in each hole could adjust their positions to allow a size-maximized packing into superstructures whose symmetry, size, and shape is mainly determined by the template cavities. The drying process allows for meticulous control of particle deposition across areas as extensive as square centimeters, while facilitating the formation of densely packed nanoparticle structures. PDMS is commonly used as template material, created through soft lithography replication of prepatterned surfaces or masters. These molds repeatedly replicate

the original surface by pressing and curing against photoresists, polymers and various other materials, offering virtually unlimited replication cycles.[135]

While techniques like capillary assisted, spin coating or wrinkled template-assisted self-assembly[81,118,127,129,136,137] offer precise nanoparticle positioning but at the expense of transferring or dissolution subsequent steps, as already mentioned, template-assisted self-assembly has arisen as a promising one-step method.[134] This approach is highly versatile and can be integrated with nanoimprint lithography, making it compatible with roll-to-roll fabrication and adaptable to various colloids, solvents, and surfaces.[26,138–140]

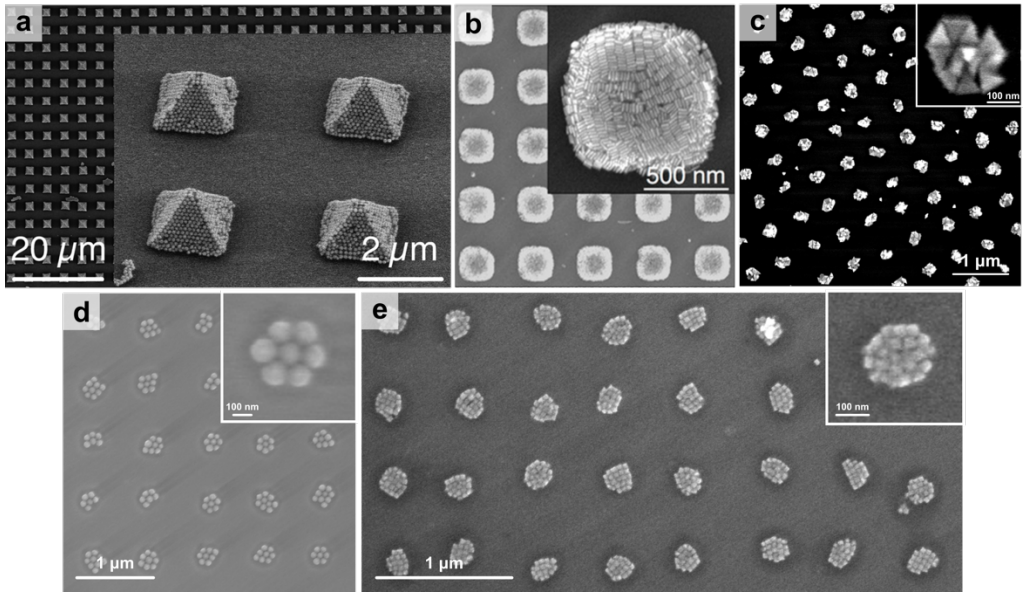

Figure 2.9 Scanning Electron Microscopy (SEM) images of TASA of (**a**) spherical NPs, (**b**) rods NPs, (**c**) triangular NPs, (**d**, **e**) core (Au) shell (Ag) spherical NPs (**d**), and cubic NPs (**e**) in squared arrays. **Panel a**: Copyright 2017, ACS. Adapted with permission.[29] **Panel b**: Copyright 2019, ACS. Adapted with permission.[17]

Particle-template and particle-substrate interactions influence the preferential adhesion of nanoparticles to either surface, thereby affecting the quality of the final product.

Modifying the physico-chemical properties of substrate surfaces offers the potential to alter their interaction and adhesion with colloidal nanoparticles. NPs in liquid phase experience Brownian motion, while Van der Waals interactions between particles and capillary forces, triggered by solvent evaporation under the template stamp, drive the spontaneous assembly. Typically, resulting nanostructures exhibit hexagonal symmetry with face-centered cubic (fcc) or

hexagonal close-packed (hcp) crystal lattices. The self-organization initiates when the solvent layer thickness approximates the particle diameter, thus solvent evaporation rate, particle shape, and surface chemistry significantly influence lattice quality. Drop-casting induces various effects discussed in **Paragraph 2.3.5**, including the Marangoni effect and the coffee ring effect, caused by differential solvent evaporation along the air-liquid interface during drying process.

To mitigate these challenges, the interaction between particles and substrate can be adjusted by modulating the solvent composition and hydrophilic/hydrophobic effects. For example, PDMS offers a soft hydrophobic surface that initially contrasts with glass or silicon substrates; however, further treatments such as UV-O_3 exposure, deposition of silane layers on the surface of the substrate/stamp, changes of the substrate material, variation in colloidal concentration, drop-casted volume, or surfactant concentration can improve the quality of the final assembly.

The periodic configuration of the nanoparticles allows to generate colloidal-based plasmonic metasurfaces showing peculiar optical properties discussed in **Chapter 1**. In most of the cases, supercrystals formed through template-induced assembly present individual nanoparticles arranged in more intricate repeating structures like clusters or meta-molecules.[141,142] In these structures, both near-field and far-field coupling alter the distribution of the electric field. Near-field coupling concentrates strong electric fields within localized regions, while far-field coupling exhibits more moderate electric field values across broader areas, extending beyond the metal surface. However, far-field coupling is affected by the strong localized near-field behavior within the clusters, characterized by many intense hot-spots. An increase of the cluster dimension leads to the red shifts and broadening of the LSPR, which affect the hybridization with the diffractive modes. The typical diffraction modes arising from these structures are shifted towards the blue compared to the plasmonic response, resulting in asymmetric extinction profiles. The collective optical response of the array in the far field results affected to adequately compensate for the optical losses within the clusters, thereby limiting the corresponding quality factors. In essence,

the optical behavior of the system is primarily influenced by the LSPR within each cluster influencing deeply the quality factor of the optical response.

To reduce the effects of near-field coupling in the clusters, calculation and experiments have proven that smaller nanoparticles (< 25 nm in diameter) can be more effective, resulting in blue-shifted and narrower LSPRs.[134,143] Although the sharpest resonances have been observed in single-particle plasmonic arrays,[129,144] from the point of view of colloidal self-assembly employing small nanoparticles is a more straightforward method for creating resonances with high quality factors at the expense of possible structural defects which can impact the lattice response of single nanoparticle plasmonic arrays.[145] On the other hand, employing index matching layers offer the opportunity to compensate the mismatch between superstrate and substrate and observe the far-field optical response even in lower quality structures but sealing the metasurface and making it inaccessible.

For this thesis, different type of colloidal metasurfaces were prepared circumventing the issue of index matching steps while ensuring a high quality of the lattice, translated in high quality factors of the optical cavity. Specifically, square lattice and chiral Ag nanoparticle arrays were prepared by exploiting the refractive index mismatch approach and the hydrophobicity induced using a high refractive index epoxy-resin, which allowed the metasurfaces to remain freely labelled and fully accessible for further modification, while ensuring a high-quality optical response, as will be discussed in **Chapter 3**.

2.4.1 Preparation of the plasmonic metasurfaces

Before moving into self-assembling, we first had to optimize the synthesis of monodispersed spherical NPs to use as building blocks., which influence the packing arrangements, to ensure high degree of uniformity and reproducibility of the assembly, while precisely controlling the optical properties arising from the structures. This leads also to easily approximate the experiments to the theoretical model applied to these systems. Considering that this thesis is

centered around the visible port of the EM spectra, in order to facilitate the metasurface engineering of the optical response, we needed to keep the localized resonances and the collective lattice resonances spectrally separated. Compared to gold, silver presents a blue shifted localized resonance around 400 nm (compared to 520 nm of gold) and presents higher plasmonic performance with less optical losses, promoting the formation of narrower SLRs. These reasons motivated our choice of silver for the fabrication of 2D squared and chiral arrays, which could be applied as optical cavities for the promotion of NL optical phenomena.

Colloidal nanoparticles were synthetized and functionalized with thiol-terminated polyethylene glycol (PEG-SH, with a molecular weight of 2000 g/mol), concentrated (as described in **Experimental Section**) in the assembly mixture of water and ethanol (6:4 ratio), with a small concentration of cationic surfactant (cetyltrimethylammonium chloride, or CTAC, at 50 μM). To initiate the self-assembly of colloids into plasmonic arrays, a 1 μL portion of the chosen colloidal suspension was dropped onto the substrate and the ordered assembly is induced by a polydimethyl siloxane (PDMS) mold patterned as squared array of holes, obtained via NIL as described in the **Experimental Section**. The final height of the clusters forming the array is regulated by the concentration of the colloid, which adheres to a close packed hexagonal (hcp) arrangement of the nanoparticles within each cluster.[17]

The optimization of the self-assembly was achieved by varying concentration of the colloids, drop-casted volume, and the surfactant concentration (**Figure 2.10**).

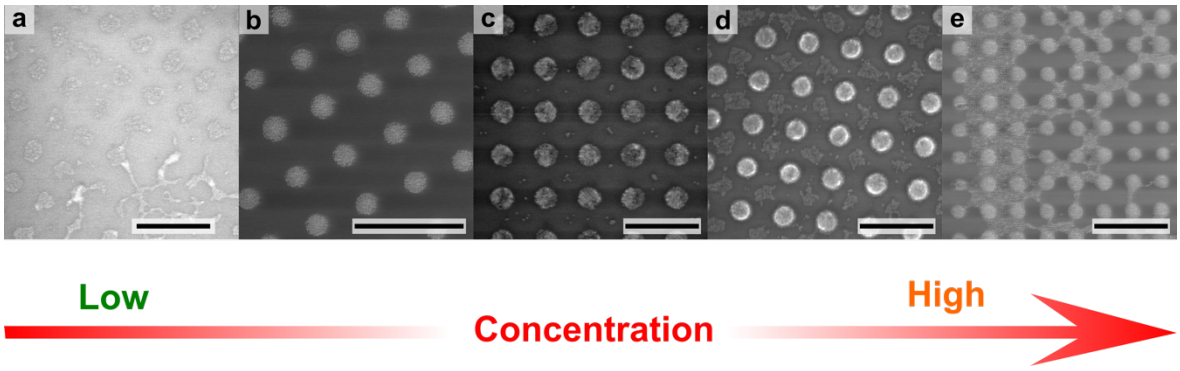

Figure 2.10 (**a**-**e**) SEM images representing samples prepared using an increasing concentration of AgNPs dropcasted. The optimized concentration (**b**) was selected to avoid empty regions (**a**), as well as excess of nanoparticles accumulated outside the pattern (**c**-**e**). **Scale bars**: 1 μm.

Another important feature of our metasurfaces is constituted by a high refractive index photoresist (SU8-200.5), which was implemented in the architecture to induce a refractive index mismatch between substrate and superstrate (air) that ensure the formation of hybrid waveguided-lattice resonances (as discussed in **Chapter 3**) which allowed to observe a narrow bandwidth optical response from the structures while keeping them completely exposed to the surrounding environment. Moreover, we observed anther important role for SU8. Being a hydrophobic polymer, we noticed that it improved the self-assembly performance by creating a more hydrophobic environment and inducing the particles (hydrophilic) to remain trapped in the holes, leading to the formation of a higher quality of the final array and improved optical performance (see **Experimental Section**).

The SU8 resin is spin coated on the glass coverslip and the monomer undergoes activation upon exposure to UV light. However, polymerization remains significantly incomplete until the subsequent hard bake step, which also determines the porosity of the final layer. During the hard bake process, as the temperature rises, epoxy groups cross-link to create a thoroughly cured structure. This effectively prevents the interaction between the solvents in nanoparticle drop and dyes embedded in the SU8 layer, which could disrupt the desired architecture. The duration of baking depends on the final thickness of the SU8 layer. It's important to note that both the UV exposure dose and the baking times are critical for achieving successful self-assembled

architecture. They enable control over the number of cross-linking sites and allow for adjustments to the chemical and mechanical stability of the film.[146] The fabricated plasmonic arrays exhibit both mechanical and chemical stability for several days at room temperature.

In order to explore the effect of the fabricated metasurfaces on various emission phenomena, which will be discussed in the next chapters, we needed to interface them with an emitting gain medium. The first fabrication protocol that we optimized is schematized in **Figure 2.11**. Here a high quantum yield die, Rhodamine B, was mixed directly with the SU8, and served as substrate for the self-assembly process. Details and discussion of the procedure can be found in the Experimental section, but the high-quality and large scale of the prepared metasurfaces can be appreciated looking at the SEM pictures in **Figure 2.12**.

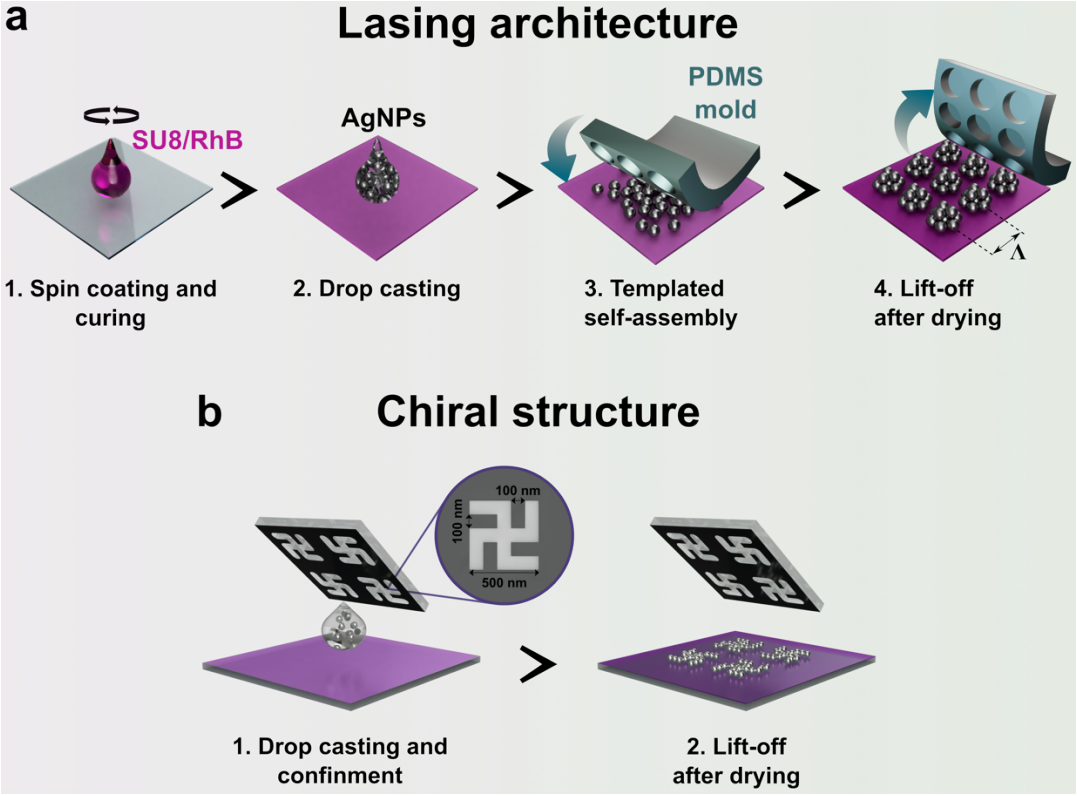

Figure 2.11 Fabrication schemes of the (**a**) 2D squared array of spherical AgNPs for the Lasing architecture, and (**b**) the array of Gammadions. Both the samples involve the use of an epoxy resin (SU8-2000.5) mixed with the Rhodamine B dye (see **Experimental Section**) spin coated onto the glass substrate. The template-assisted self-assembly is performed directly onto the SU8 layer.

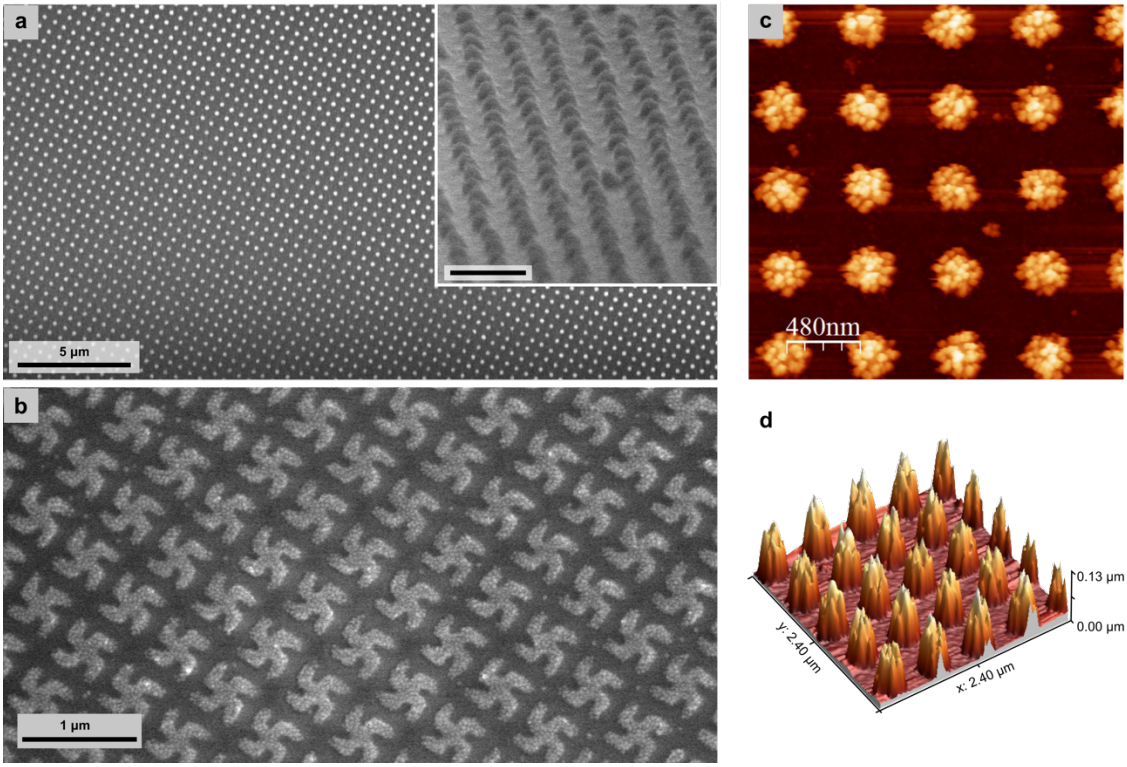

Figure 2.12 (**a**) Low magnification SEM characterization to show the large area quality of the fabricated AgNPs (25 nm in diameter) array with lattice period Λ = 400 nm on top of a layer of SU8-RhB. The **inset** shows the cross section (45°) of a sample of AgNPs array with lattice period Λ = 400 nm (**scale bar**: 1 µm). (**b**) R-Gammadion shaped array of AgNPs (50 nm in diameter).

The second self-assembly protocol was optimized for the exploration of two-photon emission phenomena. Here, the need for a more photostable emitter forced us to adopt a slightly different fabrication strategy. Specifically, the difference in solubility of the core-shell QDs prevented us from dispersing them within the photoresist layer. Instead, the QDs were spin coated on top of the SU8 (250 nm thickness) once it was already cured (**Figure 2.13**). Once the QDs layer was formed, the self-assembly step was performed directly on top. Once again, the SEM analysis show excellent large-scale assembly, and high-magnification imaging clearly reveal the presence of the QDs underneath the silver NPs. Finally, the analysis of a cross-section of the prepared architecture revealed the QD layer to be very thin, within 5 and 10 nm, which corresponds to 1-2 layer of QDs.

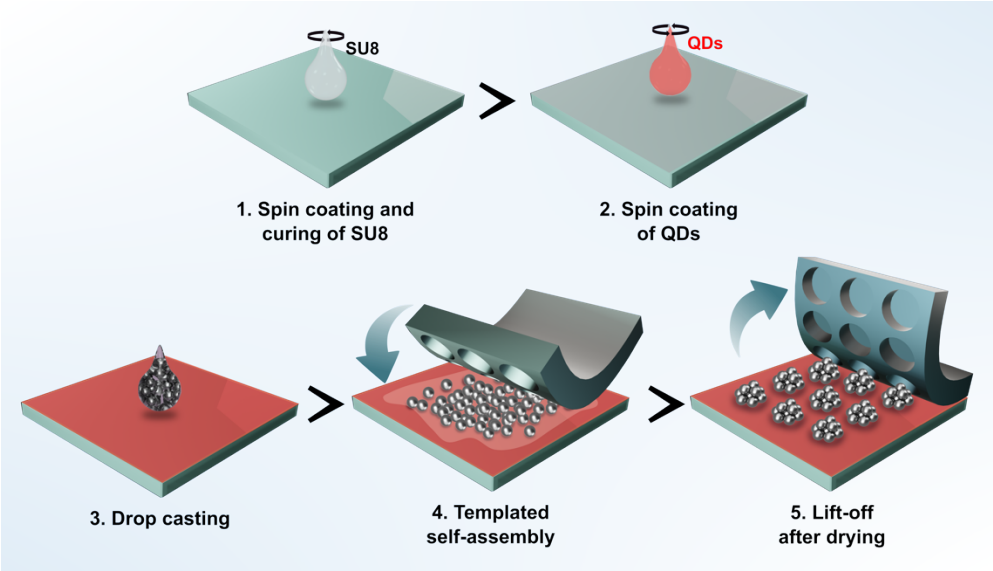

Figure 2.13 Fabrication scheme for the 2D squared array of spherical AgNPs with core-shell QDs (CdSe/ZnS) used for two-photon excited emission.

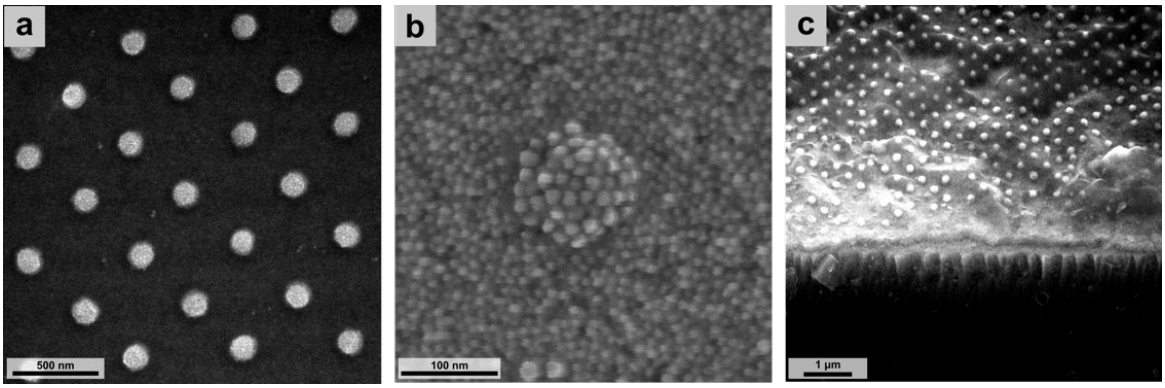

Figure 2.14 SEM images of: (**a**) Array (Λ = 600 nm) of AgNPs (25 nm in diameter) on top of a layer of QDs. (**b**) High magnification SEM image of the AgNPs cluster on top a layer of core-shell type of QDs. (**c**) SEM cross section (45°) of the array assembled on top of a layer of QDs deposited onto the SU8.

Apart from interfacing our plasmonic metasurfaces with different emitters, we also focused our attention to investigate the effect of pre- and post-assembly modification of the repeating unit over the optical properties of the assembled structure (**Chapter 3**). To do so, particles with different sizes but same composition (Au) and a combination of gold and silver nanoparticles were assembled on untreated glass cover slips.

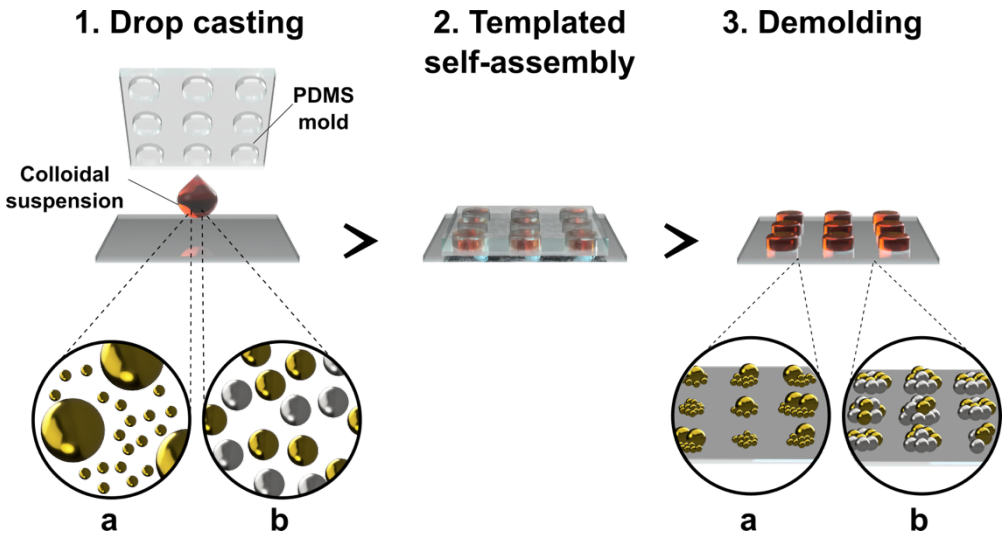

Figure 2.15 Templated self-assembly for pre- and post-assembly modification analysis. The zoom illustrations **a** and **b** show the colloidal suspension of (**a**) NPs with different sizes but same composition (Au), and (**b**) NPs with same size and different composition (Au, Ag) with the final arrangement.

Scanning electron microscopy analysis (**Figure 2.15**) shows that for bimodal size distributions, the internal organization is affected, and the final clusters do not exhibit the usual hcp internal arrangement (**Figure 2.15 a**, **b**).

Notably, in the case of a **1**:**1** ratio of 25 and 100 nm particles, several clusters containing solely 25 nm colloids were observed (**Figure 2.15 c**, **d**). This can be attributed to variations in translational diffusion coefficients, which are determined by the colloid diameter according to the Stokes–Einstein equation ($D \propto 1/R$, where R is the radius of the particles). This suggests that small colloids rapidly occupy the cavities of the mold, preventing the larger gold particles from occupying the same space.

On the other hand, the simultaneous assembly of Au and Ag colloidal did not affect the self-assembly process, resulting in the statistic organization of both building blocks into plasmonic arrays on a large scale. Notably, despite the significant volume disparity (64-fold difference), both small and large colloids were able to self-assemble within the same cluster structures.

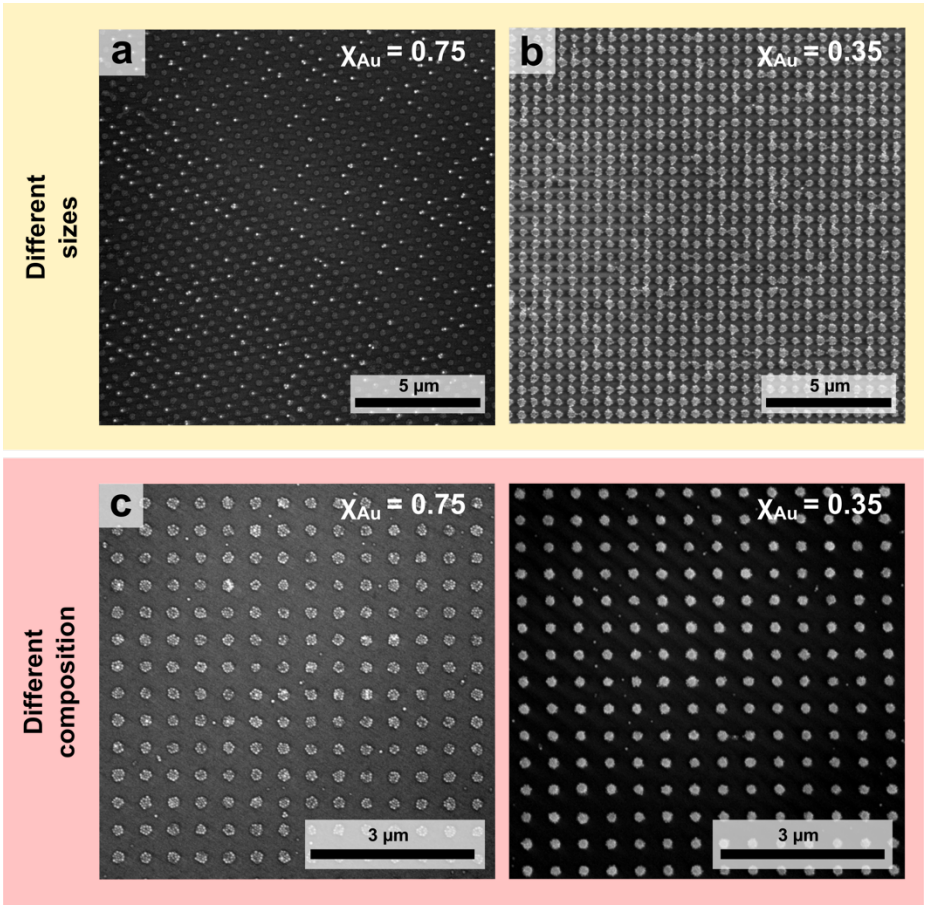

Figure 2.16 SEM images of array with lattice period 500 nm. (**a**, **b**) 24 ± 3 and 96 ± 9 nm in diameter AuNPs in portion (**a**) **1**:**1** and (**b**) **1**:**3**. (**c**-**d**) gold and silver nanoparticles arrays with fraction of the gold colloid of (**c**) χAu = 0.75 and (**d**) χAu = 0.35.

In conclusion, in this thesis work we optimized several TASA protocols for the preparation of plasmonic colloidal arrays over cm scale. The quality of all the colloidal-based plasmonic metasurfaces prepared was proven *via* SEM morphological analysis. The images show a high uniformity degree and structures with low ratio of defects. Experimental details, and additional discussion can be found in the **Experimental Sections**.

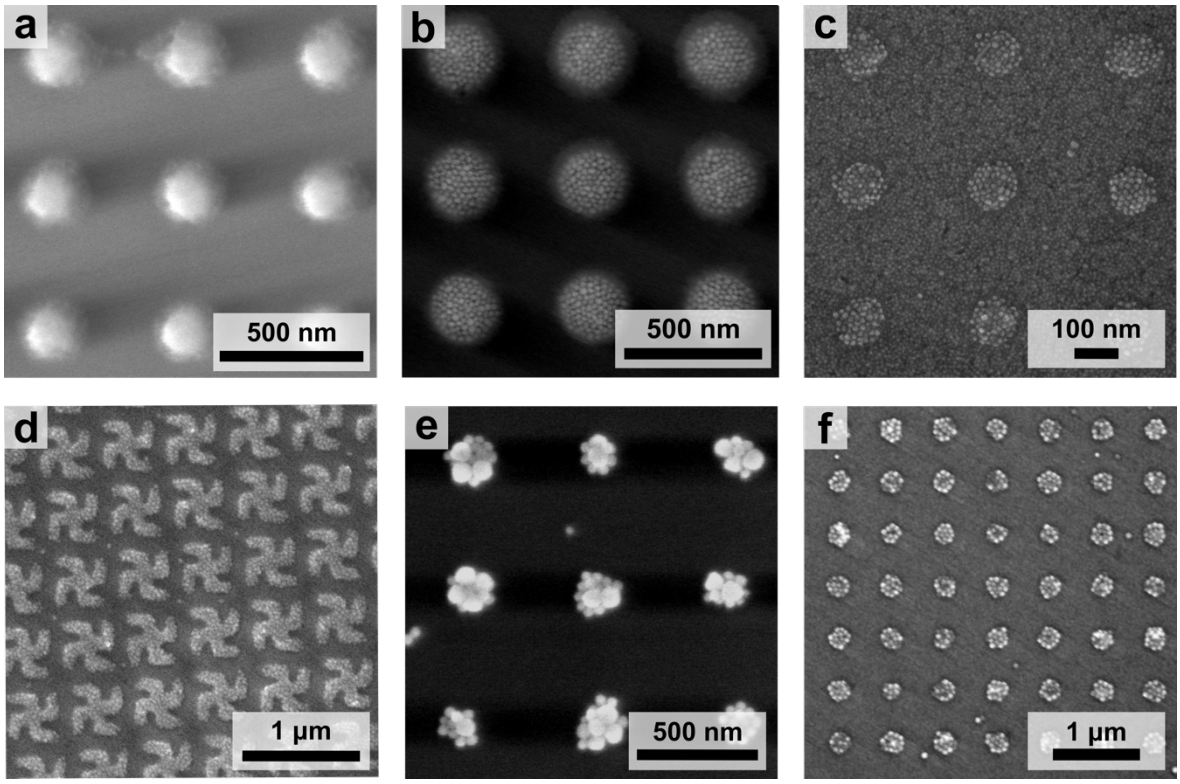

Figure 2.17 High and mid-magnification SEM images of all type of samples prepared for the thesis. AgNPs array of 25 nm in diameter with lattice period Λ = 500 nm on (**a**) glass, and on (**b**) SU8-RhB. (**c**) AgNPs array (25 nm in diameter) on a layer of QDs (~10 nm). (**d**) R-Gammadion shaped array of AgNPs 50 nm in diameter. (**e**) Array of AuNPs with a mixture of 100 and 50 nm nanoparticles (Λ = 500 nm). (**f**) Array with lattice pitch of 500 nm of a mixture of Au and Ag NPs with same size (50 nm).

2.5 Chemical contrast *in situ* growth

Despite all the advantages of colloidal self-assembly, the preparation of monodisperse colloidal suspensions with the correct surface chemistry is often a complex, and time-consuming process which is not always easily scalable. On one side, precise temperature and addition rate control are required for liter-scale pre-synthesis, while on the other side, ligand-exchange requires the addition of significant excesses of capping ligands involving multiple centrifugation steps for purification.[147,148]

In situ growth is an unconventional fabrication approach where plasmonic structures are formed directly onto the target substrate material from inorganic precursors, bypassing all the initial colloidal synthesis steps.[36,149] Avoiding time-consuming process such as batch synthesis, self-

assembly and ligand exchange, the particles nucleate directly on the substrate, achieving tunable nano-patterns formed by single-nanoparticle-wide features.

Until now, pattern accessibility using *in situ* strategies has been limited with resolutions of microns to hundreds of nanometers, with reduced control over particle morphology.[150–152] Despite block copolymer micelle lithography raised as a prominent technique that uses *in situ* growth to create addressable structures containing plasmonic units with precise shapes and sizes, achieving uniform and reproducible results at single particle resolution,[153–156] the reliance on assembling block copolymer micelles limits the arrays to hexagonal lattices, and the casting process remains time-consuming.

In this thesis, we developed an innovative *in situ* growth method, which targets tunable plasmonic lattices through rapid *bottom-up* growth of gold nanoparticles onto chemically patterned reactive areas created by soft lithography. For this purpose, water-soluble hydroxypropyl cellulose (HPC) sacrificial hole masks (or stencils) were used to create patterned regions containing chemically active ink for gold nanoparticle growth. In a single and rapid (< 10 min) synthesis step, the subsequent site-selective growth of gold nanoparticles was achieved by adding a droplet of growth solution to the chemically patterned substrates (**Figure 2.18**). Moreover, by adjusting the composition of the growth solution, particle size and shape can be modified during substrate growth.

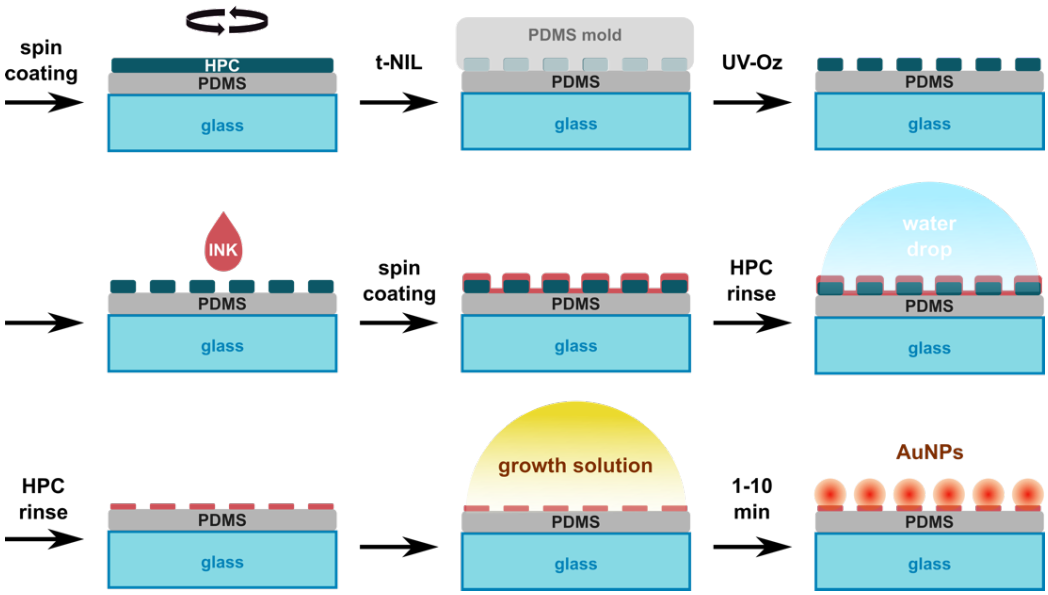

Figure 2.18 Schematic of the *in situ* growth procedure: after preparing the flat, glass supported PDMS, a layer of HPC is spin coated on top of the substrate and thermal nanoimprinting (T=140°C) is performed on top of it to achieve a pattern of wells; after the UV-O_3 treatment to reduce the residual HPC layer, the procedure involves the spin coating of the PMHS ink. After, the HPC stencil is let swell and dissolve by dropping Milli-Q water on top of the substrate for 30 min, and then rinsed away with abounded water. Thus, the substrates are dried with air compression gun. At this point the substrate should appear as a squared pattern of reductant inked regions. When the growth solution is applied with different growth time (1-10 min), the gold precursor starts to nucleate directly on top of the substrate forming an ordered array of AuNPs.

2.5.1 Fabrication of the HPC stencils

Thermal nanoimprint lithography (t-NIL) was originally developed on rigid substrates, and one of the main drawbacks of the technique is the formation of a residual layer with a minimum thickness ~20 nm, which is left underneath the imprinted features.[157] This is typically removed in a later step *via* wet or dry etching techniques such as reactive ion etching (RIE). Avoiding the formation of the residual layer is made impossible by physical requirement of the t-NIL process. In fact, the volume of the material to be mechanically deformed has to be bigger than the volume required to fill the stamp completely.[157,158] In order to satisfy the volume conservation condition, the volume of the initial HPC layer ($V_{initial}$) needs to be equal to the final volume of the patterned HPC film (V_{final}). For the specific case of square arrays used in the thesis, to calculate the V_{final} it is considered its correspondence to the volume of the negative space around the pillar (or the total volume of the patterned HPC film):

$$V_{final} = (V_1 - V_2) = A_1(h_{pillar}) = (\Lambda^2 - A_2)\ (h_{pillar}) = (\Lambda^2 - \pi r^2)\ (h_{pillar}) \qquad \textbf{(2.1)}$$

where V_1 is the pillar volume corresponding to the square area A_1, and V_2 is the volume corresponding to area A_2; Λ is the lattice parameter, r is the ray of the circular cavity with dimension (Φ), and h_{pillar} is the pillar height (390 nm). The $V_{initial}$ (**Figure 2.19 b**) of the film with minimum starting height (h_{min}) of an unpatterned area corresponding to the square area A_1 can be calculated as: $V_{initial} = \Lambda^2 \cdot h_{min}$.

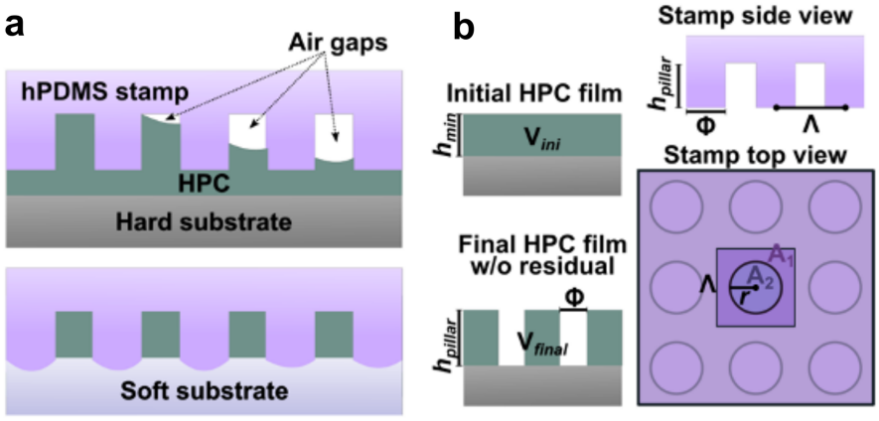

Figure 2.19 (**a**) Schematic of the thermal t-NIL on hard and soft substrate. (**b**) Hydroxypropyl cellulose (HPC) film parameters before and after t-NIL and h-PDMS stamp dimensions used for the volume conservation calculations.

Since for the HPC film $V_{initial} = V_{final}$, h_{min} can be calculated as:

$$h_{min} = [(\Lambda^2 - \pi r^2) \cdot (h_{pillar})]/\Lambda^2 \qquad \textbf{(2.2)}$$

While the depth of the holes of the silicon master used for the imprinting dictate the pillar height (390 nm), once replicated with the h-PDMS, the actual h_{pillar} tends to be lower (from 390 nm to ~350 nm).

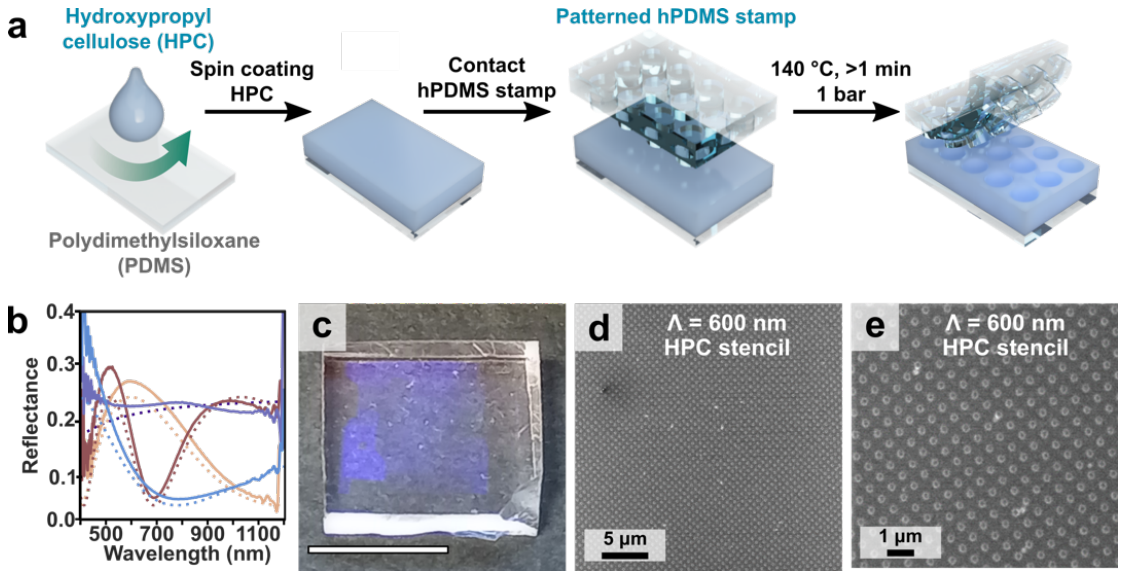

Figure 2.20 (**a**) Thermal nanoimprint lithography of hydroxypropyl cellulose (HPC) schematic. (**b**) Reflectance spectra were used to estimate film thickness on silicon. The following thicknesses were observed: 30 nm (**solid purple**), 125 nm (**solid blue**), 192 nm (**solid orange**), and 330 nm (**solid red**) for the HPC aqueous solutions at various concentrations. **Dotted** lines represent the simulated interference generated by differential refraction for thin films with heights of 30 nm (**dotted purple**), 125 nm (**dotted blue**), 192 nm (**dotted orange**), and 330 nm (dotted **red**). (**c**) Photograph of the ≈30 nm patterned HPC stencil with periodicities (Λ) of 600 nm resulting from the 21 mg/mL aqueous HPC solution (patterned area is 0.49 cm^2, **scale bar**: 0.7 cm). (**d**-**e**) SEM images of different areas of the thinnest (30 nm) patterned HPC layer.

However, the use of polydimethylsiloxane (PDMS) as susbtrate actually allowed us to avoid the formation of a measurable residual layer, ultimately enabling the fabrication of sacrificial HPC stencils with a volume lower than the negative volume of the stamp, with the minimum required HPC film height for uniformly patternable silicon substrates ranging from ~250 to 295 nm.

In fact, by comparing the measured and simulated reflectance spectra for HPC stencils (**Figure 2.20 b**), we demonstrated the precise patterning of films with heights ranging from 30 to 330 nm, suggesting that we were able to avoid the formation of a residual layer.

To explain these results, we hypothesized that the implementation of a deformable (soft) underneath substrate plays a key role by, enabling to take advantage of the applied pressure during the t-NIL step to push the HPC into the empty features, facilitating precise patterning at reduced heights and minimizing the residual layer as shown in **Figure 2.19**.

The SEM analysis confirmed the optical characterization and did not identify the presence of any residual layer. However, the resolution of the instrument would not allow the identification of very thin layers (<5 nm) (**Figure 2.20 e**). For this reason, a brief (30 s) isotropic UV–ozone etching step was performed in order to remove any residual HPC within the holes of the stencils and expose the underneath PDMS substrate. Overall, our protocol enabled us to prepare HPC films with volumes lower than the negative volume of the stamp.

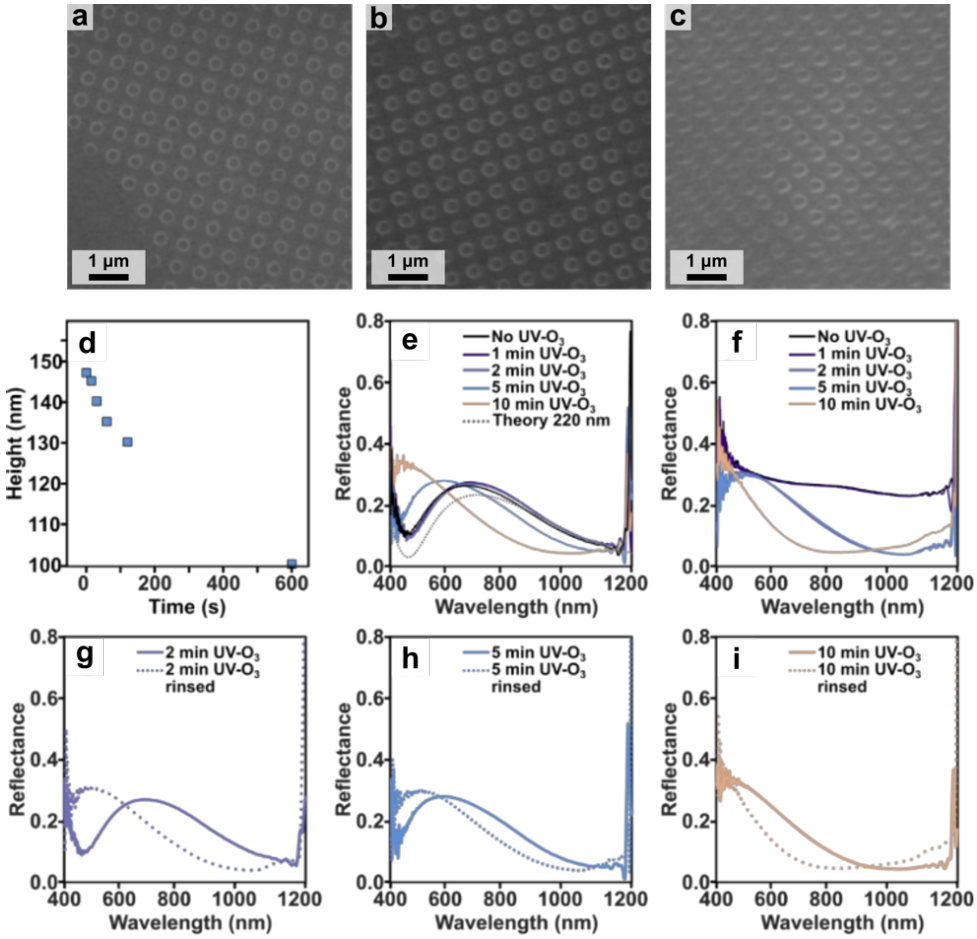

Figure 2.21 (**a**-**c**) SEM images showing hydroxypropylcellulose (HPC) films on polydimethylsiloxane (PDMS) after (**a**) 5 s, (**b**) 10 s, and (b) 30 s of ultraviolet-ozone (UV-O_3) treatment. (**d**) Graph of the estimated film height on silicon with increasing UV-O_3 treatment time (15, 30 s and 1, 2, 10 min). (**e**-**f**) Reflectance spectra of HPC films on silicon are shown in panels following (**e**) UV-O_3 treatment and (**f**) after rinsing the HPC with water. Panels (**g**-**i**) present a comparison of the reflectance spectra for UV-O_3 treated films before and after rinsing to evaluate the changes in thickness. (**e**-**i**) The **dotted** lines represent the corresponding simulated differential refraction spectra.

Interestingly, for HPC films exceeding the negative volume of the stamp (330 nm thick), we indeed observed the formation of a residual layer (as expected). In fact, these fishnets didn't result in any patterned in situ growth, indicating that that the 30 s UV-O_3 etch was insufficient to remove the residual material within the hole features and efficiently exposed the PDMS substrate for selective surface functionalization. Experimentally, only films with thickness ranging from 30 to 192 nm have been observed to give successful gold nanoparticle arrays patterning results (**Figure 2.24**).

SEM analysis confirms the pattern integrity of the HPC film after undergoing UV-O_3 treatment and ink application steps (**Figure 2.22 a**).

Negative controls on films treated with 10 sec UV-O_3 etching before the application of the ink did not reliably yield patterned gold nanoparticle arrays, highlighting that if the ink was applied while HPC residual layer was still present, the removal of HPC will also remove the ink in the following rinsing steps (**Figure 2.21 b**), affecting the NPs growth in ordered array.

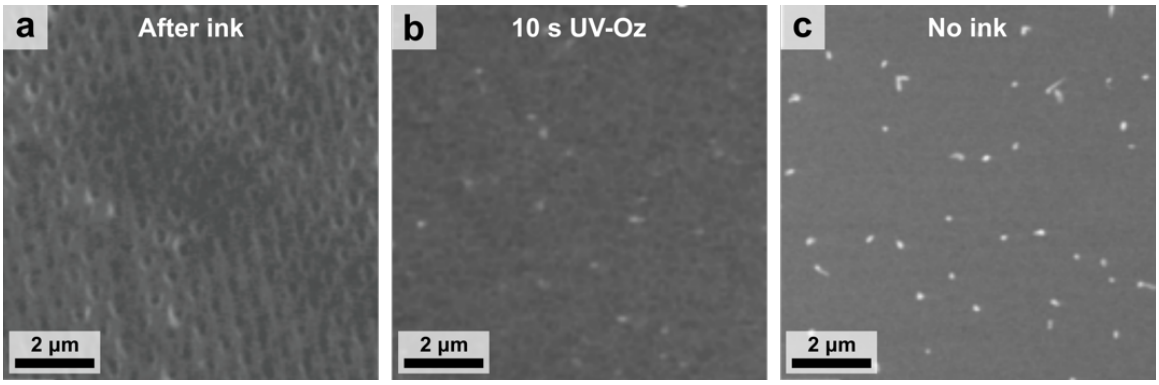

Figure 2.22 (**a**-**c**) SEM illustrating the patterned HPC film (**a**) after chemical inking with PMHS, (**b**) the PDMS following the *in situ* nanoparticle growth procedure with only 10 s of UV-O_3 treatment to reduce the HPC residual layer, and (**c**) following the procedure without applying any chemical ink.

Additionally, in the cases where ink was not applied to the HPC stencils, besides some large particles observed on the substrate likely resulting from secondary nucleation, patterned growth did not occur. (**Figure 2.22 c**).

After optimizing the fishnet fabrication on PDMS (**Figure 2.23**), we adapted the same protocol for glass supported PDMS. These substrates offered improved handling during the processing steps necessary for patterned gold nanoparticle growth.

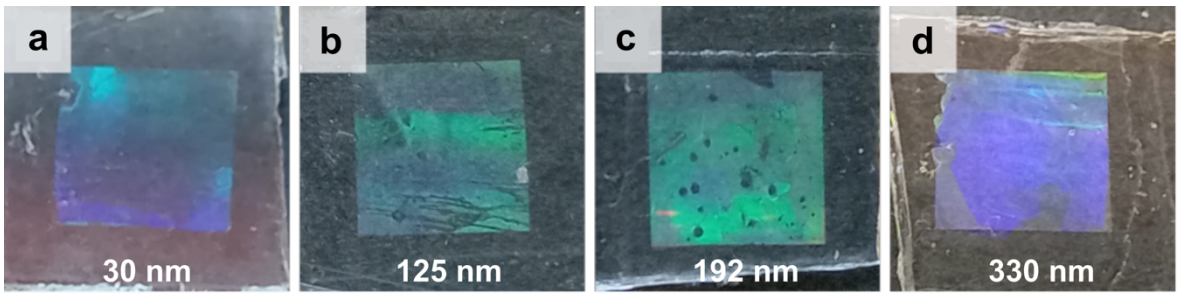

Figure 2.23 Photography of HPC film fishnet on glass-supported polydimethylsiloxane (PDMS) with thickness of (**a**) 30 nm, (**b**) 125 nm, (**c**) 192 nm, and (**d**) 330 nm (patterned area is 0.49 cm^2).

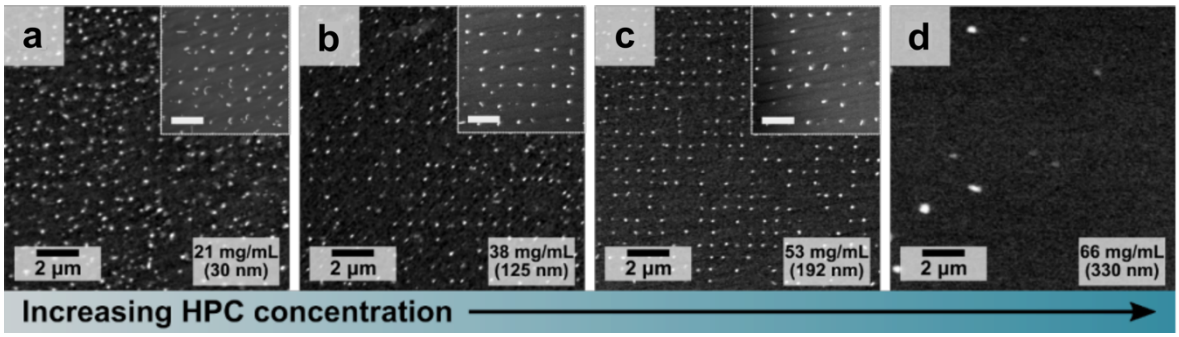

Figure 2.24 SEM images of the substrates following removal of the HPC stencil and subsequent nanoparticle growth for initial stencils made from (**a**) 30, (**b**) 125, (**c**) 192, and (**d**) 330 nm initial thickness HPC films (**inset** scale bar: 500 nm).

2.5.2 Chemical inking step

Polymethylhydrosiloxane (PMHS) is inherently present in PDMS due to residual unreacted oligomers leftover after elastomer preparation, and previous studies have demonstrated its efficiency in acting as reducing agent for gold salts, through oxidation of unreacted Si-H groups, leading to particles formation on surfaces and within the elastomeric polymer.[150,159,160] The excess of PMHS present in PDMS can vary depending on curing agent and base ratio, curing conditions, and substrate age, all making its concentration and distribution challenging to control.[161] For this reasons, as indicated in the Experimental Section, all PDMS substrates

undergo PMHS extraction before HPC fishnet preparation and *in situ* growth step. This step will yield a "growth-negative" surface where gold nanoparticles do not nucleate.

However, PMHS can be conveniently reintroduced in the system after the preparation of the HPC stencils, yielding a net chemical contrast between the exposed and unexposed areas of the PDMS substrates. The protocol adapted for the application of the PMHS ink used was optimized in order to avoid nucleation in solution. The chemical ink was tested on an unpatterned, flat soft-PDMS substrate combining UV-vis analysis on the growth solution during substrate exposure, and SEM measurements taken on the substrate after growth.

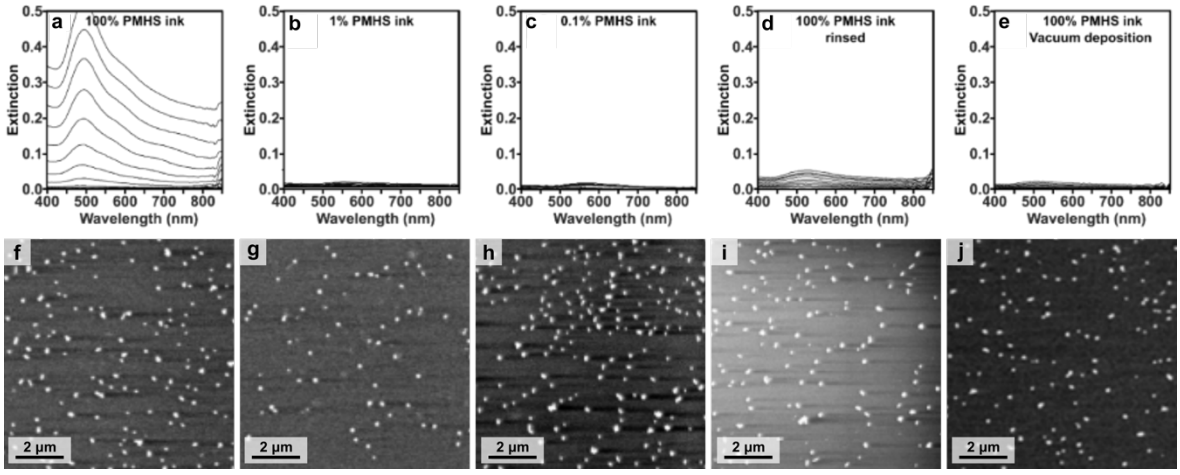

Figure 2.25 Spectra were obtained to study the nucleation in solution during growth conducted on an unpatterned stamp, with the following conditions: (**f**) 100% PMHS, (**b**) 1% PMHS in hexane, (b) 0.1% PMHS in hexane, (**d**) 100% PMHS spin coated after rinsing with water, (**e**) PMHS deposited in vacuum through CVD method. (**f**-**j**) SEM images corresponding to the (**a**-**e**) samples respectively.

When pure polymethylhydrosiloxane was spin-coated onto the PDMS substrate, rapid particle nucleation in the solution occurred, likely due to the leaching of excess ink into the solution (**Figure 2.25 f**). Thoroughly rinsing with water, the substrates after inking with pure polymethylhydrosiloxane also led to decreased nucleation, supporting this hypothesis (**Figure 2.25 d, e**). Furthermore, diluting the ink used for spin coating in hexane resulted in reduced nucleation (**Figure 2.25 b, c**). Apart from spin coating, the ink application was also carried out through simple vapor deposition under vacuum using a desiccator. This method likewise resulted in minimal nucleation away from the substrate surface (**Figure 2.25 e**).

Scanning electron microscopy was employed to monitor particle growth on the unpatterned supported PDMS surface. No discernible trend in density was observed when comparing 100% ink to the diluted inks and the substrate that was rinsed following ink application. This lack of trend suggests that, for each of these conditions, the substrate is saturated with ink, and increasing the concentration in the spin-coated solution only results in the addition of excess ink, which leaches into the solution (**Figure 2.25 f, i**). Additionally, **Figure 2.25 h-j** illustrates that the density of nucleation sites created by vapor deposition is similar to the density achieved with 0.1% ink solutions. Between these 2 methodologies we selected spin coating as our method of choice moving forward, as it allows for faster sample processing.

2.5.3 *In situ* growth

In our *in situ* growth approach, gold NPs arrays are formed in a single growth step, where the first nucleation occurs directly on the substrate., A strong reductant ink is only applied on the substrate to mimic the spatially selective nucleation and growth processes used in colloidal synthesis. Meanwhile, a mild reductant such as ascorbic acid is introduced into the growth medium to aid the initial reduction of the gold salt from Au(III) to Au(I).

Although only strong reductants are provided at the substrate surface in our *in situ* growth setup, colloidal nanoparticles can still spontaneously form from the precursors in the growth solution, a process commonly referred to as secondary or homogenous nucleation. Similarly, a secondary nucleation in an *in situ* systems refers to the uncontrolled formation of nuclei away from sites explicitly containing the strong reducing agent, leading to unpredictable reagent consumption and deposition of particles outside the intended pattern. While nucleation can be attained solely with the physiosorbed ink, the reason why we have incorporating ascorbic acid is to accelerate growth and reduce the concentrations of gold precursor needed.[161,162] Indeed, relying only on a surface-bound strong reductant typically necessitates approximately five times more gold salt and extended incubation periods spanning hours to days.[150,163]

The preparation of the growth solutions was consequently optimized to limit secondary nucleation as much as possible. Two standard surfactants were tested for AuNPs *in situ* growth, cetyltrimethylammonium chloride (CTAC) and bromide (CTAB), with concentrations ranging from 0.025 to 0.1 M in water. The occurring of secondary nucleation was passed through UV-vis spectroscopy, following the emergence of a LSPR peak. Monitoring the maximum intensity of these peaks over 15 minutes allowed for tracking the extent of undesired nuclei formation across various growth conditions.

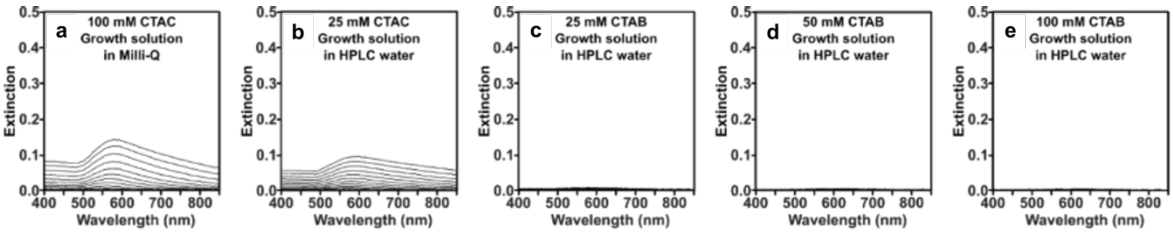

Figure 2.26 UV-Vis spectra of AuNPs growth solution over 15 min with 100 mM of CTAC in (**a**) Milli-Q water, and (**b**) HPLC water. (**c**-**e**) Kinetic dynamics of growth solutions with concentrations of (**c**) 25, (**d**) 50, (**e**) 100 mM of CTAB in HPLC water.

Firstly, it was observed that using HPLC-grade water for the preparation of the solutions significantly limited secondary nucleation compared to Milli-Q water (**Figure 2.26 a**, **b**). In addition, the use of CTAB allowed to slow down the secondary nucleation compared to CTAC (**Figure 2.26 c**-**e**). It can be observed that surfactant concentration increase also plays a role in slowing secondary nucleation, but since CTAB is less soluble in water at higher concentrations, 0.025 M was the concentration chosen for the standard synthesis of gold nanoparticles in this work, even if little secondary nucleation is still observed, as it appears after over 10 min since growth begun (**Figure 2.26 c**). In general, growth solutions comprising high-performance liquid chromatography (HPLC) grade water and 0.025-0.05 M CTAB exhibited the lowest levels of secondary nucleation. Having both the methodology for applying the chemical ink (**Paragraph 2.5.2)** and the growth solution optimized and standardized, we were able to move on and test the patterned in situ growth of gold NPs.

To initiate the patterned growth, an aliquote (150 µL) of growth solution is placed on top of the substrate (**Figure 2.27**). This is done instead of immersing the substrate directly in the solution, once again to avoid unwanted secondary nucleation, this time from the contaminated backside of the substrates. As can be clearly observed from the SEM analysis in **Figure 2.27**, we were able to control the spatial distribution of the nucleation site, inducing the direct growth of plasmonic arrays on PDMS.

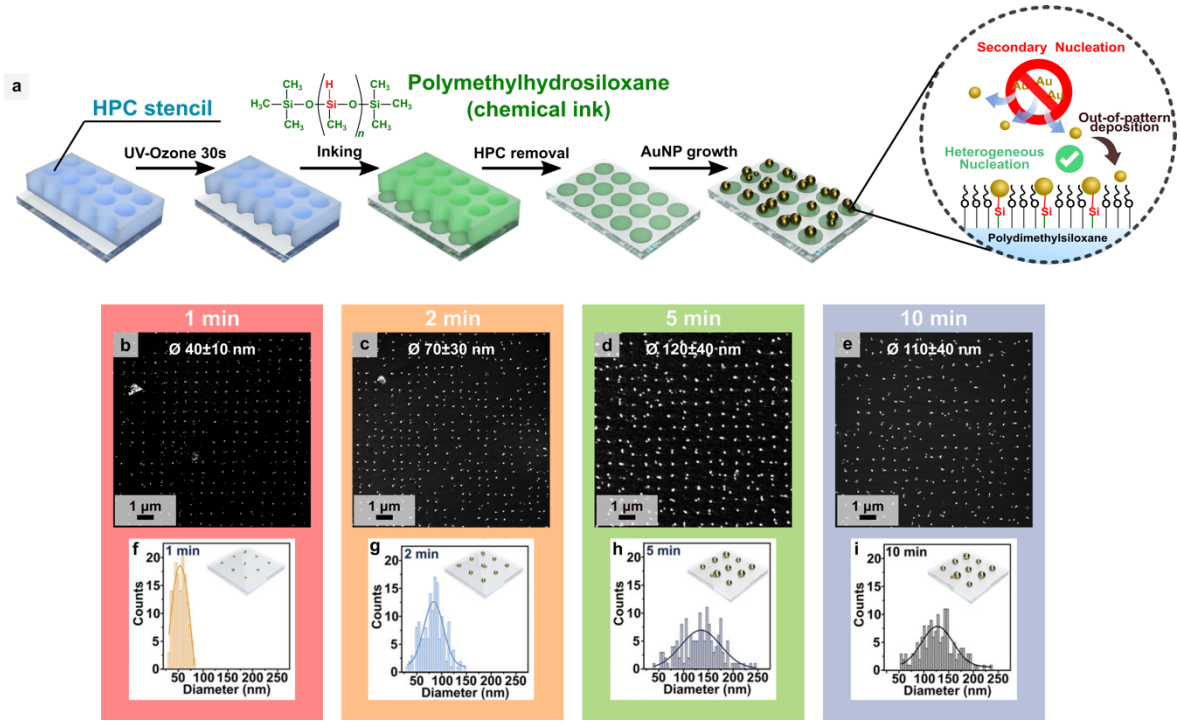

Figure 2.27 Schematic of the in situ growth procedure: after HPC etching of the residual layer with UV–Oz, the ink with poly(methylhydrosiloxane) is spin coated, and then HPC stencil is removed with water. Finally, the growth solution is dropped on top of the substrate to form gold nanoparticles (AuNPs). The **zoom in** show a schematic depicting competition between secondary solution nucleation and surface growth. (**b**) SEM images of patterned NPs substrates grown after (**a**) 1, (**b**) 2, (**c**) 5, and (**d**) 10 min with a growth solution containing CTAB (capping ligand/surfactant), gold salt, and ascorbic acid as a mild reducing agent. (**f-i**) Evaluation of NPs size distribution for the (**f**) 1, (**g**) 2, (**h**) 5, (**i**) 10 min time growth (150 nanoparticles each).

Throughout the growth period (1-10 min), the color the growth solution remained unchanged, confirming the absence of any secondary nucleation process. Moreover, by regulating the incubation time between 1-10 min, we managed to control nuclei grow and size of the obtained particles between). Following 1 minute of growth, the average particle size reaches 40 ± 10 nm (**Figure 2.27 b, f**), which is relatively rapid compared to colloidal synthesis.[29,147,164] By 2 minutes,

the particle sizes nearly double to 70 ± 30 nm (**Figure 2.27 c**, **g**). Growth periods of 5 and 10 minutes yield nanoparticles with similar diameters (120 ± 40 and 110 ± 40 nm, respectively, **Figure 2.27 d**-**e**, **h**-**i**). This trend confirms observations from other *in situ* growth studies.[165–168] For what concern the patterning evaluation, many kinds of defects can be observed in the arrays. Standard defects include vacancies, multiple particles per region, and particles outside the patterned region (**Figure 2.28**). Besides nanospheres, during a colloidal synthesis different anisotropic (rods and platelets-like structures) and isotropic (multi-twinned polyhedra, cubes, pyramids) products can be obtained if no shape-control strategies are applied during the growth.[169,170] A similar behavior is observed for *in situ* growth, where by decreasing the growth time from 10 to 1 min, the percentage of isotropic products increased to ~90% (**Table 2.1**).

Table 2.1 Percentage of products observed at different growth times.

Growth time (min)	1	2	5	10
# total NPs counted	255	328	329	201
% platelet	3.9	2.7	2.7	24.4
% sphere	88.2	82.0	82.4	57.2
% rod	6.3	11.3	12.5	15.9
% unclear	1.6	4.0	2.4	2.5
% total anisotropic	10.2	14.0	15.2	40.3
% total platelets and spheres	92.2	84.8	85.1	81.6

Moreover, it was evaluated the patterning yield (**Table 2.2**), observing that with time increase from 5 to 10 min, the number of NPs outside the pattern areas slightly increase from 10% to 14%, probably due to the onset of secondary nucleation effects.

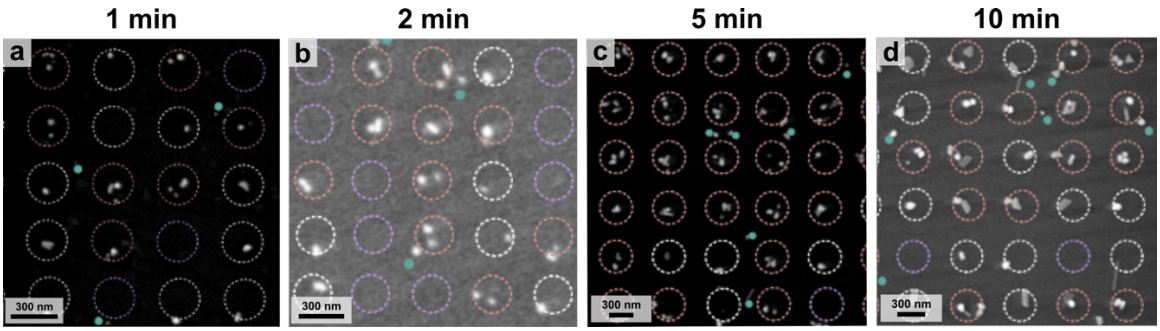

Figure 2.28 SEM images from which patterning yield was calculated (**Table 2.2**). For each time condition, enough images were analyzed and an average of 150 Au nanoparticles were counted. **Pink** circles represent regions with multiple nanoparticles, **white** circles represent areas with single particles, **purple** circles indicate vacancies defects, and **green** dots are used to indicate out-of-pattern gold nanoparticles**.**

Table 2.2 Patterning yield characterization across growth times.

Growth time (min)	1	2	5	10	TOTAL
total # of particles counted (including outside pattern)	247	212	279	203	**941**
% pattern yield (% non-empty)	89.6	61.7	97.4	83.8	**83 ± 15**
% single	19.4	35.4	10.3	23.0	**22 ± 10**
% multiple	76.1	54.4	78.9	63.2	**68 ± 12**
% nanoparticles in pattern	95.5	87.7	89.2	86.2	**90 ± 4**

The identification of a main reason for these defects is still challenging but crucial for the future development of this *in situ* growth. For example, the NPs outside the patterned areas, (about 10% of the total) can be the result of secondary homogeneous nucleation events in the growth solution and their consequent deposition on the surface, the spontaneous nucleation on regions with no ink, and/or defects formed in the HPC mask. Moreover, since the quality of the pattern was evaluated through SEM analysis, the appearance of vacancies in the pattern (which number results constant during the growth period of 1-10 min) could be attributed on one side to limits in the instrument resolution, which affects imaging of NPs smaller then 5 nm, and to the other side to the effect of ink removal caused during the HPC stencil washing steps. In the future, it will be interesting to investigate different chemical inks to increase the chemical contrast between the patterned regions and the substrate to mitigate defects.

Another important consideration is the size mismatch between the growing particles and the patterned features, the latter being significantly larger (>270 nm). This may explain the occurrence of nanoparticles not centered within the designated patterned area and the development of multiple particles in certain regions. Nonetheless, a significant result is that an average of 2 particles per patterned area was observed, suggesting the growth process is favored over the subsequent creation of new nuclei, due to charge transfer affecting the transport of gold salt to the substrate.[14,171]

From simple geometrical and back-of-a-napkin calculation, and assuming 100% yield of the imprinting and ink patterning, we could estimate that the number of particles nucleating on each substrate to be ~ 2×10^8 particles/substrate, or about 2×10^9 particles mL^{-1} of growth solution (assuming 150 μL volume). This number is significantly smaller compared to the concentrations in batch synthesis, which are usually 2-4 orders of magnitude higher (10^{11}- 10^{13} seeds/mL of growth solution). Being able to reduce the concentration of the precursors in growth solution has the potential to not only minimize secondary nucleation, but also enabling a more controlled and uniform *in situ* growth of particles.

In order to demonstrate the versatility of our methodology, a further step was carried out to overgrowth the particles and create stars shaped NPs. As already presented in a previous work,[172] the incubation overgrowth step was carried out by depositing a solution containing gold precursor and shape-directing reagents (silver nitrate, laurylsulfobetaine (LSB), hydrochloric acid (HCl), and ascorbic acid (AA)) (**Figure 2.29**). Similarly to the first growth process, the synthesis conditions were optimized to minimize secondary nucleation away from the substrate during the 5 min overgrowth period. This was achieved by reducing the pH of the growth medium, thereby restricting the reducing strength of ascorbic acid. After the overgrowth process, the substrate underwent a transition in color, shifting from red to dark blue. After 5 min of overgrowth, LSPR band resulted peaked in the NIR at 985 nm.

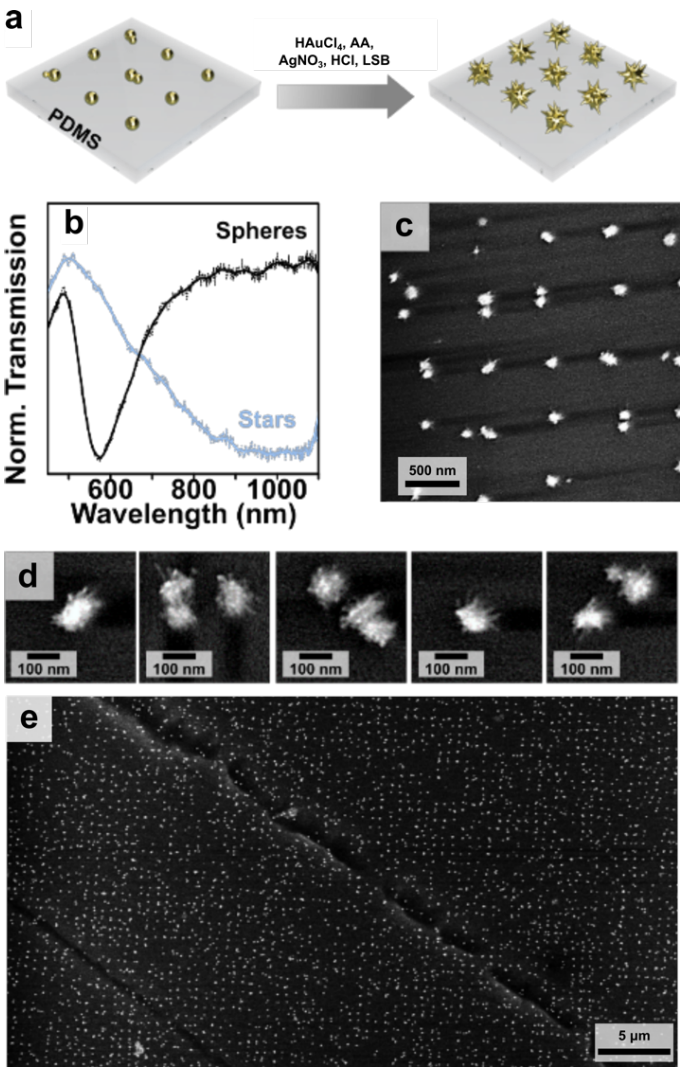

Figure 2.29 (**a**) Schematic of the overgrowth process into nanostars. (**b**)Normalized transmission spectra comparing the position of the plasmon band before (spheres, **black** curve) and after (stars, **light blue** curve) overgrowth. (**c**-**e**) SEM images of the nanostar arrays at different magnifications.

The colloid recipe used here yields three main products: spheres, low aspect ratio nanostars, and high aspect ratio nanostars.[173] However, electron microscopy characterization revealed a predominant and highly branched product (**Figure 2.29 c**, **d**). The nanostar arrays extended over a larger area (approximately 2000 μm^2) is depicted in **Figure 2.29 e**. Overall, the data presented in **Figure 2.29** suggest that while certain concepts may transfer from colloidal to substrate growth (such as applying shape-directing reagents to promote anisotropic growth), significant differences persist between the two environments, which can greatly influence the final product shapes. The *in situ* surface growth approach reported here provides an ideal platform for investigating such effects.[172]

These branched nanostars structures are appealing because of the concentrated electromagnetic fields at their sharp tips, their significant extinction in the NIR biological window, and their efficiency for thermoplasmonic applications.[172,174,175]

2.5.4 *In situ* growth on spin-coated thin PDMS films

Moving another step forward, we optimized a spin coating protocol to minimize the thickness of the supported PDMS layer, improve reproducibility, and dramatically reduce the fabrication time. Specifically, the PDMS was utilized in a 10:1 weight ratio of monomer and crosslinker (the same ratio used in all other prepareations), but to facilitate the formation of a more uniform film, the viscosity of the solution was reduced by dilution with toluene, chosen for its compatibility with PDMS and slower evaporation rate compared to other organic solvents such as hexane. Excessive dilutions led to dewetting on the glass slide, whereas concentrations surpassing 70% yielded films that were excessively thick and viscous, hindering the creation of a uniform and flat PDMS film. Quantitative evaluation of the PDMS thickness were obtained by reflectance measurements. As expected, our experimental analysis unveiled that films were thinner and more uniform at lower concentrations and higher rpm. These results supported the theoretical expectation that thickness is nearly proportional to the inverse square root of the spin speed (**Figure 2.30**).[176]

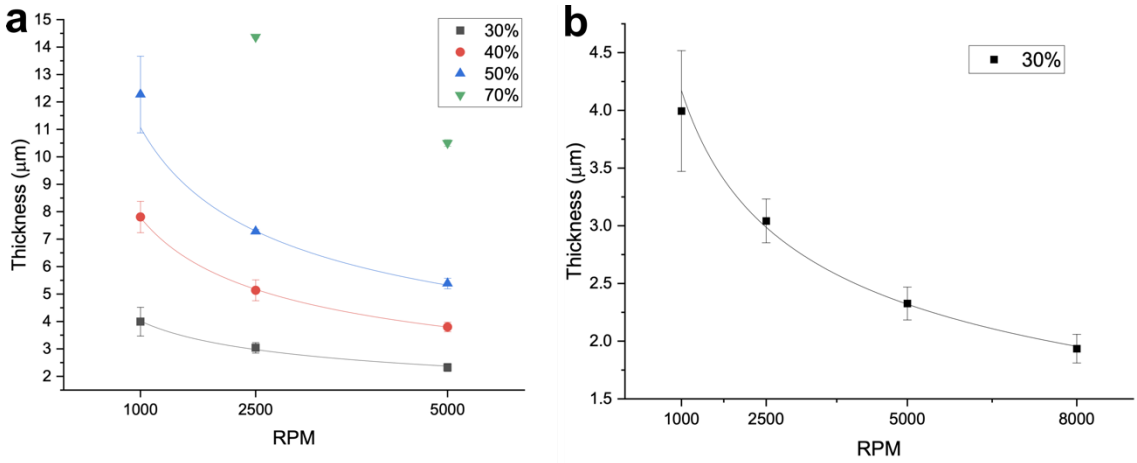

Figure 2.30 The heights of the substrates at various rpm and dilutions were fitted with a power law function ($y = ax^b$). For the 40% and 50% dilutions, the value of b is -0.45, while for the 30% dilution, it is -0.34. Additionally, the height of the 30% dilution extended to include 8000 rpm, yielded a b value of -0.37.

A PDMS concentration of 30% was selected, granting films below 3 µm thick and good reproducibility. In addition, this dilution offered the advantage of a longer shelf life of the PDMS precursor solution, allowing a larger quantity of substrates to be produced in a single batch. The highest spin coating speed assessed was 8000 rpm. However, increasing the spin speed did not result in a significant reduction in film thickness, and operating at this speed posed practical challenges, as the samples tended to detach from the spin-coater holder. Ultimately, we selected 5000 rpm for the rest of the experiments.

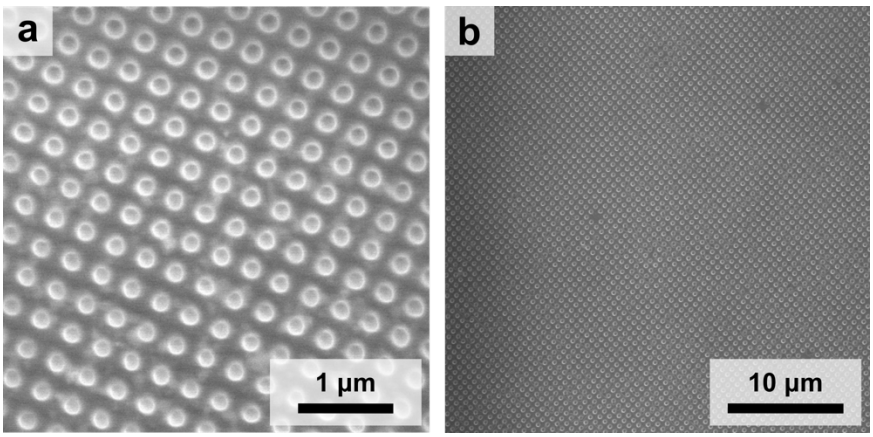

Figure 2.31 (**a**) High-mag and (**b**) low-mag SEM images of the HPC stencils with PDMS dilution at 70% with different lattice parameters 400 nm of lattice parameter.

After selecting the best spin coating conditions, SEM analysis was performed to verify the uniformity of the imprinting process and the quality of the HPC stencils. Testing with various

lattices demonstrated successful imprinting and high-quality reproduction of the patterned geometry.

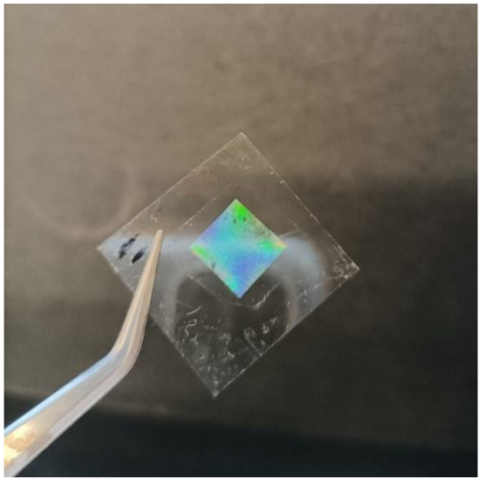

Figure 2.32 Sample appearance after t-NIL process. Diffraction grating created on the HPC film glass supported diluted PDMS.

Without doubt, the diluted glass supported PDMS method represented a significant step forward in optimizing the *in situ* protocol, and in reducing the processing time of the whole procedure, which could now be completed in under 1 hour (from clean substrate to plasmonic array). However, we still had to verify that patterned growth can be achieved also for this type of substrates.

In order to conduct an appropriate analysis and vary the original protocol (**Paragraph 2.5.3**) by changing one parameter at a time, the samples on these substrates obtained with the new protocol were grown while keeping the reagent concentration, growth time, and Lattice parameter fixed. Unfortunately, among all the characterized samples, only a few exhibited a discernible pattern on the surface, and in most the samples there were traces of secondary nucleation (**Figure 2.33**).

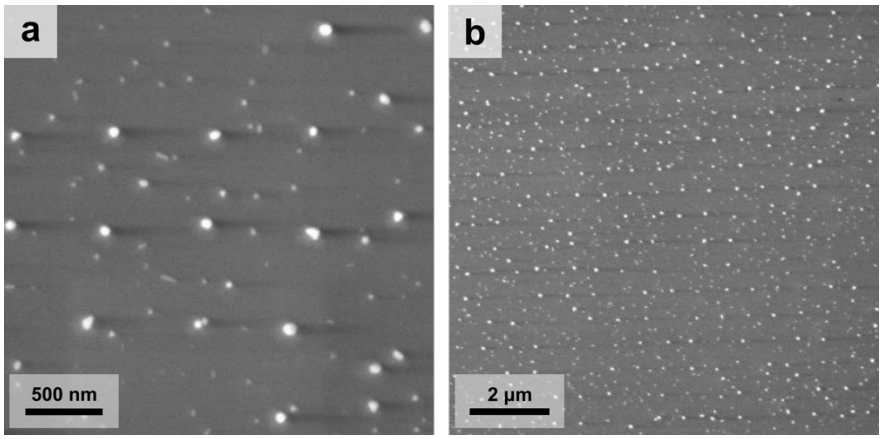

Figure 2.33 SEM images of AuNPs grown on a 30% diluted PDMS substrate (spin coat at 5000 rpm), pattern with periodicity of 600 nm.

Despite the presence of numerous anisotropic nanoparticles such as nanorods or platelets on the surface, the nanoparticles grown on the pattern tended to form primarily isotropic shapes, mainly spheres. Causes for the elevated number of defects (vacancies, multiple particles per region, and non-spherical NPs) can be attributable to various factors, such as residues of unrinsed HPC and PDMS oligomers, leaching of excess reagents, and/or impurities in the growth solution/substrate.

To tackle this challenge, we further adjusted the growth solution by incorporating hydrochloric acid (HCl) to slow secondary nanoparticle even further.[10] Specifically, 10 µL of HCl (0.1 M) were added before the ascorbic acid. This modification of the growth conditions enabled us to confine the nucleation of the NPs exclusively in the highly reductant PMHS regions.

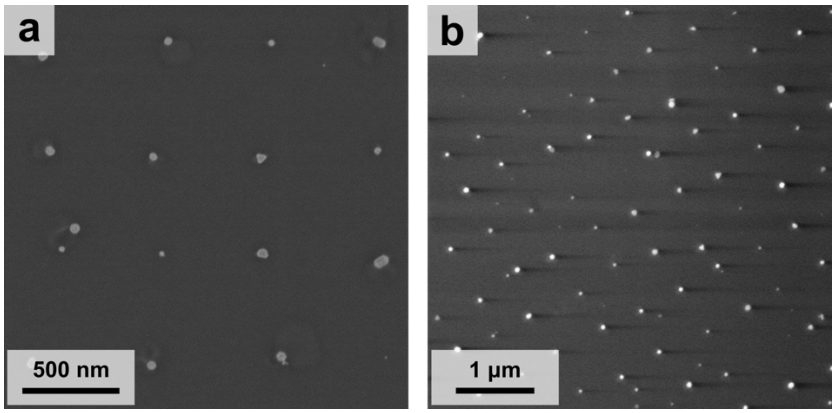

Figure 2.34 SEM images of sample array with lattice period Λ = 600 nm, 5 min growth on a 30% dilution PDMS substrate spin coated at 2500 rpm of.

The efficacy of this approach is clear in **Figure 2.34**, where the occurrence of secondary nucleation is significantly reduced.

Moreover, considering the NPs size distribution counting an average of 120 particles per sample, the introduction of the HCl led to a noticeable reduction in the diameter of the nanoparticles compared to the original method.

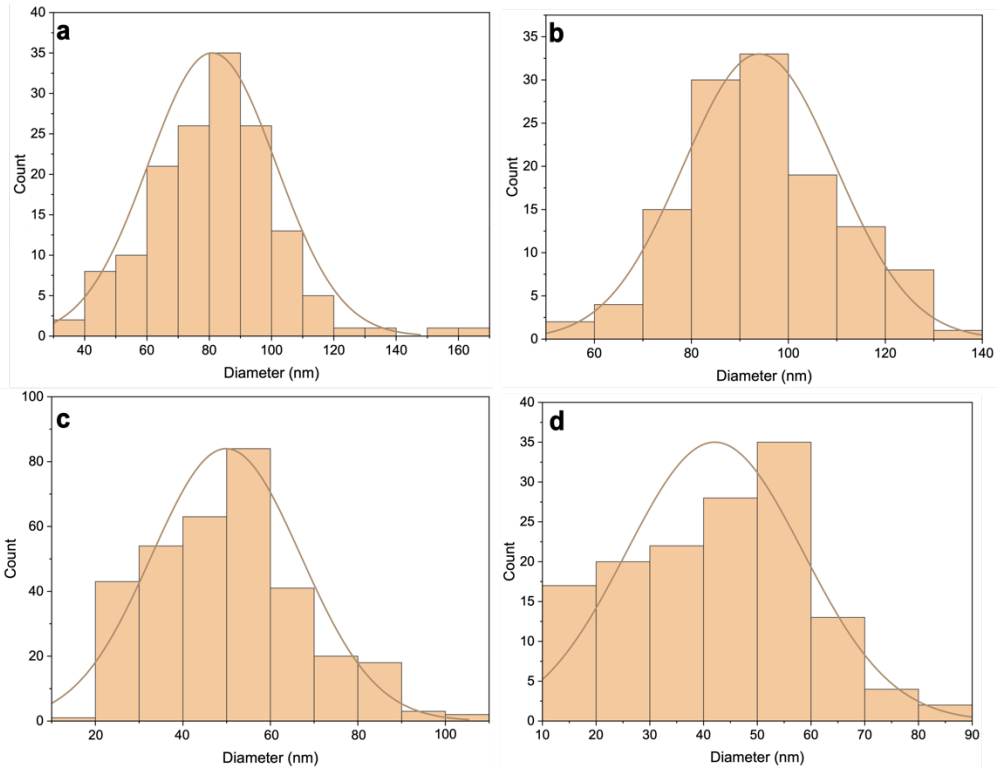

Figure 2.35 Nanoparticles size distribution of array of growth NPs through (**a**) original method, (**b**) 30% diluted PDMS spin coated at 5000 rpm, (**c**) 30% dilution PDMS at 5000 rpm with 10µL of HCl in the growth solution

(sample in **Figure 2.33 a**), (**d**) 30% dilution PDMS at 5000 rpm with 10μL of HCl in the growth solution (sample in **Figure 2.33 b**)

For both the original substrate method and the conditions of 30% diluted PDMS at 5000 rpm without HCl, the diameters obtained were very similar (80 ± 20 nm and 90 ± 20 nm, respectively). These results suggest that although the use of spin-coated PDMS introduces additional challenges when it comes to keep the substrates clean and avoid secondary nucleation, it remains compatible with our *in situ* growth. Moreover, the introduction of HCl cut the size of the grown particles in half, indicating the potential for longer growth times.

The mean NPs diameter values are reported in the following **Table 2.3**.

Table 2.3 Evaluation of the NPs size in the sample presented by the histograms.

Protocol	Mean diameter (nm)
Original	80±20
30% diluted PDMS at 5000 rpm	90±20
30% diluted PDMS at 5000 rpm-Figure 2.33 a	40±20
30% diluted PDMS at 5000 rpm-Figure 2.33 b	50±20

Although these results represent an improvement over the original method, several challenges remain. Some degree of secondary nucleation persists and there remains limited control over nanoparticle growth. In addition, differences in diameter between the PMHS inked regions and the effective nanoparticles resulted in displacement of some nanoparticles from the center, or multiple nanoparticles occupying a single PMHS well. These challenges highlight the need for comprehensive studies of the *in situ* growth process of gold nanoparticles, with the ultimate aim of developing an alternative fabrication tool to control nanoscale properties directly on the substrate.

2.4 References

(1) Yin, Y.; Alivisatos, A. P. Colloidal Nanocrystal Synthesis and the Organic–Inorganic Interface. *Nature* **2005**, *437* (7059), 664–670. https://doi.org/10.1038/nature04165.

(2) Liz-Marzán, L. *Colloidal Synthesis of Plasmonic Nanometals*; CRC Press, 2020.

(3) Scarabelli, L.; Sun, M.; Zhuo, X.; Yoo, S.; Millstone, J. E.; Jones, M. R.; Liz-Marzán, L. M. Plate-Like Colloidal Metal Nanoparticles. *Chem. Rev.* **2023**, *123* (7), 3493–3542. https://doi.org/10.1021/acs.chemrev.3c00033.

(4) Karst, J.; Hentschel, M.; Cho, N. H.; Kim, H.; Nam, K. T.; Giessen, H. *Plasmonic Materials and Metastructures*; Materials Today; Elsevier, 2024; pp 285–317. https://doi.org/10.1016/B978-0-323-85379-8.00010-1.

(5) Chou, S. Y.; Krauss, P. R.; Renstrom, P. J. Imprint Lithography with 25-Nanometer Resolution. *Science* **1996**, *272* (5258), 85–87. https://doi.org/10.1126/science.272.5258.85.

(6) Guo, L. J. Nanoimprint Lithography: Methods and Material Requirements. *Adv. Mater.* **2007**, *19* (4), 495–513. https://doi.org/10.1002/adma.200600882.

(7) Lan, H.; Ding, Y.; Lan, H.; Ding, Y. Nanoimprint Lithography. In *Lithography*; IntechOpen, 2010. https://doi.org/10.5772/8189.

(8) Xia, Y.; Whitesides, G. M. Soft Lithography. *Angew. Chem. Int. Ed Engl.* **1998**, *37* (5), 550–575. https://doi.org/10.1002/(SICI)1521-3773(19980316)37:5<550::AID-ANIE550>3.0.CO;2-G.

(9) Whitesides, G. M.; Grzybowski, B. Self-Assembly at All Scales. *Science* **2002**, *295* (5564), 2418–2421. https://doi.org/10.1126/science.1070821.

(10) Sun, Y.; Xia, Y. Shape-Controlled Synthesis of Gold and Silver Nanoparticles. *Science* **2002**, *298* (5601), 2176–2179. https://doi.org/10.1126/science.1077229.

(11) Nguyen, Q. N.; Wang, C.; Shang, Y.; Janssen, A.; Xia, Y. Colloidal Synthesis of Metal Nanocrystals: From Asymmetrical Growth to Symmetry Breaking. *Chem. Rev.* **2023**, *123* (7), 3693–3760. https://doi.org/10.1021/acs.chemrev.2c00468.

(12) Nikhil R. Jana, *; Latha Gearheart, and; Murphy*, C. J. *Wet Chemical Synthesis of High Aspect Ratio Cylindrical Gold Nanorods*. ACS Publications. https://doi.org/10.1021/jp0107964.

(13) Jin, R.; Cao, Y.; Mirkin, C. A.; Kelly, K. L.; Schatz, G. C.; Zheng, J. G. Photoinduced Conversion of Silver Nanospheres to Nanoprisms. *Science* **2001**, *294* (5548), 1901–1903. https://doi.org/10.1126/science.1066541.

(14) Scarabelli, L.; Sánchez-Iglesias, A.; Pérez-Juste, J.; Liz-Marzán, L. M. A “Tips and

Tricks" Practical Guide to the Synthesis of Gold Nanorods. *J. Phys. Chem. Lett.* **2015**, *6* (21), 4270–4279. https://doi.org/10.1021/acs.jpclett.5b02123.

(15) Haji-Akbari, A.; Engel, M.; Keys, A. S.; Zheng, X.; Petschek, R. G.; Palffy-Muhoray, P.; Glotzer, S. C. Disordered, Quasicrystalline and Crystalline Phases of Densely Packed Tetrahedra. *Nature* **2009**, *462* (7274), 773–777. https://doi.org/10.1038/nature08641.

(16) Glotzer, S. C.; Solomon, M. J. Anisotropy of Building Blocks and Their Assembly into Complex Structures. *Nat. Mater.* **2007**, *6* (8), 557–562. https://doi.org/10.1038/nmat1949.

(17) Hanske, C.; Hill, E. H.; Vila-Liarte, D.; González-Rubio, G.; Matricardi, C.; Mihi, A.; Liz-Marzán, L. M. Solvent-Assisted Self-Assembly of Gold Nanorods into Hierarchically Organized Plasmonic Mesostructures. *ACS Appl. Mater. Interfaces* **2019**, *11* (12), 11763–11771. https://doi.org/10.1021/acsami.9b00334.

(18) Scarabelli, L. Recent Advances in the Rational Synthesis and Self-Assembly of Anisotropic Plasmonic Nanoparticles. *Pure Appl. Chem.* **2018**, *90* (9), 1393–1407. https://doi.org/10.1515/pac-2018-0510.

(19) Murphy, C. J.; Sau, T. K.; Gole, A. M.; Orendorff, C. J.; Gao, J.; Gou, L.; Hunyadi, S. E.; Li, T. Anisotropic Metal Nanoparticles: Synthesis, Assembly, and Optical Applications. *J. Phys. Chem. B* **2005**, *109* (29), 13857–13870. https://doi.org/10.1021/jp0516846.

(20) Rodriguez, S. R. K.; Schaafsma, M. C.; Berrier, A.; Gómez Rivas, J. Collective Resonances in Plasmonic Crystals: Size Matters. *Phys. B Condens. Matter* **2012**, *407* (20), 4081–4085. https://doi.org/10.1016/j.physb.2012.03.053.

(21) Mayer, M.; Schnepf, M. J.; König, T. A. F.; Fery, A. Colloidal Self-Assembly Concepts for Plasmonic Metasurfaces. *Adv. Opt. Mater.* **2019**, *7* (1), 1800564. https://doi.org/10.1002/adom.201800564.

(22) Zhang, H.; Bu, X.; Yip, S.; Liang, X.; Ho, J. C. Self-Assembly of Colloidal Particles for Fabrication of Structural Color Materials toward Advanced Intelligent Systems. *Adv. Intell. Syst.* **2020**, *2* (1), 1900085. https://doi.org/10.1002/aisy.201900085.

(23) Conti, Y.; Passarelli, N.; Mendoza-Carreño, J.; Scarabelli, L.; Mihi, A. Colloidal Silver Nanoparticle Plasmonic Arrays for Versatile Lasing Architectures via Template-Assisted Self-Assembly. *Adv. Opt. Mater.* **2023**, *n/a* (n/a), 2300983. https://doi.org/10.1002/adom.202300983.

(24) Herran, M.; Sousa-Castillo, A.; Fan, C.; Lee, S.; Xie, W.; Döblinger, M.; Auguié, B.; Cortés, E. Tailoring Plasmonic Bimetallic Nanocatalysts Toward Sunlight-Driven H2

Production. *Adv. Funct. Mater.* **2022**, 2203418. https://doi.org/10.1002/adfm.202203418.

(25) Cortés, E.; Wendisch, F. J.; Sortino, L.; Mancini, A.; Ezendam, S.; Saris, S.; de S. Menezes, L.; Tittl, A.; Ren, H.; Maier, S. A. Optical Metasurfaces for Energy Conversion. *Chem. Rev.* **2022**. https://doi.org/10.1021/acs.chemrev.2c00078.

(26) Matricardi, C.; Hanske, C.; Garcia-Pomar, J. L.; Langer, J.; Mihi, A.; Liz-Marzán, L. M. Gold Nanoparticle Plasmonic Superlattices as Surface-Enhanced Raman Spectroscopy Substrates. *ACS Nano* **2018**, *12* (8), 8531–8539. https://doi.org/10.1021/acsnano.8b04073.

(27) Plou, J.; Charconnet, M.; García, I.; Calvo, J.; Liz-Marzán, L. M. Preventing Memory Effects in Surface-Enhanced Raman Scattering Substrates by Polymer Coating and Laser-Activated Deprotection. *ACS Nano* **2021**, *15* (5), 8984–8995. https://doi.org/10.1021/acsnano.1c01878.

(28) Plou, J.; García, I.; Charconnet, M.; Astobiza, I.; García-Astrain, C.; Matricardi, C.; Mihi, A.; Carracedo, A.; Liz-Marzán, L. M. Multiplex SERS Detection of Metabolic Alterations in Tumor Extracellular Media. *Adv. Funct. Mater.* **2020**, *30* (17), 1910335. https://doi.org/10.1002/adfm.201910335.

(29) Hanske, C.; González-Rubio, G.; Hamon, C.; Formentín, P.; Modin, E.; Chuvilin, A.; Guerrero-Martínez, A.; Marsal, L. F.; Liz-Marzán, L. M. Large-Scale Plasmonic Pyramidal Supercrystals via Templated Self-Assembly of Monodisperse Gold Nanospheres. *J. Phys. Chem. C* **2017**, *121* (20), 10899–10906. https://doi.org/10.1021/acs.jpcc.6b12161.

(30) Flauraud, V.; Mastrangeli, M.; Bernasconi, G. D.; Butet, J.; Alexander, D. T. L.; Shahrabi, E.; Martin, O. J. F.; Brugger, J. Nanoscale Topographical Control of Capillary Assembly of Nanoparticles. *Nat. Nanotechnol.* **2017**, *12* (1), 73–80. https://doi.org/10.1038/nnano.2016.179.

(31) Hanske, C.; Tebbe, M.; Kuttner, C.; Bieber, V.; Tsukruk, V. V.; Chanana, M.; König, T. A. F.; Fery, A. Strongly Coupled Plasmonic Modes on Macroscopic Areas via Template-Assisted Colloidal Self-Assembly. *Nano Lett.* **2014**, *14* (12), 6863–6871. https://doi.org/10.1021/nl502776s.

(32) Ángel Fernández-Rodríguez, M.; Elnathan, R.; Ditcovski, R.; Grillo, F.; Marc Conley, G.; Timpu, F.; Rauh, A.; Geisel, K.; Ellenbogen, T.; Grange, R.; Scheffold, F.; Karg, M.; Richtering, W.; H. Voelcker, N.; Isa, L. Tunable 2D Binary Colloidal Alloys for Soft Nanotemplating. *Nanoscale* **2018**, *10* (47), 22189–22195. https://doi.org/10.1039/C8NR07059H.

(33) Goerlitzer, E. S. A.; Mohammadi, R.; Nechayev, S.; Volk, K.; Rey, M.; Banzer, P.; Karg, M.; Vogel, N. Chiral Surface Lattice Resonances. *Adv. Mater.* **2020**, *32* (22), 2001330.

https://doi.org/10.1002/adma.202001330.

(34) Mark, A. G.; Gibbs, J. G.; Lee, T.-C.; Fischer, P. Hybrid Nanocolloids with Programmed Three-Dimensional Shape and Material Composition. *Nat. Mater.* **2013**, *12* (9), 802–807. https://doi.org/10.1038/nmat3685.

(35) Krishnamoorthy, S.; Hinderling, C.; Heinzelmann, H. Nanoscale Patterning with Block Copolymers. *Mater. Today* **2006**, *9* (9), 40–47. https://doi.org/10.1016/S1369-7021(06)71621-2.

(36) Vinnacombe-Willson, G. A.; Conti, Y.; Jonas, S. J.; Weiss, P. S.; Mihi, A.; Scarabelli, L. Surface Lattice Plasmon Resonances by Direct In Situ Substrate Growth of Gold Nanoparticles in Ordered Arrays. *Adv. Mater.* **2022**, *n/a* (n/a), 2205330. https://doi.org/10.1002/adma.202205330.

(37) Xia, D.; Brueck, S. R. J. A Facile Approach to Directed Assembly of Patterns of Nanoparticles Using Interference Lithography and Spin Coating. *Nano Lett.* **2004**, *4* (7), 1295–1299. https://doi.org/10.1021/nl049355x.

(38) He, L.; Wang, M.; Zhang, Q.; Lu, Y.; Yin, Y. Magnetic Assembly and Patterning of General Nanoscale Materials through Nonmagnetic Templates. *Nano Lett.* **2013**, *13* (1), 264–271. https://doi.org/10.1021/nl3040256.

(39) Park, J. E.; Park, S. J.; Urbas, A.; Ku, Z.; Wie, J. J. Programmable Stepwise Collective Magnetic Self-Assembly of Micropillar Arrays. *ACS Nano* **2022**, *16* (2), 3152–3162. https://doi.org/10.1021/acsnano.1c10844.

(40) Lin, Q.-Y.; Mason, J. A.; Li, Z.; Zhou, W.; O'Brien, M. N.; Brown, K. A.; Jones, M. R.; Butun, S.; Lee, B.; Dravid, V. P.; Aydin, K.; Mirkin, C. A. Building Superlattices from Individual Nanoparticles via Template-Confined DNA-Mediated Assembly. *Science* **2018**, *359* (6376), 669–672. https://doi.org/10.1126/science.aaq0591.

(41) Kooy, N.; Mohamed, K.; Pin, L. T.; Guan, O. S. A Review of Roll-to-Roll Nanoimprint Lithography. *Nanoscale Res. Lett.* **2014**, *9* (1), 320. https://doi.org/10.1186/1556-276X-9-320.

(42) Perret, C.; Gourgon, C.; Lazzarino, F.; Tallal, J.; Landis, S.; Pelzer, R. Characterization of 8-in. Wafers Printed by Nanoimprint Lithography. *Microelectron. Eng.* **2004**, *73–74*, 172–177. https://doi.org/10.1016/j.mee.2004.02.036.

(43) Kim, J.-G.; Sim, Y.; Cho, Y.; Seo, J.-W.; Kwon, S.; Park, J.-W.; Choi, H. G.; Kim, H.; Lee, S. Large Area Pattern Replication by Nanoimprint Lithography for LCD–TFT Application. *Microelectron. Eng.* **2009**, *86* (12), 2427–2431. https://doi.org/10.1016/j.mee.2009.05.006.

(44) Lan, S.; Song, J.-H.; Lee, M. G.; Ni, J.; Lee, N. K.; Lee, H.-J. Continuous Roll-to-Flat Thermal Imprinting Process for Large-Area Micro-Pattern Replication on Polymer Substrate. *Microelectron. Eng.* **2010**, *87* (12), 2596–2601. https://doi.org/10.1016/j.mee.2010.07.021.

(45) Lim, H.; Choi, K.-B.; Kim, G.; Park, S.; Ryu, J.; Lee, J. Roller Nanoimprint Lithography for Flexible Electronic Devices of a Sub-Micron Scale. *Microelectron. Eng.* **2011**, *88* (8), 2017–2020. https://doi.org/10.1016/j.mee.2011.02.018.

(46) Tan, H.; Gilbertson, A.; Chou, S. Y. Roller Nanoimprint Lithography. *J. Vac. Sci. Technol. B Microelectron. Nanometer Struct. Process. Meas. Phenom.* **1998**, *16* (6), 3926–3928. https://doi.org/10.1116/1.590438.

(47) Jiang, W.; Liu, H.; Ding, Y.; Shi, Y.; Yin, L.; Lu, B. Investigation of Pattern Coating on Mould Roller in Roller-Reversal Imprint Process. *Microelectron. Eng.* **2009**, *86* (12), 2412–2416. https://doi.org/10.1016/j.mee.2009.05.003.

(48) Ahn, S. H.; Guo, L. J. High-Speed Roll-to-Roll Nanoimprint Lithography on Flexible Plastic Substrates. *Adv. Mater.* **2008**, *20* (11), 2044–2049. https://doi.org/10.1002/adma.200702650.

(49) Ahn, S. H.; Guo, L. J. Large-Area Roll-to-Roll and Roll-to-Plate Nanoimprint Lithography: A Step toward High-Throughput Application of Continuous Nanoimprinting. *ACS Nano* **2009**, *3* (8), 2304–2310. https://doi.org/10.1021/nn9003633.

(50) Guo, L. J.; Ahn, S. H. Roll to Roll Nanoimprint Lithography. US8027086B2, September 27, 2011. https://patents.google.com/patent/US8027086B2/en (accessed 2024-01-18).

(51) Mäkelä, T.; Haatainen, T.; Majander, P.; Ahopelto, J. Continuous Roll to Roll Nanoimprinting of Inherently Conducting Polyaniline. *Microelectron. Eng.* **2007**, *84* (5), 877–879. https://doi.org/10.1016/j.mee.2007.01.131.

(52) Ahn, S.; Cha, J.; Myung, H.; Kim, S.; Kang, S. Continuous Ultraviolet Roll Nanoimprinting Process for Replicating Large-Scale Nano- and Micropatterns. *Appl. Phys. Lett.* **2006**, *89* (21), 213101. https://doi.org/10.1063/1.2392960.

(53) Jeong, J.-H.; Choi, Y.-S.; Shin, Y.-J.; Lee, J.-J.; Park, K.-T.; Lee, E.-S.; Lee, S.-R. Flow Behavior at the Embossing Stage of Nanoimprint Lithography. *Fibers Polym.* **2002**, *3* (3), 113–119. https://doi.org/10.1007/BF02892627.

(54) Sohn, K.-J.; Park, J. H.; Lee, D.-E.; Jang, H.-I.; Lee, W. I. Effects of the Process Temperature and Rolling Speed on the Thermal Roll-to-Roll Imprint Lithography of Flexible Polycarbonate Film. *J. Micromechanics Microengineering* **2013**, *23* (3), 035024.

https://doi.org/10.1088/0960-1317/23/3/035024.

(55) Schift, H. Nanoimprint Lithography: An Old Story in Modern Times? A Review. *J. Vac. Sci. Technol. B Microelectron. Nanometer Struct. Process. Meas. Phenom.* **2008**, *26* (2), 458–480. https://doi.org/10.1116/1.2890972.

(56) Vogler, M.; Wiedenberg, S.; Mühlberger, M.; Bergmair, I.; Glinsner, T.; Schmidt, H.; Kley, E.-B.; Grützner, G. Development of a Novel, Low-Viscosity UV-Curable Polymer System for UV-Nanoimprint Lithography. *Microelectron. Eng.* **2007**, *5–8* (84), 984–988. https://doi.org/10.1016/j.mee.2007.01.184.

(57) Pfeiffer, K.; Fink, M.; Ahrens, G.; Gruetzner, G.; Reuther, F.; Seekamp, J.; Zankovych, S.; Sotomayor Torres, C. M.; Maximov, I.; Beck, M.; Graczyk, M.; Montelius, L.; Schulz, H.; Scheer, H.-C.; Steingrueber, F. Polymer Stamps for Nanoimprinting. *Microelectron. Eng.* **2002**, *61–62*, 393–398. https://doi.org/10.1016/S0167-9317(02)00577-4.

(58) Schift, H.; Kristensen, A. Nanoimprint Lithography. In *Springer Handbook of Nanotechnology*; Bhushan, B., Ed.; Springer: Berlin, Heidelberg, 2007; pp 239–278. https://doi.org/10.1007/978-3-540-29857-1_8.

(59) Li, R.; Bourgeois, M. R.; Cherqui, C.; Guan, J.; Wang, D.; Hu, J.; Schaller, R. D.; Schatz, G. C.; Odom, T. W. Hierarchical Hybridization in Plasmonic Honeycomb Lattices. *Nano Lett.* **2019**, *19* (9), 6435–6441. https://doi.org/10.1021/acs.nanolett.9b02661.

(60) Guo, C.; Yu, J.; Deng, S. Hybrid Metasurfaces of Plasmonic Lattices and 2D Materials. *Adv. Funct. Mater.* **2023**, *33* (42), 2302265. https://doi.org/10.1002/adfm.202302265.

(61) Henzie, J.; Lee, M. H.; Odom, T. W. Multiscale Patterning of Plasmonic Metamaterials. *Nat. Nanotechnol.* **2007**, *2* (9), 549–554. https://doi.org/10.1038/nnano.2007.252.

(62) Wang, D.; Wang, W.; Knudson, M. P.; Schatz, G. C.; Odom, T. W. Structural Engineering in Plasmon Nanolasers. *Chem. Rev.* **2018**, *118* (6), 2865–2881. https://doi.org/10.1021/acs.chemrev.7b00424.

(63) Wang, W.; Ramezani, M.; Väkeväinen, A. I.; Törmä, P.; Rivas, J. G.; Odom, T. W. The Rich Photonic World of Plasmonic Nanoparticle Arrays. *Mater. Today* **2018**, *21* (3), 303–314. https://doi.org/10.1016/j.mattod.2017.09.002.

(64) Volk, K.; Honold, T.; Feller, D.; Karg, M. Surface Lattice Resonances in Self-Templated Plasmonic Honeycomb and Moiré Lattices. *Adv. Mater. Interfaces* **2021**, *8* (13), 2100317. https://doi.org/10.1002/admi.202100317.

(65) Probst, P. T.; Mayer, M.; Gupta, V.; Steiner, A. M.; Zhou, Z.; Auernhammer, G. K.; König, T. A. F.; Fery, A. Mechano-Tunable Chiral Metasurfaces via Colloidal Assembly. *Nat. Mater.* **2021**, *20* (7), 1024–1028. https://doi.org/10.1038/s41563-021-00991-8.

(66) Charconnet, M.; Korsa, M. T.; Petersen, S.; Plou, J.; Hanske, C.; Adam, J.; Seifert, A. Generalization of Self-Assembly Toward Differently Shaped Colloidal Nanoparticles for Plasmonic Superlattices. *Small Methods* **2023**, *7* (4), 2201546. https://doi.org/10.1002/smtd.202201546.

(67) Conti, Y.; Chiang, N.; Scarabelli, L. Colloidal Plasmonic Metasurfaces for the Enhancement of Non-Linear Optical Processes and Molecular Spectroscopies. *ChemNanoMat* **2024**, *10* (4), e202300566. https://doi.org/10.1002/cnma.202300566.

(68) Scarabelli, L.; Coronado-Puchau, M.; Giner-Casares, J. J.; Langer, J.; Liz-Marzán, L. M. Monodisperse Gold Nanotriangles: Size Control, Large-Scale Self-Assembly, and Performance in Surface-Enhanced Raman Scattering. *ACS Nano* **2014**, *8* (6), 5833–5842. https://doi.org/10.1021/nn500727w.

(69) Chang, H.-H.; Murphy, C. J. Mini Gold Nanorods with Tunable Plasmonic Peaks beyond 1000 Nm. *Chem. Mater.* **2018**, *30* (4), 1427–1435. https://doi.org/10.1021/acs.chemmater.7b05310.

(70) Hentschel, M.; Schäferling, M.; Duan, X.; Giessen, H.; Liu, N. Chiral Plasmonics. *Sci. Adv.* **2017**, *3* (5), e1602735. https://doi.org/10.1126/sciadv.1602735.

(71) Lee, H.-E.; Ahn, H.-Y.; Mun, J.; Lee, Y. Y.; Kim, M.; Cho, N. H.; Chang, K.; Kim, W. S.; Rho, J.; Nam, K. T. Amino-Acid- and Peptide-Directed Synthesis of Chiral Plasmonic Gold Nanoparticles. *Nature* **2018**, *556* (7701), 360–365. https://doi.org/10.1038/s41586-018-0034-1.

(72) Mayer, M.; Scarabelli, L.; March, K.; Altantzis, T.; Tebbe, M.; Kociak, M.; Bals, S.; García de Abajo, F. J.; Fery, A.; Liz-Marzán, L. M. Controlled Living Nanowire Growth: Precise Control over the Morphology and Optical Properties of AgAuAg Bimetallic Nanowires. *Nano Lett.* **2015**, *15* (8), 5427–5437. https://doi.org/10.1021/acs.nanolett.5b01833.

(73) Agnihotri, S. K.; Prashant, D. V.; Samajdar, D. P. Role of Metallic Nanoparticles in the Optoelectronic Performance Enhancement of InP Ultrathin Film Solar Cell. *Opt. Mater.* **2022**, *134*, 113129. https://doi.org/10.1016/j.optmat.2022.113129.

(74) Howes, P. D.; Rana, S.; Stevens, M. M. Plasmonic Nanomaterials for Biodiagnostics. *Chem. Soc. Rev.* **2014**, *43* (11), 3835–3853. https://doi.org/10.1039/C3CS60346F.

(75) Tizei, L. H. G.; Mkhitaryan, V.; Lourenço-Martins, H.; Scarabelli, L.; Watanabe, K.;

Taniguchi, T.; Tencé, M.; Blazit, J.-D.; Li, X.; Gloter, A.; Zobelli, A.; Schmidt, F.-P.; Liz-Marzán, L. M.; García de Abajo, F. J.; Stéphan, O.; Kociak, M. Tailored Nanoscale Plasmon-Enhanced Vibrational Electron Spectroscopy. *Nano Lett.* **2020**, *20* (5), 2973–2979. https://doi.org/10.1021/acs.nanolett.9b04659.

(76) Karg, M.; König, T. A. F.; Retsch, M.; Stelling, C.; Reichstein, P. M.; Honold, T.; Thelakkat, M.; Fery, A. Colloidal Self-Assembly Concepts for Light Management in Photovoltaics. *Mater. Today* **2015**, *18* (4), 185–205. https://doi.org/10.1016/j.mattod.2014.10.036.

(77) Grzelczak, M.; Vermant, J.; Furst, E. M.; Liz-Marzán, L. M. Directed Self-Assembly of Nanoparticles. *ACS Nano* **2010**, *4* (7), 3591–3605. https://doi.org/10.1021/nn100869j.

(78) Courty, A.; Mermet, A.; Albouy, P. A.; Duval, E.; Pileni, M. P. Vibrational Coherence of Self-Organized Silver Nanocrystals in f.c.c. Supra-Crystals. *Nat. Mater.* **2005**, *4* (5), 395–398. https://doi.org/10.1038/nmat1366.

(79) Zang, L.; Che, Y.; Moore, J. S. One-Dimensional Self-Assembly of Planar π-Conjugated Molecules: Adaptable Building Blocks for Organic Nanodevices. *Acc. Chem. Res.* **2008**, *41* (12), 1596–1608. https://doi.org/10.1021/ar800030w.

(80) Cargnello, M.; Johnston-Peck, A. C.; Diroll, B. T.; Wong, E.; Datta, B.; Damodhar, D.; Doan-Nguyen, V. V. T.; Herzing, A. A.; Kagan, C. R.; Murray, C. B. Substitutional Doping in Nanocrystal Superlattices. *Nature* **2015**, *524* (7566), 450–453. https://doi.org/10.1038/nature14872.

(81) Gupta, V.; Probst, P. T.; Goßler, F. R.; Steiner, A. M.; Schubert, J.; Brasse, Y.; König, T. A. F.; Fery, A. Mechanotunable Surface Lattice Resonances in the Visible Optical Range by Soft Lithography Templates and Directed Self-Assembly. *ACS Appl. Mater. Interfaces* **2019**, *11* (31), 28189–28196. https://doi.org/10.1021/acsami.9b08871.

(82) Mueggenburg, K. E.; Lin, X.-M.; Goldsmith, R. H.; Jaeger, H. M. Elastic Membranes of Close-Packed Nanoparticle Arrays. *Nat. Mater.* **2007**, *6* (9), 656–660. https://doi.org/10.1038/nmat1965.

(83) Müller, M. B.; Kuttner, C.; König, T. A. F.; Tsukruk, V. V.; Förster, S.; Karg, M.; Fery, A. Plasmonic Library Based on Substrate-Supported Gradiential Plasmonic Arrays. *ACS Nano* **2014**, *8* (9), 9410–9421. https://doi.org/10.1021/nn503493c.

(84) Si, K. J.; Sikdar, D.; Chen, Y.; Eftekhari, F.; Xu, Z.; Tang, Y.; Xiong, W.; Guo, P.; Zhang, S.; Lu, Y.; Bao, Q.; Zhu, W.; Premaratne, M.; Cheng, W. Giant Plasmene Nanosheets, Nanoribbons, and Origami. *ACS Nano* **2014**, *8* (11), 11086–11093. https://doi.org/10.1021/nn504615a.

(85) Min, Y.; Akbulut, M.; Kristiansen, K.; Golan, Y.; Israelachvili, J. The Role of Interparticle and External Forces in Nanoparticle Assembly. *Nat. Mater.* **2008**, *7* (7), 527–538. https://doi.org/10.1038/nmat2206.

(86) Luo, D.; Yan, C.; Wang, T. Interparticle Forces Underlying Nanoparticle Self-Assemblies. *Small Weinh. Bergstr. Ger.* **2015**, *11* (45), 5984–6008. https://doi.org/10.1002/smll.201501783.

(87) Bishop, K. J. M.; Wilmer, C. E.; Soh, S.; Grzybowski, B. A. Nanoscale Forces and Their Uses in Self-Assembly. *Small* **2009**, *5* (14), 1600–1630. https://doi.org/10.1002/smll.200900358.

(88) Sunny, S.; Vogel, N.; Howell, C.; Vu, T. L.; Aizenberg, J. Lubricant-Infused Nanoparticulate Coatings Assembled by Layer-by-Layer Deposition. *Adv. Funct. Mater.* **2014**, *24* (42), 6658–6667. https://doi.org/10.1002/adfm.201401289.

(89) Vogel, N.; Retsch, M.; Fustin, C.-A.; del Campo, A.; Jonas, U. Advances in Colloidal Assembly: The Design of Structure and Hierarchy in Two and Three Dimensions. *Chem. Rev.* **2015**, *115* (13), 6265–6311. https://doi.org/10.1021/cr400081d.

(90) Freymann, G. von; Kitaev, V.; Lotsch, B. V.; Ozin, G. A. Bottom-up Assembly of Photonic Crystals. *Chem. Soc. Rev.* **2013**, *42* (7), 2528–2554. https://doi.org/10.1039/C2CS35309A.

(91) Galisteo-López, J. F.; Ibisate, M.; Sapienza, R.; Froufe-Pérez, L. S.; Blanco, Á.; López, C. Self-Assembled Photonic Structures. *Adv. Mater.* **2011**, *23* (1), 30–69. https://doi.org/10.1002/adma.201000356.

(92) Hoang, T. B.; Akselrod, G. M.; Argyropoulos, C.; Huang, J.; Smith, D. R.; Mikkelsen, M. H. Ultrafast Spontaneous Emission Source Using Plasmonic Nanoantennas. *Nat. Commun.* **2015**, *6* (1), 7788. https://doi.org/10.1038/ncomms8788.

(93) Bigioni, T. P.; Lin, X.-M.; Nguyen, T. T.; Corwin, E. I.; Witten, T. A.; Jaeger, H. M. Kinetically Driven Self Assembly of Highly Ordered Nanoparticle Monolayers. *Nat. Mater.* **2006**, *5* (4), 265–270. https://doi.org/10.1038/nmat1611.

(94) Brasse, Y.; Müller, M. B.; Karg, M.; Kuttner, C.; König, T. A. F.; Fery, A. Magnetic and Electric Resonances in Particle-to-Film-Coupled Functional Nanostructures. *ACS Appl. Mater. Interfaces* **2018**, *10* (3), 3133–3141. https://doi.org/10.1021/acsami.7b16941.

(95) Chen, J.; Dong, P.; Di, D.; Wang, C.; Wang, H.; Wang, J.; Wu, X. Controllable Fabrication of 2D Colloidal-Crystal Films with Polystyrene Nanospheres of Various Diameters by Spin-Coating. *Appl. Surf. Sci.* **2013**, *270*, 6–15. https://doi.org/10.1016/j.apsusc.2012.11.165.

(96) Volk, K.; Fitzgerald, J. P. S.; Retsch, M.; Karg, M. Time-Controlled Colloidal Superstructures: Long-Range Plasmon Resonance Coupling in Particle Monolayers. *Adv. Mater.* **2015**, *27* (45), 7332–7337. https://doi.org/10.1002/adma.201503672.

(97) Chattopadhyay, P.; Wang, L.; Eychmüller, A.; Simmchen, J. An Undergraduate Project on the Assembly of Langmuir–Blodgett Films of Colloidal Particles. *J. Chem. Educ.* **2022**, *99* (2), 952–956. https://doi.org/10.1021/acs.jchemed.1c00667.

(98) Onsager, L. The Effects of Shape on the Interaction of Colloidal Particles. *Ann. N. Y. Acad. Sci.* **1949**, *51* (4), 627–659. https://doi.org/10.1111/j.1749-6632.1949.tb27296.x.

(99) Frenkel, D. Order through Entropy. *Nat. Mater.* **2015**, *14* (1), 9–12. https://doi.org/10.1038/nmat4178.

(100) de Nijs, B.; Dussi, S.; Smallenburg, F.; Meeldijk, J. D.; Groenendijk, D. J.; Filion, L.; Imhof, A.; van Blaaderen, A.; Dijkstra, M. Entropy-Driven Formation of Large Icosahedral Colloidal Clusters by Spherical Confinement. *Nat. Mater.* **2015**, *14* (1), 56–60. https://doi.org/10.1038/nmat4072.

(101) Whitelam, S.; Jack, R. L. The Statistical Mechanics of Dynamic Pathways to Self-Assembly. *Annu. Rev. Phys. Chem.* **2015**, *66* (1), 143–163. https://doi.org/10.1146/annurev-physchem-040214-121215.

(102) Heuer-Jungemann, A.; Feliu, N.; Bakaimi, I.; Hamaly, M.; Alkilany, A.; Chakraborty, I.; Masood, A.; Casula, M. F.; Kostopoulou, A.; Oh, E.; Susumu, K.; Stewart, M. H.; Medintz, I. L.; Stratakis, E.; Parak, W. J.; Kanaras, A. G. The Role of Ligands in the Chemical Synthesis and Applications of Inorganic Nanoparticles. *Chem. Rev.* **2019**, *119* (8), 4819–4880. https://doi.org/10.1021/acs.chemrev.8b00733.

(103) Si, K. J.; Chen, Y.; Shi, Q.; Cheng, W. Nanoparticle Superlattices: The Roles of Soft Ligands. *Adv. Sci.* **2018**, *5* (1), 1700179. https://doi.org/10.1002/advs.201700179.

(104) Cheng, W.; Campolongo, M. J.; Cha, J. J.; Tan, S. J.; Umbach, C. C.; Muller, D. A.; Luo, D. Free-Standing Nanoparticle Superlattice Sheets Controlled by DNA. *Nat. Mater.* **2009**, *8* (6), 519–525. https://doi.org/10.1038/nmat2440.

(105) Liu, Y.; Li, Y.; He, J.; Duelge, K. J.; Lu, Z.; Nie, Z. Entropy-Driven Pattern Formation of Hybrid Vesicular Assemblies Made from Molecular and Nanoparticle Amphiphiles. *J. Am. Chem. Soc.* **2014**, *136* (6), 2602–2610. https://doi.org/10.1021/ja412172f.

(106) van Dommelen, R.; Fanzio, P.; Sasso, L. Surface Self-Assembly of Colloidal Crystals for Micro- and Nano-Patterning. *Adv. Colloid Interface Sci.* **2018**, *251*, 97–114. https://doi.org/10.1016/j.cis.2017.10.007.

(107) Vold, M. J. The Effect of Adsorption on the van Der Waals Interaction of Spherical Colloidal Particles. *J. Colloid Sci.* **1961**, *16* (1), 1–12. https://doi.org/10.1016/0095-8522(61)90057-5.

(108) Lekkerkerker, H. N. W.; Tuinier, R. *Colloids and the Depletion Interaction*; Lecture Notes in Physics; Springer Netherlands: Dordrecht, 2011; Vol. 833. https://doi.org/10.1007/978-94-007-1223-2.

(109) Matter, F.; Luna, A. L.; Niederberger, M. From Colloidal Dispersions to Aerogels: How to Master Nanoparticle Gelation. *Nano Today* **2020**, *30*, 100827. https://doi.org/10.1016/j.nantod.2019.100827.

(110) Sapir, L.; Harries, D. Is the Depletion Force Entropic? Molecular Crowding beyond Steric Interactions. *Curr. Opin. Colloid Interface Sci.* **2015**, *20* (1), 3–10. https://doi.org/10.1016/j.cocis.2014.12.003.

(111) Tuinier, R.; Rieger, J.; de Kruif, C. G. Depletion-Induced Phase Separation in Colloid–Polymer Mixtures. *Adv. Colloid Interface Sci.* **2003**, *103* (1), 1–31. https://doi.org/10.1016/S0001-8686(02)00081-7.

(112) Hierrezuelo, J.; Sadeghpour, A.; Szilagyi, I.; Vaccaro, A.; Borkovec, M. Electrostatic Stabilization of Charged Colloidal Particles with Adsorbed Polyelectrolytes of Opposite Charge. *Langmuir* **2010**, *26* (19), 15109–15111. https://doi.org/10.1021/la102912u.

(113) Ghezelbash, A.; Koo, B.; Korgel, B. A. Self-Assembled Stripe Patterns of CdS Nanorods. *Nano Lett.* **2006**, *6* (8), 1832–1836. https://doi.org/10.1021/nl061035l.

(114) Moncho-Jordá, A.; Martínez-López, F.; González, A. E.; Hidalgo-Álvarez, R. Role of Long-Range Repulsive Interactions in Two-Dimensional Colloidal Aggregation: Experiments and Simulations. *Langmuir* **2002**, *18* (24), 9183–9191. https://doi.org/10.1021/la0258805.

(115) Agmo Hernández, V. An Overview of Surface Forces and the DLVO Theory. *ChemTexts* **2023**, *9* (4), 10. https://doi.org/10.1007/s40828-023-00182-9.

(116) Adair, J. H.; Suvaci, E.; Sindel, J. Surface and Colloid Chemistry. In *Encyclopedia of Materials: Science and Technology*; Buschow, K. H. J., Cahn, R. W., Flemings, M. C., Ilschner, B., Kramer, E. J., Mahajan, S., Veyssière, P., Eds.; Elsevier: Oxford, 2001; pp 1–10. https://doi.org/10.1016/B0-08-043152-6/01622-3.

(117) Nalwa, H. S. Handbook of Surfaces and Interfaces of Materials. In *Handbook of Surfaces and Interfaces of Materials*; Nalwa, H. S., Ed.; Academic Press: Burlington, 2001; pp xxv–xxviii. https://doi.org/10.1016/B978-012513910-6/50003-7.

(118) Zhou, M.; Liu, Y.; Zhang, P.; Miao, Y.; Luo, H.; Jing, G. Capillary Assembly of

Colloidal Particles on Patterned Surfaces. *New J. Phys.* **2020**, *22* (5), 053005. https://doi.org/10.1088/1367-2630/ab7f90.

(119) Di Leonardo, R.; Saglimbeni, F.; Ruocco, G. Very-Long-Range Nature of Capillary Interactions in Liquid Films. *Phys. Rev. Lett.* **2008**, *100* (10), 106103. https://doi.org/10.1103/PhysRevLett.100.106103.

(120) Leenaars, A. F. M.; Huethorst, J. A. M.; Van Oekel, J. J. Marangoni Drying: A New Extremely Clean Drying Process. *Langmuir* **1990**, *6* (11), 1701–1703. https://doi.org/10.1021/la00101a014.

(121) Anyfantakis, M.; Baigl, D. Manipulating the Coffee-Ring Effect: Interactions at Work. *Chemphyschem Eur. J. Chem. Phys. Phys. Chem.* **2015**, *16* (13), 2726–2734. https://doi.org/10.1002/cphc.201500410.

(122) Deegan, R. D.; Bakajin, O.; Dupont, T. F.; Huber, G.; Nagel, S. R.; Witten, T. A. Capillary Flow as the Cause of Ring Stains from Dried Liquid Drops. *Nature* **1997**, *389* (6653), 827–829. https://doi.org/10.1038/39827.

(123) Hamon, C.; Sanz-Ortiz, M. N.; Modin, E.; Hill, E. H.; Scarabelli, L.; Chuvilin, A.; Liz-Marzán, L. M. Hierarchical Organization and Molecular Diffusion in Gold Nanorod/Silica Supercrystal Nanocomposites. *Nanoscale* **2016**, *8* (15), 7914–7922. https://doi.org/10.1039/C6NR00712K.

(124) Hamon, C.; Novikov, S. M.; Scarabelli, L.; Solís, D. M.; Altantzis, T.; Bals, S.; Taboada, J. M.; Obelleiro, F.; Liz-Marzán, L. M. Collective Plasmonic Properties in Few-Layer Gold Nanorod Supercrystals. *ACS Photonics* **2015**, *2* (10), 1482–1488. https://doi.org/10.1021/acsphotonics.5b00369.

(125) Zhang, H.; Kinnear, C.; Mulvaney, P. Fabrication of Single-Nanocrystal Arrays. *Adv. Mater.* **2020**, *32* (18), 1904551. https://doi.org/10.1002/adma.201904551.

(126) Rey, A.; Billardon, G.; Lörtscher, E.; Moth-Poulsen, K.; Stuhr-Hansen, N.; Wolf, H.; Bjørnholm, T.; Stemmer, A.; Riel, H. Deterministic Assembly of Linear Gold Nanorod Chains as a Platform for Nanoscale Applications. *Nanoscale* **2013**, *5* (18), 8680–8688. https://doi.org/10.1039/C3NR02358C.

(127) Lee, J. B.; Walker, H.; Li, Y.; Nam, T. W.; Rakovich, A.; Sapienza, R.; Jung, Y. S.; Nam, Y. S.; Maier, S. A.; Cortés, E. Template Dissolution Interfacial Patterning of Single Colloids for Nanoelectrochemistry and Nanosensing. *ACS Nano* **2020**, *14* (12), 17693–17703. https://doi.org/10.1021/acsnano.0c09319.

(128) Juodėnas, M.; Peckus, D.; Tamulevičius, T.; Yamauchi, Y.; Tamulevičius, S.; Henzie, J. Effect of Ag Nanocube Optomechanical Modes on Plasmonic Surface Lattice

Resonances. *ACS Photonics* **2020**, *7* (11), 3130–3140. https://doi.org/10.1021/acsphotonics.0c01187.

(129) Juodėnas, M.; Tamulevičius, T.; Henzie, J.; Erts, D.; Tamulevičius, S. Surface Lattice Resonances in Self-Assembled Arrays of Monodisperse Ag Cuboctahedra. *ACS Nano* **2019**, *13* (8), 9038–9047. https://doi.org/10.1021/acsnano.9b03191.

(130) Maibaum, L.; Dinner, A. R.; Chandler, D. Micelle Formation and the Hydrophobic Effect. *J. Phys. Chem. B* **2004**, *108* (21), 6778–6781. https://doi.org/10.1021/jp037487t.

(131) Zhang, J.; Zeng, H. Intermolecular and Surface Interactions in Engineering Processes. *Engineering* **2021**, *7* (1), 63–83. https://doi.org/10.1016/j.eng.2020.08.017.

(132) Chandler, D. Interfaces and the Driving Force of Hydrophobic Assembly. *Nature* **2005**, *437* (7059), 640–647. https://doi.org/10.1038/nature04162.

(133) Ding, T.; Valev, V. K.; Salmon, A. R.; Forman, C. J.; Smoukov, S. K.; Scherman, O. A.; Frenkel, D.; Baumberg, J. J. Light-Induced Actuating Nanotransducers. *Proc. Natl. Acad. Sci.* **2016**, *113* (20), 5503–5507. https://doi.org/10.1073/pnas.1524209113.

(134) Scarabelli, L.; Vila-Liarte, D.; Mihi, A.; Liz-Marzán, L. M. Templated Colloidal Self-Assembly for Lattice Plasmon Engineering. *Acc. Mater. Res.* **2021**, *2* (9), 816–827. https://doi.org/10.1021/accountsmr.1c00106.

(135) Odom, T. W.; Love, J. C.; Wolfe, D. B.; Paul, K. E.; Whitesides, G. M. Improved Pattern Transfer in Soft Lithography Using Composite Stamps. *Langmuir* **2002**, *18* (13), 5314–5320. https://doi.org/10.1021/la020169l.

(136) Hanske, C.; Müller, M. B.; Bieber, V.; Tebbe, M.; Jessl, S.; Wittemann, A.; Fery, A. The Role of Substrate Wettability in Nanoparticle Transfer from Wrinkled Elastomers: Fundamentals and Application toward Hierarchical Patterning. *Langmuir* **2012**, *28* (49), 16745–16750. https://doi.org/10.1021/la304028f.

(137) Tebbe, M.; Mayer, M.; Glatz, B. A.; Hanske, C.; Probst, P. T.; Müller, M. B.; Karg, M.; Chanana, M.; König, T. A. F.; Kuttner, C.; Fery, A. Optically Anisotropic Substrates via Wrinkle-Assisted Convective Assembly of Gold Nanorods on Macroscopic Areas. *Faraday Discuss.* **2015**, *181* (0), 243–260. https://doi.org/10.1039/C4FD00236A.

(138) Rycenga, M.; Camargo, P. H. C.; Xia, Y. Template-Assisted Self-Assembly: A Versatile Approach to Complex Micro- and Nanostructures. *Soft Matter* **2009**, *5* (6), 1129–1136. https://doi.org/10.1039/B811021B.

(139) Vila-Liarte, D.; Feil, M. W.; Manzi, A.; Garcia-Pomar, J. L.; Huang, H.; Döblinger, M.; Liz-Marzán, L. M.; Feldmann, J.; Polavarapu, L.; Mihi, A. Template-basierte Herstellung von 2D-photonischen Superkristallen mit verstärkter spontaner Emission aus

CsPbBr3-Perowskit-Nanokristallen. *Angew. Chem.* **2020**, *132* (40), 17903–17909. https://doi.org/10.1002/ange.202006152.

(140) Yin, Y.; Lu, Y.; Gates, B.; Xia, Y. Template-Assisted Self-Assembly: A Practical Route to Complex Aggregates of Monodispersed Colloids with Well-Defined Sizes, Shapes, and Structures. *J. Am. Chem. Soc.* **2001**, *123* (36), 8718–8729. https://doi.org/10.1021/ja011048v.

(141) Baur, S.; Sanders, S.; Manjavacas, A. Hybridization of Lattice Resonances. *ACS Nano* **2018**, *12* (2), 1618–1629. https://doi.org/10.1021/acsnano.7b08206.

(142) Manjavacas, A.; Zundel, L.; Sanders, S. Analysis of the Limits of the Near-Field Produced by Nanoparticle Arrays. *ACS Nano* **2019**, *13* (9), 10682–10693. https://doi.org/10.1021/acsnano.9b05031.

(143) Molet, P.; Passarelli, N.; Pérez, L. A.; Scarabelli, L.; Mihi, A. Engineering Plasmonic Colloidal Meta-Molecules for Tunable Photonic Supercrystals. *Adv. Opt. Mater.* **2021**, *9* (20), 2100761. https://doi.org/10.1002/adom.202100761.

(144) Henzie, J.; Barton, J. E.; Stender, C. L.; Odom, T. W. Large-Area Nanoscale Patterning: Chemistry Meets Fabrication. *Acc. Chem. Res.* **2006**, *39* (4), 249–257. https://doi.org/10.1021/ar050013n.

(145) Auguié, B.; Barnes, W. L. Diffractive Coupling in Gold Nanoparticle Arrays and the Effect of Disorder. *Opt. Lett.* **2009**, *34* (4), 401–403. https://doi.org/10.1364/OL.34.000401.

(146) Matarèse, B. F. E.; Feyen, P. L. C.; Falco, A.; Benfenati, F.; Lugli, P.; deMello, J. C. Use of SU8 as a Stable and Biocompatible Adhesion Layer for Gold Bioelectrodes. *Sci. Rep.* **2018**, *8* (1), 5560. https://doi.org/10.1038/s41598-018-21755-6.

(147) Chiang, N.; Scarabelli, L.; Vinnacombe-Willson, G. A.; Pérez, L. A.; Dore, C.; Mihi, A.; Jonas, S. J.; Weiss, P. S. Large-Scale Soft-Lithographic Patterning of Plasmonic Nanoparticles. *ACS Mater. Lett.* **2021**, *3* (3), 282–289. https://doi.org/10.1021/acsmaterialslett.0c00535.

(148) Laghrissi, A.; Gupta, P.; Rubahn, H.-G.; Fiutowski, J. Rapid Template-Assisted Self-Assembly: A Practical Route to the Fast Assembly of Colloidal Particles. *J. Nanoparticle Res.* **2023**, *25* (6), 103. https://doi.org/10.1007/s11051-023-05755-w.

(149) Vinnacombe-Willson, G. A.; Conti, Y.; Stefancu, A.; Weiss, P. S.; Cortés, E.; Scarabelli, L. Direct Bottom-Up In Situ Growth: A Paradigm Shift for Studies in Wet-Chemical Synthesis of Gold Nanoparticles. *Chem. Rev.* **2023**, *123* (13), 8488–8529. https://doi.org/10.1021/acs.chemrev.2c00914.

(150) Park, K.; Woo, M.-A.; Lim, J.-A.; Kim, Y.-R.; Choi, S.-W.; Lim, M.-C. In Situ

Synthesis of Directional Gold Nanoparticle Arrays along Ridge Cracks of PDMS Wrinkles. *Colloids Surf. Physicochem. Eng. Asp.* **2018**, *558*, 186–191. https://doi.org/10.1016/j.colsurfa.2018.08.075.

(151) Lim, M.-C.; Kim, S.-H.; Park, K.; Kim, Y.-R.; Kim, J.-H.; Ok, G.; Choi, S.-W. Facile Synthesis of Self-Aligned Gold Nanoparticles by Crack Templated Reduction Lithography. *RSC Adv.* **2017**, *7* (22), 13228–13231. https://doi.org/10.1039/C7RA00768J.

(152) Ellsworth, A. A.; Walker, A. V. From Nanowires to Nanopores: A Versatile Method for Electroless Deposition of Nanostructures on Micropatterned Organic Substrates. *Langmuir* **2016**, *32* (11), 2668–2674. https://doi.org/10.1021/acs.langmuir.5b04674.

(153) Alvarez-Fernandez, A.; Cummins, C.; Saba, M.; Steiner, U.; Fleury, G.; Ponsinet, V.; Guldin, S. Block Copolymer Directed Metamaterials and Metasurfaces for Novel Optical Devices. *Adv. Opt. Mater.* **2021**, *9* (16), 2100175. https://doi.org/10.1002/adom.202100175.

(154) Stefik, M.; Guldin, S.; Vignolini, S.; Wiesner, U.; Steiner, U. Block Copolymer Self-Assembly for Nanophotonics. *Chem. Soc. Rev.* **2015**, *44* (15), 5076–5091. https://doi.org/10.1039/C4CS00517A.

(155) Karayianni, M.; Pispas, S. Block Copolymer Solution Self-Assembly: Recent Advances, Emerging Trends, and Applications. *J. Polym. Sci.* **2021**, *59* (17), 1874–1898. https://doi.org/10.1002/pol.20210430.

(156) Cui, H.; Chen, Z.; Zhong, S.; Wooley, K. L.; Pochan, D. J. Block Copolymer Assembly via Kinetic Control. *Science* **2007**, *317* (5838), 647–650. https://doi.org/10.1126/science.1141768.

(157) Espinha, A.; Dore, C.; Matricardi, C.; Alonso, M. I.; Goñi, A. R.; Mihi, A. Hydroxypropyl Cellulose Photonic Architectures by Soft Nanoimprinting Lithography. *Nat. Photonics* **2018**, *12* (6), 343–348. https://doi.org/10.1038/s41566-018-0152-1.

(158) Dore, C.; Osmond, J.; Mihi, A. A Water-Processable Cellulose-Based Resist for Advanced Nanofabrication. *Nanoscale* **2018**, *10* (37), 17884–17892. https://doi.org/10.1039/C8NR04851G.

(159) Kim, J. H.; Park, H.; Seo, S. W. In Situ Synthesis of Silver Nanoparticles on the Surface of PDMS with High Antibacterial Activity and Biosafety toward an Implantable Medical Device. *Nano Converg.* **2017**, *4* (1), 33. https://doi.org/10.1186/s40580-017-0126-x.

(160) Tsuge, Y.; Moriya, T.; Moriyama, Y.; Tokura, Y.; Shiratori, S. Slippery Liquid-Immobilized Coating Films Using in Situ Oxidation–Reduction Reactions of Metal Ions in Polyelectrolyte Films. *ACS Appl. Mater. Interfaces* **2017**, *9* (17), 15122–15129.

https://doi.org/10.1021/acsami.7b01869.

(161) Dunklin, J. R.; Forcherio, G. T.; Berry, K. R. Jr.; Roper, D. K. Gold Nanoparticle–Polydimethylsiloxane Thin Films Enhance Thermoplasmonic Dissipation by Internal Reflection. *J. Phys. Chem. C* **2014**, *118* (14), 7523–7531. https://doi.org/10.1021/jp4112124.

(162) Fortuni, B.; Fujita, Y.; Ricci, M.; Inose, T.; Aubert, R.; Lu, G.; Hutchison, J. A.; Hofkens, J.; Latterini, L.; Uji-I, H. A Novel Method for in Situ Synthesis of SERS-Active Gold Nanostars on Polydimethylsiloxane Film. *Chem. Commun. Camb. Engl.* **2017**, *53* (37), 5121–5124. https://doi.org/10.1039/c7cc01776f.

(163) Wang, B.; Chen, K.; Jiang, S.; Reincke, F.; Tong, W.; Wang, D.; Gao, C. Chitosan-Mediated Synthesis of Gold Nanoparticles on Patterned Poly(Dimethylsiloxane) Surfaces. *Biomacromolecules* **2006**, *7* (4), 1203–1209. https://doi.org/10.1021/bm060030f.

(164) Chhour, P.; Kim, J.; Benardo, B.; Tovar, A.; Mian, S.; Litt, H. I.; Ferrari, V. A.; Cormode, D. P. Effect of Gold Nanoparticle Size and Coating on Labeling Monocytes for CT Tracking. *Bioconjug. Chem.* **2017**, *28* (1), 260–269. https://doi.org/10.1021/acs.bioconjchem.6b00566.

(165) Landeke-Wilsmark, B.; Nyholm, L.; Hägglund, C. Seeded Growth of Large-Area Arrays of Substrate Supported Au Nanoparticles Using Citrate and Hydrogen Peroxide. *Langmuir* **2020**, *36* (24), 6848–6858. https://doi.org/10.1021/acs.langmuir.0c00374.

(166) Muench, F.; Schaefer, S.; Hagelüken, L.; Molina-Luna, L.; Duerrschnabel, M.; Kleebe, H.-J.; Brötz, J.; Vaskevich, A.; Rubinstein, I.; Ensinger, W. Template-Free Electroless Plating of Gold Nanowires: Direct Surface Functionalization with Shape-Selective Nanostructures for Electrochemical Applications. *ACS Appl. Mater. Interfaces* **2017**, *9* (36), 31142–31152. https://doi.org/10.1021/acsami.7b09398.

(167) Sun, Y. Direct Growth of Dense, Pristine Metal Nanoplates with Well-Controlled Dimensions on Semiconductor Substrates. *Chem. Mater.* **2007**, *19* (24), 5845–5847. https://doi.org/10.1021/cm7022407.

(168) Lohmueller, T.; Bock, E.; Spatz, J. P. Synthesis of Quasi-Hexagonal Ordered Arrays of Metallic Nanoparticles with Tuneable Particle Size. *Adv. Mater.* **2008**, *20* (12), 2297–2302. https://doi.org/10.1002/adma.200702635.

(169) Tao, A. R.; Habas, S.; Yang, P. Shape Control of Colloidal Metal Nanocrystals. *Small* **2008**, *4* (3), 310–325. https://doi.org/10.1002/smll.200701295.

(170) Pastoriza-Santos, I.; Liz-Marzán, L. M. Formation of PVP-Protected Metal Nanoparticles in DMF. *Langmuir* **2002**, *18* (7), 2888–2894.

https://doi.org/10.1021/la015578g.

(171) Brown, K. R.; Walter, D. G.; Natan, M. J. Seeding of Colloidal Au Nanoparticle Solutions. 2. Improved Control of Particle Size and Shape. *Chem. Mater.* **2000**, *12* (2), 306–313. https://doi.org/10.1021/cm980065p.

(172) Vinnacombe-Willson, G. A.; Chiang, N.; Scarabelli, L.; Hu, Y.; Heidenreich, L. K.; Li, X.; Gong, Y.; Inouye, D. T.; Fisher, T. S.; Weiss, P. S.; Jonas, S. J. In Situ Shape Control of Thermoplasmonic Gold Nanostars on Oxide Substrates for Hyperthermia-Mediated Cell Detachment. *ACS Cent. Sci.* **2020**, *6* (11), 2105–2116. https://doi.org/10.1021/acscentsci.0c01097.

(173) Jimenez de Aberasturi, D.; Serrano-Montes, A. B.; Langer, J.; Henriksen-Lacey, M.; Parak, W. J.; Liz-Marzán, L. M. Surface Enhanced Raman Scattering Encoded Gold Nanostars for Multiplexed Cell Discrimination. *Chem. Mater.* **2016**, *28* (18), 6779–6790. https://doi.org/10.1021/acs.chemmater.6b03349.

(174) Vinnacombe-Willson, G. A.; Lee, J. K.; Chiang, N.; Scarabelli, L.; Yue, S.; Foley, R.; Frost, I.; Weiss, P. S.; Jonas, S. J. Exploring the Bottom-Up Growth of Anisotropic Gold Nanoparticles from Substrate-Bound Seeds in Microfluidic Reactors. *ACS Appl. Nano Mater.* **2023**, *6* (8), 6454–6460. https://doi.org/10.1021/acsanm.3c00440.

(175) Lenzi, E.; Jimenez de Aberasturi, D.; Henriksen-Lacey, M.; Piñeiro, P.; Muniz, A. J.; Lahann, J.; Liz-Marzán, L. M. SERS and Fluorescence-Active Multimodal Tessellated Scaffolds for Three-Dimensional Bioimaging. *ACS Appl. Mater. Interfaces* **2022**, *14* (18), 20708–20719. https://doi.org/10.1021/acsami.2c02615.

(176) Xia, D.; Li, D.; Ku, Z.; Luo, Y.; Brueck, S. R. J. Top-Down Approaches to the Formation of Silica Nanoparticle Patterns. *Langmuir* **2007**, *23* (10), 5377–5385. https://doi.org/10.1021/la7005666.

Chapter 3

OPTICAL CHARACTERIZATIONS AND METASURFACES ENGINEERING

"I have gotten a lot of results! I know several thousand things that won't work."

(Thomas Alva Edison-1910)

Introduction

The essential requirement for applications that range from highly sensitive molecular sensing to nanoscale lasing is the presence of plasmonic nanostructures capable of amplifying localized optical fields and sustaining ultra-narrow resonances. Overcoming the great challenge of effectively engineering and sustaining these resonances over a wide range of wavelengths within a single system, opens new prospects for groundbreaking progresses in many fields. Beyond advancing the understanding of plasmonic nanostructures behavior, this quest holds the key to unlock unprecedented opportunities in advanced technologies and scientific exploration.

Compared to nanohole arrays, metal particle arrays lack continuous metal interfaces for the conventional propagation of surface plasmon polaritons (SPPs). Nevertheless, these arrays can still maintain delocalized nature of the resonance by diffractively coupling the localized plasmon resonances, as discussed in **Chapter 1**.[1,2] One intriguing aspect of metasurfaces lies in their capacity to engineer and tailor optical properties with high precision. By strategically designing the geometry, composition, and arrangement of subwavelength elements, it is possible to modulate absorption, reflection, transmission, and dispersion properties.

Despite the advantages of nanohole arrays such as higher light-to-heat conversion and the ability to act as electrodes,[3] nanoparticle arrays exhibit reduced metal content per unit area (assuming the same thickness). Consequently, they exhibit reduced material absorption and increased

direct transmission, which leads to the determination of the resonance directly by the position of the dips in the transmission spectra.[4]

To highlight the flexibility and versatility of plasmonic systems fabricated *via* the alternative strategies presented in **Chapter 2**, this chapter will recollect the results of optical characterization achieved in the context of this thesis. This dataset will showcase different strategies that can be taken to engineer a metasurface optical response, including changing the refractive index (*n*) of the environment, the plasmonic units' morphology, and the substrate material.

3.1 Plasmonic metasurfaces: the role of a high refractive index layer

In this study, we created nanolasing architectures based on surface lattice resonances (SLRs) by self-assembling pre-synthesized silver colloids. The plasmonic optical cavity is directly fabricated onto a photoresist layer (SU8-2000.5) containing the dye molecules of Rhodamine B (RhB), used as gain medium (discussion on the fabrication in **Paragraph 2.4.1** of **Chapter 2**). This approach yields high quality factor (Q_f) resonances without the necessity of additional processing or annealing steps, a major improvement compared to conventional top-down lithography methods. Moreover, the use of colloidal self-assembly offers high throughput and versatility, facilitating the exploration of various nanoparticle geometries and materials. Finally, this method also allows dynamic control of chemical and physical interactions at the interface between the plasmonic/photonic structures and the underlying gain media, as well as at the exposed surface of the assembled plasmonic system.

By exploiting the hydrophobicity of the SU8 high refractive index layer (see discussion in **Paragraph 2.4.1** of **Chapter 2**), the quality of the overall array is improved, which leads to narrower lattice plasmon resonances. However, the most dramatic effect is strongly related to the thickness of the spin-coated SU8-RhB gain medium layer.

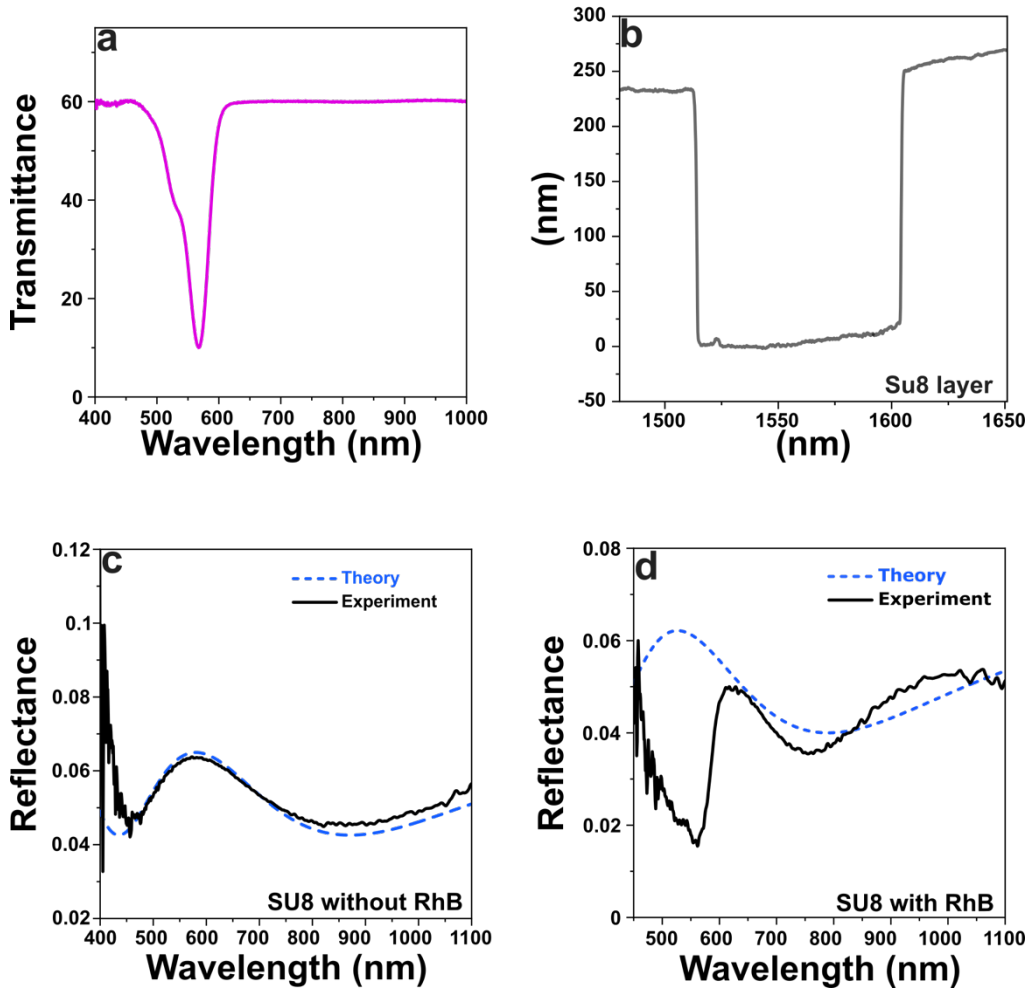

Figure 3.1 **Study on the su8 layer**. (**a**) Transmittance spectrum of the Su8/RhB layer corresponding to the RhB extinction profile. (**b**) SU8 layer thickness measured by profilometry. The thickness as an average value of 232 nm. (**c**), (**d**) Interferometry measurements for the evaluation of the thickness through reflectance experiment. The data were processed *via* transfer matrix model which fits the experimental data by using *MathLab* licensed program. The small deviation between the fit and the experimental data can be ascribed to heterogeneity on the film deposition and the omission of the presence of the dye in the theoretical curve which may introduce an error in the model.

The Q-factor of a resonance characterizes its ability to store and retain energy and provides an indication of the balance between stored and dissipated energy in an oscillator.

Surface plasmon resonance presenting a high Q_f will manifest amplified intensity and precision in its optical response. Achieving narrow bandwidth lattice resonances typically requires enclosing the metal array with a uniform refractive index.

In fact, the presence of a substrate (*i.e.* a mismatch in refractive index) can hinder long-range interactions between particles and damp the lattice resonances, as the refractive index contrast

between the substrate and the superstrate, together with the distance between the array and the interface, are key factors in determining the strength of the diffractive coupling.[5]

However, in recent studies was found that by using high refractive index layer to match the array can induce the formation of waveguided modes that hybridize the SLRs. By changing the thickness of the high refractive index layer, it is observed a significant effect on the optical response applied to boost the emission properties of gain media.[6]

In our study, we have used a different approach to study the outcoupling effects arising from the refractive index mismatch between the substrate and the air superstrate ($n = 1$). Specifically, in our case the plasmonic metasurfaces are on top of the high refractive index layer, and not embedded into it, leaving them completely exposed to the surroundings. By the rational choice of the photoresist thickness a waveguiding effect, namely the confinement and guiding of incident light waves within the higher refractive index material (SU8, $n = 1.6$), was expoited to improve the outcoupling and the quality factor of the surface lattice resonances, by generating a hybridization and formation of waveguide-SLR (W-SLR) modes.

Specifically, the thickness (t) of the SU8-RhB layer (250 nm) was adjusted to maintain waveguide mode operation of light propagation within the photoresist layer, and sufficient mode overlap with the gain medium.[7,8]

Ultimately, this contributes to increasing the system's far-field out-coupling efficiency and results in the formation of a narrower peak bandwidth without using an index matching layer.

The simulated transmittance spectrum in **Figure 3.2 a** demonstrates the presence of waveguided modes supported by the SU8 epoxy resin layer.

The waveguide and diffractive systems match the wavevector analytical relations, making possible to derive analytical solutions for both TE and TM modes within the dielectric slab, related to the propagation constants $q^2 = n_w^2 k^2 - \beta^2$, $p^2 = \beta^2 - n_s^2 k^2$ and $r^2 = \beta^2 - n_{air}^2 k^2$ as:[9]

$$\tan dq = \frac{q(p+r)}{q^2-pr} \quad \textbf{(3.1)}$$

$$\tan dq = \frac{n_w^2 q(n_{air}^2 p+n_s^2 r)}{n_s^2 n_{air}^2 q^2-n_w^4 pr} \quad \textbf{(3.2)}$$

where $k = 2\pi/\lambda_0$ is the wavenumber, and the refractive index are referred to the superstrate (n_{air}), the dielectric layer (n_w) with thickness *t*, and substrate (n_s). Numerically solving these equations allows to extract the effective refractive index values ($n_{eff} = \beta/k$) for both TE and TM modes, depending on n_s and n_w values.

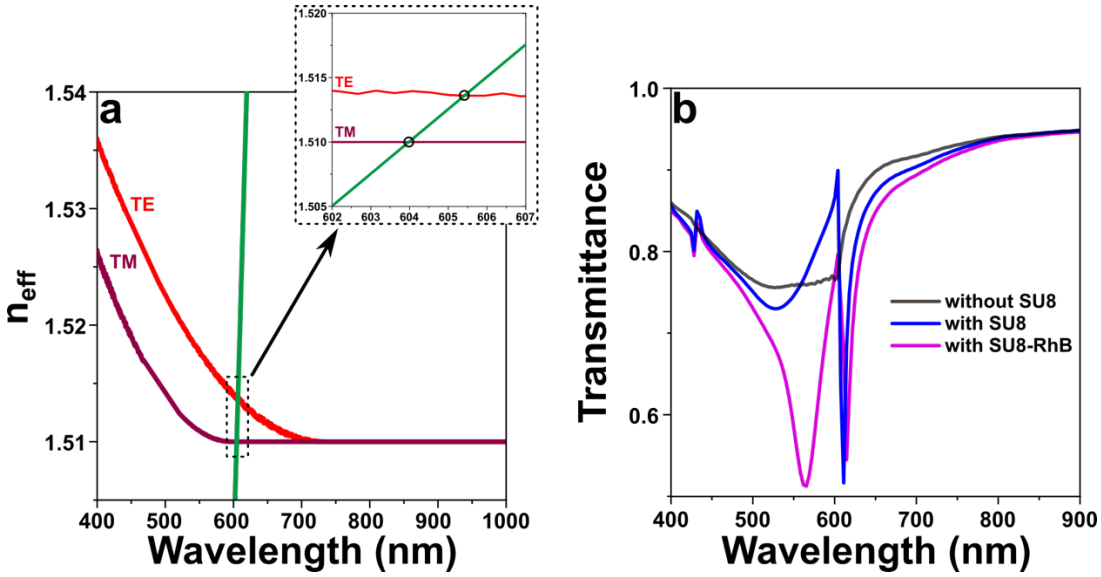

Figure 3.2 **Simulation on the role of SU8 layer**. (**a**) Variation of the simulated TE and TM modes effective refractive index as function of the wavelength (**red** and **burgundy** traces). The **green** line represents the spectral position of the first diffraction order (±1,0) for an array with lattice period of 400 nm. The **inset** represents a zoom of the spectral region of interest, where the crossing points (**black** circles) corresponds to the position where the coupling between diffraction and waveguided modes is expected. (**b**) The simulated transmission spectra show the appearance of a sharp SLR for an array in presence of a SU8 and SU8-RhB layer.

The intersection points of the Rayleigh-Wood anomaly of the square grating with the solution of the TE and TM mode derived from **Eq. 3.1**, and **3.2**, enable the identification of the wavelength at which the coupling takes place (**black** circles in **Figure 3.2 a**). This coupling arises within a spectral region where the effective refractive indices for TE and TM modes

closely approximates the substrate refractive index, specifically at λ = 604 nm and λ = 605.5 nm (no plasmonic contribution is considered).

The comparison of the simulated 0^{th}-order transmission spectra of the cluster array with and without a 250 nm thick SU8 layer, highlights the role of the high refractive index layer (**Figure 3.2 b**). As the system lacks index matching (in both scenarios air represents the superstrate), the transmission spectrum of the cluster array on glass (**black** curve in **Figure 3.2 b**) exhibits no significant diffractive or SLR modes. Conversely, the simulation of the cluster array transmittance spectrum on the SU8 thin film reveals a pronounced and sharp dip at 611 nm. The red shift respect to the positions predicted in **Figure 3.2 a**, can be attributed to the localized plasmon resonance contribution of the cluster. Additionally, the presence of RhB in the epoxy-resin matrix, evident in the intense minimum at 567 nm (**pink** curve in **Figure 3.2 b**), leads to an increase in optical losses, resulting in a slightly broader and further red shifted SLR.

It is important to emphasize that the experimental detection of the two SLR hybrid modes (WTE-SLR and WTM-SLR) would require a coherent light source. Specifically, the bandwidth of the light source ($\Delta\nu$) depends on the inverse of the coherence time (t_c), which is closely related to the coherence length (l_c) and the speed of light (c) by the equation $l_c = c \cdot t_c$. Temporal coherence refers to the degree of correlation between the phases of different wavelengths in a light source. When a light source has low temporal coherence (such in the case of the white light halogen lamp source coupled to our transmission setup), the phase relation between different wavelengths is rapidly or randomly changing, leading to fluctuations in the interference patterns. Consequently, a wide light coherence length (short t_c) leads to a better spectral resolution.

Overall, these results highlight that the presence of narrow optical modes in the absence of a homogeneous dielectric environment can be derived from the formation of hybrid waveguided SLR modes.[10] Further simulated characterization of the generated hybrid modes was performed involving the electric-field distribution maps at the associated wavelengths, along the (xz) and (yx) planes.

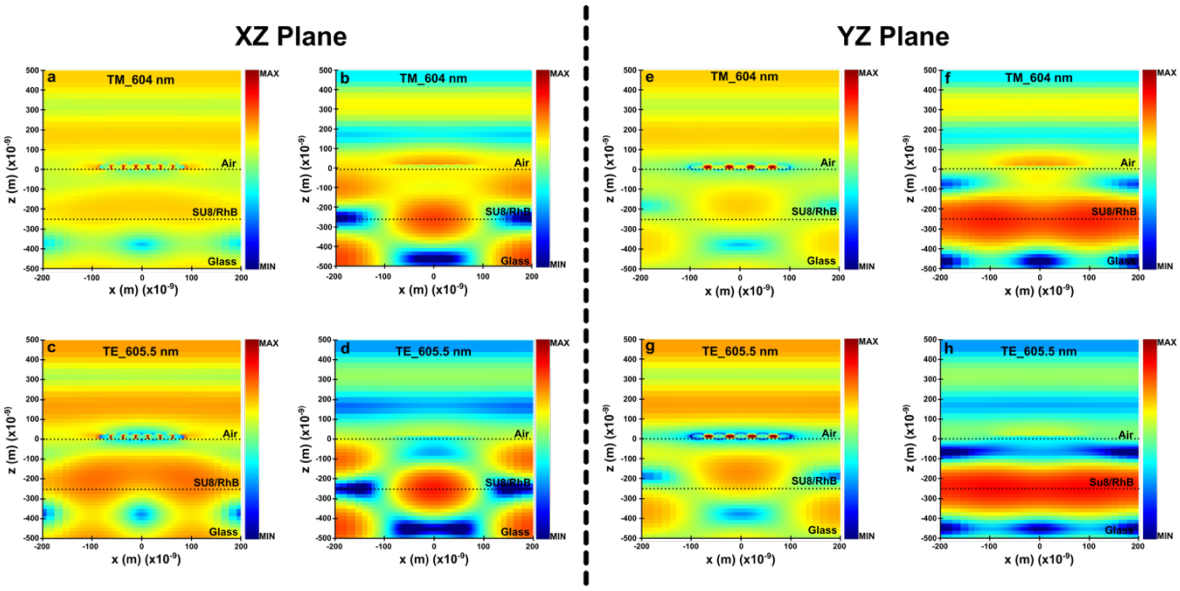

Figure 3.3 Near field distribution in logarithmic scale of the electric (**a**-**c**, **e**-**g**) and magnetic (**b**-**d**, **f**-**h**) fields at the wavelength corresponding to the waveguided TE- and TM- SLR modes. A plane wave with electric field amplitude E_0 = 1 V/m and approximated magnetic field amplitude of 2.65×10^{-3} A/m is injected as excitation source, considering the propagation in vacuum with impedance Z_0 = 376.73 Ω.

The simulation in **Figure 3.3** shows the near-field distribution along the section of the lasing architecture, where a remarkable enhancement of the electric field is observed in proximity of the SU8/glass interface. This can be attributed to the interplay between the plasmonic resonances of the array and the dielectric properties of the surrounding media, considering that SU8-glass interface facilitates efficient extraction of light from the gain medium due to enhanced electromagnetic field confinement and increased photon-exciton coupling.

3.2 Optical characterization of plasmonic metasurfaces

For experimental transmission measurements, the sample is rotated automatically by a software designed to vary the illumination angle (θ) from 0° to 35° with a resolution of 0.1° (**Figure 3.4**). Additionally, the mounted sample is placed vertically and aligned along the high symmetry direction of the clusters on a custom-made sample holder, allowing to control the azimuthal angle (φ) alignment within ±3°. This customized setup was utilized for all transmittance measurements (calculated as $\%T = I/I_0$, where I and I_0 are the intensity of the incident and transmitted light respectively) throughout the thesis.

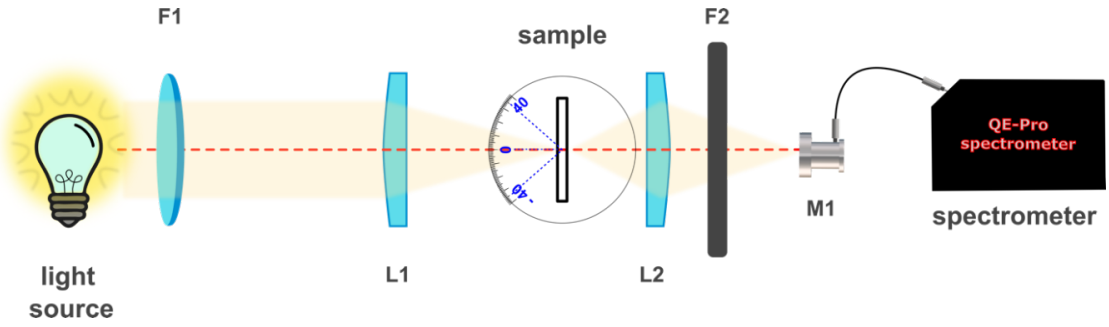

Figure 3.4 **Optical set up for transmission measurements**. F1 represent the response-flattening filter used to improve the non-uniform response of white light lamp, resulting in a shaped responsivity curve; L1, L2 are the achromatic doublet lenses with focal length *f* = 100.00 mm and *f* = 50.00 mm respectively; F2 is the density filter used to avoid the detector saturation; M1 is the reflective collimator based on a 90° off-axis parabolic mirror with a protected silver coating, for high reflectivity in the 450 nm to 20 μm wavelength range.

The spectral position of the Rayleigh-Wood anomalies of square gratings can be predicted by solving the equation:

$$1 - \left[\left(\frac{m\lambda_{RW}}{n_{eff}\Lambda} - \frac{n_{air}}{n_{eff}} sin\theta_{inc} cos\varphi_{inc}\right)^2 + \left(\frac{l\lambda_{RW}}{n_{eff}\Lambda} - \frac{n_{air}}{n_{eff}} sin\theta_{inc} sin\varphi_{inc}\right)^2\right] = 0 \quad \textbf{(3.3)}$$

where Λ represents the lattice period, n_{eff} the effective refractive index, θ the illumination angle with respect to the normal direction, φ is the incident azimuthal angle, and *m* and *l* are integers indicating the diffraction orders. The 0th-order transmission of the designed photonic grating is subjected to Snell's law.

However, as discussed in **Chapter 1**, the spectral position of the R-W anomalies of the square grating can be approximated to:

$$\lambda_{RW} = \frac{\Lambda_{x,y}}{\sqrt{m^2+l^2}} \cdot \left(n_{eff} \pm sin\theta\right) \qquad \textbf{(3.4)}$$

In **Figure 3.5** is reported the morphological and optical characterization of the completed devices, fabricated as discussed in **Paragraph 2.4.1**.

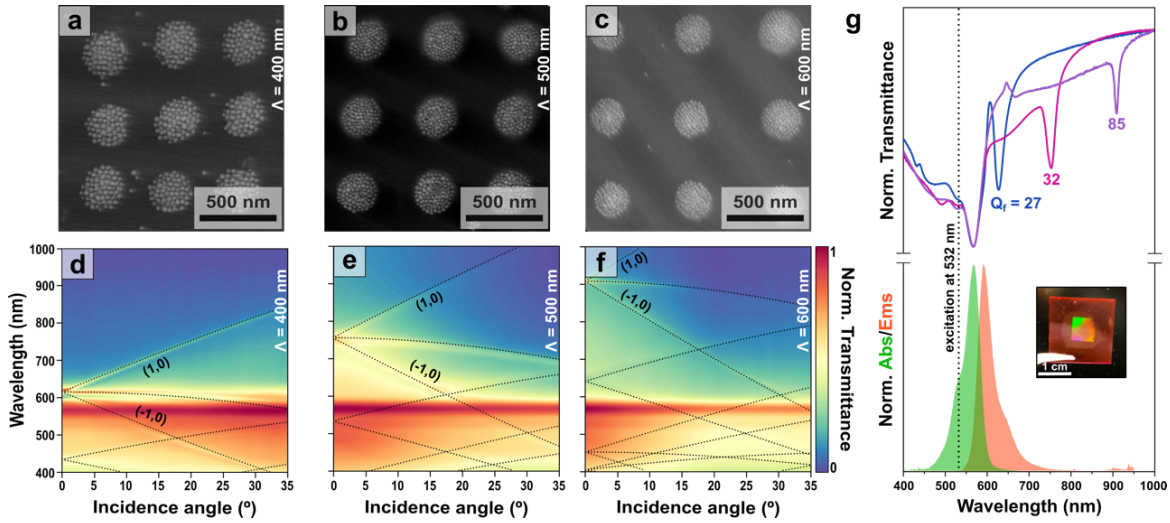

Figure 3.5 **Morphological and optical characterization**. (**a**-**c**) Scanning Electron Microscopy (*SEM*) images of the arrays with lattice period Λ = 400, 500, 600 nm. (**d**-**f**) The intensity maps (contour plots) display the dependence λ(θ) of the lattice resonances and are scaled to same value range to facilitate the comparison between three lattice parameters. The **black dashed** lines represent the simulated diffraction orders predicted using equation 3.4. (**g**-**top**) Normalized transmittance spectra at normal incidence of the array with lattice parameter 400 nm (**blue**), 500 nm (**pink**), 600 nm (**purple**) compared with (**g**-**bottom**) the absorption (**green**) and emission (**orange**) of the Rhodamine B in SU8 (sample pictured in the **inset**).

SLRs positioned at 627, 752 and 909 nm are observed in plasmonic arrays fabricated with increasing Λ values from 400 to 500 and 600 nm (**Figure 3.5 g**). In addition, the presence of RhB within the SU8 layer is indicated by the transmission dip at 565 nm, in line with the absorption band of the dye. The combination of highly uniform plasmonic substrates and the presence of the thin SU8 layer leads to narrow SLRs,[11] with Q_f as high as 85 for the sample with Λ = 600 nm. A higher Q_f indicates a narrower peak, a longer resonance lifetime, and, consequently, lower energy loss per cycle of oscillation. Different aspects can contribute to this increase such as higher mode stability, a reduced coupling and consequent decrease of radiative losses as the distance between adjacent units increases, and a decrease in non-radiative decay pathways, such as energy transfer to surrounding species.

The local plasmon band associated with the AgNPs cluster remains blue-shifted with respect to the 0th-order, and the effect of variation in the structure, such as the number of particles per

clusters, on the collective optical response of the arrays is expected to be minimal (**Figure 3.6 a**).

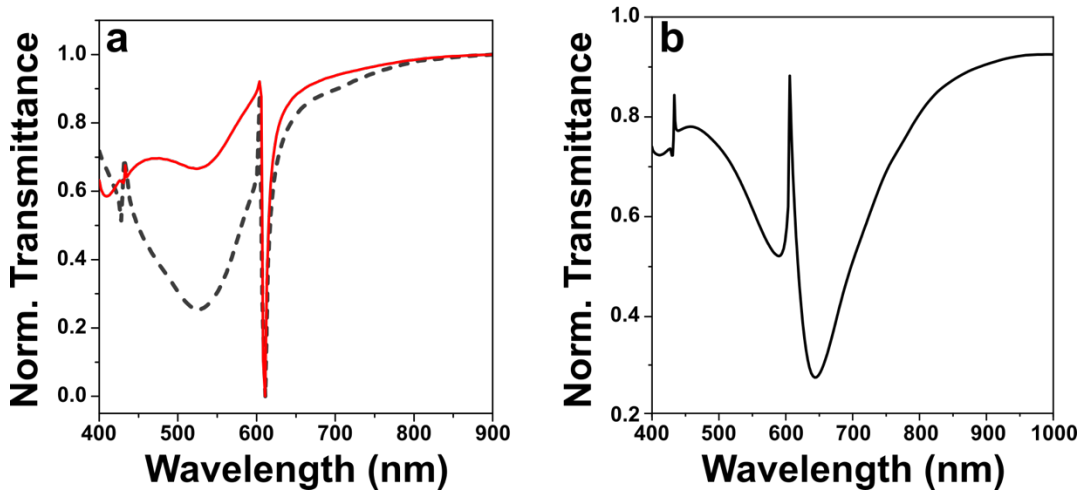

Figure 3.6 Simulated transmission spectra of an array with lattice period of 400 nm. (**a**) AgNPs (with 23 nm diameter) cluster distributed into 1 (**black dashed** line) and 5 (**red solid** line) layers; (**b**) AgNPs with 50 nm diameter monolayer cluster.

It is important to stress that, as reported in a previous study, the use of bigger NPs would increase the near-field coupling effects, having a negative impact on the quality factor of the lattice resonances,[12] as shown by simulation in **Figure 3.6 b**.

The absence of annealing or further index matching steps underlines the potential of colloidal plasmonic-based metasurfaces to explore new avenues for post-assembly modifications of the optical cavity, including ligand exchanges, colloidal overgrowth steps and dynamic chemical interactions with the surrounding media. All these possibilities are normally precluded by the presence of an index-matching layer that is needed for the collective resonant response to emerge.

To showcase the dispersive nature of the SLRs, transmission measurements were conducted at different incidence angles (**Figure 3.5 d-f**) ranging from 0° to 35° (angular resolution of 0.1°) using the custom-built optical setup described above. This allows the diffraction orders to be observed in their interaction with the angularly invariant plasmon band (around 450 nm) associated to the AgNP cluster.[7]

As mentioned in the previous paragraph, due to the relatively small refractive index mismatch between the SU8 layer (n = 1.6) and the underlying glass coverslip (n = 1.52), the hybrid waveguided-SLR modes (TE and TM) result spectrally close. Also, the low coherence of our light source hinders the clear distinction of the modes in experimental transmittance measurements. Consequently, we expected the hybrid modes to appear experimentally as a single narrow dip in the spectrum, whose position can be predicted using basic Bragg conditions (for square gratings is valid **Eq. 3.4**) and employing an effective refractive index that considers both glass and SU8. The remarkable agreement observed between the measured and predicted behavior of the SLRs provides strong confirmation of the low optical losses within our systems.[13]

For all lattice cases, SLRs related to the first diffraction order exhibit two degenerate lateral branches, denoted by the (1,0), which red shifts for higher illumination angles, and the (-1,0) order, which blue shifts instead. The contour plots in **Figure 3.5 d, e, f** also reveal the existence of other degenerate branches at higher frequencies, corresponding to higher order diffraction lines. The detection of these higher diffraction orders serves as further confirmation of the large uniformity of the assembled arrays.

Our experimental results were also confirmed by numerical simulation. The periodicity of the lattice gives rise to SLR dispersion energies, that are periodic in k-space.[14]

To understand the electronic band structure and determining the properties of materials, including their electronic, optical, and mechanical behavior, for each of the three lattice parameters arrays employed in this study, a band diagram was simulated to visualize all available photonic and plasmonic modes within the first Brillouin zone. These simulations depict the energy levels of electrons (eV) as function of the momentum E($k_{//}$) in the reciprocal space, considering a periodic cluster array over an SU8 layer 250 nm thick in presence of RhB, as schematized in **Figure 3.7 a**.

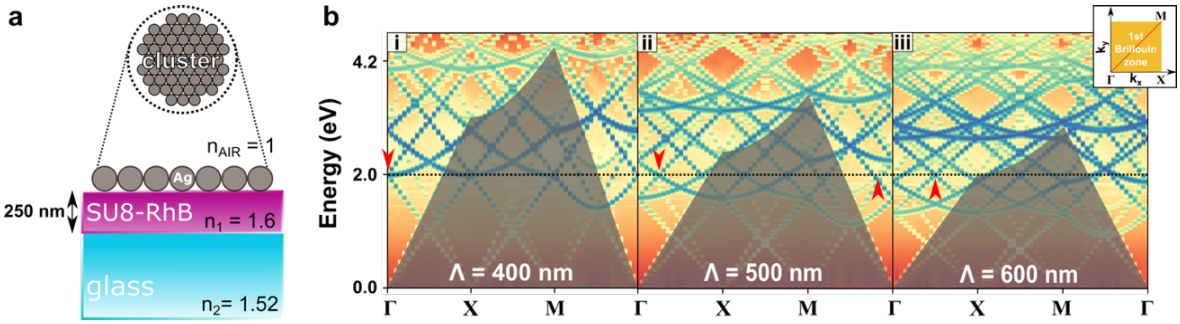

Figure 3.7 **Simulated band diagrams.** The diagrams of the three lattice parameters show large photonic density of states *i.e.* all possible energy states (or bands) for the electrons within the material as function of in-plane wavevector $k_{//}$ of the incident light. The **grey shadowed** area delimitates the light cones dispersion $\omega = c \cdot |k_{//}|$. Horizontal dotted lines represent the maximum of the dye emission (around 600 nm), and the red arrows indicate the crossing-points between the diffractive modes and the dye emission, where the lasing activity is then registered.

Similar angular displacements of the experiment (contour plots in **Figure 3.5 d-f**), in terms of wavelength vs illumination angle, is observed in the simulation displayed as energy *vs* in-plane wavevector $k_{//}$ in the band diagram, based on the relations $E = h \cdot c/\lambda$ and $k_{//} = (2\pi/\lambda) \cdot \sin\theta$.

To visualize these systems, it is necessary to consider that incident waves impinging upon the lattice at certain high-symmetry points, they undergo constructive interference with the waves scattered by adjacent lattice planes. This constructive interference leads to the formation of energy states known as "band-edge" states, representing transition regions formed between different electronic bands in a material, such as the valence and conductive bands. Bragg scattering occurring at high-symmetry points within the Brillouin zone results in the creation of band-edge states distinguished by a high photonic density of states. These states can be used to mediate interactions between surface lattice resonances (SLRs) and quantum emitters.[15]

Diffractive features representing both TE and TM polarizations are shown in **blue**, in contrast to other sources of optical losses (RhB and AgNPs absorption) contributing to **light-yellow** background. Only the modes lying outside the light line region (**grey shaded** area) are considered able to coupling in the far-field resulting not confined to the array plane.[16]

The ideal conditions for compensating optical losses are identified by the crossing points between these modes, where the promotion of a laser emission should be facilitated.

In the case of Λ = 400 nm, 1st-order R-W anomaly (crossing point indicated by the **red** arrow in **Figure 3.7 b-i**) with four-fold degeneracy can be distinguished at $k_{//} = 0$, in correspondence to the high symmetry point (Γ), representing the center of the first Brillouin zone. These resonant modes arising around 620 nm (or 2.0 eV) are responsible of facilitating the outcoupling of the light into the far-field. As we will see in the next chapter of this thesis, this will ultimately be responsible for lowering the lasing emission threshold along the normal direction.

For Λ = 500 and 600 nm cases, the crossing points in the band diagram can be distinguished as being off-normal ($k_{//} > 0$) to the lattice plane (**red** arrows in **Figure 3.7 b-ii** and **b-iii**), located along the Γ-X direction and the M-Γ direction respectively. Indeed, the low threshold lasing emission found for these two cases was detected along off-normal directions, as discussed in the following **Chapter 4**.

To illustrate discrete shifts in wavevector values within the (*xy*) plane, due to the presence of the plasmonic cluster array behaving like a diffractive grating, k-space circles diagrams where simulated to depict the distribution of in-plane modes coupled with the light able to scatter into free space. Here, the center of the circle represents the origin (zero wavevector), and the circumference corresponds to the maximum value of wavevector within the specific range of angles.

$$\boldsymbol{k}_{out,xy} = \boldsymbol{k}_{in,xy} + \frac{2\pi M}{\Lambda}\hat{x} + \frac{2\pi M}{\Lambda}\hat{y} \qquad \textbf{(3.5)}$$

$\boldsymbol{k}_{out,xy}$ represents the resulting wavevector after interaction with the medium; the incident wavevector depends on the refractive index of the medium as $\boldsymbol{k}_{in,xy} = 2\pi n/\lambda_0$, while $k_0 = 2\pi/\lambda_0$ represents the magnitude of the free-space or vacuum wavevector, and λ_0 is the light wavelength in vacuum. The wavevector in the medium has components $k_x = nk_0 \sin\theta\cos\phi$, $k_y = nk_0 \sin\theta\sin\phi$, and $k_z = \sqrt{(k_0^2 - k_x^2 - k_y^2)}$, where θ is the polar angle, φ is the azimuthal angle, n is the medium refractive index, and Λ is lattice period. Finally, the light line (**black** circle in **Figure 3.8 a**, **c**) is centered at the coordinates $x_c = 0$, $y_c = 0$ and has a radius $R = k_0$. For higher orders,

the circles with radius R = nk_0 have center coordinates $x_c = M \cdot \Lambda$ and $y_c = N \cdot \Lambda$, where M, N = …-2,-1,0,1,2 … represents the diffractive mode order.

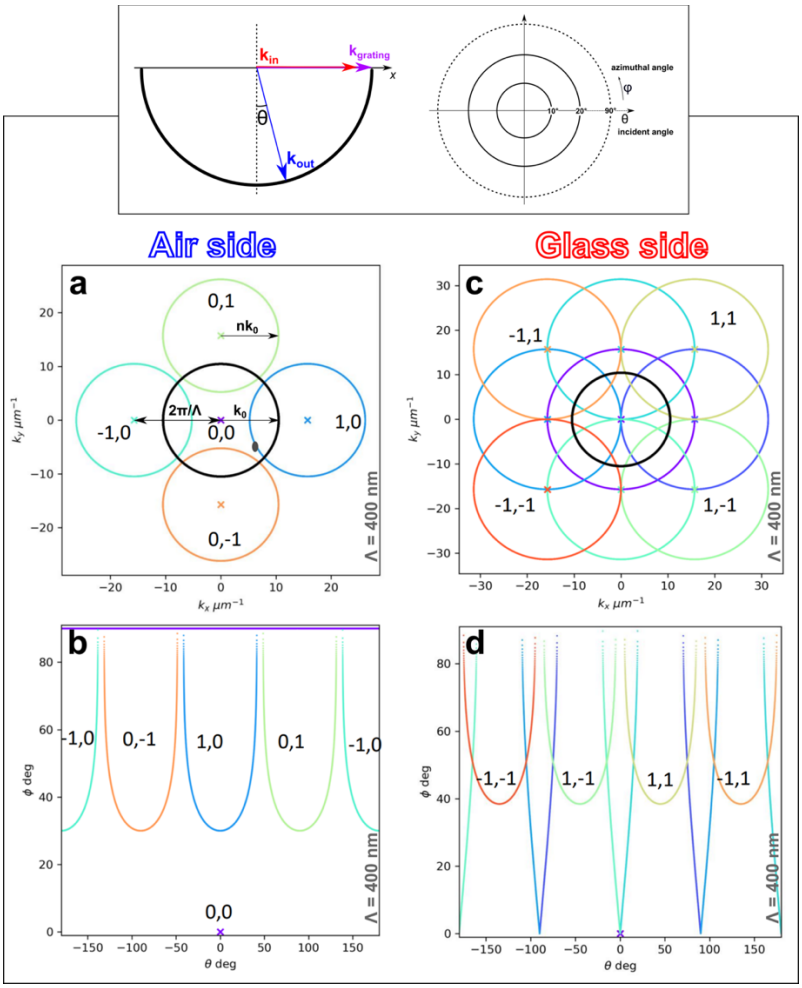

Figure 3.8 **k-space diagram**. (**a**, **c**) The circles represent the diffractive modes, and the center (x_c, y_c) represents where the maxima light extraction can be achieved. Considering the horizontal direction (x) where the polar angle q = 0°, by changing the azimuthal (φ) is possible to evaluate the light extracted along the direction deviated from the normal. The simulations include the cavity modes available by extracting light from the air side (**b**) and glass side (**d**) in function of the polar and the azimuthal angles.

In particular, we focused our attention on two extreme cases: the first considers that all the incoming light is aligned along the grating plane (*xy*) at a certain frequency, and thus all the light contributes to the appearance of a R-W anomaly, which for a given frequency forms circles of radius k_0; the second case takes into accounts the incident light propagating along the normal direction to the surface ($\hat{z}$). The crossing points in the center of circles, spaced by a quantity $2\pi/\Lambda$, represent the points in the reciprocal k-space where the light extraction is expected to be

maximum. Thus, all the detectable modes must fall inside the light line (**black** circle in **Figure 3.8 a**, **c**). In the case Λ = 400 nm, considering to extract light from the air side, **Figure 3.8 a**, **b** illustrate the absence of detectable modes (here the light line coincides with the 0^{th} of R-W anomaly order). Conversely, by extracting light from the glass side, is possible to observe the presence of diffractive modes, identified by crosses at 0° of θ, which enables efficient light outcoupling (**Figure 3.8 d**).

3.2.1 Exploring plasmonic metasurfaces for NL optics

Motivated by the sharp SLRs obtained in the previous work, we set out to investigate nonlinear optical processes, evaluating the suitability and efficiency of our structures for such applications. Recognizing the demanding nature of these phenomena, which often necessitate high pump power sources, we selected gain media renowned for their high quantum yields and exceptional photostability.

Colloidal quantum dots have become a cornerstone of recent scientific research of the last 10 years, revolutionizing fields ranging from optoelectronics to biomedical imaging. Due to their remarkable properties, including tunable emission spectra, high quantum efficiency, and exceptional photostability, quantum dots play a pivotal role in advancing in quantum phenomena and offer unprecedented opportunities for innovation and discovery across various disciplines, which recently resulted in the Nobel Prize in Chemistry 2023 being assigned for their discovery.

However, particularly for room temperature applications, colloidal QDs experience a significant degradation in optical coherence, which affects their ability to emit light, primarily due to phonon scattering and fluctuations in the spin states (spin noise) of the electrons. The consequence of this de-coherence is that despite being bright single-photon sources,[17,18] individual colloidal QDs remain not efficient enough for applications in information-based technology.[19] One way that can be used to increase the QD emission efficiency, is to couple

them with photonic and plasmonic cavities to exploit their long propagation length and delocalized nature of surface lattice resonances. In fact, when the intrinsic optical losses of plasmonic systems are mitigated by the emergence of plasmonic lattice resonances, as discussed previously, it is possible to induce coupling with the energy states of the QDs to generate strong light-matter interactions, directional emission, and to promote lasing emission from high-density emitter configurations.[20,21]

During my research stay in the group of Prof. N. Chiang at the University of Houston, I have coupled the colloidal silver nanocluster metasurface to a layer of core-shell QDs (CdSe/ZnS stabilized with octadecylamine ligand) spin coated onto a layer of SU8 photoresist (see **Paragraph 2.4.1** of **Chapter 2**). This architecture was used to promote two-photon emission processes, introduced in **Chapter 1**.

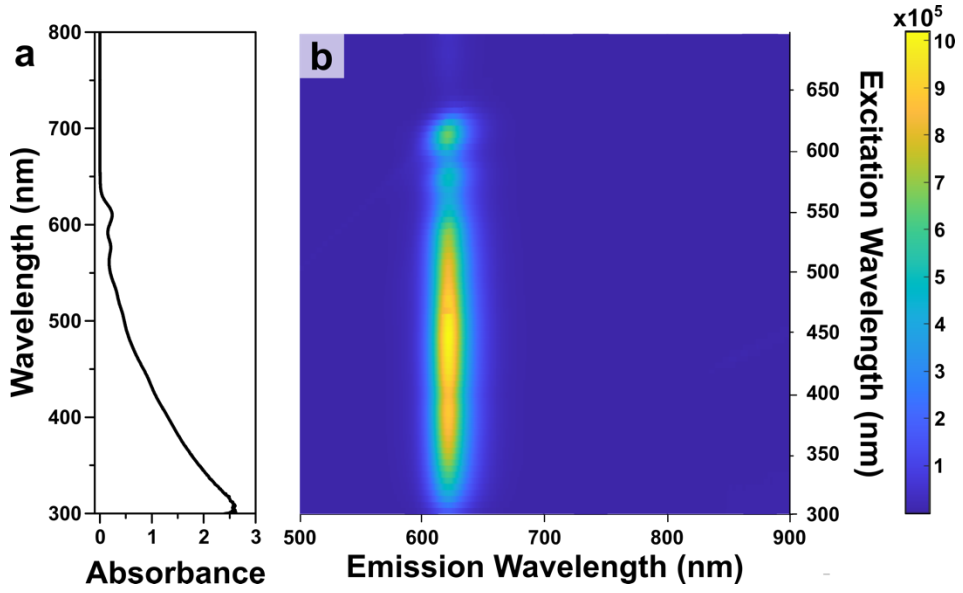

Figure 3.9 UV-Vis and fluorescence analysis of CdSe/ZnS QDs in solution dispersed in Toluene [0.1M].

This core-shell QDs show a broad absorption band ranging from the UV (around 300 nm) to the Vis spectral range (around 620 nm). The lattice period of 400 nm was used for preparing this plasmonic metasurface, and it was chosen in order to ensure the overlap of the SLR with the emission of the QDs at 610 nm. The transmission spectra for the SLRs and LSPRs arising

from the samples fabricated and illustrated in **Paragraph 2.4.1** of **Chapter 2**, were achieved with same customized optical set up and they are illustrated in **Figure 3.10**.

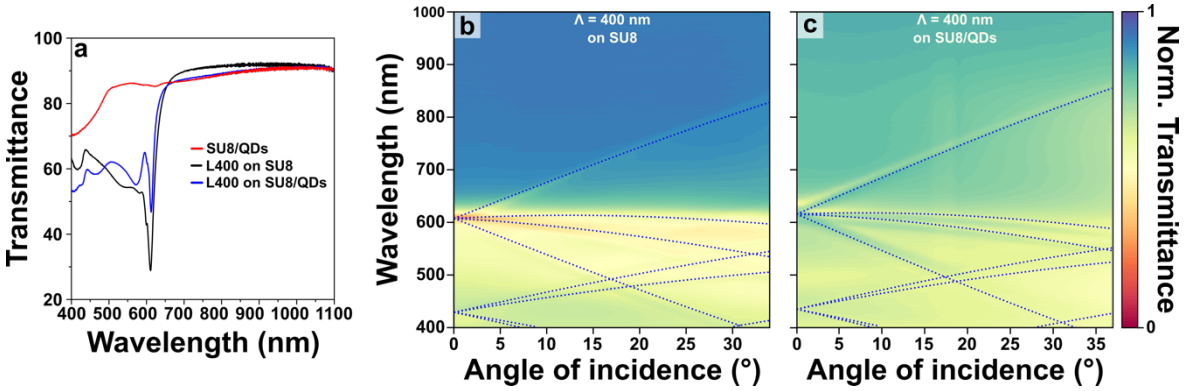

Figure 3.10 (**a**) Transmittance spectra of a AgNPs array on top of a QDs layer. (**b**-**c**) Contour plots showing the angular dependence of the diffractive grating assembled on top of (**b**) SU8 alone, and (**c**) SU8/QDs layer, from the illumination angle. The **black dashed** lines represent the simulated diffraction orders predicted using equation 3.4. The degeneracy of the first diffraction order, visible with the appearance of 4 branches, is due to misalignment of the sample azimuthal angle respect the illumination.

The presence of the plasmonic array strongly modulate the optical properties of the system, as emerges by comparing the normal incidence transmission of the sample without array (**red** curve in **Figure 3.10 a**), and with array (**blue** and **black** curve in **Figure 3.10 a**). A clear lattice mode appears in the cases where the plasmonic grating is present at around 611 nm. The increased intensity of the localized plasmonic response in the UV region of the spectra, and some spectral difference between the samples with (**black** curve) and without (**blue** curve) quantum dots layer, can be attributed to a difference in the spots investigated and a more irregular surface on which the assembly is performed due to the presence of the QDs. The Contour plots in **Figure 3.10 b**, **c** show the clear dependence from the illumination angle for both the samples (with and without quantum dots), confirming that the adapted open-cavity architecture works, and the optical response is only partially affected by the presence of the QDs layer.

3.2.3 Optical characterization of *in situ* growth plasmonic array

As described in **Paragraph 2.5** of **Chapter 2**, the *in situ* growth method developed in this thesis overcomes two significant challenges: the need for time-consuming self-assembly steps and excess of reagents generally used for batch synthesis.

Optical transmission experiments were conducted to evaluate the lattice plasmon resonances arising from *in situ* growth arrays successfully achieved with lattice period of 400, 500, and 600 nm (fabricated as depicted in **Figure 2.17** of **Chapter 2**). In this case, the absence of any waveguided mode requires the application of a superlayer in order to create a uniform dielectric environment around the plasmonic metasurface. This was achieved applying a thin layer of PDMS to cover the particles after growth is completed. Under refractive index match conditions, all the transmission profile displays sharp lattice plasmon resonances.

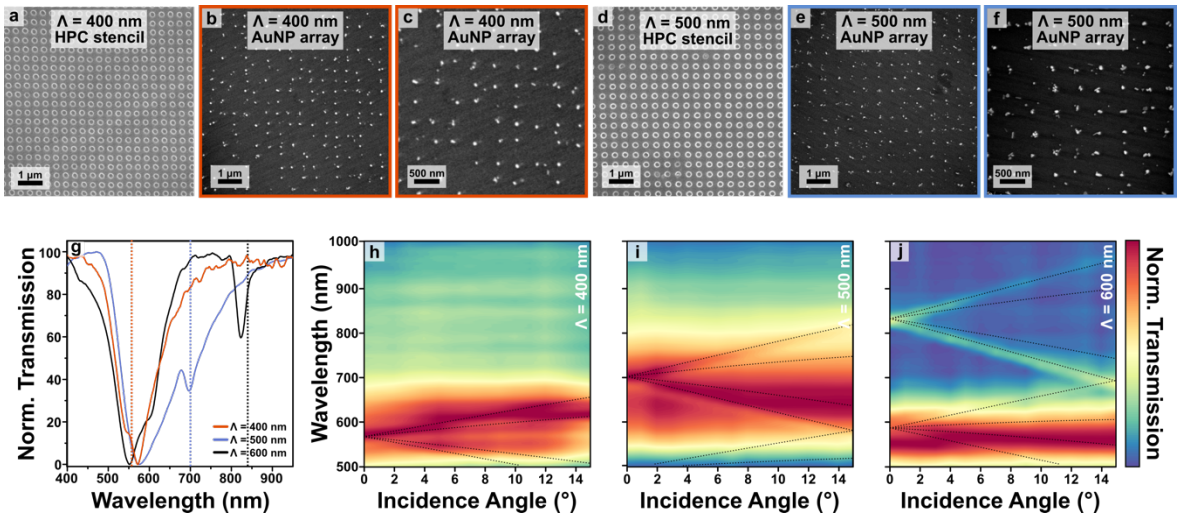

Figure 3.11 SEM images of (**a**) the patterned hydroxypropyl cellulose (HPC) films with lattice parameter Λ = 400 nm, (**b**, **c**) the resulting patterned nanoparticle substrates, (**d**) HPC stencil with Λ = 500 nm, (**e**, **f**) corresponding patterned nanoparticles array with Λ = 500 nm. (**g**) Smoothed and normalized transmission spectra of the substrates following refractive index matching. The **dashed** lines represent the predicted position of R-W anomalies by using **Eq. 3.4**, considering the refractive index of the index matching layer (n_{PDMS}=1.45). (**h**-**j**) Contour plots showing the illumination angle dependence of the SLR wavelength for (**h**) Λ = 400 nm, (**i**) Λ = 500 nm, and (**j**) Λ = 600 nm lattices. The **dashed** lines are the predicted positions of the R-W anomalies.

These results represent the first demonstration of lattice plasmon resonances arising from metasurfaces fabricated *via* a purely *in situ* synthetic route, without the need for batch synthesis,

self-assembly, top-down fabrication, or expensive and specialized equipments.[22] Depending on the lattice parameters used to fabricate the HPC masks, the wavelengths associated with lattice plasmon resonances are expected to vary (**Figure 3.11 g**), with the most intense SLRs are expected to occur near the first-order diffraction line.[23]

At normal incidence, the predicted wavelengths correspond to 560 nm for Λ = 400 nm, 700 nm for Λ = 500 nm, and 840 nm for Λ = 600 nm.

For the lattice of 400 nm, the predicted lattice plasmon resonance overlaps the LSPR band of the AuNPs, identified as a shoulder at 560 nm in the transmission spectrum. In the case of 500 nm, a dip is observed at 698 nm, while for the lattice period of 600 nm, the lattice resonance emerges at 826 nm, both in good agreement with the predictions (**Figure 3.11 g**).

The discrepancies observed between the experiment and predicted positions, can be attributed to various factors, such as the effects of the surfactant coating of AuNPs and/or variations in the PDMS refractive index due to differences in composition and curing conditions.[24] The contour plots in **Figure 3.11 h-j** display the spectral angular distribution of the lattice resonances, studied by changing the illumination angle from 0 to 15°. The appearance of a second order diffraction line (**Figure 3.11 j**) confirms the higher quality of the Λ = 600 nm array. Moreover, the quality factor $Q_f = \omega/\Delta\omega$ was evaluated for the experimental SLRs and results equal to 29 for Λ = 600 nm, and 21 for Λ = 500 nm.In the case of the Λ = 400 nm array, it wasn't possible to estimate the Q_f due to the blue-shifted diffraction line relative to the lattice resonance peak, resulting in an asymmetric Fano profile.

The Q_f associated to single-nanoparticle arraysfabricated from colloidal suspensions generally ranges between 10 and 40. Consequently, despite a patterning yield of around 80% (**Table 3.2** in **Chapter 2**), our array performance is comparable to state-of-the-art methods based on single-particle assembly.[10,12] Manjavacas and co-workers have conducted some theoretical studies suggesting that by reducing the dimension of the repeating unit below to 100 nm, it is possible

to achieve narrower lattice resonances and how this effect is even more pronounced for realistic systems (*i.e.,* a limited array size).[13]

These results suggest that the reduced dimensions of our *in situ* grown nanoparticles, together with the lack of optical losses attributed to strong near-field coupling within the repeating unit (as observed in cluster plasmonic arrays), can explain the presence of relatively sharp lattice resonances despite the existence of defects.

The demonstration of SLRs by bottom-up *in situ* substrate growth underscores its potential as a simple and readily accessible route to plasmonic materials engineering, even though the fabricated arrays exhibit less uniformity than those fabricated by state-of-the-art top-down[25] or colloidal synthesis/self-assembly methods.[26]

3.3 Chiral plasmonic metasurfaces

Symmetries, which govern electronic structures, crystallographic arrangements, chemical bonding and more, underlie the properties of almost every physical system.[27]

Chirality, for instance, is a fundamental property linked to the handedness of a structure that does not present mirror planes or inversion symmetry, and it is valid for diverse natural systems at different length scales, from enantiomeric molecules to chiral asymmetries observed in biological structures at the micro-organism level.[28]

The chirality of a medium, can be optically revealed comparing the interaction with right- or left- circularly polarized light (RCP and LCP), representing the "*chiral state*" of light. When light with different polarizations interacts with a chiral medium, it experiences a variation in the complex refractive indices reflected in how the medium refracts, absorbs, and transmits light.[29] This gives rise to a difference in absorption of RCP and LCP light, a phenomenon known as circular dichroism (CD). Another related optical phenomenon is the optical rotatory dispersion (ORD), when linearly polarized light passing through a chiral medium undergoes rotation relative to its initial orientation. This phenomenon can be understood by considering that a

linearly polarized light field comprises a combination of LCP and RCP light components. As such, a difference in the real part of the refractive index leads to a phase mismatch between the two perpendicular polarizations. As a result, the plane of polarization is rotated and a difference in the absorption of the linearly polarized light occurs, respect to parallel or perpendicular orientation, along the propagation axis.[30]

Chiral plasmonic metasurfaces can be finely tuned at the nanoscale to surpass the chiroptical capabilities of natural systems,[31] offering unique optical features such as selective polarization control and efficient circular dichroism. By integrating chiral elements into metasurface designs, it becomes feasible to manipulate light propagation, control its spin angular momentum, and tailor optical responses over a wide spectral range, opening the way for advanced application in photonic, sensing, bioimaging. For example, optical chirality detection could play a key role in understanding DNA function and various biological processes, supporting drug design and clinical biomarker identification, such as D-amino acid enantiomers associated with neurodegenerative diseases. Furthermore, a recent shift in quantum information processing involves exploiting the chiral light-matter coupling for transmission, manipulation, and storage of information. However, existing fabrication methods struggle to simultaneously enhance and tune both chirality and resonances Q-factor, limiting their versatility and effectiveness in advanced photonics applications.

We can distinguish two types of chiral metamaterials. Intrinsic chiral metamaterials are identified by their constitutive elements displaying geometric chirality.[32,33] These materials can often be tailored to demonstrate optically intrinsic electromagnetic behavior, particularly a chiral response at normal incidence.[30]

In contrast to intrinsic metamaterials, extrinsic chiral metamaterials consist of geometric units that are geometrically achiral or homogeneous.[34,35] The extrinsic chiral activity arises from the interaction of the metamaterial with its environment. Typically, this interaction is achieved by symmetry breaking induced by another material or by interaction with light at off-normal

incidence angles.[36,37] One limitation of extrinsically chiral metamaterials is that the magnitude of the extrinsic chiroptical response tends to diminish at normal incidence and change sign when the angle of incidence is varied. Nevertheless, the magnitude of the chiroptical response typically increases for large off-normal angles of the incidence light, allowing geometrically achiral structures to generate a pronounced chiral response, due to altered phase relationships and wavefront distortions.

Chiral plasmonic metasurfaces represent a category of 2D metamaterials carefully designed at the nanoscale to induce enhanced chiral optical behavior.[38–40] Metasurface with chiroptical activity have shown potential as a versatile platform for advanced optical applications such as negative refraction, super-resolution imaging and invisibility cloaking.[41,42]

In this work, we have used plasmonic chiral metasurfaces to enhance the photoluminescence of a common dye, which revealed the capability of the lattice resonance, arising from achiral plasmonic units (AgNPs spheres) patterned in well-known chiral shapes Gammadion (Γ), to transfer the chiroptical behavior to the emission of achiral dye molecules (Rhodamine B).

3.3.1 Optical characterization of chiral plasmonic metasurfaces

Circularly polarized luminescent (CPL) materials have recently emerged as hot topic for scientific research, offering significant advances in various technological applications, including optical data storage, displays and quantum communication.[43]

Despite numerous strategies have been proposed for assembled materials[44] comprising inorganic, organic, and hybrid systems, within chiral orientationally ordered structure such as chiral liquid crystals[45] and polymers,[46] achieving prronounced and controllable circularly polarized light emission remains a challenge.

In this project we used achiral plasmonic building blocks (spherical AgNPs) self-assembled into chiral arrays (left (L-), right (R-), and racemic or mixed (M-) Gammadions to induce chiral

luminescence from molecular emitters placed in proximity of the chiral metasurface (the fabrication details were discussed in **Paragraph 2.4.1** of **Chapter 2**).

In non-scattering samples, variations in transmittance for each circular polarization of light will depend only on molecular absorption within the materials, since reflection and scattering processes are negligible. This gives rise to the well-known phenomenon of circular dichroism (CD) defined as:[47]

$$\mathrm{CD} = \alpha_{LCP} - \alpha_{RCP} \qquad \textbf{(3.6)}$$

where α_{LCP}, and α_{RCP} represent the absorption of left- and right- handedness respectively.

The CD is evaluated as the differential transmittance (1-T) passing through the sample, and the magnitude of this process is typically expressed by a quantity known as g-factor:[48]

$$g - factor = \frac{\alpha_{LCP} - \alpha_{RCP}}{1/2(\alpha_{LCP} + \alpha_{RCP})} \qquad \textbf{(3.7)}$$

However, in the scenario where periodic arrays act as scattering centers, the conventional definitions tend to underestimate the observed differences in transmission spectra for incident left- and right- circularly polarized light (LCP and RCP respectively). Absorption alone is not sufficient to quantify CD when circularly polarized light, generated by a linear polarizer set at ±45° respect to the fast axis of a quarter-wave plate, encounters a chiral metasurface. This is due to the additional effect of light scattering process,[49] which deflects the light away from the propagation axis, resulting in differences in the transmitted signals.

Thus, considering a metasurface able to scatter one circular polarization out of the propagation axis without absorbing its energy, a measurable differential transmittance in the normal direction persists, which can still be considered as CD:[50]

$$\mathrm{CD} = T_{LCP} - T_{RCP} \qquad \textbf{(3.8)}$$

Experimentally, the magnitude of the process is quantified by the *dissymmetry factor* (g), which takes into account the CD normalized over the transmission of unpolarized light (T_{up}) as:

$$g = \frac{\Delta T}{1/2(T_{up})} = \frac{T_{LCP} - T_{RCP}}{1/2(T_{up})} \qquad (3.9)$$

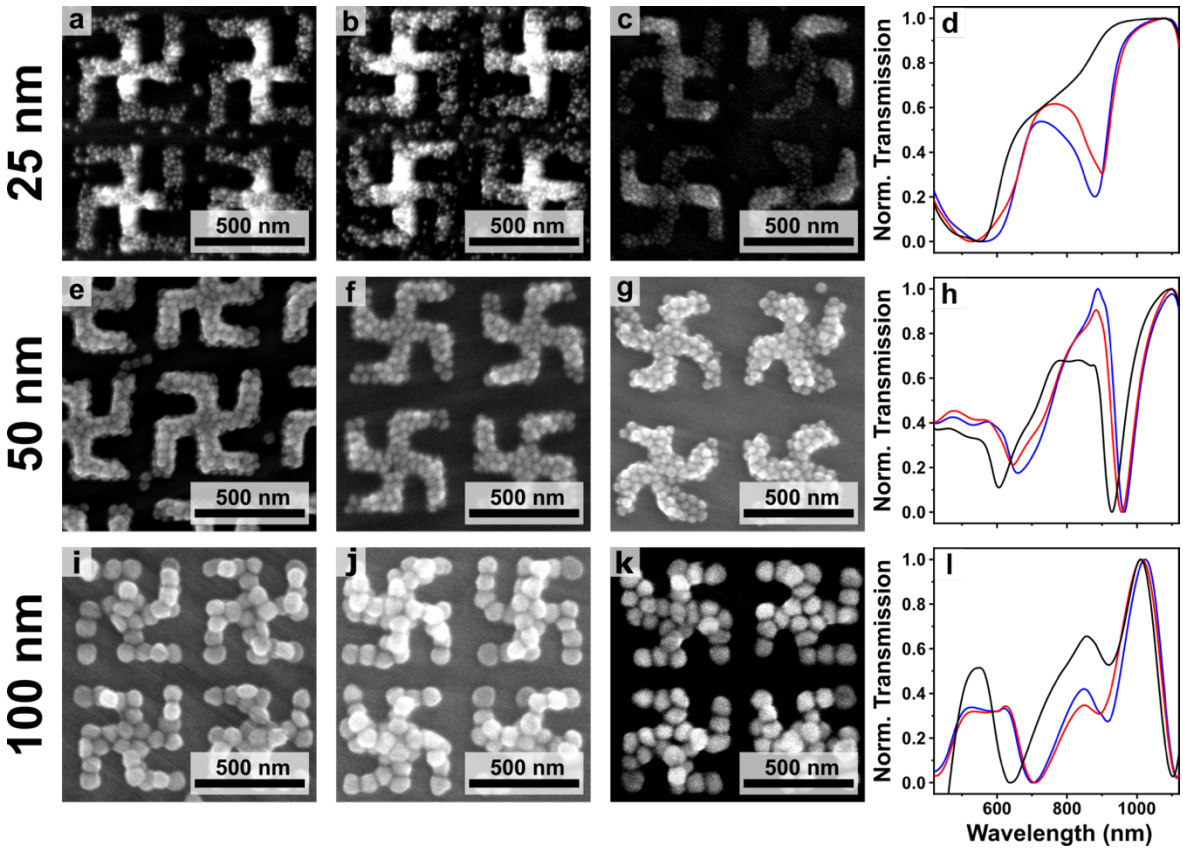

Figure 3.12 **Morphological and Optical characterization of the Γ-metasurfaces**. (**a**) left-, (**b**) right-, and (**c**) mixed- (racemic) handedness structure of 25 nm AgNPs assembly. (**d**) Transmittance spectrum of 25 nm NPs with unpolarized white light. The peak represents the position of the SLR for right (**red**) at 900 nm and racemic (**blue**) at 880 nm Gammadion. The left Gammadion (**black** curve) do not show the emergence of a SLR. (**e**) left-, (**f**) right-, and (**g**) mixed- (racemic) handness structure of 50 nm AgNPs assembly. (**h**) Transmittance spectrum of 50 nm NPs for left (**black**), right (**red**) and racemic (**blue**) Gammadion. The peak represents the position of the SLR for left (**black**) at 926 nm, right (**red**) at 960 nm, and racemic (**blue**) at 966 nm Gammadion. (**i**) left, (**j**) right, and (**k**) mixed (racemic) handedness structure of 100 nm AgNPs assembly. (**l**) Transmittance spectrum of 100 nm NPs. The peak around 1100 nm represents the position of the SLR for left (**black**), right (**red**) and racemic (**blue**) Gammadion.

The four-fold rotational symmetry (C4 symmetry) of the Γ-geometry imply that an object remains invariant under rotations of 90°. In terms of linear polarization of light, this means that the optical properties, including the polarization state, remain unchanged after the object undergoes such rotations. Thus, the linear polarization contribute to the dissymmetry factor is negligible and pure circular polarization can be considered. First, the metasurfaces were optically

characterized with white light to evaluate the position of the lattice resonances arising from the Γ-structures (**Figure 3.12 d, h, l**), as done for the squared array samples (see **Paragraph 3.2**). The angular characterization revealed the diffractive nature of the observed peak, leading to categorizing them as SLR (**Figure 3.13**).

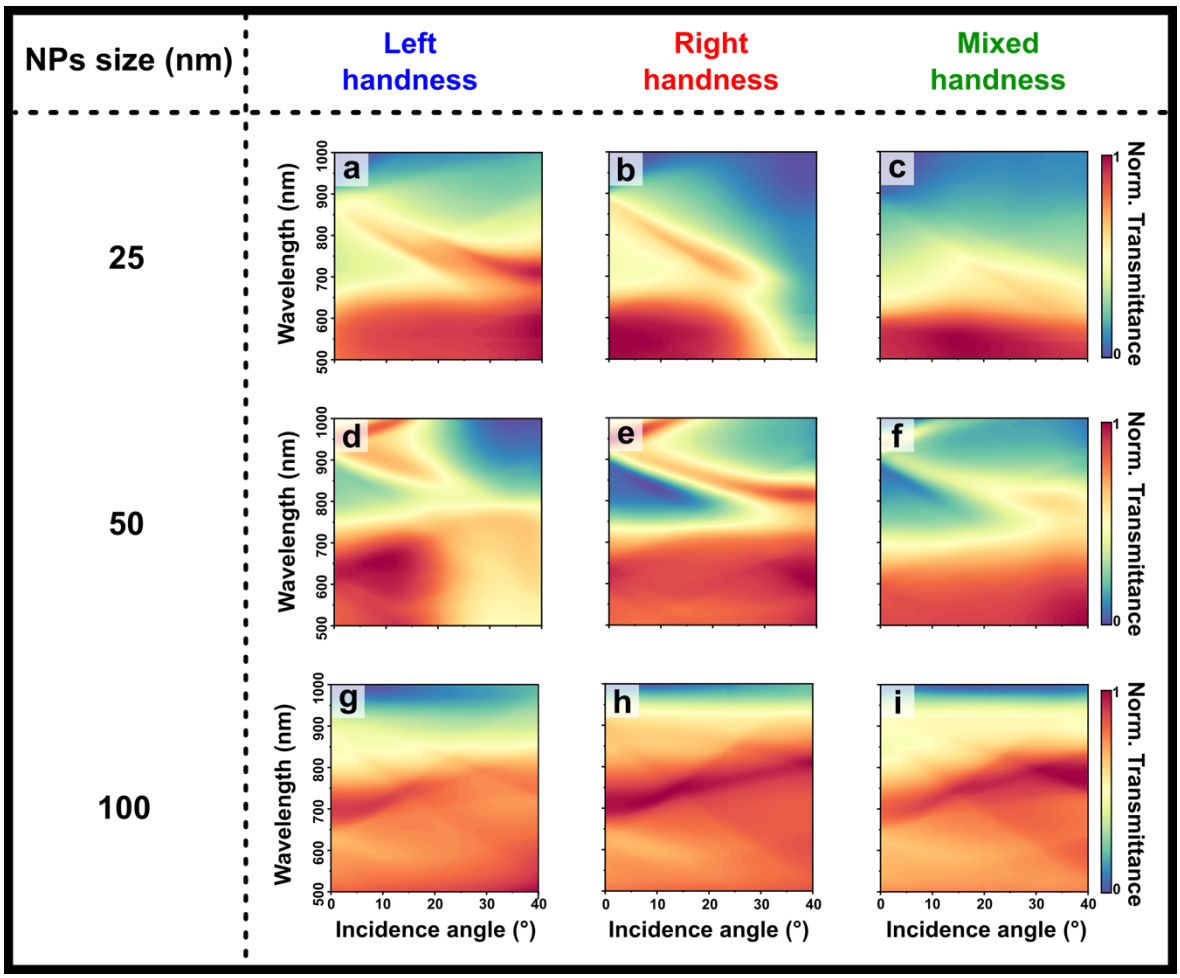

Figure 3.13 Contour plots of SLRs arising from the chiral metasurfaces. The intensity maps show the wavelength position dependence of the lattice resonances as function of the illumination.

An experimental study on the different NPs sizes was conducted, with the idea of identifying the most effective conditions for compensating near-field optical losses associated to the structure assembly, while at the same time maintaining enough coupling to generate a high g-factors. The localized plasmon red shifts with the particle dimension, generating different couplings with the diffraction lines,[12] as confirmed by the contour plots in **Figure 3.13**. Once

the samples transmission was fully characterized, the CD measures were performed as described in the following schematic (**Figure 3.12**):

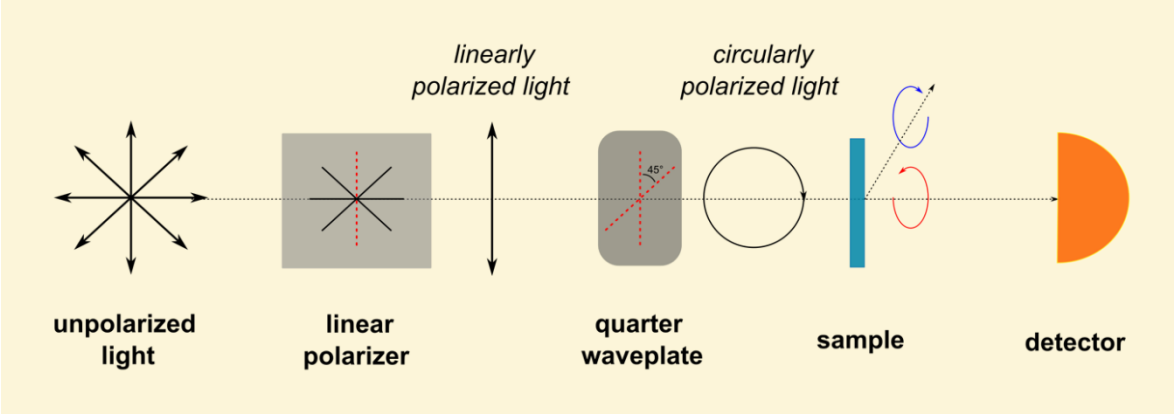

Figure 3.14 Optical set up used for CD measures to evaluate the absorption/extinction processes of incident circularly polarized light. Depending on the handedness of the structure, the metasurface is considered to scatter one circular polarization out of the propagation axis without absorbing its energy.

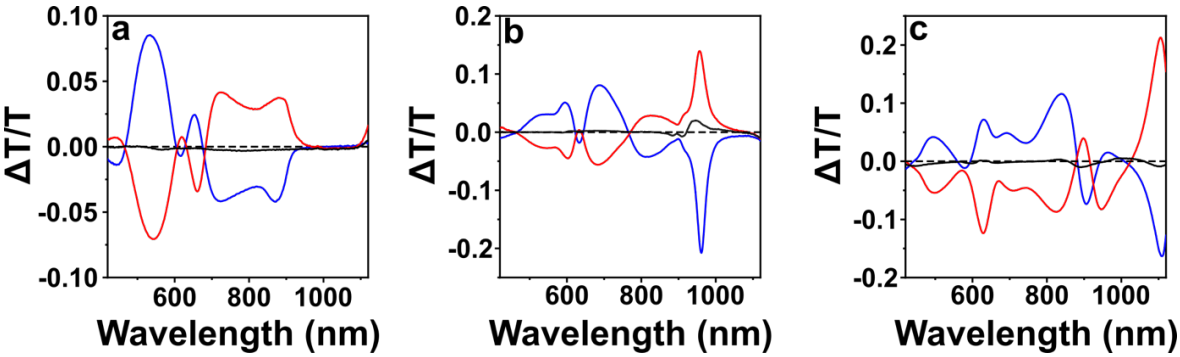

Figure 3.15 Normal incidence CD transmittance analysis of the array with (**a**) 25, (**b**) 50, (**c**) 100 nm AgNPs clusters. The **black**, **red** and **blue** curve represents the left-, right- and mixed- (racemic) handness.

An intense chiroptical activity modulated by the light circular handness was registered in all samples in correspondence of the position the lattice resonance at 870, 960, 1100 nm (**Figure 3.15 a**, **b**, **c** respectively) suggesting the synergic interaction between the chiral geometry and the plasmonic lattice resonances. In other words, we were able to verify that the chirality of the repeating unit is translated into a chiral property of the lattice resonance arising from isotropic and achiral colloids.

3.4 Plasmonic metasurfaces modification

Due to the parameters involved in the shaping of their optical response, colloidal plasmonic metasurfaces offers unprecedented flexibility compared to simple colloidal suspension, including the possibility of engineering their structure in post assembly steps. For example, Prof. Fery's group have fabricated array of colloidal gold nanoparticles squared lattice on polydimethylsiloxane (PDMS) substrate demonstrating a significant and reversable alteration in the optical response of the system when a mechanical strain is applied, causing the array to transit from a square lattice to a rectangular one. The SLR peaks were finely tuned over a range of 70 nm and the uniaxial strain introduces an optical anisotropy.[51]

Thus, they demonstrated that it was possible to dynamically tune narrow plasmons lattice resonances (bandwidth <5 nm) over the entire visible spectrum, introducing exciting prospects for real-time optical systems and flexible electronics.[52]

In this thesis, we have investigated the possibility of modifying the optical properties of plasmonic arrays by acting on the internal structure of the repeating unit, an interesting direction that remains relatively unexplored by the community.

This perspective holds promise for colloidal assemblies, where such modifications can be deliberately engineered into the colloidal building blocks used for assembly. This can be achieved through tailoring surface chemistry, specific interactions with substrates, crystallinity adjustments, or chemical reactivity.[53,54]

In this study, we delve deeper into the concepts of controlling optical losses for enhancing the quality factor of lattice plasmon resonances in arrays of metal nanoparticle clusters, examining both pre- and post-assembly modifications of the repeating unit and analyzing their impact on the collective plasmonic response (**Figure 3.16**).

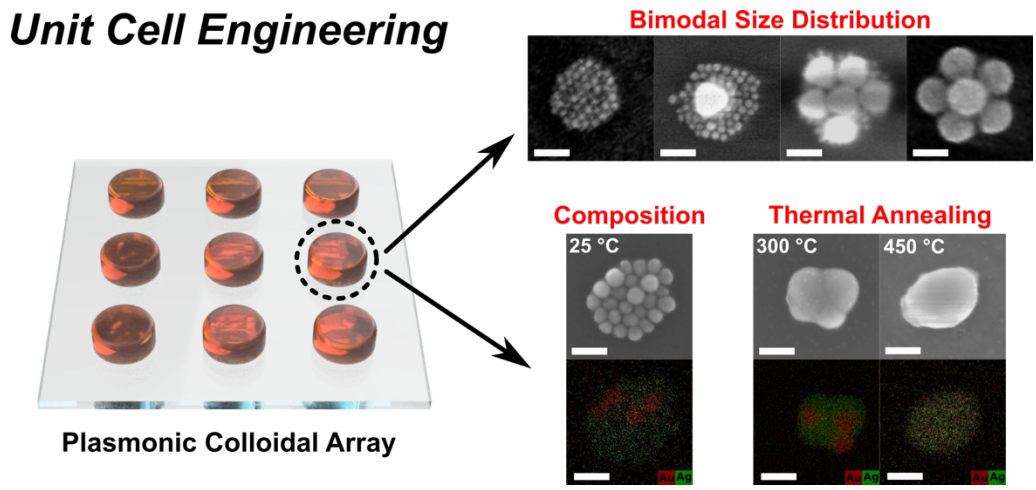

Figure 3.16 Internal organization and composition of plasmonic colloidal array unit cells engineered by exploring both pre- and post- assembly modifications such as the size distribution and composition of the colloids within the clusters, and thermal annealing treatments. **Scale bars:** 100 nm.

In the first approach, we co-assembled colloids of different sizes (25, 100 nm) and compositions (Au, Ag) to fabricate mixed plasmonic arrays (as discussed in **Paragraph 2.4.1**). In the second explored approach, we investigated a thermal post-modification technique applied to the assembled structures, allowing for the creation of heterogeneous agglomerates and facilitates an alloying process of the original components, depending on temperature and dwell time.

Since the study's focus was on modifying the repeating unit properties, the lattice pitch chosen for the squared array, which depends on the mold geometry, was kept constant for all samples (500 nm lattice period, hole diameter 280 nm, hole height 390 nm).

In contrast to the plasmonic metasurfaces prepared in combination with emitters (**Paragraph 2.4.1**), here we avoided the emergence of waveguided modes by assembling the plasmonic arrays directly on glass. This allowed us to simplify the system and isolate the effect of the modification of the repeating unit over the optical profile of the sample. Consequently, before preceding to optical characterization a layer of PDMS (>100 μm) was deposited onto the plasmonic units to index match the system and create a uniform dielectric environment in terms of refractive index. This superstrate enhances in-plane coupling mediated by grazing diffraction modes, thereby facilitating the emergence and investigation of lattice resonances.[5,55,56]

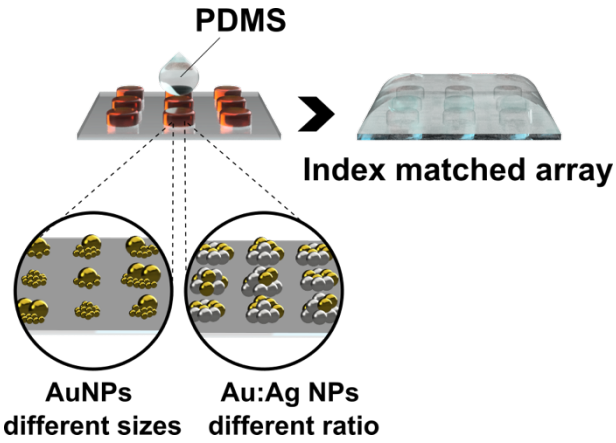

Figure 3.17 Index match procedure used before proceeding with the optical characterization. Some PDMS, prepared in ratio 10:1 of the monomer with the curing agent, is dropped on top of the plasmonic array in order to form an index matched transparent layer.

As explained in Chapter1, the optical behavior of colloidal plasmonic crystals can be roughly characterized by two main spectral features: the LSPR relative to the plasmonic clusters, observable between 400 and 650 nm, and the collective response of the entire array which position at normal is predictable by using **Eq. 3.4**. In this study, the lattice period Λ = 500 nm and n_{eff} = 1.49, considering an average of both n_{glass} = 1.52 and n_{PDMS} = 1.45. These values lead to predict the primary SLR position to appear approximately at 745 nm.

3.6.2 Pre-assembly modifications: effect of size distribution

To study the effect of the particle's dimensions on the optical response, gold nanoparticles with two distinct sizes (96 ± 9 nm and 24 ± 3 nm) were assembled into 500 nm square arrays. In particular, after being standardized in terms of concentration ($[Au^0]$ = 50 mM) by controlling the absorbance at 400 nm of the gold interband transition in UV-Vis experiment,[57] two colloidal mixtures were preparate using different volume ratios of 25 and 100 nm NPs.

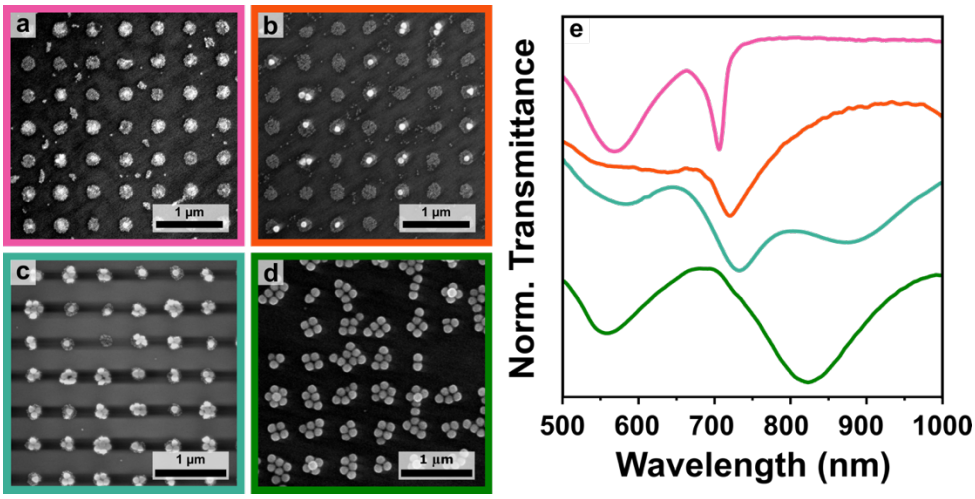

Figure 3.18 (**a**-**d**) SEM analysis of plasmonic arrays (Λ = 500 nm) fabricated by co-assembling of AuNPs with diameters of 25 and 100 nm. The 25 nm colloids were used with volume fraction of (**a**) 1, (**b**) 0.5, (**c**) 0.25, and (**d**) 0, respectively. (**e**) Transmittance spectra with the same color code: 25 nm colloids with volume fraction equal to 1 (**pink**), 0.5 (**orange**), 0.3 (**cyan**), and 0 (**green**).

Transmittance measurements were conducted on all the samples as described in **Paragraph 3.2**. An evident trend in their collective response was observed. Specifically, while the SLR band manifests as a sharp peak at 745 nm for the 25 nm colloid, it gradually shifts towards longer wavelengths and broadens as the percentage of the 100 nm colloid increases (Figure **3.18 e**). Different combinations of particle sizes were tested by replacing either the larger or smaller colloids with 49 ± 3 nm gold nanoparticles. As shown in **Figure 3.19**, a higher percentage of clusters containing both sizes of colloids were observed for both 100:50 nm and 50:25 nm combinations.

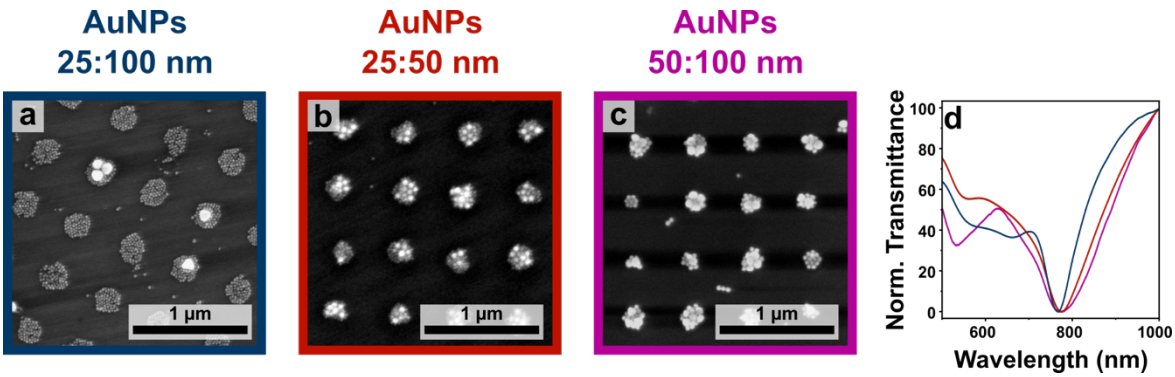

Figure 3.19 (**a**-**c**) SEM analysis of plasmonic arrays (Λ = 500 nm) fabricated by co-assembling AuNPs 25:100 (**a**), 25:50 (**b**), and 50:100 nm (**c**) in equal ratio (1:1). (**d**) Normalized transmittance spectra with the same color code: 25:100 (**blue**), 25:50 (**red**), and 50:100 nm (**purple**).

The behavior observed in the cluster formed by particles with different size in the two cases displayed in **Figure 3.19** suggests that the distribution of the two nanoparticle populations is closely related to the difference between their translational diffusion coefficients (see discussion in **Chapter 2**).

To try and minimize the defects in the structure and maximize the inclusion of the larger colloids within the repeating unit, an alternative multistep assembly approach was explored. Here, the low-diffusion component (bigger particles) is pre-loaded into the PDMS mold and then transferred to the substrate while simultaneously co-assembled with the high-diffusion component (smaller particles). This was achieved by treating the PDMS mold with UV-O_3 light for 25 minutes to make the surface more hydrophilic, thereby enhancing its affinity with colloids prepared in an aqueous environment. This affinity contrast is further accentuated by performing templated self-assembly on a highly hydrophobic surface, such as silanized glass coverslips in this case. Upon a demolding step, the colloids remain trapped inside the mold, adhering to the most hydrophilic surface (**Figure 3.20 a**-**d**).

This pre-loaded mold is then utilized for the standard templated self-assembly process of a high-diffusivity smaller colloid, resulting in a mixed plasmonic array comprising the 96 ± 9 and 24 ± 3 nm gold nanoparticles.

Despite the SEM analysis in **Figure 3.20** shows that a higher percentage of clusters is being occupied by at least one large nanoparticle, the formation of empty rings consisting of smaller colloids is also observed. This indicates that some of the 100 nm nanoparticles are not transferred from the PDMS template during the second assembly step. A weaker activation of the PDMS mold or the replacement of the UV-O_3 treatment with a chemical modification may help to overcome this issue. The emergence of a lattice optical response is confirmed by a relatively sharp signal peaked at 780 nm in the transmittance spectra of the samples prepared by sequential deposition assembly (**Figure 3.20 e**).

The presence of a collective plasmonic response is observed in all the mixtures studied, despite the increased losses within the repeating unit cell, suggesting the feasibility to assemble colloids that differ significantly in terms of size and/or shape.

The adaptability and robustness of this procedure can be leveraged to engineer both near-and far-field responses of the assembled system, which represents a great advantage for sensing and photonic application respectively, opening avenues for designing complex architectures wherein diverse nanoparticles are organized into hierarchical structures.

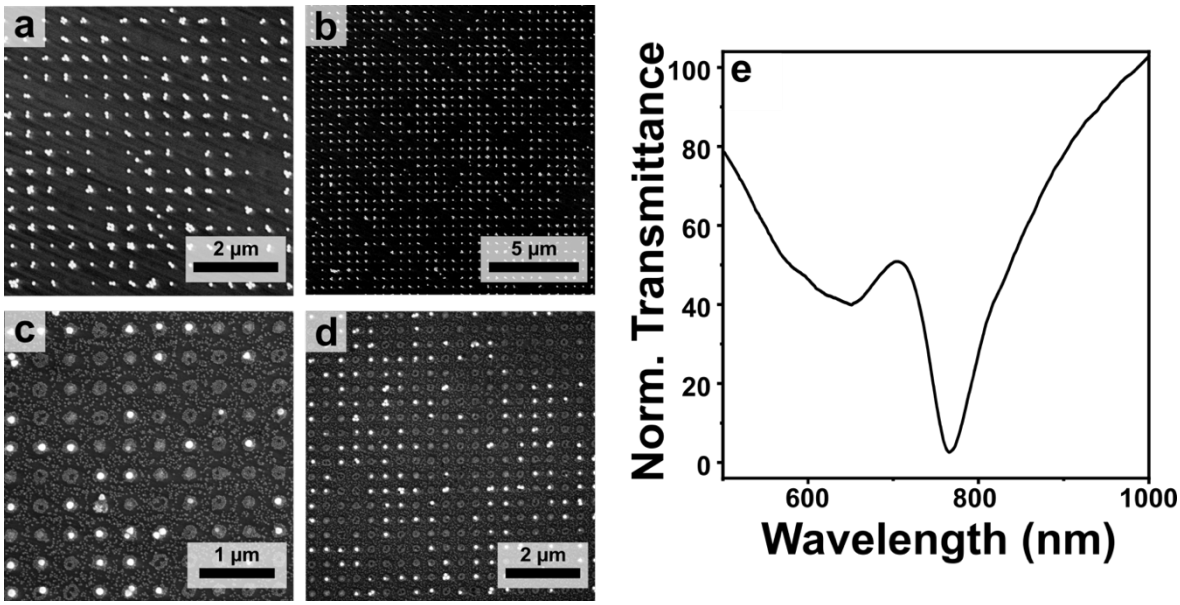

Figure 3.20 (**a**-**d**) SEM images of the PDMS mold pre-loaded with 96 ± 9 nm AuNPs (**a**, **b**), and the final assembly obtained after (**c**, **d**) sequential deposition with 24 ± 3 nm nanoparticles. (**e**) Normalized transmission spectra of the final array of co-assembled particles with different sizes (25:100 nm). Lattice period is Λ = 500 nm.

3.6.3 Pre-assembly modifications: the effect of composition

In the second part of this work, we studied the impact on plasmonic properties of the arrays by altering the composition of the repeating units. Gold nanoparticles with a diameter of 49 ± 3 nm were combined with silver nanoparticles with a diameter of 45 ± 4 nm, and their ratio was varied preparing different mixture before proceeding with self-assembly. Specifically, four colloidal suspensions were preparate with different volume fractions of gold and silver nanoparticles.

The mixtures yielded a fraction of gold nanoparticles (χ_{Au}) of 0.75, and 0.35 respectively (χ_{Au}=1 corresponds to pure gold and χ_{Au}=0 pure silver mixture). All the mixtures were characterized by UV-Vis spectroscopy and their composition was confirmed by energy dispersive X-ray (EDX) spectroscopy (**Experimental Section**).

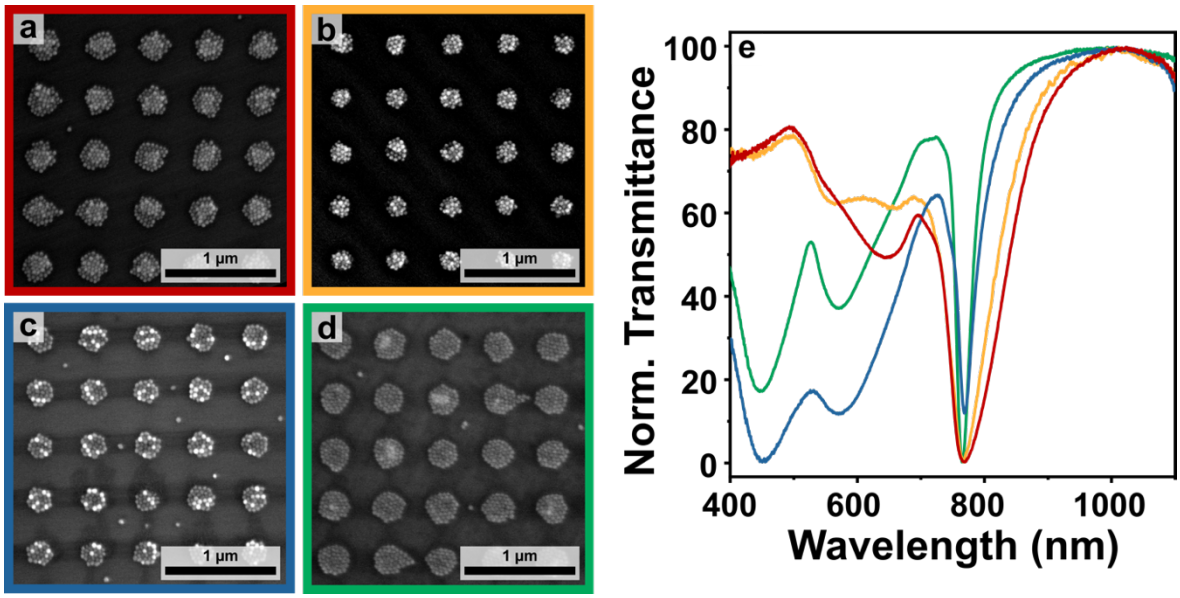

Figure 3.21 SEM analysis plasmonic array (Λ = 500 nm) obtained by co-assembly of Au and Ag NPs of ~50 nm in diameter with different molar volume fractions: χ_{Au} of (**a**) 1, (**b**) 0.75, (**c**) 0.35, (**d**) 0. (**e**) The corresponding normalized transmittance spectra follows the same color code: χ_{Au} of 1 (**red**), 0.75 (**yellow**), 0.35 (**blue**), and 0 (**green**).

SEM analysis (**Figure 3.21** (**a**-**d**)) confirmed the successful fabrication of the plasmonic arrays. Using the distinct electronic contrast between Au and Ag, both particle types are visible in SEM images, like what is typical observed for bimetallic structures,[58] revealing a statistical distribution of the two colloids within the different clusters. Since both gold and silver nanoparticles share similar sizes, coatings, and dispersion medium, they display a comparable distribution pattern. The variation in composition of the four colloidal suspensions is evident in the transmission spectra of the assembled structures (**Figure 3.21 e**).

The LSPRs band associated with the clusters emerge in the 400-700 nm in the blue region of the spectra as the amount of silver colloid is increased, in contrast to the pronounced red shifted localized plasmons associated with gold nanoparticles (>600 nm). Additionally, the optical

characterization confirms the appearance of a lattice plasmon resonance centered around 780 nm for all samples (**Figure 3.21 e**), which diffractive nature was confirmed by the angular distribution evaluated by changing the illumination angle (**Figure 3.22**)

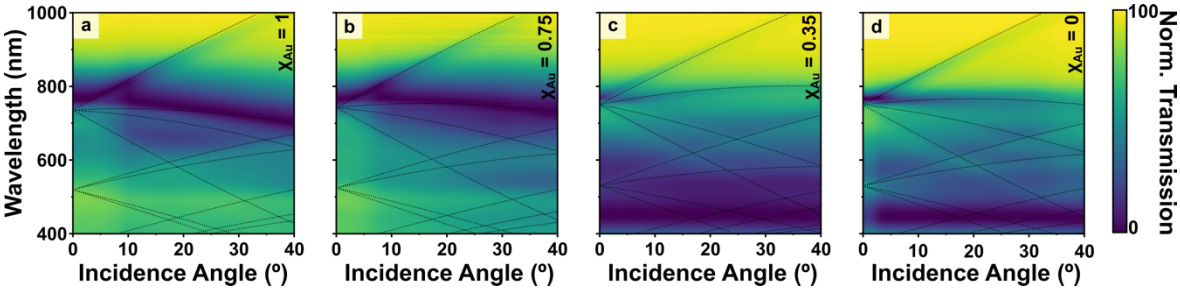

Figure 3.22 Normalized contour plots representing the wavelength position as function of the angle of incidence, for the arrays (Λ =500 nm) prepared using a mixture of Au and Ag NPs in different ratio: χ_{Au} of (**a**) 1, (**b**) 0.75, (**c**) 0.35, and (**d**) 0. The **black dashed** lines represent the analytical calculation of the R-W anomalies predicted considering the effective refractive index, the angle distribution, and the azimuthal angle.

Along the normal incidence direction, it can be observed a gradual red shift in the spectral peak position of the SLRs, from 770 nm of pure gold (**Figure 3.22 a**) to 765 nm of pure silver clusters (**Figure 3.22 b**). However, this variation cannot be considered significant since the discrepancies observed sample to sample can induce similar shifts in the position of lattice resonances (**Figure 3.23**).

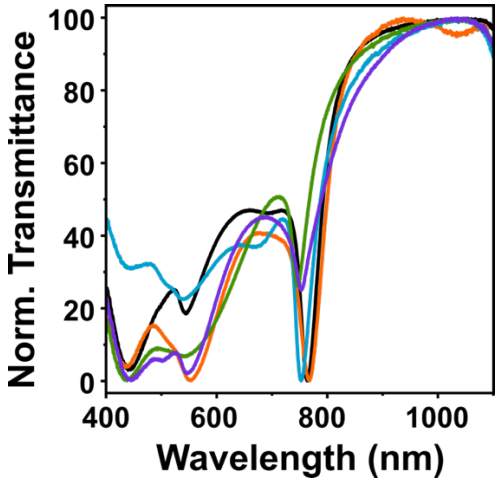

Figure 3.23 SLRs position varying sample-to-sample for plasmonic arrays (Λ = 500 nm) prepared with AgNPs. All the other samples show a similar variation behavior.

This is most likely due to slight variations in n_{eff} or incomplete uniformity of the colloidal distribution as the solvent evaporates. Secondly, while increasing silver content, an increase of

the SLRs' Q-factor (from 6 to 7, 15 and 25) is observed, which can be explained by the lower optical losses ascribed to Ag structures. This enhancement illustrates how different compositions influence the collective plasmonic properties of the array.

3.6.4 Post-assembly modifications: thermal annealing

A third way to tune the collective plasmonic properties of the array was carried out by post-assembly modifications, where the internal structure of the repeating units is altered after the self-assembly process is complete. In top-down lithographic approaches, it is common practice to use thermal annealing steps to increase the crystallinity of deposited films.[59] Inspired by such treatments, the same plasmonic arrays analyzed in **Figure 3.21** have been heated by rapid thermal annealing (RTA) treatment, under nitrogen atmosphere and mild vacuum conditions (10^{-2} Torr). Compared to standard methods, which often require thermal steps of up to 900°C,[60] the nanoscale size of the colloids allowed the use of lower annealing temperatures for this study. Specifically, temperatures ramps (20 °C/s) to 300 and 450 °C were used for each sample, with same dwell time of 60 min.[61]

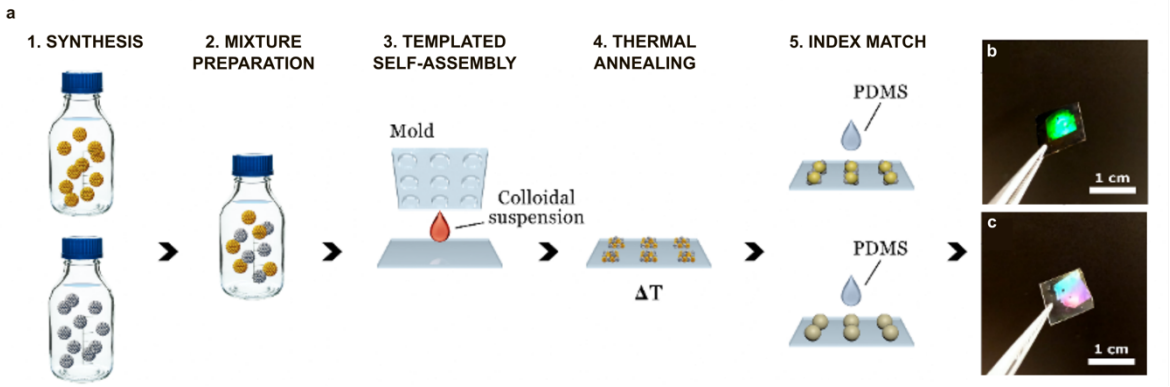

Figure 3.24 (**a**) Fabrication scheme involving post-assembly modification: 1. Synthesis of colloidal Au and Ag NPs; 2. Preparation of the mixtures; 3. Template-assisted self-assembly of the colloidal mixtures; 4. Thermal annealing treatment (T = 300, 450 °C); 5. Index match before the optical characterization. (**b**-**c**) Picture of the samples before the index match step prepared on (**b**) glass and on (**c**) silicon.

There are two distinct effects to consider during the annealing process. The first is the removal of the organic ligands that surround and stabilize the individual nanoparticles within the clusters.

The thermal decomposition of the coating shell increases the surface energy of the nanoparticles, allowing the more energetic surface atoms to rearrange even below the nanoparticles melting point.[61–63] This effect, coupled with the short interparticle distance within the clusters (<2 nm), leads to the coalescence of the 50 nm colloids into a single plasmonic unit. The near field coupling within the clusters results to be significantly disrupted and enables a reduction in optical losses within the system, leading the formation of sharper lattice plasmon resonances (**Figure 3.21 e**).

The second effect to be evaluated is the internal migration of atoms within the formed structure, which is particularly interesting in the case of heterogeneous cluster compositions. Recent *in situ* studies of bimetallic systems using advanced electron microscopy suggest that complete alloying of the two metals should be achievable at 450°C,[64,65] while low temperatures may prevent or significantly slow down atom migration. SEM analysis confirms the modification of the aggregates after annealing, but there is a remarkable difference that emerges between the two metals.

The first step was to investigate the effect of thermal annealing on plasmonic arrays composed solely of gold or silver NPs (**Figure 3.25**).

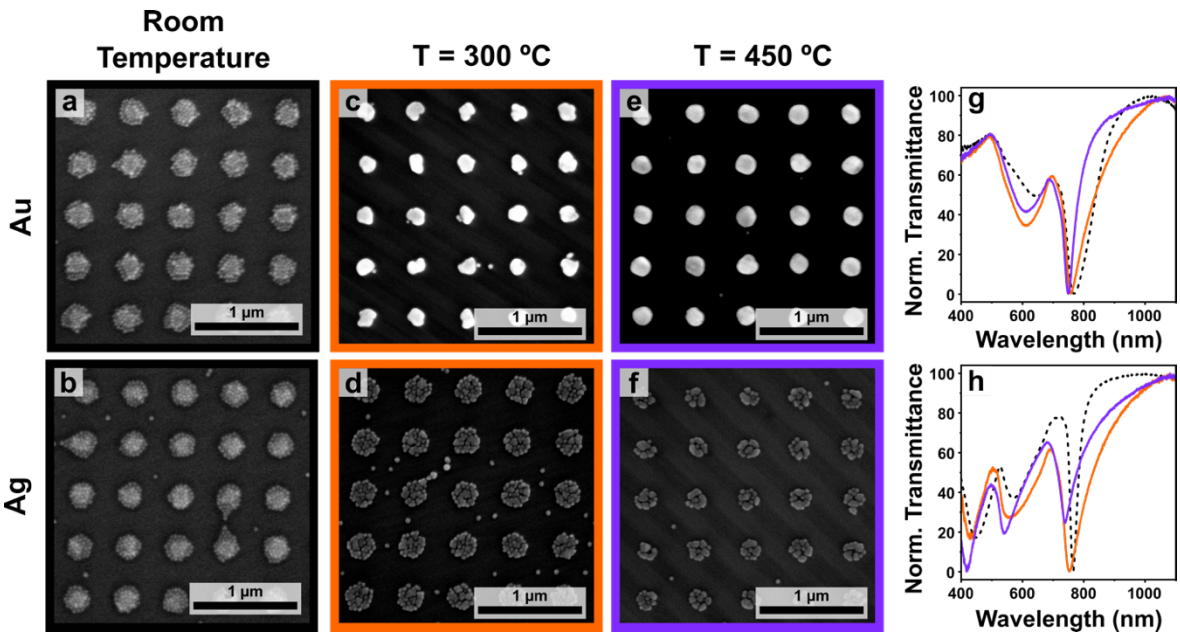

Figure 3.25 SEM analysis of plasmonic ordered arrays (Λ = 500 nm) composed of Au (top row) and Ag (bottom row) NPs at (**a**, **b**) room temperature, after thermal annealing at (**c**, **d**) 300°C and (**e**, **f**) 450 °C. (**g**, **h**) the normalized transmittance spectra correspond to the treatments with the same color code: room temperature (**dashed black** curve), annealing at 300°C (**orange solid** lines), and 450 °C (**purple solid** lines) in the case of (**g**) gold and (**h**) silver.

At both annealing temperatures (**Figure 3.24**) a single, almost isotropic shape is obtained for gold. As the heated particles tend to dewet from the surface, a slight reduction in size is expected.[66–68]

On the other hand, clusters of silver spheres do not completely combine, resulting in irregular and heterogeneous structures consisting of only few sintered nanoparticles (**Figure 3.24 b**, **d**, **f**). This behavior is evident in a much smaller size reduction of the clusters (**Table 3.1**), which cannot be explained by differences in melting point alone. In particular, the melting point is higher for 50 nm silver nanoparticles (1064 °C) compared to gold (962 °C).[69,70]

Table 3.1 Average diameters of the clusters composing the plasmonic arrays at room temperature (RT) and after thermal annealing at 300 and 400 °C.

Annealing T (°)	$\chi_{Au} = 1$	$\chi_{Au} = 0.75$	$\chi_{Au} = 0.35$	$\chi_{Au} = 0$
RT	250 ± 20	200 ± 20	200 ± 20	240 ± 20
300	160 ± 20	150 ± 20	170 ± 20	220 ± 20
450	170 ± 10	130 ± 20	140 ± 20	170 ± 20

Higher annealing temperature has an evident effect in the reduction of cluster size (**Table 3.1**). As the fraction of silver increases ($\chi_{Au} \rightarrow 0$) and after annealing at 300 °C, the cluster has the tendency to resist the reduction of their diameter, indicating a lower degree of coalescence between neighbor particles composing the mixed clusters. However, this separation is drastically reduced when the annealing temperature is increased to 450°C.

Metal alloying provides a versatile approach to tailoring a material's dielectric constant, which can significantly affect the system's plasmonic properties.[71] Indeed, our fabrication scheme can be extended to any other composition to achieve the desired alloy depending on the specific property or application of interest.

Since the entire annealing process is carried out under nitrogen atmosphere and vacuum conditions, which minimize the partial pressure of oxygen and thus inhibit the adsorption of oxygen on the particles surface, the possibility of oxidation of the silver colloids seems implausible.[72] Instead, two effects could explain the observed size clusters reduction behavior.

The first effect involves the formation of silver sulphide species resulting from degrading the PEG-SH ligands coating the nanoparticles.[73] The second effect relay on the tendency of gold and silver particles to coalesce, a phenomenon directly influenced by differences in surface atomic mobility[64] related to surface energy, cohesive energy and vacancy formation.[74]

Now that we have analyzed the behavior of the monometallic metasurfaces, we investigate the potential benefits of using mixed colloids for the fabrication of annealed plasmonic arrays, maintaining a consistent RTA profile across all samples.

As shown in **Figure 3.25 g, h**, the morphology variation affects the resulting optical responses of the arrays. For the Au colloid, a significant narrowing of the SLR bandwidth was observed, registering Q_f of 6, 11 and 16 at room temperature, 300°C and 450°C, respectively **Figure 3.25g**). On the other hand, the silver plasmons arrays showed widening and intensity decrease of the SLR peaks, resulting in reduction of the Q_f (25, 10 and 12 for RT, 300 and 450 °C respectively) as seen in **Figure 3.25 h**). This is indicative of the occurrence of increased optical losses in the system or a reduction in the far-field coupling between the repeating units.

The study of the annealing process was extended to the plasmonic arrays fabricated from the gold and silver colloids mixtures (**Figure 3.26**).

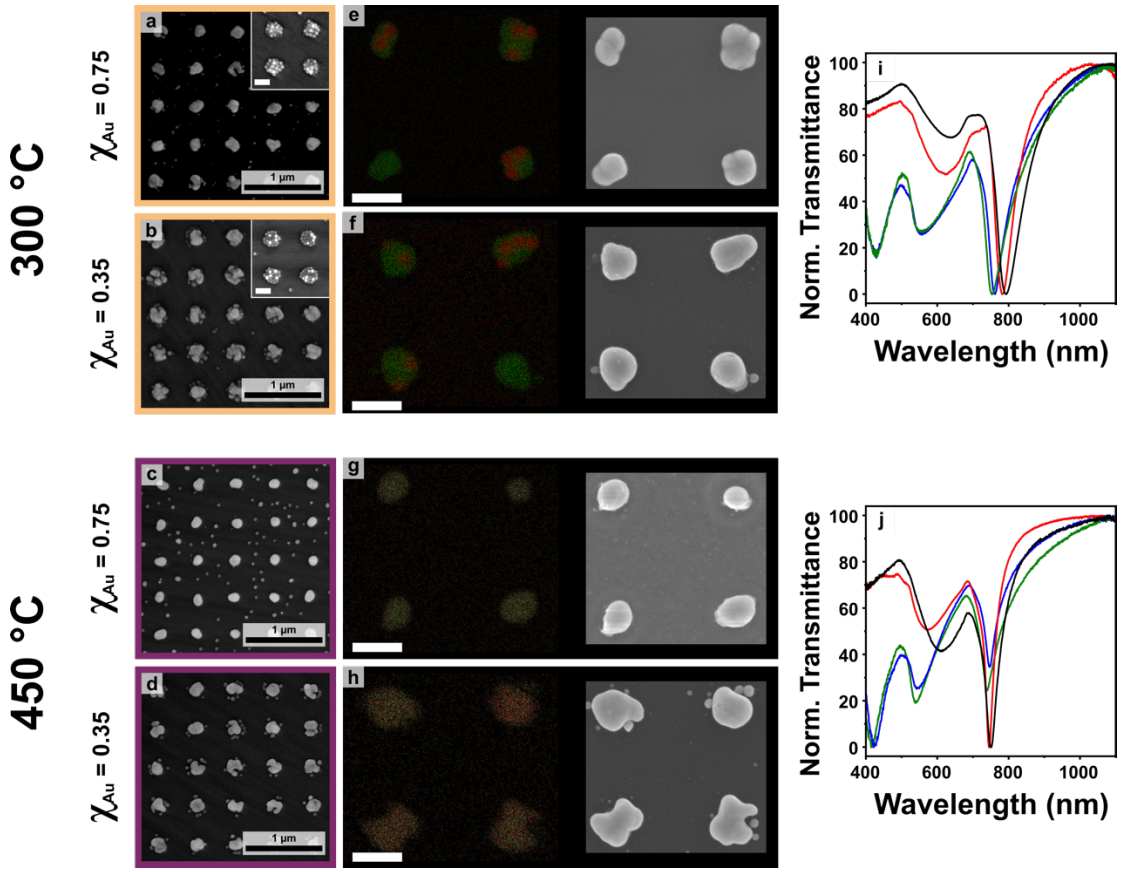

Figure 3.26 (**a**-**d**) SEM analysis of plasmonic arrays (Λ = 500 nm) composed of a mixture of Au and Ag colloids with χ_{Au} = 0.75 (**a**), (**c**), and 0.35 (**b**), (**d**) subjected to thermal annealing at 300 (**a**), (**b**) and 450 °C (**c**), (**d**). The inset in (**a**) and (**b**) show the clusters at room temperature (scale bar: 200 nm). (**e**-**h**) Energy dispersive X-ray (EDX) spectroscopy mapping of the plasmonic arrays (Λ = 500 nm) composed of a mixture of Au (**red** trace) and Ag (**green** trace) colloids with χ_{Au} = 0.75 (**e**), (**g**), and 0.35 (**f**), (**h**) subjected to thermal annealing at (**e**), (**f**) 300 and (**g**), (**h**) 450 °C. On the right side the corresponding bright-field images (**scale bar**: 200 nm).

Interestingly, the presence of gold in the clusters seems to promote the coalescence of the colloids into singular structures, even when it is the minority component of the mixture (**Figure 3.26**).

In addition to SEM characterization, EDX mapping (with the red trace representing gold and the green trace representing silver) was conducted on the resulting structures for both annealing temperatures (**Figure 3.26 e**-**f**, **g**-**h**). Elemental analysis at 300°C revealed the formation of heterogeneous regions within the same plasmonic unit cells for both mixtures. These results have significant potential for plasmonic-driven (photo)catalysis, where energy or electron transfer between the plasmonic unit and the catalytic site requires precise engineering and suggest the possibility of manipulating the formation of patchy structures where the positioning of different elements could be controlled during assembly. When the annealing temperature is increased to 450 °C, the spatial distribution of gold and silver recorded by EDX mapping shows a significantly different scenario, with the two elements completely overlapping, indicating the formation of alloyed structures (**Figure 3.26 g**, **h**)

The transmittance profiles of the mixed arrays in **Figure 3.26** shows similar trends to those shown in **Figure 3.25**. The Q_f of the SLRs increases with annealing temperature for gold-richer colloidal mixture, while it decreases for arrays where silver predominates. Remarkably, the best optical performance is achieved by the sample where $\chi_{Au} = 0.75$ for both annealing temperatures (**red** curve in **Figure 3.26 i**, **j**), underlying that the combination of Au and Ag could enhance the optical performance of these colloidal metasurfaces combining the greater optical properties of silver and the advantageous chemical and physical stability of gold. A Q_f of 20 was recorded for the SLR after annealing at 450°C, which is the second highest value reported in this study, after the Q_f of 24 obtained for pure silver arrays. This represents an increment of approximately 20% compared to a monometallic gold array annealed at the same temperature. The angular distribution, evaluated by changing the angle of illumination as done for other samples,

confirmed once again the diffractive nature of these SLRs (**Figure 3.27**), and the quality of the array is confirmed by the appearance of higher orders of diffraction.

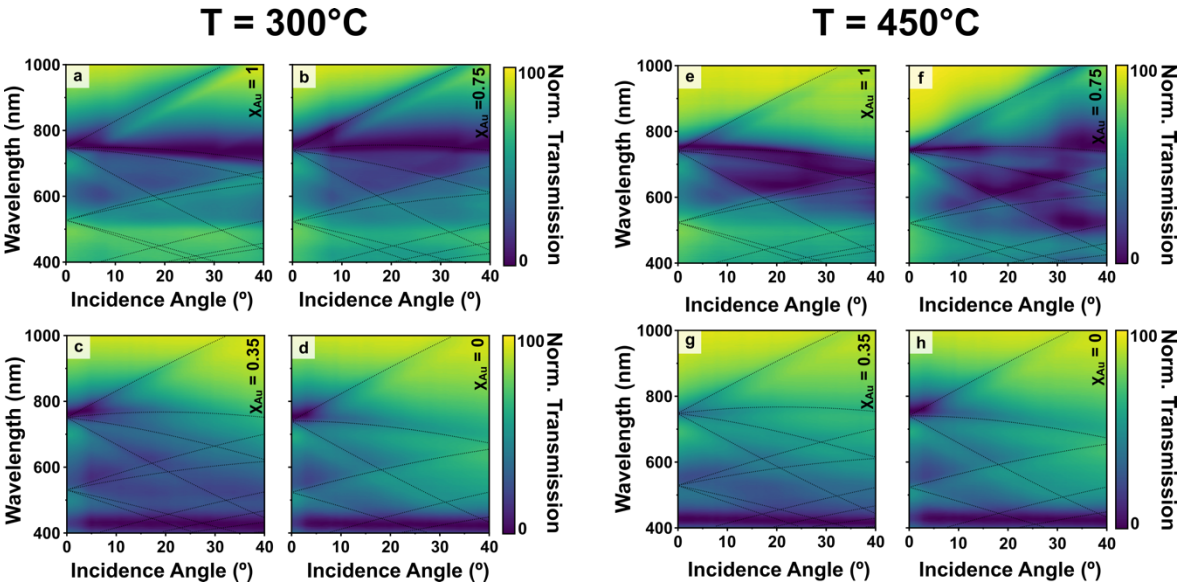

Figure 3.27 Contour plots of the SLRs as function of the illumination angle for the arrays with lattice period of 500 nm after annealing treatment at (**a**-**d**) 300 °C, and (**e**-**h**) 450 °C. Array of clusters with Au and Ag colloids in different volume fractions: (**a**, **e**) χ_{Au} = 1, (**b**, **f**) 0.75, (**c**, **g**) 0.35, (**d**, **h**) and 0. The **black dashed** lines represent the calculation of the R-W anomalies of the array following **Eq. 3.4**, considering the range of angles, the azimuthal angle, and effective refractive index.

3.6 Reference

(1) Kravets, V. G.; Kabashin, A. V.; Barnes, W. L.; Grigorenko, A. N. Plasmonic Surface Lattice Resonances: A Review of Properties and Applications. *Chem. Rev.* **2018**, *118* (12), 5912–5951. https://doi.org/10.1021/acs.chemrev.8b00243.

(2) Kang, E. S. H.; Shiran Chaharsoughi, M.; Rossi, S.; Jonsson, M. P. Hybrid Plasmonic Metasurfaces. *J. Appl. Phys.* **2019**, *126* (14), 140901. https://doi.org/10.1063/1.5116885.

(3) Tordera, D.; Zhao, D.; Volkov, A. V.; Crispin, X.; Jonsson, M. P. Thermoplasmonic Semitransparent Nanohole Electrodes. *Nano Lett.* **2017**, *17* (5), 3145–3151. https://doi.org/10.1021/acs.nanolett.7b00574.

(4) Miroshnichenko, A. E.; Flach, S.; Kivshar, Y. S. Fano Resonances in Nanoscale Structures. *Rev. Mod. Phys.* **2010**, *82* (3), 2257–2298. https://doi.org/10.1103/RevModPhys.82.2257.

(5) Auguié, B.; Barnes, W. L. Diffractive Coupling in Gold Nanoparticle Arrays and the Effect of Disorder. *Opt. Lett.* **2009**, *34* (4), 401–403. https://doi.org/10.1364/OL.34.000401.

(6) Watkins, N. E.; Guan, J.; Diroll, B. T.; Williams, K. R.; Schaller, R. D.; Odom, T. W. Surface Normal Lasing from CdSe Nanoplatelets Coupled to Aluminum Plasmonic Nanoparticle Lattices. *J. Phys. Chem. C* **2021**, *125* (36), 19874–19879. https://doi.org/10.1021/acs.jpcc.1c05662.

(7) Sarkar, S.; Gupta, V.; Kumar, M.; Schubert, J.; Probst, P. T.; Joseph, J.; König, T. A. F. Hybridized Guided-Mode Resonances via Colloidal Plasmonic Self-Assembled Grating. *ACS Appl. Mater. Interfaces* **2019**, *11* (14), 13752–13760. https://doi.org/10.1021/acsami.8b20535.

(8) Schokker, A. H.; Koenderink, A. F. Lasing at the Band Edges of Plasmonic Lattices. *Phys. Rev. B* **2014**, *90* (15), 155452. https://doi.org/10.1103/PhysRevB.90.155452.

(9) Guan, J.; Sagar, L. K.; Li, R.; Wang, D.; Bappi, G.; Wang, W.; Watkins, N.; Bourgeois, M. R.; Levina, L.; Fan, F.; Hoogland, S.; Voznyy, O.; de Pina, J. M.; Schaller, R. D.; Schatz, G. C.; Sargent, E. H.; Odom, T. W. Quantum Dot-Plasmon Lasing with Controlled Polarization Patterns. *ACS Nano* **2020**, *14* (3), 3426–3433. https://doi.org/10.1021/acsnano.9b09466.

(10) Juodėnas, M.; Tamulevičius, T.; Henzie, J.; Erts, D.; Tamulevičius, S. Surface Lattice Resonances in Self-Assembled Arrays of Monodisperse Ag Cuboctahedra. *ACS Nano* **2019**, *13* (8), 9038–9047. https://doi.org/10.1021/acsnano.9b03191.

(11) Zou, S.; Schatz, G. C. Narrow Plasmonic/Photonic Extinction and Scattering Line

Shapes for One and Two Dimensional Silver Nanoparticle Arrays. *J. Chem. Phys.* **2004**, *121* (24), 12606. https://doi.org/10.1063/1.1826036.

(12) Molet, P.; Passarelli, N.; Pérez, L. A.; Scarabelli, L.; Mihi, A. Engineering Plasmonic Colloidal Meta-Molecules for Tunable Photonic Supercrystals. *Adv. Opt. Mater.* **2021**, *9* (20), 2100761. https://doi.org/10.1002/adom.202100761.

(13) Manjavacas, A.; Zundel, L.; Sanders, S. Analysis of the Limits of the Near-Field Produced by Nanoparticle Arrays. *ACS Nano* **2019**, *13* (9), 10682–10693. https://doi.org/10.1021/acsnano.9b05031.

(14) Guo, R.; Hakala, T. K.; Törmä, P. Geometry Dependence of Surface Lattice Resonances in Plasmonic Nanoparticle Arrays. *Phys. Rev. B* **2017**, *95* (15), 155423. https://doi.org/10.1103/PhysRevB.95.155423.

(15) Wang, D.; Yang, A.; Wang, W.; Hua, Y.; Schaller, R. D.; Schatz, G. C.; Odom, T. W. Band-Edge Engineering for Controlled Multi-Modal Nanolasing in Plasmonic Superlattices. *Nat. Nanotechnol.* **2017**, *12* (9), 889–894. https://doi.org/10.1038/nnano.2017.126.

(16) Guan, J.; Bourgeois, M. R.; Li, R.; Hu, J.; Schaller, R. D.; Schatz, G. C.; Odom, T. W. Identification of Brillouin Zones by In-Plane Lasing from Light-Cone Surface Lattice Resonances. *ACS Nano* **2021**, *15* (3), 5567–5573. https://doi.org/10.1021/acsnano.1c00449.

(17) Sapienza, L.; Davanço, M.; Badolato, A.; Srinivasan, K. Nanoscale Optical Positioning of Single Quantum Dots for Bright and Pure Single-Photon Emission. *Nat. Commun.* **2015**, *6* (1), 7833. https://doi.org/10.1038/ncomms8833.

(18) Utzat, H.; Sun, W.; Kaplan, A. E. K.; Krieg, F.; Ginterseder, M.; Spokoyny, B.; Klein, N. D.; Shulenberger, K. E.; Perkinson, C. F.; Kovalenko, M. V.; Bawendi, M. G. Coherent Single-Photon Emission from Colloidal Lead Halide Perovskite Quantum Dots. *Science* **2019**, *363* (6431), 1068–1072. https://doi.org/10.1126/science.aau7392.

(19) Yadav, R. K.; Liu, W.; Li, R.; Odom, T. W.; Agarwal, G. S.; Basu, J. K. Room-Temperature Coupling of Single Photon Emitting Quantum Dots to Localized and Delocalized Modes in a Plasmonic Nanocavity Array. *ACS Photonics* **2021**, *8* (2), 576–584. https://doi.org/10.1021/acsphotonics.0c01635.

(20) Törmä, P.; Barnes, W. L. Strong Coupling between Surface Plasmon Polaritons and Emitters: A Review. *Rep. Prog. Phys.* **2014**, *78* (1), 013901. https://doi.org/10.1088/0034-4885/78/1/013901.

(21) Shi, L.; Hakala, T. K.; Rekola, H. T.; Martikainen, J.-P.; Moerland, R. J.; Törmä, P. Spatial Coherence Properties of Organic Molecules Coupled to Plasmonic Surface Lattice

Resonances in the Weak and Strong Coupling Regimes. *Phys. Rev. Lett.* **2014**, *112* (15), 153002. https://doi.org/10.1103/PhysRevLett.112.153002.

(22) Vinnacombe-Willson, G. A.; Conti, Y.; Jonas, S. J.; Weiss, P. S.; Mihi, A.; Scarabelli, L. Surface Lattice Plasmon Resonances by Direct In Situ Substrate Growth of Gold Nanoparticles in Ordered Arrays. *Adv. Mater.* **2022**, *n/a* (n/a), 2205330. https://doi.org/10.1002/adma.202205330.

(23) Kasani, S.; Curtin, K.; Wu, N. A Review of 2D and 3D Plasmonic Nanostructure Array Patterns: Fabrication, Light Management and Sensing Applications. *Nanophotonics* **2019**, *8* (12), 2065–2089. https://doi.org/10.1515/nanoph-2019-0158.

(24) Rossner, C.; König, T. A. F.; Fery, A. Plasmonic Properties of Colloidal Assemblies. *Adv. Opt. Mater.* **2021**, *9* (8), 2001869. https://doi.org/10.1002/adom.202001869.

(25) Le-Van, Q.; Zoethout, E.; Geluk, E.-J.; Ramezani, M.; Berghuis, M.; Gómez Rivas, J. Enhanced Quality Factors of Surface Lattice Resonances in Plasmonic Arrays of Nanoparticles. *Adv. Opt. Mater.* **2019**, *7* (6), 1801451. https://doi.org/10.1002/adom.201801451.

(26) Charconnet, M.; Korsa, M. T.; Petersen, S.; Plou, J.; Hanske, C.; Adam, J.; Seifert, A. Generalization of Self-Assembly Toward Differently Shaped Colloidal Nanoparticles for Plasmonic Superlattices. *Small Methods* **2023**, *7* (4), 2201546. https://doi.org/10.1002/smtd.202201546.

(27) Haken, H.; Wolf, H. C. *Molecular Physics and Elements of Quantum Chemistry: Introduction to Experiments and Theory*; Springer Science & Business Media, 2013.

(28) Lininger, A.; Palermo, G.; Guglielmelli, A.; Nicoletta, G.; Goel, M.; Hinczewski, M.; Strangi, G. Chirality in Light–Matter Interaction. *Adv. Mater.* **2023**, *35* (34), 2107325. https://doi.org/10.1002/adma.202107325.

(29) Rodger, A.; Nordén, B. *Circular Dichroism and Linear Dichroism*; Oxford University Press, 1997.

(30) Hentschel, M.; Schäferling, M.; Duan, X.; Giessen, H.; Liu, N. Chiral Plasmonics. *Sci. Adv.* **2017**, *3* (5), e1602735. https://doi.org/10.1126/sciadv.1602735.

(31) Luo, Y.; Chi, C.; Jiang, M.; Li, R.; Zu, S.; Li, Y.; Fang, Z. Plasmonic Chiral Nanostructures: Chiroptical Effects and Applications. *Adv. Opt. Mater.* **2017**, *5* (16), 1700040. https://doi.org/10.1002/adom.201700040.

(32) Yin, S.; Ji, W.; Xiao, D.; Li, Y.; Li, K.; Yin, Z.; Jiang, S.; Shao, L.; Luo, D.; Liu, Y. J. Intrinsically or Extrinsically Reconfigurable Chirality in Plasmonic Chiral Metasurfaces. *Opt. Commun.* **2019**, *448*, 10–14. https://doi.org/10.1016/j.optcom.2019.05.006.

(33) Kim, J.; Rana, A. S.; Kim, Y.; Kim, I.; Badloe, T.; Zubair, M.; Mehmood, M. Q.; Rho, J. Chiroptical Metasurfaces: Principles, Classification, and Applications. *Sensors* **2021**, *21* (13), 4381. https://doi.org/10.3390/s21134381.

(34) Cao, T.; Wei, C.; Li, Y. Dual-Band Strong Extrinsic 2D Chirality in a Highly Symmetric Metal-Dielectric-Metal Achiral Metasurface. *Opt. Mater. Express* **2016**, *6* (2), 303–311. https://doi.org/10.1364/OME.6.000303.

(35) Papakostas, A.; Potts, A.; Bagnall, D. M.; Prosvirnin, S. L.; Coles, H. J.; Zheludev, N. I. Optical Manifestations of Planar Chirality. *Phys. Rev. Lett.* **2003**, *90* (10), 107404. https://doi.org/10.1103/PhysRevLett.90.107404.

(36) Plum, E.; Fedotov, V. A.; Zheludev, N. I. Extrinsic Electromagnetic Chirality in Metamaterials. *J. Opt. Pure Appl. Opt.* **2009**, *11* (7), 074009. https://doi.org/10.1088/1464-4258/11/7/074009.

(37) Plum, E.; Liu, X.-X.; Fedotov, V. A.; Chen, Y.; Tsai, D. P.; Zheludev, N. I. Metamaterials: Optical Activity without Chirality. *Phys. Rev. Lett.* **2009**, *102* (11), 113902. https://doi.org/10.1103/PhysRevLett.102.113902.

(38) Govorov, A. O.; Gun'ko, Y. K.; Slocik, J. M.; Gérard, V. A.; Fan, Z.; Naik, R. R. Chiral Nanoparticle Assemblies: Circular Dichroism, Plasmonic Interactions, and Exciton Effects. *J. Mater. Chem.* **2011**, *21* (42), 16806–16818. https://doi.org/10.1039/C1JM12345A.

(39) Collins, J. T.; Kuppe, C.; Hooper, D. C.; Sibilia, C.; Centini, M.; Valev, V. K. Chirality and Chiroptical Effects in Metal Nanostructures: Fundamentals and Current Trends. *Adv. Opt. Mater.* **2017**, *5* (16), 1700182. https://doi.org/10.1002/adom.201700182.

(40) Qiu, M.; Zhang, L.; Tang, Z.; Jin, W.; Qiu, C.-W.; Lei, D. Y. 3D Metaphotonic Nanostructures with Intrinsic Chirality. *Adv. Funct. Mater.* **2018**, *28* (45), 1803147. https://doi.org/10.1002/adfm.201803147.

(41) Wong, Z. J.; Wang, Y.; O'Brien, K.; Rho, J.; Yin, X.; Zhang, S.; Fang, N.; Yen, T.-J.; Zhang, X. Optical and Acoustic Metamaterials: Superlens, Negative Refractive Index and Invisibility Cloak. *J. Opt.* **2017**, *19* (8), 084007. https://doi.org/10.1088/2040-8986/aa7a1f.

(42) Pendry, J. B. A Chiral Route to Negative Refraction. *Science* **2004**, *306* (5700), 1353–1355. https://doi.org/10.1126/science.1104467.

(43) Liu, J.; Song, Z.-P.; Sun, L.-Y.; Li, B.-X.; Lu, Y.-Q.; Li, Q. Circularly Polarized Luminescence in Chiral Orientationally Ordered Soft Matter Systems. *Responsive Mater.* **2023**, *1* (1), e20230005. https://doi.org/10.1002/rpm.20230005.

(44) Sang, Y.; Han, J.; Zhao, T.; Duan, P.; Liu, M. Circularly Polarized Luminescence in

Nanoassemblies: Generation, Amplification, and Application. *Adv. Mater.* **2020**, *32* (41), 1900110. https://doi.org/10.1002/adma.201900110.

(45) Wang, L.; Urbas, A. M.; Li, Q. Nature-Inspired Emerging Chiral Liquid Crystal Nanostructures: From Molecular Self-Assembly to DNA Mesophase and Nanocolloids. *Adv. Mater.* **2020**, *32* (41), 1801335. https://doi.org/10.1002/adma.201801335.

(46) Wei, W.; Farooq, M. A.; Xiong, H. Cholesteric Liquid Crystalline Polyether with Broad Tunable Circularly Polarized Luminescence. *Langmuir ACS J. Surf. Colloids* **2021**, *37* (40), 11922–11930. https://doi.org/10.1021/acs.langmuir.1c02144.

(47) Schäferling, M. *Chiral Nanophotonics: Chiral Optical Properties of Plasmonic Systems*; Springer Series in Optical Sciences; Springer International Publishing: Cham, 2017; Vol. 205. https://doi.org/10.1007/978-3-319-42264-0.

(48) Tang, Y.; Cohen, A. E. Optical Chirality and Its Interaction with Matter. *Phys. Rev. Lett.* **2010**, *104* (16), 163901. https://doi.org/10.1103/PhysRevLett.104.163901.

(49) Zhu, A. Y.; Chen, W. T.; Zaidi, A.; Huang, Y.-W.; Khorasaninejad, M.; Sanjeev, V.; Qiu, C.-W.; Capasso, F. Giant Intrinsic Chiro-Optical Activity in Planar Dielectric Nanostructures. *Light Sci. Appl.* **2018**, *7*, 17158. https://doi.org/10.1038/lsa.2017.158.

(50) Mendoza-Carreño, J.; Molet, P.; Otero-Martínez, C.; Alonso, M. I.; Polavarapu, L.; Mihi, A. Nanoimprinted 2D-Chiral Perovskite Nanocrystal Metasurfaces for Circularly Polarized Photoluminescence. *Adv. Mater.* **2023**, *35* (15), 2210477. https://doi.org/10.1002/adma.202210477.

(51) Gupta, V.; Probst, P. T.; Goßler, F. R.; Steiner, A. M.; Schubert, J.; Brasse, Y.; König, T. A. F.; Fery, A. Mechanotunable Surface Lattice Resonances in the Visible Optical Range by Soft Lithography Templates and Directed Self-Assembly. *ACS Appl. Mater. Interfaces* **2019**, *11* (31), 28189–28196. https://doi.org/10.1021/acsami.9b08871.

(52) Yang, A.; Hryn, A. J.; Bourgeois, M. R.; Lee, W.-K.; Hu, J.; Schatz, G. C.; Odom, T. W. Programmable and Reversible Plasmon Mode Engineering. *Proc. Natl. Acad. Sci.* **2016**, *113* (50), 14201–14206. https://doi.org/10.1073/pnas.1615281113.

(53) Baur, S.; Sanders, S.; Manjavacas, A. Hybridization of Lattice Resonances. *ACS Nano* **2018**, *12* (2), 1618–1629. https://doi.org/10.1021/acsnano.7b08206.

(54) Hamon, C.; Sanz-Ortiz, M. N.; Modin, E.; Hill, E. H.; Scarabelli, L.; Chuvilin, A.; Liz-Marzán, L. M. Hierarchical Organization and Molecular Diffusion in Gold Nanorod/Silica Supercrystal Nanocomposites. *Nanoscale* **2016**, *8* (15), 7914–7922. https://doi.org/10.1039/C6NR00712K.

(55) Novotny, L.; Hecht, B. *Principles of Nano-Optics*; Cambridge University Press:

Cambridge, 2006. https://doi.org/10.1017/CBO9780511813535.

(56) Khlopin, D.; Laux, F.; Wardley, W. P.; Martin, J.; Wurtz, G. A.; Plain, J.; Bonod, N.; Zayats, A. V.; Dickson, W.; Gérard, D. Lattice Modes and Plasmonic Linewidth Engineering in Gold and Aluminum Nanoparticle Arrays. *JOSA B* **2017**, *34* (3), 691–700. https://doi.org/10.1364/JOSAB.34.000691.

(57) Scarabelli, L.; Sánchez-Iglesias, A.; Pérez-Juste, J.; Liz-Marzán, L. M. A "Tips and Tricks" Practical Guide to the Synthesis of Gold Nanorods. *J. Phys. Chem. Lett.* **2015**, *6* (21), 4270–4279. https://doi.org/10.1021/acs.jpclett.5b02123.

(58) Mayer, M.; Schnepf, M. J.; König, T. A. F.; Fery, A. Colloidal Self-Assembly Concepts for Plasmonic Metasurfaces. *Adv. Opt. Mater.* **2019**, *7* (1), 1800564. https://doi.org/10.1002/adom.201800564.

(59) Deng, S.; Li, R.; Park, J.-E.; Guan, J.; Choo, P.; Hu, J.; Smeets, P. J. M.; Odom, T. W. Ultranarrow Plasmon Resonances from Annealed Nanoparticle Lattices. *Proc. Natl. Acad. Sci.* **2020**, *117* (38), 23380–23384. https://doi.org/10.1073/pnas.2008818117.

(60) Higashino, M.; Murai, S.; Tanaka, K. Improving the Plasmonic Response of Silver Nanoparticle Arrays via Atomic Layer Deposition Coating and Annealing above the Melting Point. *J. Phys. Chem. C* **2020**, *124* (50), 27687–27693. https://doi.org/10.1021/acs.jpcc.0c09112.

(61) Bronchy, M.; Roach, L.; Mendizabal, L.; Feautrier, C.; Durand, E.; Heintz, J.-M.; Duguet, E.; Tréguer-Delapierre, M. Improved Low Temperature Sinter Bonding Using Silver Nanocube Superlattices. *J. Phys. Chem. C* **2022**, *126* (3), 1644–1650. https://doi.org/10.1021/acs.jpcc.1c09125.

(62) Inasawa, S.; Sugiyama, M.; Yamaguchi, Y. Laser-Induced Shape Transformation of Gold Nanoparticles below the Melting Point: The Effect of Surface Melting. *J. Phys. Chem. B* **2005**, *109* (8), 3104–3111. https://doi.org/10.1021/jp045167j.

(63) Cha, S. K.; Mun, J. H.; Chang, T.; Kim, S. Y.; Kim, J. Y.; Jin, H. M.; Lee, J. Y.; Shin, J.; Kim, K. H.; Kim, S. O. Au–Ag Core–Shell Nanoparticle Array by Block Copolymer Lithography for Synergistic Broadband Plasmonic Properties. *ACS Nano* **2015**, *9* (5), 5536–5543. https://doi.org/10.1021/acsnano.5b01641.

(64) van der Hoeven, J. E. S.; Welling, T. A. J.; Silva, T. A. G.; van den Reijen, J. E.; La Fontaine, C.; Carrier, X.; Louis, C.; van Blaaderen, A.; de Jongh, P. E. In Situ Observation of Atomic Redistribution in Alloying Gold–Silver Nanorods. *ACS Nano* **2018**, *12* (8), 8467–8476. https://doi.org/10.1021/acsnano.8b03978.

(65) Mychinko, M.; Skorikov, A.; Albrecht, W.; Sánchez-Iglesias, A.; Zhuo, X.; Kumar,

V.; Liz-Marzán, L. M.; Bals, S. The Influence of Size, Shape, and Twin Boundaries on Heat-Induced Alloying in Individual Au@Ag Core–Shell Nanoparticles. *Small* **2021**, *17* (34), 2102348. https://doi.org/10.1002/smll.202102348.

(66) Haynes, C. L.; Van Duyne, R. P. Nanosphere Lithography: A Versatile Nanofabrication Tool for Studies of Size-Dependent Nanoparticle Optics. *J. Phys. Chem. B* **2001**, *105* (24), 5599–5611. https://doi.org/10.1021/jp010657m.

(67) Tan, B. J. Y.; Sow, C. H.; Koh, T. S.; Chin, K. C.; Wee, A. T. S.; Ong, C. K. Fabrication of Size-Tunable Gold Nanoparticles Array with Nanosphere Lithography, Reactive Ion Etching, and Thermal Annealing. *J. Phys. Chem. B* **2005**, *109* (22), 11100–11109. https://doi.org/10.1021/jp045172n.

(68) Bechelany, M.; Maeder, X.; Riesterer, J.; Hankache, J.; Lerose, D.; Christiansen, S.; Michler, J.; Philippe, L. Synthesis Mechanisms of Organized Gold Nanoparticles: Influence of Annealing Temperature and Atmosphere. *Cryst. Growth Des.* **2010**, *10* (2), 587–596. https://doi.org/10.1021/cg900981q.

(69) Lee, J.; Lee, J.; Tanaka, T.; Mori, H. In Situ Atomic-Scale Observation of Melting Point Suppression in Nanometer-Sized Gold Particles. *Nanotechnology* **2009**, *20* (47), 475706. https://doi.org/10.1088/0957-4484/20/47/475706.

(70) Little, S. A.; Begou, T.; Collins, R. W.; Marsillac, S. Optical Detection of Melting Point Depression for Silver Nanoparticles via in Situ Real Time Spectroscopic Ellipsometry. *Appl. Phys. Lett.* **2012**, *100* (5), 051107. https://doi.org/10.1063/1.3681367.

(71) Gong, C.; Leite, M. S. Noble Metal Alloys for Plasmonics. *ACS Photonics* **2016**, *3* (4), 507–513. https://doi.org/10.1021/acsphotonics.5b00586.

(72) Ozawa, S.; Morohoshi, K.; Hibiya, T.; Fukuyama, H. Influence of Oxygen Partial Pressure on Surface Tension of Molten Silver. *J. Appl. Phys.* **2010**, *107* (1), 014910. https://doi.org/10.1063/1.3275047.

(73) Battocchio, C.; Meneghini, C.; Fratoddi, I.; Venditti, I.; Russo, M. V.; Aquilanti, G.; Maurizio, C.; Bondino, F.; Matassa, R.; Rossi, M.; Mobilio, S.; Polzonetti, G. Silver Nanoparticles Stabilized with Thiols: A Close Look at the Local Chemistry and Chemical Structure. *J. Phys. Chem. C* **2012**, *116* (36), 19571–19578. https://doi.org/10.1021/jp305748a.

(74) Nanda, K. K.; Sahu, S. N.; Behera, S. N. Liquid-Drop Model for the Size-Dependent Melting of Low-Dimensional Systems. *Phys. Rev. A* **2002**, *66* (1), 013208. https://doi.org/10.1103/PhysRevA.66.013208.

Chapter 4

NANOPTICS APPLICATION: PHOTOLUMINESCENCE AND LASING EMISSION

E.: "But what happens during the emission of light? […] Do you think that my conception is correct? Or can you describe the transition from one stationary state to another in a more precise way?"

H.: "Bohr has taught me that one cannot describe this process by means traditional concepts, i.e., as a process in time and space. With that, of course, we have said very little, no more, in fact, than that we do not know."

W. Heisenberg, "Quantum mechanics and a talk with Einstein" -Physics and beyond (1926)

Introduction

Exciton-photon interaction within coupled systems can dramatically alter the emission properties of a material. This synergistic coupling enables manipulation of emission spectra, enhancement of emission rates, and control over emission directionality, allowing the development of nanoscale functional light sources. Recent advancements in nanofabrication techniques have demonstrated a range of coupled nanosystems, exhibiting significant improvements in emitter decay rates, alongside intensity enhancements of up to 1000 times, achieving precise control over light emission characteristics.[1] For example, advances in plasmonic nanolaser design offer advantages such as reduced threshold emission, real-time wavelength tunability,[2,3] and control on emission characteristics such as off-normal[4] and azimuthal polarization.[5] Given the current success, the surface chemistry and crystallographic control facilitated by colloidal systems could profoundly influence the use of this emerging class of metamaterials for innovative applications in a wide range of scientific and technological fields. The exceptional adaptability of self-assembled colloidal nanoparticle arrays offers a potential route for engineering metasurfaces that enhance the optical response efficiency and, at the same time, allow to engineer a dynamic chemical interaction with the surrounding environment. In this chapter we will discuss the application of our colloidal-based plasmonic metasurfaces in different nanophotonic devices, exploiting the fabrication strategies described in **Paragraph 2.4.1** of **Chapter 2**. In particular, we studied the behavior of squared array colloidal metasurfaces

for promoting lasing emission of a common laser dye (Rhodmine B), two-photon excitation photoluminescence emission of core-shell type QDs, and chiral emission of achiral emitter (Rhodamine B) molecules induced by resonant coupling with colloids arranged into chiral shaped arrays.

4.1 One photon excited stimulated emission in plasmonic metasurfaces

As an, coherent source of narrow bandwidth light, the laser is undoubtedly a cornerstone in the advancement of photonics research. Not only it represents a key tool for many important scientific experiments that rely on photons, but it's also a convenient and effective source of light across a range of wavelengths for technological applications such as optical communications, materials processing, biomedical imaging and therapy.

The research community continues to strive to develop lasers with unprecedented properties and achieve nanolasers that push the limits of size, pulsed lasers with extremely peak powers, devices that operate at new wavelengths or achieve greater efficiencies. However, despite the typically distinct operational signature dictated by laser physics, there is concern within the scientific community about the adequacy of the evidence supporting laser claims in the literature.[6,7]Lasing emission based on plasmonic platforms holds great potential for developing nanoscale light sources and bring biosensing technologies to the next level. This phenomenon relies on Surface Lattice Resonances (SLRs) to coordinate the lasing activity, exploiting the resonances as optical cavities. These cavities not only counteract optical losses but also amplify the localized electromagnetic field, leading to significant enhancements in the emission of gain media.[8,9] The plasmonic nanostructure can function as an optical resonator, amplifying the relaxation rates in the emitter at the emission frequency.

When a radiative dipole (dye molecules) is positioned inside a resonant cavity, its emission intensity is amplified when it matches the resonance frequency (on-resonance) of the cavity and a quenching when it deviates from it (off-resonance). These effects are related to the change in

cavity density of states (DOS) available for the system to radiate. This, in turn, induces a significant increase in the local density of optical states.[10]114 The consequent plasmon-exciton coupling promotes preferential radiative decay for excited molecules, resulting in emissions that are not only enhanced but also highly directional.[11] As such, the presence of plasmonic array cavities can be used to lower lasing thresholds through the high photonic density of states and facilitate the enhancement of optical emission,[12] since $\rho^{LDOS}(\omega) \sim |E_{loc}(\omega)|^2$, where $|E_{loc}(\omega)|^2$ is the local electric field of the cavity normalized to the incident intensity.

Groundbreaking research carried out by Odom's group demonstrated the successful achievement of lasing action *via* lattice modes within plasmonic lattices surrounded by a uniform gain media.[13] They also showcased real-time dynamic tuning of the plasmonic laser spectral output by manipulating the refractive index of the surrounding medium within microfluidic setups.[2] SLRs-based lasing architectures go beyond the mere condition of the emission wavelength and offer additional advantages. They allow the fine control of the emission direction and polarization by changing the lattice parameters, such as period and symmetry points (Γ or M), to match the emission of the emitter.[4,14] The incorporation of hybrid waveguided SLR modes, which arise from variations in the refractive indices between the emitter layer and the substrate, provides a method of tailoring the polarization of the laser emission either radially or azimuthally.[5,15]

The laser emission can also be manipulated through surface engineering of the plasmonic system. Deng and coworkers, for example, have demonstrated that the addition of few-layer graphene over lattices of copper nanoparticles, and combining it with molecular dyes as gain media, can enhance lasing action at lower concentrations and thresholds compared to bare Cu NP lattices.[16] The observed improvements were attributed to π–π interactions between aromatic molecules and graphene, supported by calculations of adhesion energy and simulations of a surface-dye lasing model.

This adaptability in manipulating different facets of the lasing process highlights the potential of plasmonic-based lasing platforms for applications in nanophotonics and biosensing. However, due to the precise control required to achieve high quality optical cavities, the manufacture of photo-emissive metasurfaces device is still restricted to top-down fabrication techniques, such as electron beam lithography (EBL) and focus ion beam (FIB).

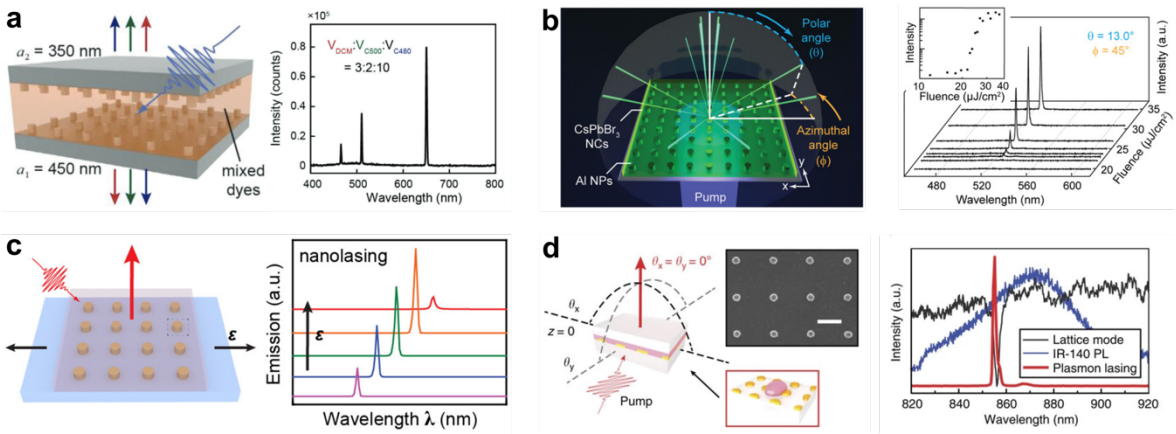

Figure 4.1 **Plasmonic metasurfaces coupled with emitters for room-temperature nanolasers**. (**a**) white laser device based on a sandwiched plasmonic nanoparticle lattice device. The white lasing emission spectra is achieved a mixture of red (DCM), green (C500), and blue (C480) dyes. (**b**) perovskites thin film integrated with Al NPs array lasing emission (threshold 21.9 μJcm^{-2}). (**c**) Stretchable nanolasing device from hybrid quadrupole lattice plasmons modes, reversibly tunable by releasing the elastomeric substrate (applied strain ε). (**d**) Lasing device consisting in Au NP arrays fabricated onto transparent substrate and sandwiched between an IR-140 dye dissolved in an organic solvent and a glass coverslip. SEM image scale bar, 400 nm. **Panel a**: Copyright 2021, Wiley-VCH. Adapted with permission.[17] **Panel b**: Copyright 2022, Wiley-VCH. Adapted with permission.[15] **Panel c**: Copyright 2018, ACS. Adapted with permission.[3] **Panel d**: Copyright 2015, Springer Nature. Adapted with permission.[2]

4.1.1 Lasing emission: the case of 400 nm lattice period

Compared to enhanced spontaneous emission, amplified spontaneous emission (ASE) or related phenomena, the lasing emission can be identified by some characteristics such as: a clear indication of a threshold of output energy as a function of input (or pump) energy, supported by high lasing efficiency above the threshold; strong polarization of the output beam; spatial coherence indicated by a diffraction-limited output beam or speckle; significant narrow emission line; and high directionality.

Moreover, the analysis of the emission characteristics must take into account the specific gain medium, and resonator employed, given the wide array of micro and nano scaled resonators available. While many lasers boast linewidths of a nanometer or less and exhibit beams approaching diffraction-limited quality, the precise values of these parameters vary depending on the design of the resonator and the resolution of the detection instruments, resulting in variability from one laser to another.[6]

Optically, both the absorption and emission characteristics of the system are important for the generation of a stable laser emission. As mentioned in **Paragraph 4.1**, the lasing process requires the presence of a radiative cavity mode aligned with the emission spectrum of the gain medium, which provides the optical feedback crucial to achieve population inversion.[18]

Plasmonic arrays represent an interesting choice of optical cavity since they combine the unique features of both plasmonic building blocks and diffraction gratings, merging amplified scattering cross-section that is inherent to plasmonic resonances, with narrow bandwidths, high-quality factors,[19] and spatial delocalization typical of diffractive phenomena.[13]

These properties make surface lattice resonances (SLRs) suitable to promote such exceptional phenomena like surface-enhanced Raman[20,21] and lasing emission.[15,22,23]

In our case, the choice of RhB, a dye known for its high quantum yield, is motivated by its effective absorption of the pump light at 532 nm.[24] Moreover, the fabricated arrays (see **Chapter 2** and **Experimental Section**) ensure the spectral overlap with the emission of the dye at normal incidence (in the case of $\Lambda = 400$), and off- normal (for $\Lambda = 500$).

The lasing capabilities of our samples were proven utilizing a customized optical setup schematized in **Figure 4.12**

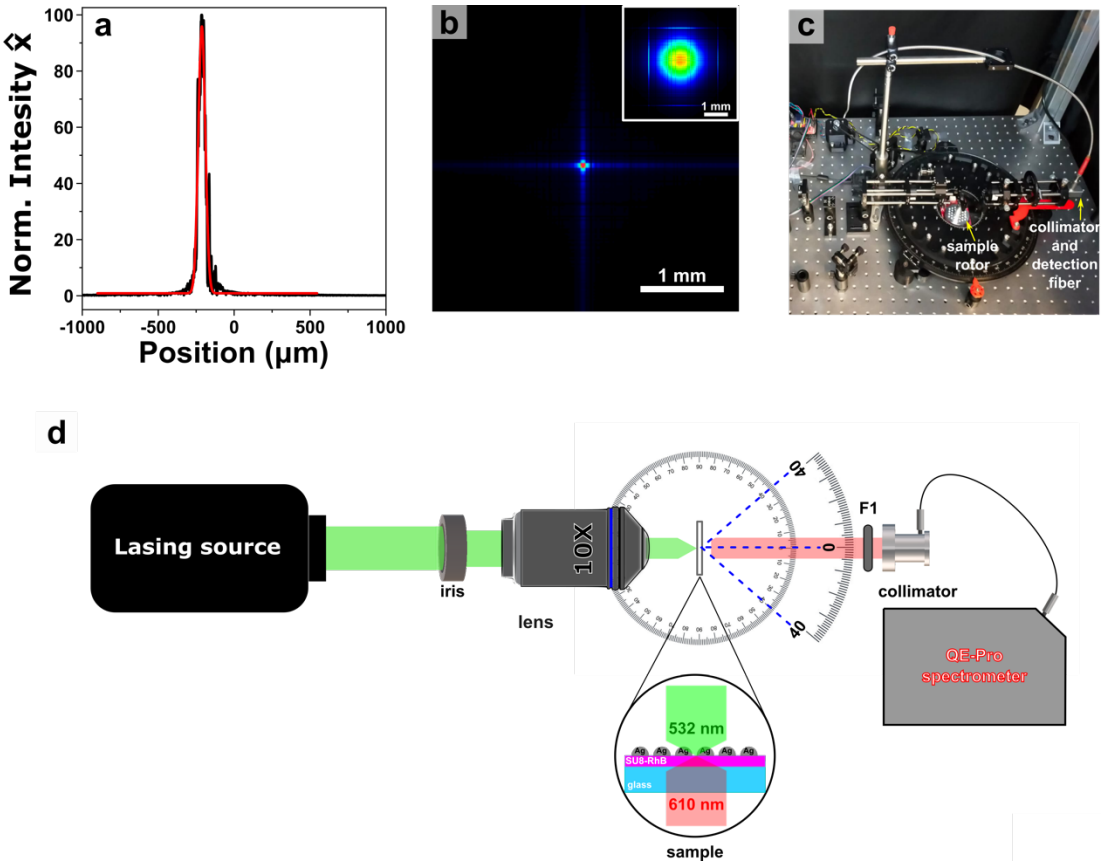

Figure 4.2 **Beam profile and lasing experiment optical set up**. The x, and y profiles of the pumping laser were evaluated by using a beam profiler, to extrapolate an illumination spot area. (**a**) Representation of the Gaussian fit of the laser profile incident on the sample along the $\hat{x}$ direction, after passing through a 10x objective lens. The spot size profile results 46.0 ± 0.4 μm with (R-square = 0.95). (**b**) Beam profiler image acquired by software and referred to the spot captured beyond the 10x objective lens. The original laser spot evaluated without any optical element is showed in the inset. (**c**) Digital picture of the experimental set up on built on the optical bench. (**d**) Scheme of the set up used for the lasing characterization (F1 is the long pass edge filter with high transmission to suppress the 532 nm wavelength).

In brief, a pump laser (532 nm wavelength, with a pulse width of 1.5 ns, illumination area of 46.0 ± 0.4 μm, **Figure 4.2 a**, **b**) was controlled by a custom *LabView* software (, allowing precise control of parameters such as pulse number and repetition rate using an external trigger. A low repetition rate (100 Hz) and two excitation pulses per measurement were chosen to reduce the accumulation of triplet states in the dye molecules.[15] These settings not only help to minimize photobleaching effects, but also make it easier to perform a comprehensive set of measurements at the same spot on the sample. Prior to each measurement, the average pump power was recorded using a power meter. When utilizing an array with lattice period of 400 nm, we

observed the emergence of a narrow emission line at normal incidence (with a full width at half maximum (FWHM) of 5 nm, closely matching the resolution of our spectrometer) peaked at 610 nm, in a transversal electromagnetic (TEM) configuration (**Figure 4.3 a**).

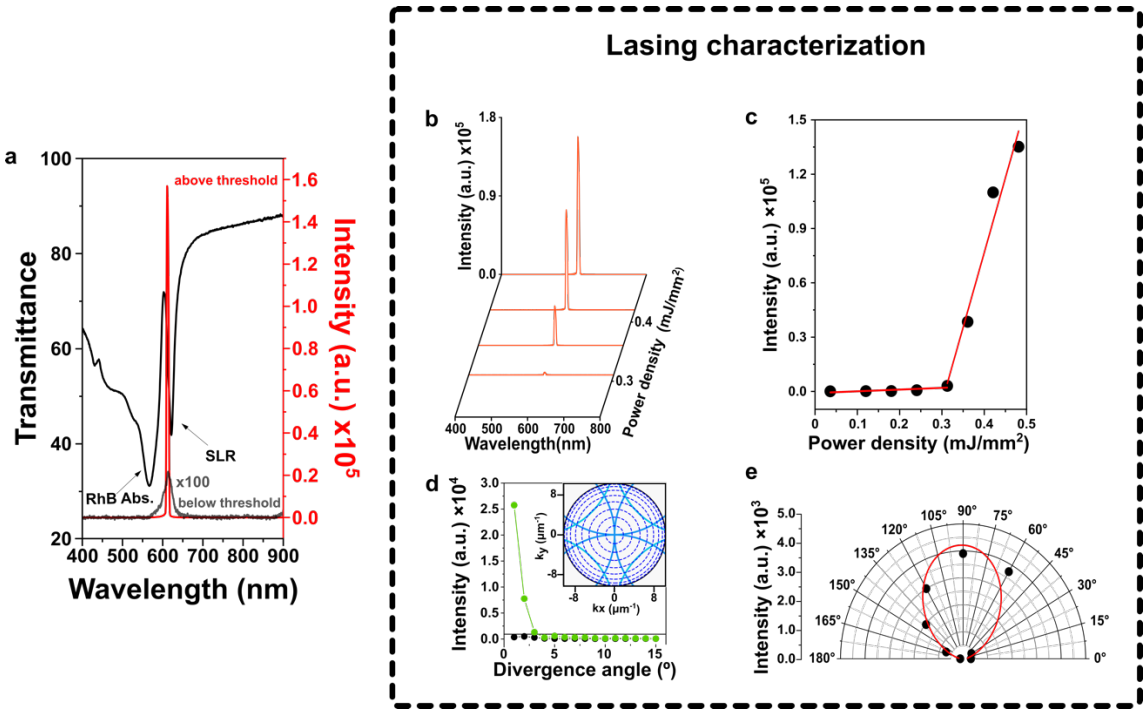

Figure 4.3 **Lasing characterization of the sample with lattice period Λ = 400 nm.** (**a**) Transmission and lasing spectra overlap considering the condition above (**orange** curve) and below (**grey** curve) threshold emission. (**b**) Waterfall graph representing the lasing emission intensity as function of the pump power density (mJ/mm²). (**c**) Power ramp of the emission peak (610 nm). (**d**) Angle divergence study of the lasing emission peak, confirming the high directionality of the lasing emission (**green** trace) compared to the normal emission fluorescence (**black** trace). **Inset**: *k*-space plot of the Rayleigh-Wood anomalies (**solid blue** lines) distributed in all angular directions; the **dotted** circles represent the illumination angles intervals (from 10° to 80°) for azimuthal angles in the full 2π range. (**e**) Intensity of the lasing emission polarization dependence, evaluated as function of the angle α between the plane of the polarizer and the incident plane arising from the sample. The fit of the data point (**red** line) shows a $\sin^2(\alpha)$ dependence.

The pump power density (in $mJ \cdot mm^{-2}$) was consistently measured in the same spot on the sample, revealing the expected threshold behavior typical of lasing emission, as evidenced by a distinct change in slope that occurs at 0.3 mJ/mm² (**Figure 4.3 b, c**). As we will discuss in the next paragraph, the collected data are in good agreement with the classical electrodynamics simulations (FDTD) of our lasing architecture (**Figure 4.7 c**).

Moreover, the laser emission spectral position correlates remarkably well with the lattice resonance of the sample recorded in the transmission spectra, as can be observed in the superimposition in **Figure 4.3 a**). The slight blue shift (<10 nm) can be explained by slight variations in the thickness of the SU8 layer, the lattice parameters, and the incoherence of the white light source.

In order to confirm the stimulated nature of the emission behavior, we evaluate both divergence and polarization dependence. As expected, the recorded laser emission was found to be highly directional (with a divergence angle < 1.5°, **Figure 4.3 d**) and to have a distinct polarization behavior consistent with a sine-squared function predicted by Malus' law (**Figure 4.3 e**).[19,25]

In summary, the formation of a narrow emission profile, characterized by a distinct threshold, linear polarization dependence, minimum deviation and significantly higher intensity (a factor of 10^4 over the PL intensity of the Rhodamine by itself), clearly indicates the stimulated nature of the recorded emission, in accordance with recent findings in the field.[6]

The prepared lasing architectures exhibited sustained performance for about a month before showing gradual degradation, probably due to oxidation of the silver clusters, which reduced the efficiency of the optical cavity. Importantly, the absence of any lasing activity outside of the delimited patterned area, *i.e.* in the presence of randomly dispersed AgNPs, confirms the central role played by the plasmonic array, as shown in **Figure 4.4 a**, **b**.

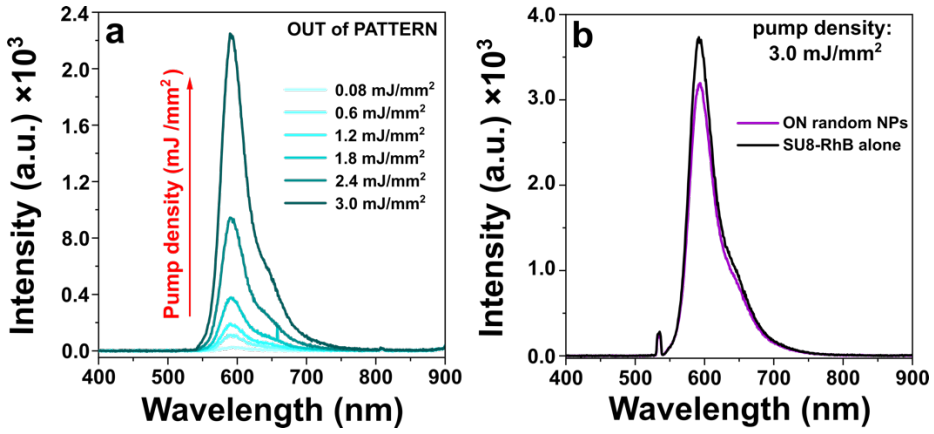

Figure 4.4 (**a**) Photoluminescence profile of Rhodamine B peaked at 590 nm and registered by pumping the system at 532 nm out of the patterned area. In absence of the plasmonic grating, no lasing action is observed,

even increasing the pump power density at the maximum (3.0 mJ/mm^2). (**b**) The role of the lattice resonances is confirmed by the photoluminescence spectra evaluated for a sample made by NPs randomly distributed on a substrate (**purple** curve), where the absence of an emission enhancement can be attributed to quenching effects of the dye molecules, confirming the strong interaction between the AgNPs and the dye molecules.

The mechanism underlying the enhanced stimulated emission involves a combination of plasmonic and photonic effects due to the hybrid nature of surface lattice resonances.[26] Time-correlated single photon counting measurements were carried out to identify any modification on the lifetime (τ) of the system with and without plasmonic array. This would constitute additional evidence of the strong interaction of the plasmonic array, and the dye molecules located in close proximity to the nanoparticle surface. The experiment was performed using a blue pulsed laser (485 nm) at high repetition rate (10 MHz). An accumulation of 10'000 counts was used for each measurement, with a resolution of 50 ps in a decay time region of interest of 40 ns.

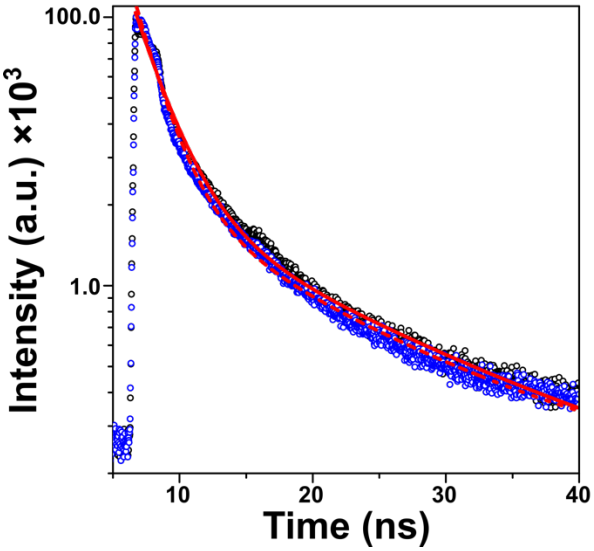

Figure 4.5 Time-resolved decays of a SU8-RhB layer with (**blue** signal) and without (**black** signal) the silver nanoparticles array with lattice period Λ= 400 nm. The **red dashed** and **solid** lines represent the two bi-exponential fits, showing a reduction in lifetime when the fluorophore interact with the plasmonic surface.

Figure 4.5 shows the bi-exponential fit function applied to the decay emission signal of a SU8-RhB layer deposited on a glass substrate, both with (**solid red** line) and without (**dashed red** line) the assembly of silver NP arrays on top. The decay signals were fitted using the function:

$y = y_0 + A_1 e^{-t/\tau 1} + A_2 e^{-t/\tau 2}$, where A_i and τ_i represent the amplitude and lifetime of each component within the sample respectively. Alterations in lifetime can be attributed to the relative contributions of radiative and non-radiative decays within the system.

For the specific case of a sample with lattice period of 400 nm, the lifetime τ_1 can be ascribed to the interaction between fluorophore molecules and the silver NP array, wherein Forster energy transfers promote a reduction in the lifetime of dye molecules situated in close proximity to the NPs (between 20 and 40 nm), from 2.4 ± 0.1 to 2.1 ± 0.1 ns.[27]

The lifetime value τ_2 remains consistent across samples, whether with or without nanoparticles on the substrate (average $\tau_2 = 14.3 \pm 0.1$ns). This contribution can be attributed to the inherent radiative emission decay of the RhB molecules in SU8, influenced by the distribution of other molecules, interactions with polymeric chains, and any surface substrate defects formed.

The relatively small variation in lifetime shown in **Figure 4.5** can be explained considering two factors. First, the conditions used for the generation of a lasing emission (**Figure 4.3**) differs significantly from the one used in the lifetime experiment, due to hardware restriction in our setup. This results in the impossibility to achieve lasing emission during the lifetime experiments. Additionally, due to the high efficiency of Rhodamine B, the effects of Purcell enhancements, determined by dividing the measured lifetime of the system without any plasmonic contribute by the shortest lifetime component ($F_P = \tau_{glass}/\tau_1^{sample}$) are expected to be small.[28]

4.1.2 Modeling of the lasing emission for 400 nm lattice period

Our experimental results were corroborated by extensive simulations. The model employed for the calculations is the classical four-level model involving two electrons (**Figure 4.6**), as described in Ref. 29

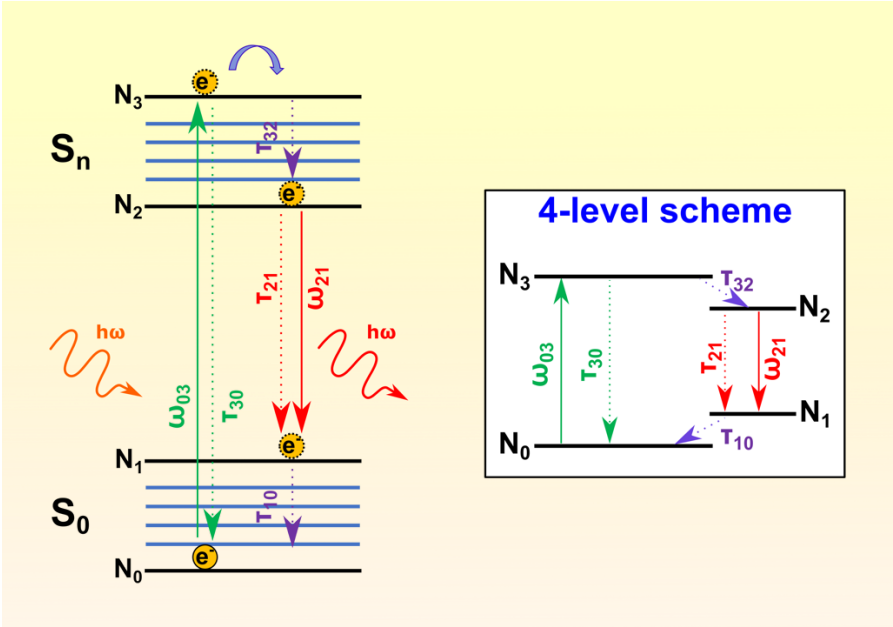

Figure 4.6 The Jablonski diagram is the model generally used for describing photoemission processes. The scheme on the right represents the absorption and stimulated emission rates (**solid green** and **red** arrows respectively). The rate of the spontaneous emission (τ_{30}) is assumed to be very large compared to internal conversion process (τ_{32}, τ_{10}) and stimulated emission (τ_{21}). N_0 and N_1 represent the fundamental level and the excited vibrational level of the ground electronic state (S_0) respectively, N_2 and N_3 represent the lowest vibrational level and the highest vibrational level of the n^{th} excited electronic state (S_n).

The gain medium consists of molecules initially in the ground state. The system is excited by a strong and long quasi-monochromatic pump pulse capable of inducing an electronic transition between N_0 and N_3 (absorption). The electron rapidly decays through a non-radiative process to the N_2 level and a following spontaneous radiative decay can occur from the N_2 to N_1 state. With a sufficiently strong pumping pulse, a population inversion arises between the intermediate states N_2 and N_1, causing the rate of stimulated emission to exceed the rate of spontaneous emission by several orders of magnitude. This facilitates the emission at a specific frequency corresponding to the 2⟶1 states transition. Thus, as the cluster of nanoparticles acts as a cavity, it partially compensates the system's losses, thereby promoting coherent enhanced emission in the far-field, *i.e.* lasing action. The frequencies corresponding to the 0⟶3 and 2⟶1 transitions were set to match respectively the absorption and emission maxima of Rhodamine B. The

lifetime for the stimulated emission was calibrated based on the experimental results of single photon counting reported in **Figure 4.5**.

The 3→2 and 1→0 vibrational transitions were considered off-resonance with the pumping field and characterized by non-radiative behavior; thus, they were presumed to have shorter lifetimes (one-tenth of the electronic transition's lifetime). The concentration of RhB in the SU8 was fixed at 78 mM, and all the other parameters utilized in the simulations are listed in **Table 4.1**.

Table 4.1 Parameters set for the evaluation of the calculated stimulated emission dynamics.

Parameter	Value
ω_{abs}	3.32E ± 15 Hz
$FWHM_{abs}$	0.22E ± 15 Hz
ω_{ems}	3.16E ± 15 Hz
$FWHM_{ems}$	0.21E ± 15 Hz
τ_{rad}	2.4E - 09 s
electron density	4.69E + 25 e^-/m^3

The electric field amplitude spectra were recorded at three different points in space, by placing monitors in air, SU8, and glass.

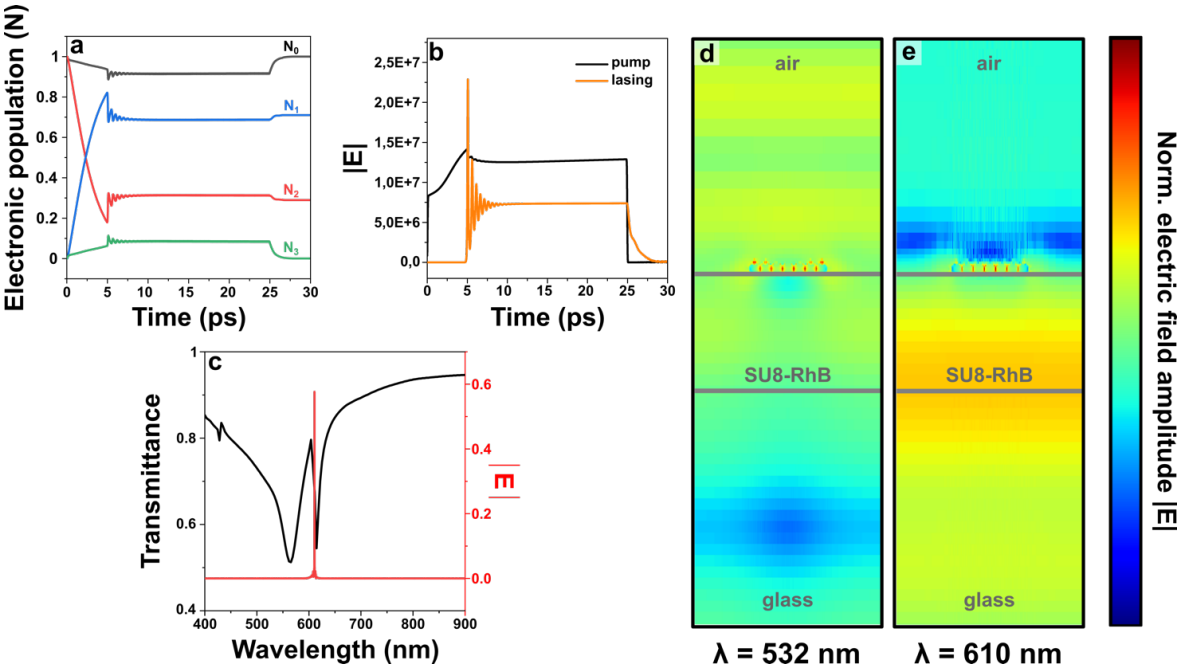

Figure 4.7 (**a**) Gain medium electronic population (N) dynamics evolution modeled as four level system with two electrons. Results monitored from the glass side. (**b**) lasing (**orange** trace) ad pump (**black** trace) pulse amplitude dynamics. The lasing pulse was set as inverse Fourier transform and evaluated with a monitor located from the glass side. The electric field amplitude is considered as $|E|=\sqrt{(E_xE_x^* + E_yE_y^* + E_zE_z^*)}$. The medium starts to lase after about 5 ps and it takes around 10 ps before reaching the steady state of the electronic population. (**c**) Simulated transmittance spectrum and lasing emission (610 nm) overlap for a Λ = 400 nm sample, obtained as the inverse Fourier transform of the frequency-filtered signals (|El) monitored in the gain media. (**d**, **e**) Near-field map calculation for the evaluation of the electric field distribution along the x and y directions. The field amplitude is expressed in logarithmic scale. Specifically, (**d**) the excitation (absorption) occurs by using a pumping pulse at 532 nm and it is monitored form the air side. This generates (**e**) an amplification of electric field at 610 nm directed from the glass side due to the lasing activity.

The frequency domain signals were collected using Lorentzian filters positioned at the pump and laser frequencies, while the time domain was derived by performing an inverse Fourier transform on the filtered signals. Since the electronic population dynamics operate at a much slower frequency than the excitation source, the system requires less than 10 ps from the initial excitation time to reach a steady state in which the populations of N_1 and N_2 remain constant. The steady state was simulated for approximately 15 ps, after which the pump laser was disabled, allowing the system to relax. The sample with Λ = 400 nm was used as a model system, and the lasing process was simulated using finite-difference time-domain method (FDTD, *Lumerical* by Ansys), solving Maxwell's equations on a mesh grid with a semi-classical approach based on a

four-level two electrons gain medium system.[29,30] The population dynamics of the four-level system are shown in **Figure 4.7 a**. The laser emission and pump dynamics are shown in **Figure 4.7 b**. Approximately 5 ps later, the population inversion between the excited and ground states generates the stimulated emission, as evidenced by the peak signal at the emission frequency of 610 nm, spectrally overlapping the simulated hybrid waveguided-SLRs. (**Figure 4.3 c**). A similar response of the system is observed in the air monitor. However, the intensity is much lower compared to the glass counterpart.

In addition, the near-field distributions of the pump and laser modes are shown in the electric field intensity maps in **Figures 4.7 d**, and **e** respectively. At the pump frequency, the gain medium acts as an absorber, with the electric field concentrated above the plasmonic cluster (monitored from the air side, as shown in **Figure 4.7 d**). Conversely, at 610 nm corresponding to the emission wavelength, the electric field is concentrated below the AgNPs array (from the glass side), and the gain medium amplifies the field, as shown in **Figure 4.7 e**.

Overall, our simulations show a remarkable overlap with the collected experimental data, corroborating the lasing nature of the recorded emission, and the important role played by our colloidal metasurface.

4.1.2 Off-normal lasing emission: 500, and 600 nm lattice period cases

The optical feedback facilitated by the presence of a photonic grating could be further enhanced by the great scattering cross-section of the metallic nanoparticle cluster. The presence of the thin SU8 layer and the consequent formation of hybrid waveguided SLR modes has an impact on the synergistic interaction with these photonic effects, providing additional ways to fine-tune the optical properties of the system. This way, through the proper geometric arrangement of the plasmonic/photonic crystals, it is possible not only to capture the emitted light that would otherwise be trapped, but also control with high precision the emission directionality achieving off-normal lasing emission.[4,23]

In this study, we examined the emission characteristics relative to lattice period Λ, leveraging the versatility of template-assisted self-assembly.

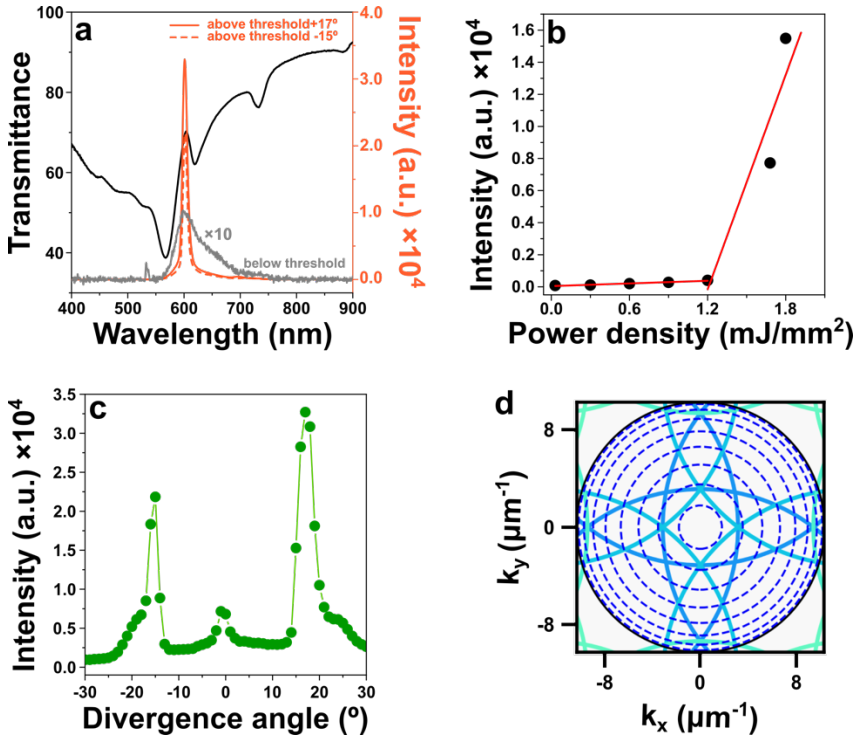

Figure 4.8 **Lasing emission characterization of the sample with lattice period of 500 nm**. (**a**) Transmittance at 17° (**black** line) emission below (**light grey** line) and above (**orange** lines) threshold spectral overlap for or both 17° and -15° (**solid** and **dashed** lines, respectively). (**b**) Power ramp of the emission peak intensity showing the threshold behavior of the stimulated emission. (**c**) Angle divergence study of the lasing emission (from -30° to 30°), confirming the high directionality of the lasing emission with two clear peaks emerging at 17° and -15°. (**d**) Simulated k-space plot of R-W anomalies (**solid blue** lines) distributed in all the angular directions, the **dashed** circles represent the angle intervals (from 10° to 80°), for azimuthal angles in the full 2π range.

Specifically, for Λ = 500 nm displayed in **Figure 4.8**, the simulated band diagram and the experimental contour plots (**Figure 3.7 b** and **3.5 d-f**) predicts that the first order diffraction mode (±1,0) of the square array would intersect with the emission peak of the gain medium at approximately 17°, leading to the generation of stimulated emission signal at off-normal direction, as observed in the k-space plot (**Figure 4.8 d**). A lasing emission activity was detected at 602 nm in both off-normal directions of +17° and -15° (**Figure 4.8 a**), exhibiting a full width at half maximum (FWHM) of 10 nm, and a minimal angular divergence (<1.5°), as shown in **Figure 4.8 c**. The variation in intensity observed between the two lasing conditions (+17° and

-15°) of **Figure 4.8 c** is probably attributable to dye molecules photobleaching effects, induced by the increased intensity pumping imposed by the higher threshold compared to normal emission case (**N.B.:** all the emission data were collected from the same spot). Overall, our experimental findings closely agree with the theoretical predictions. The spectral overlap of the lasing emission with the transmittance spectra captured at 17° (**Figure 4.8 a**) confirmed a similar correlation with the hybrid waveguided-SLR observed previously for the case of Λ = 400 nm (**Figure 4.3 a**). In comparison to Λ = 400 nm, we observed a four-fold increase in the threshold (1.2 mJ/mm^2, **Figure 4.8 b**), that can be ascribed to the shift of $k_{//}$ from 0 to higher values, which amplifies both the scattering cross-section and the radiative losses of the optical modes of the plasmonic arrays.[15]

In the case of Λ = 600 nm, both the transmittance spectrum (**Figure 3.5 g**) and the divergence contour plot (**Figure 3.5 f**) indicate the existence of two diffracted orders, characterized by a dip at 667 nm and another at 910 nm. As indicated by the band diagram illustrated in **Figure 3.7 b-iii**, this gives rise to two distinct scenarios for which lasing can occur. Firstly, the lattice resonance at 910 nm aligns with the first order of diffraction at an angle of approximately of 40°, potentially yielding off-normal emission similarly to what shown for Λ = 500 nm. Alternatively, by leveraging the second order diffraction modes at 667 nm, stimulated emission could be generated at smaller off-normal angles (around 8°).

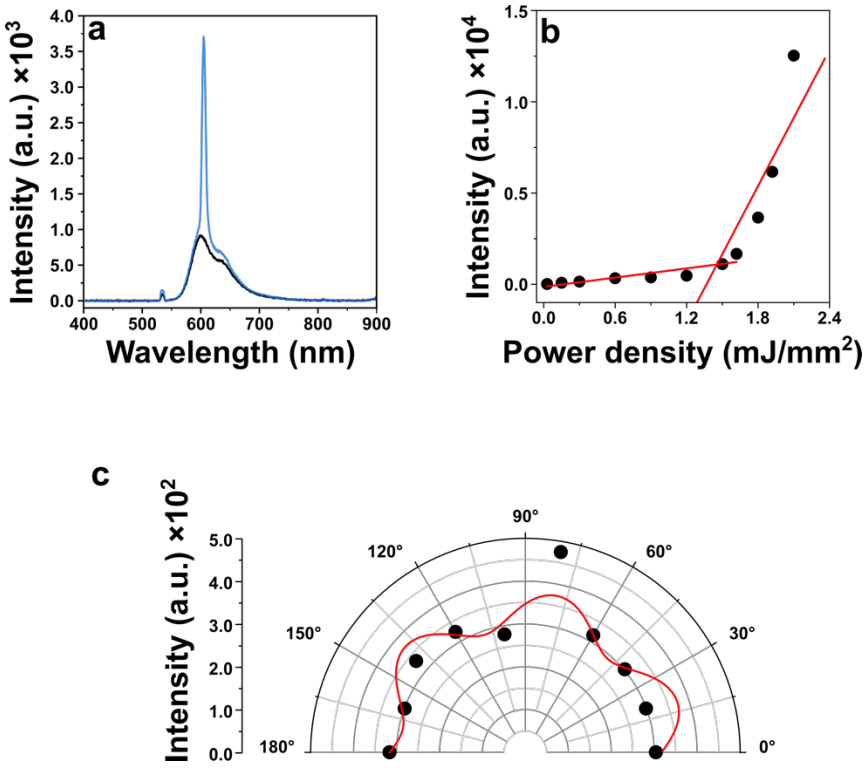

Figure 4.9 **Emission characterization for the sample with lattice period of 600 nm.** (**a**) Emission spectrum of the sample at normal incidence. The emerged peak, above the threshold (**light blue** curve), can be interpreted as amplified spontaneous emission (ASE). (**b**) Power ramp of the Intensity emitted, showing a threshold behavior as expected for ASE case. (**c**) Emission peak intensity measured as function of the polarizer angle (from 0° to 180°) that do not show a clear polarization dependence.

Due to hardware limitations, we were unable to capture emission signals at angles exceeding 35°, and unfortunately, we couldn't detect any lasing activity around 8°. Higher quality plasmonic arrays are required for the emergence of efficient second-order diffraction modes able to promote a stimulated emission, which would require to reduce the optical losses of our colloidal system even further. Interestingly, we did observe a threshold behavior under normal incidence (**Figure 4.9 b**) and the appearance of a distinct peak at 605 nm characterized by a FWHM of 8 nm. However, we interpreted this observation as enhanced spontaneous emission (ASE) caused by exciton re-absorption by the dye molecules. This conclusion was supported by the lack of polarization dependence in the emission (**Figure 4.9 c**), and by the significantly lower intensity compared to the cases with Λ = 400 and 500 nm.

Finally, by mounting a 100× objective in the collection side of the setup we were able to detect a lasing emission (**Figure 4.10**). We hypothesize that this is generated by the first order of diffraction; however, the use of a high numerical aperture to collect the emitted light (NA = 0.8 can capture ≈ 53°) makes it impossible to unequivocally identify the mode responsible for the stimulated emission.

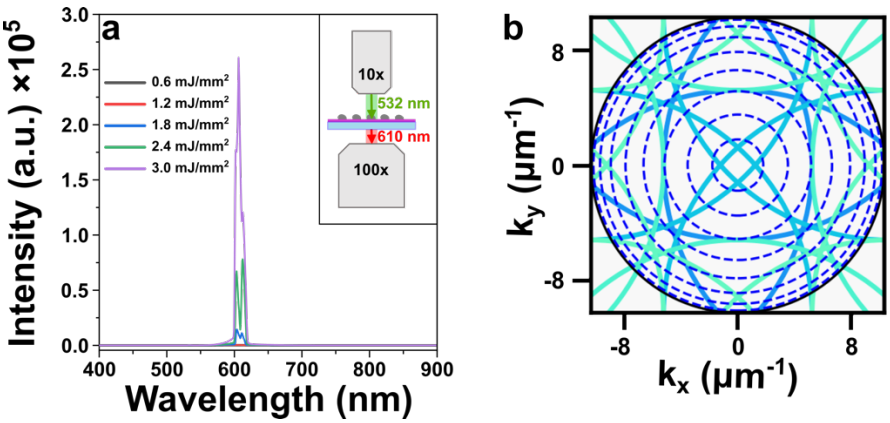

Figure 4.10 Lasing emission of the sample with Λ = 600 nm. (**a**) Two objective lenses were used in the experiment (10x with NA= 0.25, WD = 12.1 mm; 100x with NA=0.8, WD = 3.4 mm). (**b**) Simulated *k*-space plot of the R-W anomalies (**solid blue** lines) distributed in all angular directions; the dashed circles represent the inclination angle intervals (from 10° to 80°), the dashed circles represent the angle intervals (from 10° to 80°), for azimuthal angles in the full 2π range. In the first diffraction order the mode reaches the right position (overlap with the emission of the dye) for angles >35° (**dark blue** lines); the second order reaches the right position for angles <10°.

4.2 Two-photon emission mediated by plasmonic metasurfaces

Isolated noble metal nanoparticles can exhibit photoluminescence properties and optical nonlinearities such as second harmonic generation (SHG) and two-photon absorption (2PA).[31–35] These phenomena were first demonstrated by Boyd *et al.* in 1983,[36] identifying a four step-process involved in the two-photon luminescence of gold nanoparticles.[37,38]

The two-photon photoluminescence (2PPL) properties of metal nanoparticles,[32,39,40] and clusters[41] have been exploited for multiphoton microscopy,[42] enabling deeper imaging of biological systems while reducing radiation damage to cells and tissues.[43] However, compared to organic molecules and semiconductors, the photoluminescent efficiency of metal

nanoparticles is considerably weaker, and the emitted light generally shows broader spectral characteristics,[44] due to non-radiative energy processes of the photoexcited carriers in metals, leading to heating effect and subsequent quenching of photoluminescence.[45] Two-photon (2P) excited fluorescence is one of the most widespread nonlinear optical phenomena. In this process, a fluorophore simultaneously absorbs two photons with identical frequency, and emits a photon with energy higher than the one of each of the absorbed photon.[46]

The last decade has witnessed significant effort in the improvement of two-photon fluorescence efficiency in plasmon-emitter coupled systems, benefiting from fluorescent dye probes with larger two-photon absorption cross-sections, and from the rational design of metal nanoparticles capable of enhancing fluorescence intensity, shortening fluorescence lifetime, and improving photostability.[47,48]

Here, the spectral correlation between surface plasmon resonances modes of plasmonic nanostructures and the absorption/emission spectra of fluorophores is crucial, due to the strongly enhanced local excitation field. Additionally, by matching the plasmon resonance with the fluorophores emission band, metallic nanostructures can alter the total quantum efficiency of the system by altering the radiative and nonradiative decay rates.[49]

In two-photon plasmon-emitter coupled systems, a large fluorescence enhancement is expected because of the quadratic dependence of two-photon absorption on the excitation intensity, compared to the linear dependence of the one-photon process.[50] However, a fluorescence quenching always represents significant challenge to the achievement of enhanced total fluorescence by two-photon, requiring a tight control over distance between the chromophores and the metal core.[51]

Notably, systems featuring both excitation and emission enhancements demonstrated a remarkable increase in the quantum dot emission enhancement factor, increasing 5 to 10 times compared to systems relying solely on emission enhancement. This qualitative enhancement

factor highlights the superiority of the double-resonant system coupled with fluorophores over the single-resonant coupling.

The simultaneous absorption of two photons typically occurs at very high photon densities and is localized into small focal volumes defined by the strictly focused laser beam used for excitation. For "standard" one-photon excitation, a photon can trigger fluorescence emission along the entire path of the incident light beam resulting in an elongated region of excitation within the material; on the other hand, the probability of two photons combining exactly at the same place and time decreases rapidly as one moves away from the focus. As result, the emission volume under 2P excitation is highly localized around the focal point, where the excitation intensity is highest (**Figure 4.11**).

Consequently, under 2P excitation the effective interested volume is confined to significantly small regions, leading to improve the detection selectivity of the resulting fluorescence signals among the background noise, allowing the detection of single molecules or particles emitting 2P excited fluorescence, and providing unique opportunities to probe nonlinear interactions between photons and molecules.

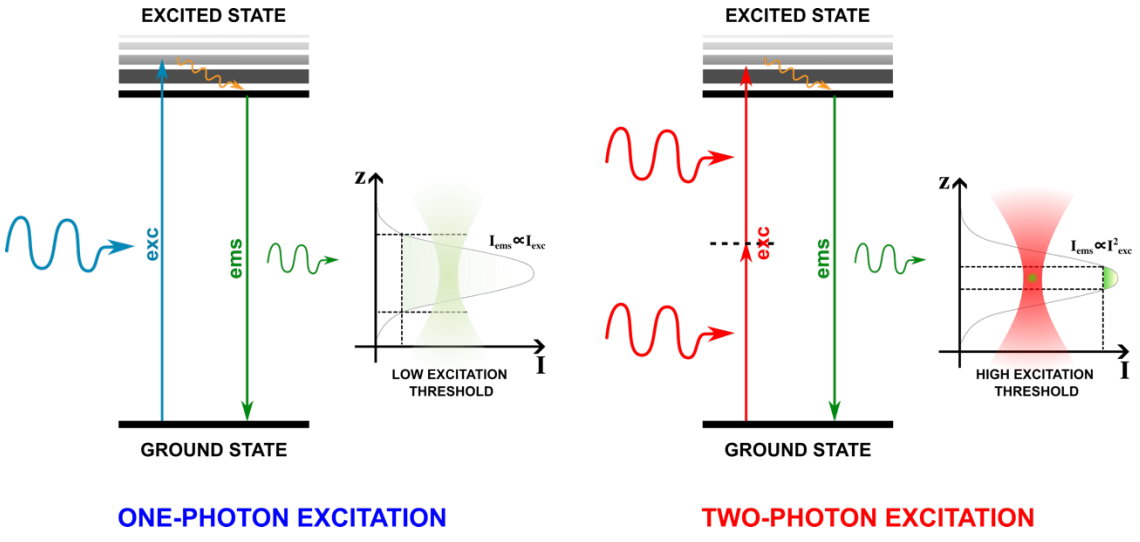

Figure 4.11 Jablonski diagrams for the one-photon (1P) and two-photon (2P) excitation processes, with corresponding emission characteristics around the gaussian focal plane. Comparing the two processes, since 2P excitation requires the simultaneous absorption of two lower-energy photons to achieve the same excitation as a single higher-energy photon in 1P excitation, the photons must have higher combined energy to reach the

excitation threshold, lowering the probability to occur spontaneously compared to single-photon excitation. Moreover, to achieve efficient excitation, this process requires higher laser intensities focused within a small focal volume that contributes to the higher excitation threshold.

First proposed by Maria Goeppert-Mayer in 1931, the two-photon excitation concept marked a turning point in quantum mechanic's research.[52] However, it was during the 1960s that the theoretical foundations of 2P excitation were validated experimentally in pioneering experiments by Franken *et al.* and Kaiser and Garrett.[53,54]

Apart from the aforementioned ability to effectively suppress background noise and improve signal clarity,[46] it enables deeper penetration into biological tissues compared to traditional one-photon excitation methods, which is particularly beneficial in various biomedical applications,[42,55] reducing the associated photodamage.[56,57] Additionally, the highly confined 2P emission volume offers intrinsic optical sectioning capabilities, allowing for precise imaging of three-dimensional structures with resolution comparable to a UV laser scanning confocal microscopy.[58,59]

In recent years, significant advances in nanooptics have paved the way for improving the efficiency (or quantum yield) of 2P excitation process exploiting the unique properties of plasmonic nanostructures to confine the excitation electromagnetic field in close proximity to the fluorophores.[60] In fact, fluorescence resulting from 2P excitation is expected to show significantly greater enhancements than one-photon excitation, attributed to the quadratic dependence of the 2P excitation process on the excitation intensity.[47,61–63]

It is important to break down the 2P absorption and emission as separated processes. In fact, the presence of the plasmon cavity can increase the efficiency of either process if the cavity mode overlaps one of the two bands (absorption or emission). In the first case, the localized electric field enhancement resulting from plasmon resonances can increase the effective cross section for two-photon absorption, facilitating the promotion of electrons to a higher energy level. In the case of emission, the enhanced local electromagnetic field can influence the radiative decay rate of the excited state, potentially leading to enhanced emission rates or altered emission

spectra compared to conventional fluorescence processes. However, some challenges stem from both theoretical and practical domains, including complexities in experimental setups, material limitations, and the possibility of separating the two processes, which often co-exist within the same system. Precise control of experimental parameters such as incident photon flux and polarization can be critical to probe and characterize the underlying mechanisms. Despite the fact that colloidal plasmonic nanoparticles have proven to be particularly advantageous for various applications in near-field enhanced spectroscopy, there are only very few examples in the literature describing the use of colloidal-based plasmonic metasurfaces for the study of two-photon excited processes.[40,60,63]

The primary challenge in these systems is represented by the low yield of the two-photon process, which consequently induces photobleaching of the molecules before the signal can be seen. To address this, one solution can be employing a circulator to replenish the dyes, a strategy unattainable with closed configurations such as Nanoparticles on mirror (NPoM) cavities, or bowties configurations. Alternatively, transitioning to non-molecular emitters, such as quantum dots (QDs), perovskites, and fluorescent polymers represents a viable option.

Motivated by the performance of the lasing architecture presented in **Paragraph 4.1**, we move forward and explore the use of self-assembled colloidal plasmonic metasurfaces as open optical cavities to enhance two-photon excited fluorescence of core-shell type quantum dots species (CdSe/ZnS). A lattice period of 400 nm was chosen to generate a lattice resonance able to overlap with the emission of the QDs around 620 nm, by exploiting the high refractive index layer (QDs/SU8). The hypothesis is that the second diffraction order related to the lattice resonance, which is arising around 420 nm, should match the QDs absorption, giving the opportunity to enhance simultaneously both absorption and emission processes.

The samples were prepared as described in **Paragraph 2.4.1** of **Chapter 2** and **Experimental Section**, and the optical characterization of the transmission profile was carried out as discussed in **Paragraph 3.2** of **Chapter 3**.

In the first experiment, we evaluated the photoluminescence of QDs without any plasmonic cavity. The architecture consists of a 250 nm thick layer of SU8 between the glass and the QDs layer, which is estimated to be around 10 nm thick. Similarly to the previous case discussed in **Paragraph 4.2**, this photoresist layer will ensure the emergence of waveguided-SLR in the presence of the plasmonic metasurface, allowing us to keep the optical cavity completely opened (no index matching layer).

The photoluminescence experiments were performed by pumping the sample first at 515 nm to test the sample under 1P pump fluence, and then with a NIR pulsed laser at 1030 nm for the 2P excitement (the fundamental wavelength of the laser, in order to dispose of the maximum power output). The collected data in the absence of any plasmonic system allowed us to have a reference point when trying to clarify the role of the plasmonic array.

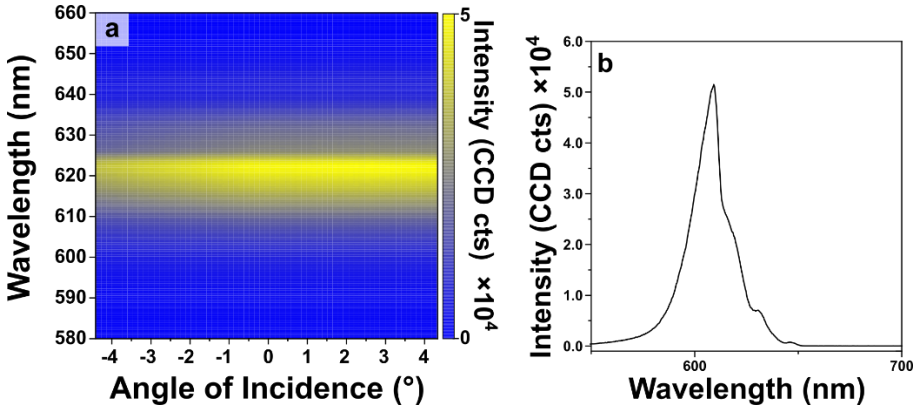

Figure 4.12 (**a**) Intensity map displaying the angular characterization of QDs alone emission pumped at 515 nm, with pump power 0.23 mW. (**b**) Emission spectra at normal incidence (0°) showing an emission maximum at 618 nm.

The QDs alone do not show any angular dependence in their fluorescence, and the pump power dependence follow a sublinear trend when evaluated in the region before photodamaging the sample.

In the presence of the plasmonic array under 1P pumping (515 nm), a strong modulation of the emission is observed while changing the illumination angle from -10° to 10° (**Figure 4.13 a**).

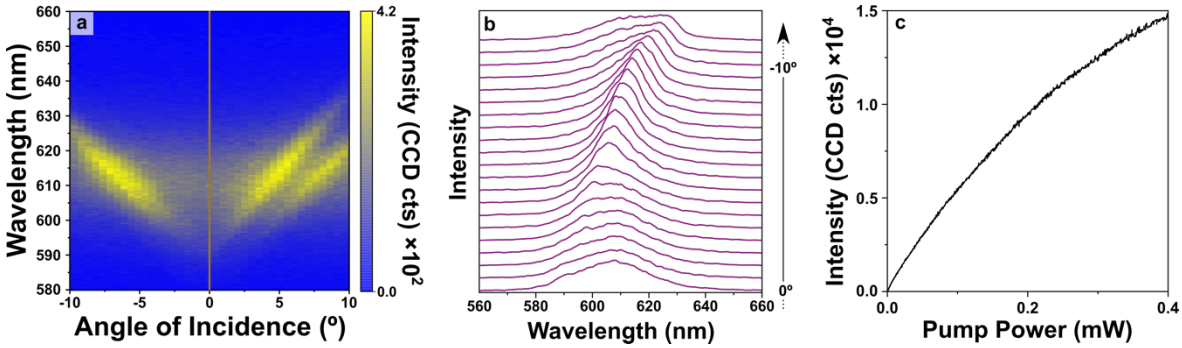

Figure 4.13 Intensity map displaying the emission angular characterization of a sample made with a plasmonic array (lattice pitch of 400 nm) assembled on top of a layer of QDs (excitation wavelength 515 nm, excitation power 6.5 mW). (**b**) Emission spectra modulation evaluated from 0° to -10°. (**c**) Emission power ramp.

Compared to the emission profile at normal incidence (0°), it becomes evident how the presence of the plasmonic arrays modifies both the spectral shape and the peak position of the emission in the region of 580-640 nm as a function of the illumination angle, due to an increase of the scattering cross-section. At normal incidence the emission appears broader (FWHM of 31.1 ± 0.2 nm) and blue shifted, with a maximum peak at 607 nm (**Figure 4.13 b**) compared to the emission of the QDs alone. On the other side, the emission profile modulated by the presence of the plasmonic array shows a narrower bandwidth (FWHM of 16.2 ± 0.2 nm) and a spectral position that follows the diffraction lines. Maximum emission enhancement is observed around -6.5° of the illumination angle when the emission is centered at 613 nm. The exact origin of this enhancement is complicated to identify, as it can also be ascribed to a better detection/excitation alignment at that angle.

Overall, the observed modulation is consistent with a coupling with the near-field enhancements and the spatial delocalization distinctive of diffractive phenomena generated by the metasurface. In order to evaluate the emission intensity dependence of the plasmonic/QDs system from the pump power, the emission profile was examined increasing the pump power up to 0.4 mW (**Figure 4.14 c**). The power ramp shows a similar sublinear dependence from the power as observed in QDs alone.

The same set of experiments was repeated for the two-photon emission of the same sample with 1030 nm excitation. As control experiment, the emission in function of the illumination angle was evaluated even for the sole QDs case.

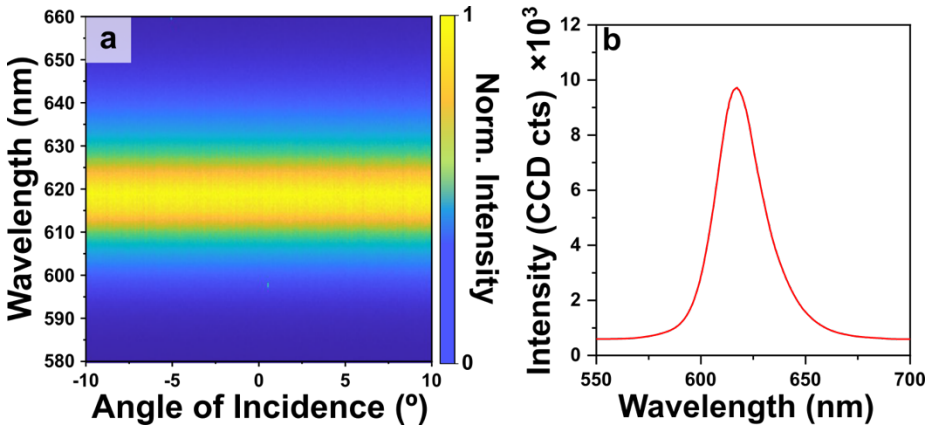

Figure 4.14 (**a**) Intensity map displaying the angular characterization of QDs alone emission pumped at 1030 nm, with pump power 5.5 mW. (**b**) Emission spectra at normal incidence (0°) showing an emission maximum at 618 nm at 18 mW.

As for the 1P excitation case, QDs alone do not show any angular dependence in their fluorescence, and the pump power dependence was evaluated before photodamaging.

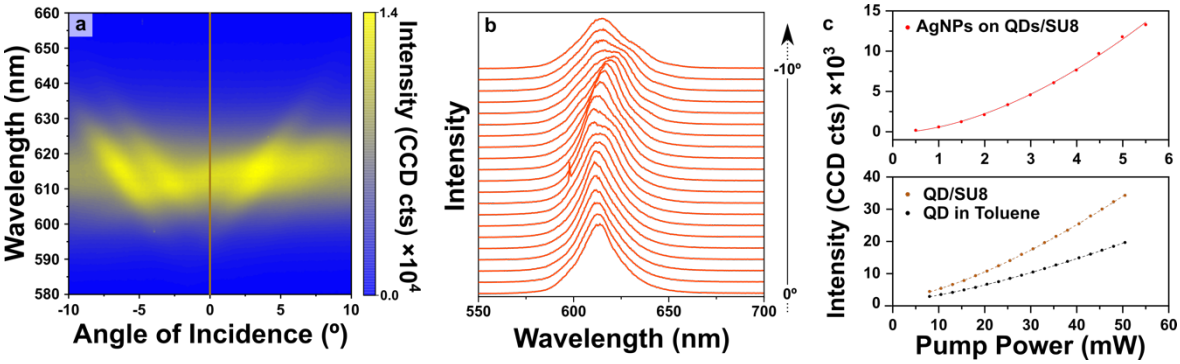

Figure 4.15 Intensity map displaying the emission angular characterization of a sample made with a plasmonic array (lattice pitch of 400 nm) assembled on top of a layer of QDs (excitation wavelength 1030 nm, excitation power 5.5 mW). (**b**) Emission spectra modulation evaluated from 0° to -10°. (**c**) Emission intensity power ramp of AgNPs array on QDs/SU8 substrate (**red** curve **above**), QDs/SU8 (**brown** curve **below**) QDs in solution (**black** curve **below**).

As in the 1P case, a strong modulation and reshaping of the emission is observed as a function of the illumination angle (from -10° to +10°) (**Figure 4.15 a**). The comparison revealed

significant changes in spectral shape of the emission enhanced by the plasmonic array, evidenced by a distinct peak around 613 nm in the spectrum (**Figure 4.15 b**). The emission profile reaches the intensity maximum at -5.5° where the increase of scattering cross-section enhances efficiently the PL emission. The slight difference in angle compared to the 1P data falls within the experimental error in mounting the sample.

The experimental results obtained by changing the illumination angle shows significant alterations in the emission spectral profile, with a second peak arising at 620 nm for illumination angles close to -8.5°.

Comparing the profile at 0° of the 1P and 2P case, in the first case, as already mentioned, the spectral profile appears broaden, probably due to the excitement of localized resonances of the clusters, that in the 2P case are not excited directly by the pump, leading to sharper emission profile. However, it is important to mention that 515 nm falls within the spectral region where a SHG signal of the plasmonic array should arise, affecting the radiative decay pathway of the QDs. The observed different spectral shapes can be the result of competing and co-existing phenomena, including the modulation of far-field spontaneous emission through Purcell enhancement *via* coupling with a plasmonic structure,[11,64] and/or waveguiding effects that led to trap the light for certain angles. Additionally, the QDs deposition onto the SU8 film can produce heterogeneity that influences the 2P photoluminescence process. Moreover, the thickness of the QD film can change the effective refractive index of the waveguide mode, and this allows the wavelengths of the W-SLR modes to be controlled.[65] As a result, specific order of the lattice mode near the Γ point (0°) in the lattice structure shift their wavelengths to match the emission range of the QDs. For this reason, inhomogeneity on the film thickness may cause the variation of the W-SLR cavity modes selection for promoting the emission, which can lead to enhance certain wavelengths or directions of the emitted light. The shape of the emission reflects the interaction among plasmonic nanoparticles within the lattice. For certain angles and directions

(high-symmetry points), the emission can display different branches due to the coupling with specific diffraction modes of the SLR modes, such as (±1, 0) and (0, ±1).[66]

Finally, the potential of plasmonic enhancements by using ultrafast laser pulses could be inherently affected by thermal reshaping effects on the structures and/or the transient broadening of plasmon resonances.[67] Despite the significant advantages offered by plasmonic enhancement, these conditions impose some constrains on the usable power of the laser pulses, that can potentially hinder practical applications.

The analysis of the emission intensity dependence from the pump power was conducted by increasing the pump output up to 6 mW, combining a OD6 filter to cut out any possible leak of the 515 nm second harmonic.

The upconversion due to the 2P excitation should be evident by a quadratic dependence of the emitted light intensity from the illumination intensity ($I_{ems} \propto I^2_{inc}$).[60] However, by fitting the data with a function $y = a+bx^c$ (**Figure 4.15 c**), the exponent c results to be:

Table 4.2 exponent values for the two-photon excited samples.

AgNPs array on QDs/SU8	1.73 ± 0.06	$R^2 = 0.99$
QDs/SU8	1.45 ± 0.013	$R^2 = 0.99$
QDs in solution	1.38 ± 0.010	$R^2 = 0.99$

This discrepancy can be attributed to the fact that with 1030 pump wavelength we are not reaching the strongest quantum yield of the QDs two-photon absorption/emission process, and part of the energy absorbed is lost in non-radiative decays of the photoexcited carriers, such as Auger recombination and exciton reabsorption.[68,69] Despite this, we observe that a good signal to noise ratio is reached at lower excitation power in presence of the plasmonic array compared to the other cases, which suggests an enhancement of the emission due to the strong plasmon-exciton coupling. It is worth noting that the emission of QDs alone comes out at around 620 nm in both 1P and 2P excitation cases, while in presence of the array the emission is observed at 613 nm. This shift can be the sign of to the strong role of the array in boosting the emission

but also the absorption of the QDs, probably through second diffraction order, and thus lowering the optical losses which typically cause the red shift of the emission wavelengths from excitation.

The presence of silver nanoparticles induce some optical nonlinearities and due to the strong excitation of the localized near-fields of both clusters and single particles components can lead to heating effects and plasmon-phonon coupling with subsequent increase of the non-radiative decay pathways and quenching of photoluminescence;[45,70] thus, we cannot exclude that samples starts showing photodamage before the power ramp measurement was complete.

In conclusion, despite the promising preliminary data, further in-depth experimental and theoretical analysis of this phenomenon are essential. One possible way forward could be to vary the emission wavelength and the concentration of the gain media, and/or the period of the array to tune the lattice resonance. This approach could allow a better separation between the far-field and near-field contributions, thus providing a more complete and detailed understanding of the phenomenon.

4.4 Chiral Photoluminescence

Induction and transfer of chirality are the two main approaches to confer chiral properties to achiral inorganic nanomaterials, including strategies such as ligand-induced chirality and chiral spatial organization.[71,72] The versatility of self-assembly emerges once again as a powerful feature for the realization of CPL-active materials. In this context, a variety of chiral or achiral building-blocks can be organized to form nanostructures showing CPL activity. For example, a chiral host can impart CPL activity to an achiral luminophore exploiting various non-covalent interactions such as π-π stacking, and H-bonds. Similarly, an achiral luminophore can be incorporated or encapsulated within a chiral entity, thereby acquiring CPL properties. Furthermore, self-assembly not only facilitates the acquisition of CPL activity but, thanks to the so called "hot-spot engineering" and the manipulation of the associated electric-field

enhancement, leading to an increase the dissymmetry factor. In fact, energy transfers have been identified as an effective route to enhance luminescence intensity, reaching an advanced stage in which the different mechanisms can be carefully designed and controlled. These mechanisms include Förster energy transfer, radiative energy transfer and photon upconversion.[64]

Overall, the combination of energy transfer and self-assembly offers a promising strategy for the development of highly efficient materials with circularly polarized luminescence activity.

In this project, we have tested chiral metasurfaces (assembly of spherical AgNPs) coupled with achiral molecular emitters (Rhodamine B), fabricated as discussed in **Paragraph 2.4.1** of **Chapter 2**, to study circularly polarization properties transfer to the photoluminescence of the emitting molecules.

To automate the measurements, the experimental optical setup was customized using *LabVIEW*-licensed programs. For the PL evaluation, a 532 nm pulsed laser was used to induce an emission in the Rhodamine B molecules embedded in SU8 resin matrix.

As shown in the scheme reproduced in **Figure 4.16**, the light emitted from the sample passes through a quarter wave ($\lambda/4$) plate which transforms each handedness polarization into orthogonal linear polarizations, both directed to a Glan Thompson linear polarizer that allows only the vertical polarization to pass through, while reflecting the horizontal polarization out of the detection axis. Each polarization handedness can be selected by a rotation of $\pm 45°$ of the $\lambda/4$ respect to the linear polarizer vertical axes.

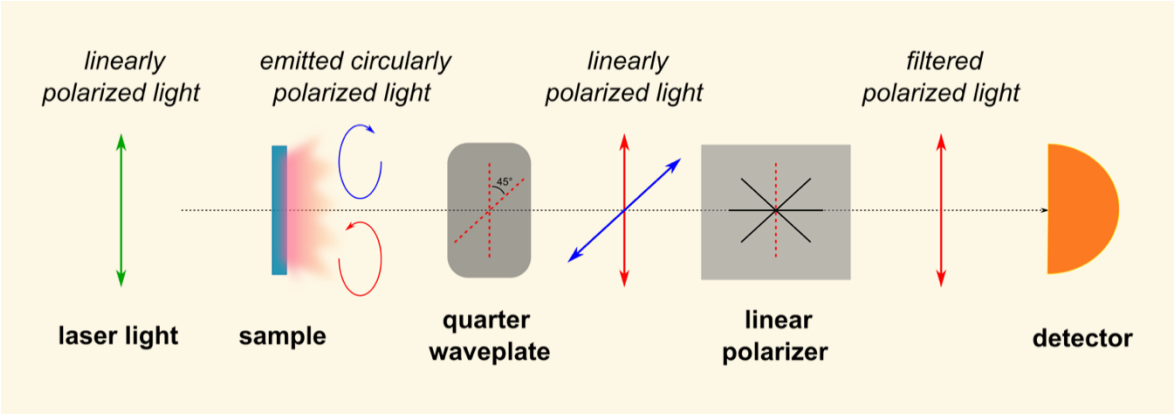

Figure 4.16 Optical set up for the chiral PL experiments.

The magnitude of the photoluminescence process for each polarization along the normal direction is quantified by the *photoluminescence dissymmetry factor* (g_{lum}) as:[73,74]

$$g_{lum} = \frac{\Delta I}{1/2(I_{tot})} = 2\frac{I_{LCP}-I_{RCP}}{(I_{LCP}+I_{RCP})} \qquad \textbf{(4.1)}$$

where the difference in intensity of the emitted light $\Delta I = I_{LCP} - I_{RCP}$ is normalized over the total emitted light Intensity ($I_{tot} = I_{LCP} + I_{RCP}$).

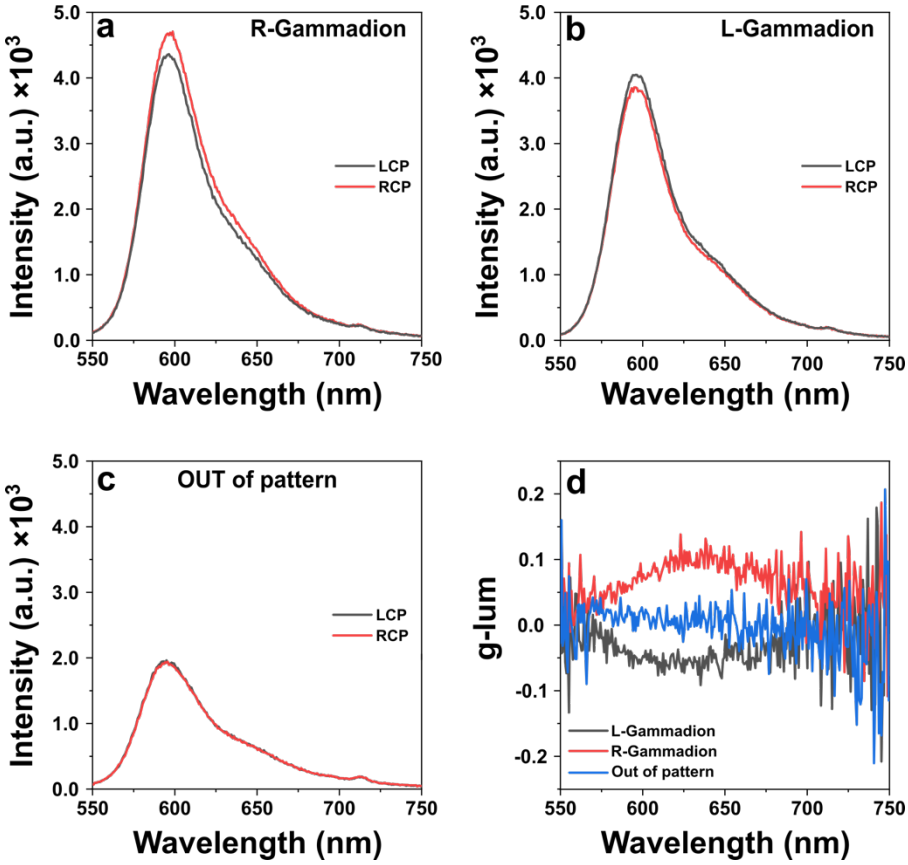

Figure 4.17 Chiral emission evaluation for the sample with AgNPs of 50 nm. (**a**) R-Gammadion, (**b**) L-Gammadion, (**c**) out of pattern, (**d**) g-lum of the metasurfaces comprising L-gammadions (**black** curve), R-gammadions (**red** curve), and out of pattern emission (**blue** curve).

One of the fundamental characteristics of 2D-chiral metasurfaces is their inversion symmetry, as highlighted in previous researches.[75–78] Gammadion shapes exhibit 2D-chirality, meaning their handedness changes when viewed from different angles.[79] This change in the chiroptical response is supported by the presence of chiral near-fields of opposite handedness on either side of the structure when illuminated from different angle.[80] The reciprocity principle in electromagnetics suggests that a system's response to an electromagnetic field remains consistent, regardless of whether the field originates from one direction or the opposite.[75] However, chiral structures are characterized by an inherent asymmetry or handedness, that leads to distinct responses depending on the light direction of propagation, challenging this principle. Typically, to evaluate the asymmetry in the electromagnetic response of the structures and the electromagnetic near fields on each side of Gammadion metasurfaces it is used a quantity known

as optical chirality factor (C), related to the vacuum dielectric permittivity, the angular frequency ω of the EM wave, and the conjugated electric and magnetic field components.

It is defined as the difference between the helicities of the left- and right-circularly polarized components of the EM field, normalized by the total electromagnetic energy density.

Higher values of the chiral factor suggest stronger chiral responses, while lower values indicate weaker or negligible chirality.

When unpolarized light impinges, for example, on a single L-Gammadion structure the integrated chiral factor along the wave's propagation direction changes values from LCP to RCP as it passes through the Gammadion. The refractive index mismatch between the superstrate (air), sample (SU8-RhB) and substrate (glass) disrupt the symmetry of the system. While traveling from air to glass or vice versa, the light refracts differently and alters its propagation direction. This asymmetry caused by the refractive index mismatch can contributes to the observed differences in the chiral activity depending on the detection side.

This change is also transferred to PL properties. As can be observed in **Figure 4.17**, a slight difference in the emission of left- and right- handedness structures were registered (**Figure 4.17 a**, **b**) measuring the PL spectra at normal incidence from the glass side.

L-Gammadion metasurface emits Right-Circularly Polarized (RCP) light, while R-Gammadion emits Left-Circularly Polarized (LCP) (**Figure 4.17 a**, **b**). Moreover, no selective CPL was observed for the case out of pattern (**Figure 4.17 c**). This suggests that the presence of the lattice resonances, generated from isotropic units arranged into chiral shapes, induces a chiral activity in the emission of common dye molecules through resonant coupling and energy transfers.

The structure exhibited preferential emissions of LCP and RCP, with maximum values of -0.08 and 0.1, respectively (**Figure 4.17 e**). These values could be improved by optimizing several structural factors such as feature height, geometry, and refractive index of the environment.

This analysis emphasizes the importance of a comprehensive optical characterization of Circularly Polarized Luminescence (CPL) from 2D metasurfaces.

High-refractive-index materials for example have found application in maximizing the interaction between light and matter in optically active nanostructures enabling to obtain strong electromagnetic resonances.[81] Increasing the refractive index mismatch (to keep the cavity exposed) could help the light extraction from the metasurface and enhance the g_{lum} values.

The fabricated Gammadion structures present several similarities with the lasing architectures discussed in **Paragraph 4.2**. As expected, by increasing the pump power it was observed a strong enhancement of emission intensity and the emergence of an amplified spontaneous emission (ASE) signal (**Figure 4.18**), originated from high internal conversion efficiency that induce the exciton re-absorption by the dye molecules.

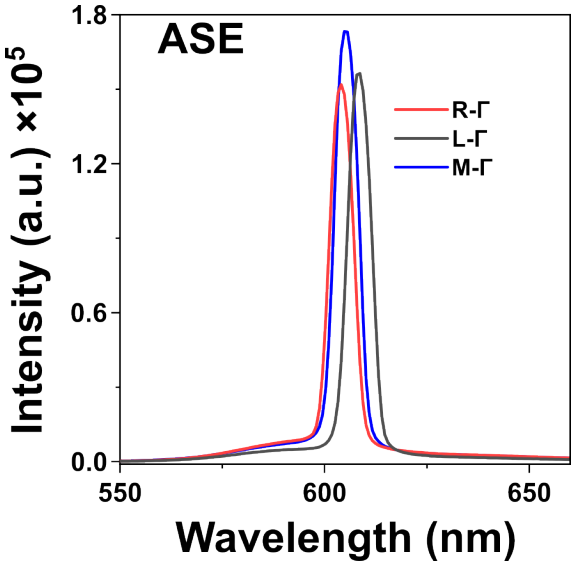

Figure 4.18 Circularly polarized amplified spontaneous emission (ASE) registered in some cases by increasing the power up to 250 μW. The ASE signal results peaked at 597 nm for the R-Gammadion (R-Γ), 596 nm for the L-Gammadion (L-Γ) and 594 nm for the M-Gammadion (M-Γ).

The slight difference between the emission signal peak can be attributed to difference in the quality of the array sample and spot investigated sample-to-sample.

Unfortunately, the high-power density required (up to 1.2 mJ/mm^2) makes it impossible to correctly evaluate the chiral nature of this emission, as the sample is photodamaged after a single

measurement, preventing us to reliably evaluate the dissymmetry factor and perform a complete characterization of a possible chiral amplified spontaneous emission.

In conclusion, we collected promising results towards the development of architectures capable of chiral lasing emission, but further experimental optimization and detail simulations of the system are needed in order to support our results.

4.5 References

(1) Kühn, S.; Håkanson, U.; Rogobete, L.; Sandoghdar, V. Enhancement of Single-Molecule Fluorescence Using a Gold Nanoparticle as an Optical Nanoantenna. *Phys. Rev. Lett.* **2006**, *97* (1), 017402. https://doi.org/10.1103/PhysRevLett.97.017402.

(2) Yang, A.; Hoang, T. B.; Dridi, M.; Deeb, C.; Mikkelsen, M. H.; Schatz, G. C.; Odom, T. W. Real-Time Tunable Lasing from Plasmonic Nanocavity Arrays. *Nat. Commun.* **2015**, *6* (1), 6939. https://doi.org/10.1038/ncomms7939.

(3) Wang, D.; Bourgeois, M. R.; Lee, W.-K.; Li, R.; Trivedi, D.; Knudson, M. P.; Wang, W.; Schatz, G. C.; Odom, T. W. Stretchable Nanolasing from Hybrid Quadrupole Plasmons. *Nano Lett.* **2018**, *18* (7), 4549–4555. https://doi.org/10.1021/acs.nanolett.8b01774.

(4) Guan, J.; Sagar, L. K.; Li, R.; Wang, D.; Bappi, G.; Watkins, N. E.; Bourgeois, M. R.; Levina, L.; Fan, F.; Hoogland, S.; Voznyy, O.; Martins de Pina, J.; Schaller, R. D.; Schatz, G. C.; Sargent, E. H.; Odom, T. W. Engineering Directionality in Quantum Dot Shell Lasing Using Plasmonic Lattices. *Nano Lett.* **2020**, *20* (2), 1468–1474. https://doi.org/10.1021/acs.nanolett.9b05342.

(5) Guan, J.; Sagar, L. K.; Li, R.; Wang, D.; Bappi, G.; Wang, W.; Watkins, N.; Bourgeois, M. R.; Levina, L.; Fan, F.; Hoogland, S.; Voznyy, O.; de Pina, J. M.; Schaller, R. D.; Schatz, G. C.; Sargent, E. H.; Odom, T. W. Quantum Dot-Plasmon Lasing with Controlled Polarization Patterns. *ACS Nano* **2020**, *14* (3), 3426–3433. https://doi.org/10.1021/acsnano.9b09466.

(6) Samuel, I. D. W.; Namdas, E. B.; Turnbull, G. A. How to Recognize Lasing. *Nat. Photonics* **2009**, *3* (10), 546–549. https://doi.org/10.1038/nphoton.2009.173.

(7) Scrutinizing Lasers. *Nat. Photonics* **2017**, *11* (3), 139–139. https://doi.org/10.1038/nphoton.2017.28.

(8) Bergman, D. J.; Stockman, M. I. Surface Plasmon Amplification by Stimulated Emission of Radiation: Quantum Generation of Coherent Surface Plasmons in Nanosystems. *Phys. Rev. Lett.* **2003**, *90* (2), 027402. https://doi.org/10.1103/PhysRevLett.90.027402.

(9) Wang, D.; Guan, J.; Hu, J.; Bourgeois, M. R.; Odom, T. W. Manipulating Light–Matter Interactions in Plasmonic Nanoparticle Lattices. *Acc. Chem. Res.* **2019**, *52* (11), 2997–3007. https://doi.org/10.1021/acs.accounts.9b00345.

(10) Fulmes, J.; Jäger, R.; Bräuer, A.; Schäfer, C.; Jäger, S.; Gollmer, D. A.; Horrer, A.; Nadler, E.; Chassé, T.; Zhang, D.; Meixner, A. J.; Kern, D. P.; Fleischer, M. Self-Aligned Placement and Detection of Quantum Dots on the Tips of Individual Conical Plasmonic

Nanostructures. *Nanoscale* **2015**, *7* (35), 14691–14696. https://doi.org/10.1039/C5NR03546E.

(11) Vecchi, G.; Giannini, V.; Gómez Rivas, J. Shaping the Fluorescent Emission by Lattice Resonances in Plasmonic Crystals of Nanoantennas. *Phys. Rev. Lett.* **2009**, *102* (14), 146807. https://doi.org/10.1103/PhysRevLett.102.146807.

(12) Boddeti, A. K.; Guan, J.; Sentz, T.; Juarez, X.; Newman, W.; Cortes, C.; Odom, T. W.; Jacob, Z. Long-Range Dipole–Dipole Interactions in a Plasmonic Lattice. *Nano Lett.* **2022**, *22* (1), 22–28. https://doi.org/10.1021/acs.nanolett.1c02835.

(13) Zhou, W.; Dridi, M.; Suh, J. Y.; Kim, C. H.; Co, D. T.; Wasielewski, M. R.; Schatz, G. C.; Odom, T. W. Lasing Action in Strongly Coupled Plasmonic Nanocavity Arrays. *Nat. Nanotechnol.* **2013**, *8* (7), 506–511. https://doi.org/10.1038/nnano.2013.99.

(14) Wang, D.; Yang, A.; Wang, W.; Hua, Y.; Schaller, R. D.; Schatz, G. C.; Odom, T. W. Band-Edge Engineering for Controlled Multi-Modal Nanolasing in Plasmonic Superlattices. *Nat. Nanotechnol.* **2017**, *12* (9), 889–894. https://doi.org/10.1038/nnano.2017.126.

(15) Tan, M. J. H.; Park, J.-E.; Freire-Fernández, F.; Guan, J.; Juarez, X. G.; Odom, T. W. Lasing Action from Quasi-Propagating Modes. *Adv. Mater.* **2022**, *34* (34), 2203999. https://doi.org/10.1002/adma.202203999.

(16) Deng, S.; Park, J.-E.; Kang, G.; Guan, J.; Li, R.; Schatz, G. C.; Odom, T. W. Interfacial Engineering of Plasmonic Nanoparticle Metasurfaces. *Proc. Natl. Acad. Sci.* **2022**, *119* (22), e2202621119. https://doi.org/10.1073/pnas.2202621119.

(17) Guan, J.; Li, R.; Juarez, X. G.; Sample, A. D.; Wang, Y.; Schatz, G. C.; Odom, T. W. Plasmonic Nanoparticle Lattice Devices for White-Light Lasing. *Adv. Mater.* **2022**, *n/a* (n/a), 2103262. https://doi.org/10.1002/adma.202103262.

(18) Svelto, O. *Principles of Lasers*; Springer US: Boston, MA, 2010. https://doi.org/10.1007/978-1-4419-1302-9.

(19) Zou, S.; Schatz, G. C. Narrow Plasmonic/Photonic Extinction and Scattering Line Shapes for One and Two Dimensional Silver Nanoparticle Arrays. *J. Chem. Phys.* **2004**, *121* (24), 12606. https://doi.org/10.1063/1.1826036.

(20) Matricardi, C.; Hanske, C.; Garcia-Pomar, J. L.; Langer, J.; Mihi, A.; Liz-Marzán, L. M. Gold Nanoparticle Plasmonic Superlattices as Surface-Enhanced Raman Spectroscopy Substrates. *ACS Nano* **2018**, *12* (8), 8531–8539. https://doi.org/10.1021/acsnano.8b04073.

(21) Zhang, J. Z.; Noguez, C. Plasmonic Optical Properties and Applications of Metal Nanostructures. *Plasmonics* **2008**, *3* (4), 127–150. https://doi.org/10.1007/s11468-008-

9066-y.

(22) Koenderink, A. F. Plasmon Nanocavity Array Lasers: Cooperating over Losses and Competing for Gain. *ACS Nano* **2019**, *13* (7), 7377–7382. https://doi.org/10.1021/acsnano.9b04091.

(23) Winkler, J. M.; Ruckriegel, M. J.; Rojo, H.; Keitel, R. C.; De Leo, E.; Rabouw, F. T.; Norris, D. J. Dual-Wavelength Lasing in Quantum-Dot Plasmonic Lattice Lasers. *ACS Nano* **2020**, *14* (5), 5223–5232. https://doi.org/10.1021/acsnano.9b09698.

(24) Tomazio, N. B.; Boni, L. D.; Mendonca, C. R. Low Threshold Rhodamine-Doped Whispering Gallery Mode Microlasers Fabricated by Direct Laser Writing. *Sci. Rep.* **2017**, *7*, 8559. https://doi.org/10.1038/s41598-017-09293-z.

(25) Khlopin, D.; Laux, F.; Wardley, W. P.; Martin, J.; Wurtz, G. A.; Plain, J.; Bonod, N.; Zayats, A. V.; Dickson, W.; Gérard, D. Lattice Modes and Plasmonic Linewidth Engineering in Gold and Aluminum Nanoparticle Arrays. *JOSA B* **2017**, *34* (3), 691–700. https://doi.org/10.1364/JOSAB.34.000691.

(26) Hamdad, S.; Diallo, A. T.; Chakaroun, M.; Boudrioua, A. The Role of Rayleigh Anomalies in the Coupling Process of Plasmonic Gratings and the Control of the Emission Properties of Organic Molecules. *Sci. Rep.* **2022**, *12* (1), 3218. https://doi.org/10.1038/s41598-022-07216-1.

(27) Reisfeld, R.; Saraidarov, Ts.; Levchenko, V. Strong Emitting Sol–Gel Materials Based on Interaction of Luminescence Dyes and Lanthanide Complexes with Silver Nanoparticles. *J. Sol-Gel Sci. Technol.* **2009**, *50* (2), 194–200. https://doi.org/10.1007/s10971-009-1892-7.

(28) Yadav, R. K.; Liu, W.; Li, R.; Odom, T. W.; Agarwal, G. S.; Basu, J. K. Room-Temperature Coupling of Single Photon Emitting Quantum Dots to Localized and Delocalized Modes in a Plasmonic Nanocavity Array. *ACS Photonics* **2021**, *8* (2), 576–584. https://doi.org/10.1021/acsphotonics.0c01635.

(29) Chang, S.-H.; Taflove, A. Finite-Difference Time-Domain Model of Lasing Action in a Four-Level Two-Electron Atomic System. *Opt. Express* **2004**, *12* (16), 3827–3833. https://doi.org/10.1364/OPEX.12.003827.

(30) Passarelli, N.; Bustos-Marún, R.; Depine, R. Lasing Conditions of Transverse Electromagnetic Modes in Metallic-Coated Micro- and Nanotubes. *J. Phys. Chem. C* **2019**, *123* (20), 13015–13026. https://doi.org/10.1021/acs.jpcc.9b01808.

(31) Yashunin, D. A.; Korytin, A. I.; Smirnov, A. I.; Stepanov, A. N. Second Harmonic Generation and Two-Photon Luminescence from Colloidal Gold Nanoparticles. *J. Phys.*

Appl. Phys. **2016**, *49* (10), 105107. https://doi.org/10.1088/0022-3727/49/10/105107.

(32) Molinaro, C.; El Harfouch, Y.; Palleau, E.; Eloi, F.; Marguet, S.; Douillard, L.; Charra, F.; Fiorini-Debuisschert, C. Two-Photon Luminescence of Single Colloidal Gold Nanorods: Revealing the Origin of Plasmon Relaxation in Small Nanocrystals. *J. Phys. Chem. C* **2016**, *120* (40), 23136–23143. https://doi.org/10.1021/acs.jpcc.6b07498.

(33) Han, F.; Guan, Z.; Tan, T. S.; Xu, Q.-H. Size-Dependent Two-Photon Excitation Photoluminescence Enhancement in Coupled Noble-Metal Nanoparticles. *ACS Appl. Mater. Interfaces* **2012**, *4* (9), 4746–4751. https://doi.org/10.1021/am301121k.

(34) Jiang, C.; Zhao, T.; Yuan, P.; Gao, N.; Pan, Y.; Guan, Z.; Zhou, N.; Xu, Q.-H. Two-Photon Induced Photoluminescence and Singlet Oxygen Generation from Aggregated Gold Nanoparticles. *ACS Appl. Mater. Interfaces* **2013**, *5* (11), 4972–4977. https://doi.org/10.1021/am4007403.

(35) Zhao, T.; Jiang, X.-F.; Gao, N.; Li, S.; Zhou, N.; Ma, R.; Xu, Q.-H. Solvent-Dependent Two-Photon Photoluminescence and Excitation Dynamics of Gold Nanorods. *J. Phys. Chem. B* **2013**, *117* (49), 15576–15583. https://doi.org/10.1021/jp405929w.

(36) Boyd, G. T.; Yu, Z. H.; Shen, Y. R. Photoinduced Luminescence from the Noble Metals and Its Enhancement on Roughened Surfaces. *Phys. Rev. B* **1986**, *33* (12), 7923–7936. https://doi.org/10.1103/PhysRevB.33.7923.

(37) Bouhelier, A.; Bachelot, R.; Lerondel, G.; Kostcheev, S.; Royer, P.; Wiederrecht, G. P. Surface Plasmon Characteristics of Tunable Photoluminescence in Single Gold Nanorods. *Phys. Rev. Lett.* **2005**, *95* (26), 267405. https://doi.org/10.1103/PhysRevLett.95.267405.

(38) Gaiduk, A.; Yorulmaz, M.; Orrit, M. Correlated Absorption and Photoluminescence of Single Gold Nanoparticles. *ChemPhysChem* **2011**, *12* (8), 1536–1541. https://doi.org/10.1002/cphc.201100167.

(39) Zhu, H.; Garai, M.; Chen, Z.; Xu, Q.-H. Two-Photon Excitation of Gold Nanorods Interrupted by Extremely Fast Solvent-to-Metal Electron Transfer. *J. Phys. Chem. C* **2017**, *121* (51), 28546–28555. https://doi.org/10.1021/acs.jpcc.7b10235.

(40) Lu, X.; Punj, D.; Orrit, M. Two-Photon-Excited Single-Molecule Fluorescence Enhanced by Gold Nanorod Dimers. *Nano Lett.* **2022**, *22* (10), 4215–4222. https://doi.org/10.1021/acs.nanolett.2c01219.

(41) Jägeler-Hoheisel, T.; Cordeiro, J.; Lecarme, O.; Cuche, A.; Girard, C.; Dujardin, E.; Peyrade, D.; Arbouet, A. Plasmonic Shaping in Gold Nanoparticle Three-Dimensional Assemblies. *J. Phys. Chem. C* **2013**, *117* (44), 23126–23132. https://doi.org/10.1021/jp406410k.

(42) Helmchen, F.; Denk, W. Deep Tissue Two-Photon Microscopy. *Nat. Methods* **2005**, *2* (12), 932–940. https://doi.org/10.1038/nmeth818.

(43) Olesiak-Banska, J.; Waszkielewicz, M.; Obstarczyk, P.; Samoc, M. Two-Photon Absorption and Photoluminescence of Colloidal Gold Nanoparticles and Nanoclusters. *Chem. Soc. Rev.* **2019**, *48* (15), 4087–4117. https://doi.org/10.1039/C8CS00849C.

(44) Krivenkov, V.; Samokhvalov, P.; Sánchez-Iglesias, A.; Grzelczak, M.; Nabiev, I.; Rakovich, Y. Strong Increase in the Effective Two-Photon Absorption Cross-Section of Excitons in Quantum Dots Due to the Nonlinear Interaction with Localized Plasmons in Gold Nanorods. *Nanoscale* **2021**, *13* (8), 4614–4623. https://doi.org/10.1039/D0NR08893E.

(45) Dulkeith, E.; Niedereichholz, T.; Klar, T.; Feldmann, J.; Von Plessen, G.; Gittins, D.; Mayya, K.; Caruso, F. Plasmon Emission in Photoexcited Gold Nanoparticles. *Phys. Rev. B* **2004**, *70* (20), 205424. https://doi.org/10.1103/PhysRevB.70.205424.

(46) So, P. T. C.; Dong, C. Y.; Masters, B. R.; Berland, K. M. Two-Photon Excitation Fluorescence Microscopy. *Annu. Rev. Biomed. Eng.* **2000**, *2* (Volume 2, 2000), 399–429. https://doi.org/10.1146/annurev.bioeng.2.1.399.

(47) Zhang, T.; Lu, G.; Liu, J.; Shen, H.; Perriat, P.; Martini, M.; Tillement, O.; Gong, Q. Strong Two-Photon Fluorescence Enhanced Jointly by Dipolar and Quadrupolar Modes of a Single Plasmonic Nanostructure. *Appl. Phys. Lett.* **2012**, *101* (5), 051109. https://doi.org/10.1063/1.4742148.

(48) Jung, J.-M.; Yoo, H.-W.; Stellacci, F.; Jung, H.-T. Two-Photon Excited Fluorescence Enhancement for Ultrasensitive DNA Detection on Large-Area Gold Nanopatterns. *Adv. Mater.* **2010**, *22* (23), 2542–2546. https://doi.org/10.1002/adma.200903745.

(49) Sönnichsen, C.; Franzl, T.; Wilk, T.; von Plessen, G.; Feldmann, J.; Wilson, O.; Mulvaney, P. Drastic Reduction of Plasmon Damping in Gold Nanorods. *Phys. Rev. Lett.* **2002**, *88* (7), 077402. https://doi.org/10.1103/PhysRevLett.88.077402.

(50) Zhang, W.; Caldarola, M.; Lu, X.; Orrit, M. Plasmonic Enhancement of Two-Photon-Excited Luminescence of Single Quantum Dots by Individual Gold Nanorods. *ACS Photonics* **2018**, *5* (7), 2960–2968. https://doi.org/10.1021/acsphotonics.8b00306.

(51) Zhao, T.; Yu, K.; Li, L.; Zhang, T.; Guan, Z.; Gao, N.; Yuan, P.; Li, S.; Yao, S. Q.; Xu, Q.-H.; Xu, G. Q. Gold Nanorod Enhanced Two-Photon Excitation Fluorescence of Photosensitizers for Two-Photon Imaging and Photodynamic Therapy. *ACS Appl. Mater. Interfaces* **2014**, *6* (4), 2700–2708. https://doi.org/10.1021/am405214w.

(52) Göppert-Mayer, M. Über Elementarakte Mit Zwei Quantensprüngen. *Ann. Phys.* **1931**, *401* (3), 273–294. https://doi.org/10.1002/andp.19314010303.

(53) Franken, P. A.; Hill, A. E.; Peters, C. W.; Weinreich, G. Generation of Optical Harmonics. *Phys. Rev. Lett.* **1961**, *7* (4), 118–119. https://doi.org/10.1103/PhysRevLett.7.118.

(54) Kaiser, W. Two-Photon Excitation in $CaF_2:Eu^{2+}$ *Phys. Rev. Lett.* **1961**, *7* (6), 229–231. https://doi.org/10.1103/PhysRevLett.7.229.

(55) Theer, P.; Hasan, M. T.; Denk, W. Two-Photon Imaging to a Depth of 1000 Mm in Living Brains by Use of a $Ti:Al_2O_3$ Regenerative Amplifier. *Opt. Lett.* **2003**, *28* (12), 1022–1024. https://doi.org/10.1364/OL.28.001022.

(56) Mohler, W. A.; Simske, J. S.; Williams-Masson, E. M.; Hardin, J. D.; White, J. G. Dynamics and Ultrastructure of Developmental Cell Fusions in the *Caenorhabditis Elegans* Hypodermis. *Curr. Biol.* **1998**, *8* (19), 1087–1091. https://doi.org/10.1016/S0960-9822(98)70447-6.

(57) Squirrell, J. M.; Wokosin, D. L.; White, J. G.; Bavister, B. D. Long-Term Two-Photon Fluorescence Imaging of Mammalian Embryos without Compromising Viability. *Nat. Biotechnol.* **1999**, *17* (8), 763–767. https://doi.org/10.1038/11698.

(58) Denk, W.; Strickler, J. H.; Webb, W. W. Two-Photon Laser Scanning Fluorescence Microscopy. *Science* **1990**, *248* (4951), 73–76. https://doi.org/10.1126/science.2321027.

(59) Gu, M.; Sheppard, C. J. R. Comparison of Three-Dimensional Imaging Properties between Two-Photon and Single-Photon Fluorescence Microscopy. *J. Microsc.* **1995**, *177* (2), 128–137. https://doi.org/10.1111/j.1365-2818.1995.tb03543.x.

(60) Harats, M. G.; Schwarz, I.; Zimran, A.; Banin, U.; Chen, G.; Rapaport, R. Enhancement of Two Photon Processes in Quantum Dots Embedded in Subwavelength Metallic Gratings. *Opt. Express* **2011**, *19* (2), 1617–1625. https://doi.org/10.1364/OE.19.001617.

(61) Zhang, D.-F.; Li, S.; Xu, Q.-H.; Cao, Y. Aggregation-Induced Plasmon Coupling-Enhanced One- and Two-Photon Excitation Fluorescence by Silver Nanoparticles. *Langmuir* **2020**, *36* (17), 4721–4727. https://doi.org/10.1021/acs.langmuir.0c00712.

(62) Jensen, R. A.; Huang, I.-C.; Chen, O.; Choy, J. T.; Bischof, T. S.; Lončar, M.; Bawendi, M. G. Optical Trapping and Two-Photon Excitation of Colloidal Quantum Dots Using Bowtie Apertures. *ACS Photonics* **2016**, *3* (3), 423–427. https://doi.org/10.1021/acsphotonics.5b00575.

(63) Ojambati, O. S.; Chikkaraddy, R.; Deacon, W. M.; Huang, J.; Wright, D.; Baumberg, J. J. Efficient Generation of Two-Photon Excited Phosphorescence from Molecules in Plasmonic Nanocavities. *Nano Lett.* **2020**, *20* (6), 4653–4658.

https://doi.org/10.1021/acs.nanolett.0c01593.

(64) Zhao, T.; Han, J.; Duan, P.; Liu, M. New Perspectives to Trigger and Modulate Circularly Polarized Luminescence of Complex and Aggregated Systems: Energy Transfer, Photon Upconversion, Charge Transfer, and Organic Radical. *Acc. Chem. Res.* **2020**, *53* (7), 1279–1292. https://doi.org/10.1021/acs.accounts.0c00112.

(65) Watkins, N. E.; Guan, J.; Diroll, B. T.; Williams, K. R.; Schaller, R. D.; Odom, T. W. Surface Normal Lasing from CdSe Nanoplatelets Coupled to Aluminum Plasmonic Nanoparticle Lattices. *J. Phys. Chem. C* **2021**, *125* (36), 19874–19879. https://doi.org/10.1021/acs.jpcc.1c05662.

(66) Guan, J.; Bourgeois, M. R.; Li, R.; Hu, J.; Schaller, R. D.; Schatz, G. C.; Odom, T. W. Identification of Brillouin Zones by In-Plane Lasing from Light-Cone Surface Lattice Resonances. *ACS Nano* **2021**, *15* (3), 5567–5573. https://doi.org/10.1021/acsnano.1c00449.

(67) Jollans, T.; Caldarola, M.; Sivan, Y.; Orrit, M. Effective Electron Temperature Measurement Using Time-Resolved Anti-Stokes Photoluminescence. *J. Phys. Chem. A* **2020**, *124* (34), 6968–6976. https://doi.org/10.1021/acs.jpca.0c06671.

(68) Jiang, Y.; Cui, M.; Li, S.; Sun, C.; Huang, Y.; Wei, J.; Zhang, L.; Lv, M.; Qin, C.; Liu, Y.; Yuan, M. Reducing the Impact of Auger Recombination in Quasi-2D Perovskite Light-Emitting Diodes. *Nat. Commun.* **2021**, *12* (1), 336. https://doi.org/10.1038/s41467-020-20555-9.

(69) Agranovich, V. M.; Ratner, A. M.; Salieva, M. Decay of Excitonic Gratings: Effect of Exciton Diffusion and Reabsorption of Exciton Fluorescence. *Solid State Commun.* **1987**, *63* (4), 329–334. https://doi.org/10.1016/0038-1098(87)90919-7.

(70) Zhu, X.; Wang, W.; Yan, W.; Larsen, M. B.; Bøggild, P.; Pedersen, T. G.; Xiao, S.; Zi, J.; Mortensen, N. A. Plasmon–Phonon Coupling in Large-Area Graphene Dot and Antidot Arrays Fabricated by Nanosphere Lithography. *Nano Lett.* **2014**, *14* (5), 2907–2913. https://doi.org/10.1021/nl500948p.

(71) Yang, D.; Duan, P.; Liu, M. Dual Upconverted and Downconverted Circularly Polarized Luminescence in Donor–Acceptor Assemblies. *Angew. Chem. Int. Ed.* **2018**, *57* (30), 9357–9361. https://doi.org/10.1002/anie.201804402.

(72) Sang, Y.; Han, J.; Zhao, T.; Duan, P.; Liu, M. Circularly Polarized Luminescence in Nanoassemblies: Generation, Amplification, and Application. *Adv. Mater.* **2020**, *32* (41), 1900110. https://doi.org/10.1002/adma.201900110.

(73) Maksimov, A. A.; Tartakovskii, I. I.; Filatov, E. V.; Lobanov, S. V.; Gippius, N. A.; Tikhodeev, S. G.; Schneider, C.; Kamp, M.; Maier, S.; Höfling, S.; Kulakovskii, V. D.

Circularly Polarized Light Emission from Chiral Spatially-Structured Planar Semiconductor Microcavities. *Phys. Rev. B* **2014**, *89* (4), 045316. https://doi.org/10.1103/PhysRevB.89.045316.

(74) Yu, C.-L.; Hsiao, Y.-H.; Chang, C.-Y.; Cheng, P.-J.; Lin, H.-T.; Lai, M.-S.; Kuo, H.-C.; Chang, S.-W.; Shih, M.-H. High Circular Polarized Nanolaser with Chiral Gammadion Metal Cavity. *Sci. Rep.* **2020**, *10* (1), 7880. https://doi.org/10.1038/s41598-020-64836-1.

(75) Lobanov, S. V.; Tikhodeev, S. G.; Gippius, N. A.; Maksimov, A. A.; Filatov, E. V.; Tartakovskii, I. I.; Kulakovskii, V. D.; Weiss, T.; Schneider, C.; Geßler, J.; Kamp, M.; Höfling, S. Controlling Circular Polarization of Light Emitted by Quantum Dots Using Chiral Photonic Crystal Slabs. *Phys. Rev. B* **2015**, *92* (20), 205309. https://doi.org/10.1103/PhysRevB.92.205309.

(76) Konishi, K.; Higuchi, T.; Li, J.; Larsson, J.; Ishii, S.; Kuwata-Gonokami, M. Polarization-Controlled Circular Second-Harmonic Generation from Metal Hole Arrays with Threefold Rotational Symmetry. *Phys. Rev. Lett.* **2014**, *112* (13), 135502. https://doi.org/10.1103/PhysRevLett.112.135502.

(77) Seo, I. C.; Lim, Y.; An, S.-C.; Woo, B. H.; Kim, S.; Son, J. G.; Yoo, S.; Park, Q.-H.; Kim, J. Y.; Jun, Y. C. Circularly Polarized Emission from Organic-Inorganic Hybrid Perovskites via Chiral Fano Resonances. *ACS Nano* **2021**, *15* (8), 13781–13793. https://doi.org/10.1021/acsnano.1c05421.

(78) Mendoza-Carreño, J.; Molet, P.; Otero-Martínez, C.; Alonso, M. I.; Polavarapu, L.; Mihi, A. Nanoimprinted 2D-Chiral Perovskite Nanocrystal Metasurfaces for Circularly Polarized Photoluminescence. *Adv. Mater.* **2023**, *35* (15), 2210477. https://doi.org/10.1002/adma.202210477.

(79) Arteaga, O.; Sancho-Parramon, J.; Nichols, S.; Maoz, B. M.; Canillas, A.; Bosch, S.; Markovich, G.; Kahr, B. Relation between 2D/3D Chirality and the Appearance of Chiroptical Effects in Real Nanostructures. *Opt. Express* **2016**, *24* (3), 2242–2252. https://doi.org/10.1364/OE.24.002242.

(80) Petronijevic, E.; Sandoval, E. M.; Ramezani, M.; Ordóñez-Romero, C. L.; Noguez, C.; Bovino, F. A.; Sibilia, C.; Pirruccio, G. Extended Chiro-Optical Near-Field Response of Achiral Plasmonic Lattices. *J. Phys. Chem. C* **2019**, *123* (38), 23620–23627. https://doi.org/10.1021/acs.jpcc.9b06556.

(81) Brongersma, M. L.; Cui, Y.; Fan, S. Light Management for Photovoltaics Using High-Index Nanostructures. *Nat. Mater.* **2014**, *13* (5), 451–460. https://doi.org/10.1038/nmat3921.

Chapter 5

CONCLUSION AND PERSPECTIVES

In summary, the aim of this thesis was to look for new solutions to explore the field of metamaterial chemistry by using colloidal plasmonic metasurfaces. My advancements in alternative fabrication strategies, including colloidal self-assembly and chemical contrast *in situ* growth, have enabled the creation of optical cavities with high quality factors, opening new avenues for investigating nonlinear optical processes.

The collected data showcase the advantages of these methodologies, such as the possibility of tailoring both the localized and collective optical responses by tuning the individual nanoparticle properties, altering the internal structure of the repeating unit, and shaping the overall geometry of the metasurface.

The versatility and flexibility of colloidal nanoparticle arrays could ultimately enable the rational design and engineer of plasmonic metasurfaces matching multiple optical fields, while keeping it freely labelled and fully accessible for further modification, while ensuring a high-quality optical response

As shown in **Chapter 3**, significant alterations in the structural and optical properties of these colloidal plasmonic metasurfaces can be achieved in pre- or post-assembly procedures, by changing the size and composition of the nanoparticles in the repeating units, or by applying thermal annealing treatments, respectively. The seamless integration of different building blocks showing vastly different sizes and compositions paves the way for the creation of arrays of hierarchical structures, offering the potential for creating more sophisticated photonic architectures combining plasmonic, semiconducting and dielectric colloids. In fact, while in our case gold and silver colloids exhibit a statistical distribution within the array, an intriguing future prospect lies in exploiting directional and specific interparticle interactions to achieve greater

control over the colloidal organization within the individual repeating unit. Post-assembly modifications could further exploit this higher level of engineering. In our study, a thermal annealing step was used to produce heterogeneous patchy structures or alloys, achieved simply by adjusting the annealing temperature within the range of 300-450°C. This strategy holds incredible potential for the fabrication of plasmonic structures that can't be precisely targeted by standard top-down lithographic methods. For example, the integration of catalytic metals such as palladium or platinum into this scheme could be particularly interesting for plasmon-based (photo)catalysis and optoelectronic devices.

Moving forward, it would be interesting to explore other chemical processing of colloidal metasurfaces. An interesting future perspectiveI would be to alter the optical response of the system by switching its behavior from metallic to dielectric or semiconductor. For example, silver nanoparticles subjected to oxygen plasma treatments undergo an oxidation reaction without altering their spatial arrangement on the substrate. This oxide layer introduces a bandgap into the electronic structure of the nanoparticles, effectively separating the valence and conduction bands. As a result, the delocalized electrons in metallic silver can no longer move freely, causing the nanoparticles to switch from metallic to dielectric, with significant consequences on their optical response. In a second example, chemical transformation of silver nanoparticles into the semiconductor Ag_2S could be achieved *via* sulfidation reaction, providing another compelling way to showcase the potential of post-assembly modifications. This process involves a controlled reaction wherein sulfur atoms from a sulfidation agent react with the silver atoms on the surface of the nanoparticles to form silver sulfide species, leading to a fundamental change in the composition and structure of the nanoparticles and their toxicity, due to the lower solubility of $A_{g2}S$ relative to elemental [Ag^0].[1] Again, as a result, the electronic structure of the nanoparticles is modified, leading to the transition from metallic to semiconductor state.

These examples allow not only to experiment the versatility of self-assembled metasurfaces but also underscore their potential in enabling precise control over optical properties for various

applications. In addition, the surface chemistry and crystallographic control offered by colloidal systems could significantly impact the use of this new generation of metamaterials in catalysis, sensing and telecommunications.

Another important contribution of this thesis was to demonstrate how colloidal plasmonic metasurfaces could reach the necessary optical quality to promote non-linear optical phenomena such as lasing and 2-photon emission.

Specifically, we have explored two different fabrication strategies*, i.e.* template-assested self-assembly and chemical contrast *in situ* growth, to prepare colloidal-based plasmonic metasurfaces to be used as high-quality optical cavities. In the case of self-assembled structures, we have tested the surface lattice resonances, emerging from free labeled metasurfaces, as optical cavity to promote the low threshold emission of some common emitters (dyes, and quantum dots) in the context of the weak coupling regime.

In the context of hybrid plasmonic-photonic nanostructures the synergy between locally enhanced electromagnetic fields and engineered diffraction effects in periodic lattice geometries can be exploited to facilitate the reduction of ohmic and radiative losses in plasmonic antennas. This hybridization of subwavelength electric field confinement and high-quality lattice resonances places these architectures as essential tools in plasmonics, applicable across a spectrum of applications.[2–6] Moving forward, we believe that our optical cavities made by colloidal nanoparticles can provide enough optical feedback to set a strong coupling regime with further optimization in the architecture such as increasing the concentration of the emitters and optimizing the geometry of the nanostructure. In the strong coupling regime, the energy levels of the hybrid system can differ significantly from those of either the emitter or the optical system alone. Here, the dynamics of the coupled system is not only determined by the original frequencies of the oscillators, but also by the energy exchange process inherent in the coupling. As a result, the energy spectrum of the system is altered, giving rise to new modes with frequencies different from those of the original oscillator modes. The magnitude of this

frequency can shift depending on the strength of the coupling.[7] The appeal of pairing excitons with plasmon modes lies in the extensive control achievable over the latter, facilitated by a variety of advanced nanofabrication methods[8] and a deep comprehension of the intricate interplay between nanostructure specifics and the characteristics of the corresponding plasmon modes.[9]

Moreover, the ability of strong coupling to alter the electromagnetic surroundings of an emitter has been exploited for modifying chemical landscapes and regulating chemical reaction rates,[10] showing catalytic effects, enhancing the selectivity in reactions with more than one product,[11] light harvesting in solar cells,[12] and facilitating the water-oxidation in splitting reactions by increasing photon-to-current conversion efficiency.[13]

After this general overview, we conclude this thesis by presenting our thoughts and perspectives for the individual projects that were carries out in these 3 years.

1. LASING EMISSION

This study showcases the use of template-assisted self-assembly, a cost-effective, versatile, and easily scalable technique, for fabricating high quality plasmonic-based metasurfaces to assist nonlinear optical emission phenomena.

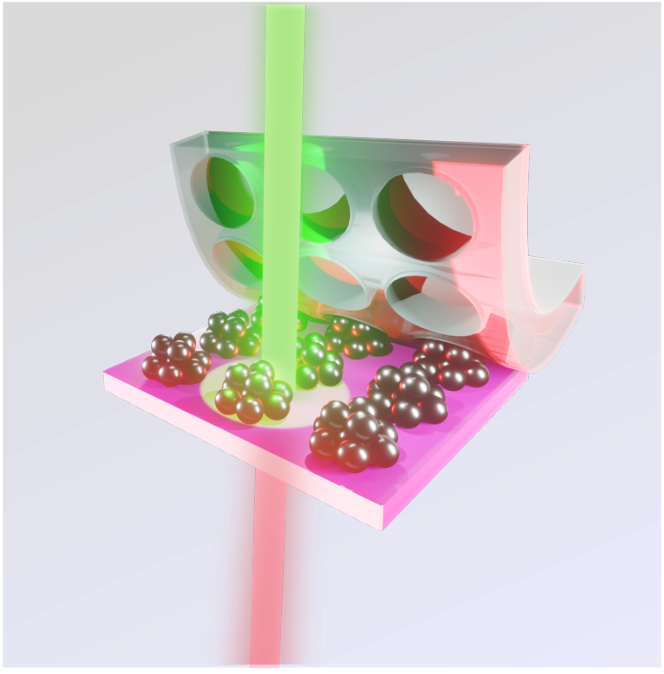

In the developed laser architecture, the gain medium layer acts as a substrate for the construction of the optical cavity, exploiting the hydrophobicity of the photoresist to improve the quality of the assembled plasmonic arrays and improve the generation of hybrid waveguided SLR modes to enhance the light extraction without using index matching layers. A threshold of 0.3 mJ/mm^2 was observed for samples with a lattice period Λ

of 400 nm; however, we believe that an improvement of the optical cavity quality and the use of a more efficient and photostable gain media could potentially lead to lower thresholds and greater performance of the device. Nevertheless, the simplicity of the fabrication process, avoiding metal evaporation steps, annealing treatment, or index matching layers, and the adaptability offered by template-assisted self-assembly mark significant advances for nonlinear optics. Notably, our fabrication methodology circumvents the necessity for clean room facilities. These benefits were shown through the easy manipulation and control achieved on the lasing angular emission through direct modification of the array's lattice parameter, which led to exploit the delocalized nature of hybrid modes and observing a lasing emission at off-normal emission for the case of lattice period of 500 nm.

Supported by numerical simulations and theoretical models, the observed results confirm the attainment of lasing emission under various conditions. Furthermore, the advantage of having an exposed optical cavity offers the opportunity for chemical modification of the plasmonic metasurface, presenting a compelling novelty compared to high-performance architectures fabricated *via* conventional lithographic methods. In the future, this adaptability and their consequent versatility makes them ideal candidate for applications such as photocatalysis, biosensing, energy conversion, and structural color display devices.

1. CHIRAL EMISSION

We have showcased the fabrication of large-area chiral structures using template-induced self-assembly of silver nanoparticles, capable of inducing circularly polarized luminescence (CPL) through resonant coupling to achiral dye molecules. By arranging different AgNPs sizes into gammadion arrays, we successfully generated 2D-chiral metasurfaces. This cost-effective and scalable fabrication method can be readily applied to various types of particles and emitters, including chiral and achiral species, to directly produce circularly polarized light with significant g_{lum} values. In this study, the fabricated 2D-chiral metasurfaces exhibited CPL selectivity, achieving g_{lum} values up to 0.1 at room temperature. We observed R- and L-handed CPL response induced to the emitter from the chiral activity arising in the metasurface. Moreover, in some cases an amplified spontaneous emission (ASE) was observed suggesting the possibility to achieve chiral lasing emission. We believe that the results presented in this study can contribute to the advancement of large-scale selective CPL sources using conventional light emitters. These sources can be further enhanced through chemical modification to achieve even higher CPL values, holding significant potential for several applications.

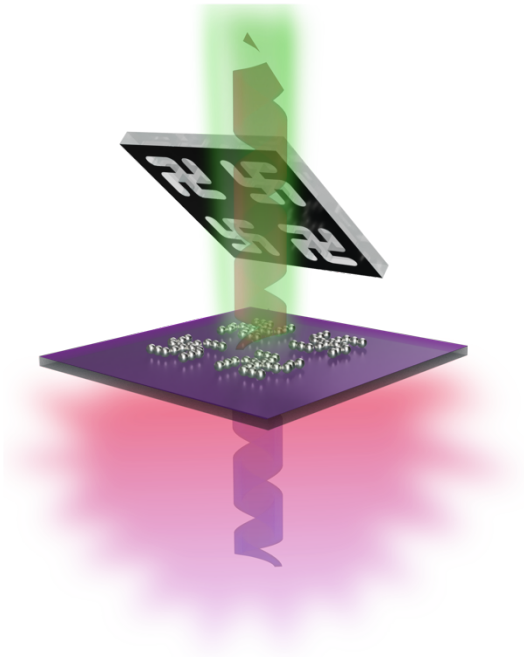

1. TWO-PHOTON EMISSION

In this study we explored the two-photon excited fluorescence of core-shell type quantum dots mediated by the presence of plasmonic lattice array, leveraging an enhancement of the phenomenon provided by self-assembled silver nanoparticles. In our experiment, a lattice period of 400 nm was selected to generate a lattice resonance that could overlap with the emission of the QDs at approximately 620 nm, utilizing the high refractive index layer (QDs/SU8). Our hypothesis is that the second diffraction order associated with the lattice resonance, occurring around 420 nm, should overlap the absorption of the QDs, leading to enhancement of both the emission and absorption processes simultaneously. The result achieved by changing the illumination angle shows significant alterations in the emission spectral profile. A deviation from the typical quadratic dependence of the emission intensity from the excitation was observed. This inconsistency can be attributed to the fact that the optimal quantum yield is not reached for the QDs' two-photon emission process and part of the absorbed energy dissipates through non-radiative pathways and plasmon-phonon coupling. Despite this, we note a favorable signal-to-noise ratio at lower excitation powers when the plasmonic array is present, indicating enhanced emission likely due to robust plasmon-exciton coupling. Our findings underscore the potential of colloidal based plasmonic metasurfaces as excellent nanostructures for exploring applications based on two-photon-excited fluorescence.

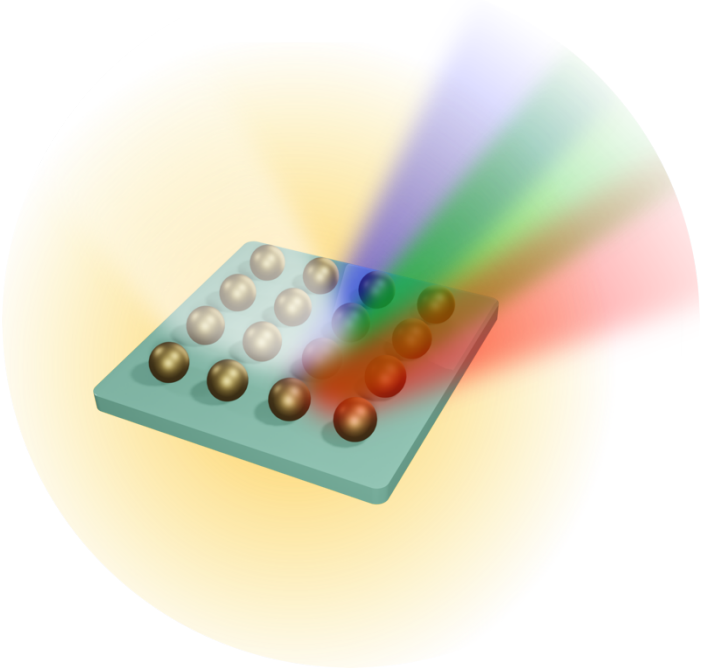

1. CHEMICAL CONTRAST *IN SITU* GROWTH

In this study we have used an unconventional fabrication approach where plasmonic structures are formed directly onto the target substrate material from inorganic precursors, bypassing all the initial colloidal synthesis steps. In terms of fundamental synthetic considerations, understanding substrate wettability, particle-substrate interaction, secondary nucleation, the interplay of reducing agents on the substrate and in solution, the effects of surface charge, the chemical environment and screening effects is crucial to establish reliable protocols for achieving direct growth of nanoparticle arrays and opening up unexplored avenues for future synthetic advances. There are a variety of techniques for the *in situ* growth and overgrowth of colloidal nanoparticles on various substrates such as polymers, oxides, 2D materials and semiconductors.

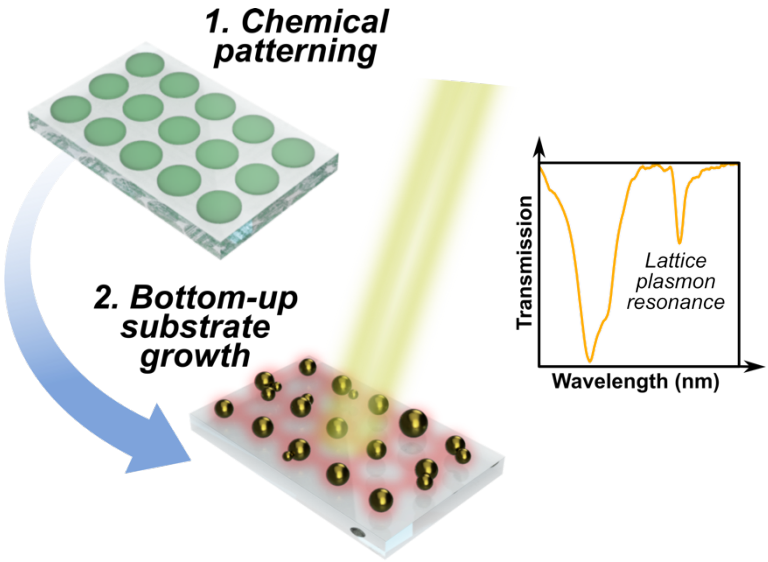

The versatility of the chemical contrast *in situ* growth method presented here makes it well-suited for future investigations into wet-chemical shape control and selective surface growth.

The formation of particles directly on the substrate offers a way of modifying particle geometries in all directions relative to the surface, a level of control typically challenging to attain through self-assembly, such as standing nanowires, oriented anisotropic structures (such as triangles, platelets, nanostars, and chiral nanohooks), truncated particles, and oriented dimers. Similarly to colloidal syntheses, adjustments to the components of the growth solution can improve the yield of a desired structure. One major advantage of *in situ* growth is the strong adhesion or binding of the particles to the substrate. This adhesion removes the need to consider colloidal

stability and solvent compatibility, allowing growth to be explored under more extreme conditions, such as high temperature, high salt concentration and extremely low or high pH environments. It also opens the door to surfactant-free synthesis, facilitating green and sustainable chemistry practices, and enables seamless integration with other materials such as graphene, 2D materials and other metals for applications in magnetism, optics, and catalysis. The demonstration of emerging lattice plasmon resonances through bottom-up, *in situ* growth substrates underlines the potential of this technique as a simple and readily accessible route to engineering plasmonic materials. The benefits of in situ growth goes even further, with exciting perspective for coupling our growth scheme with microfluidics (enabling the exploration of chemical gradients during growth and post-growth surface chemistry modifications), external electromagnetic field (using light to guide nanoparticle growth), and even electrochemical potentials.

5.1 References

(1) Levard, C.; Hotze, E. M.; Colman, B. P.; Dale, A. L.; Truong, L.; Yang, X. Y.; Bone, A. J.; Brown, G. E. Jr.; Tanguay, R. L.; Di Giulio, R. T.; Bernhardt, E. S.; Meyer, J. N.; Wiesner, M. R.; Lowry, G. V. Sulfidation of Silver Nanoparticles: Natural Antidote to Their Toxicity. *Environ. Sci. Technol.* **2013**, *47* (23), 13440–13448. https://doi.org/10.1021/es403527n.

(2) Karg, M.; König, T. A. F.; Retsch, M.; Stelling, C.; Reichstein, P. M.; Honold, T.; Thelakkat, M.; Fery, A. Colloidal Self-Assembly Concepts for Light Management in Photovoltaics. *Mater. Today* **2015**, *18* (4), 185–205. https://doi.org/10.1016/j.mattod.2014.10.036.

(3) Lozano, G.; Grzela, G.; Verschuuren, M. A.; Ramezani, M.; Rivas, J. G. Tailor-Made Directional Emission in Nanoimprinted Plasmonic-Based Light-Emitting Devices. *Nanoscale* **2014**, *6* (15), 9223–9229. https://doi.org/10.1039/C4NR01391C.

(4) Wang, H. Plasmonic Refractive Index Sensing Using Strongly Coupled Metal Nanoantennas: Nonlocal Limitations. *Sci. Rep.* **2018**, *8* (1), 9589. https://doi.org/10.1038/s41598-018-28011-x.

(5) Ramezani, M.; Lozano, G.; Verschuuren, M. A.; Gómez-Rivas, J. Modified Emission of Extended Light Emitting Layers by Selective Coupling to Collective Lattice Resonances. *Phys. Rev. B* **2016**, *94* (12), 125406. https://doi.org/10.1103/PhysRevB.94.125406.

(6) Kou, S. S.; Yuan, G.; Wang, Q.; Du, L.; Balaur, E.; Zhang, D.; Tang, D.; Abbey, B.; Yuan, X.-C.; Lin, J. On-Chip Photonic Fourier Transform with Surface Plasmon Polaritons. *Light Sci. Appl.* **2016**, *5* (2), e16034–e16034. https://doi.org/10.1038/lsa.2016.34.

(7) Törmä, P.; Barnes, W. L. Strong Coupling between Surface Plasmon Polaritons and Emitters: A Review. *Rep. Prog. Phys.* **2014**, *78* (1), 013901. https://doi.org/10.1088/0034-4885/78/1/013901.

(8) Gates, B. D.; Xu, Q.; Stewart, M.; Ryan, D.; Willson, C. G.; Whitesides, G. M. New Approaches to Nanofabrication: Molding, Printing, and Other Techniques. *Chem. Rev.* **2005**, *105* (4), 1171–1196. https://doi.org/10.1021/cr030076o.

(9) Novotny, L. Strong Coupling, Energy Splitting, and Level Crossings: A Classical Perspective. *Am. J. Phys.* **2010**, *78* (11), 1199–1202. https://doi.org/10.1119/1.3471177.

(10) Hutchison, J. A.; Schwartz, T.; Genet, C.; Devaux, E.; Ebbesen, T. W. Modifying Chemical Landscapes by Coupling to Vacuum Fields. *Angew. Chem. Int. Ed.* **2012**, *51* (7), 1592–1596. https://doi.org/10.1002/anie.201107033.

(11) Thomas, A.; Lethuillier-Karl, L.; Nagarajan, K.; Vergauwe, R. M. A.; George, J.; Chervy,

T.; Shalabney, A.; Devaux, E.; Genet, C.; Moran, J.; Ebbesen, T. W. Tilting a Ground-State Reactivity Landscape by Vibrational Strong Coupling. *Science* **2019**, *363* (6427), 615–619. https://doi.org/10.1126/science.aau7742.

(12) Bujalance, C.; Esteso, V.; Caliò, L.; Lavarda, G.; Torres, T.; Feist, J.; García-Vidal, F. J.; Bottari, G.; Míguez, H. Ultrastrong Exciton–Photon Coupling in Broadband Solar Absorbers. *J. Phys. Chem. Lett.* **2021**, *12* (43), 10706–10712. https://doi.org/10.1021/acs.jpclett.1c02898.

(13) Shi, X.; Ueno, K.; Oshikiri, T.; Sun, Q.; Sasaki, K.; Misawa, H. Enhanced Water Splitting under Modal Strong Coupling Conditions. *Nat. Nanotechnol.* **2018**, *13* (10), 953–958. https://doi.org/10.1038/s41565-018-0208-x.

EXPERIMENTAL SECTION

1. Materials

a. Synthesis of gold nanoparticles

Hydrogen tetrachloroaurate trihydrate (HAuCl4 · 3H2O, ≥99.9% CAS: 16961-25-4), L-Ascorbic Acid (AA, ≥99% CAS: 50-81-7), Sodium borohydride (NaBH4, ≥99%, CAS: 16940-66-2), Cetyltrimethylammonium chloride (CTAC, 25% w/w, 756 mM CAS: 112-02-7), Sodium bromide (NaBr, ≥99% CAS: 7647-15-6), Milli-Q water (resistivity 18.2 MΩ·cm at 25 °C).

b. Synthesis of silver nanoparticles

Silver nitrate ($AgNO_3$; 99%, CAS: 7761-88-8), sodium citrate tribasic dihydrated (SC, ≥99.0%, CAS: 6132-04-3); tannic acid (TA, CAS: 1401-55-4); poly(ethylene glycol) methyl ether thiol (PEG, MW 2000 g mol^{-1}); hexadecyltrimethylammonium chloride (CTAC, 25 wt% in water, CAS: 112-02-7), purchased from Sigma Aldrich; Milli-Q water (resistivity 18.2 MΩ·cm at 25 °C).

c. Silicon masters

Original silicon masters of squared arrays (purchased from EULITHA, Switzerland) have lattice periods of 400, 500 and 600 nm (diameter of 230, 277, 338 nm respectively, height of 390 nm) covering a 7 × 7 mm^2 area. The chiral masters (purchased from CONSCIENCE, Sweden) feature gammadion shape arrays with 500 nm width and 120 nm depth, disposed in a squared arrangement forming a lattice of 600 nm pitch in a 3 × 3 mm^2 areas.

d. Silicon master's replica

Silanization of the silicon masters with trichloro (1H,1H,2H,2H-perfluorooctyl) silane (97%, CAS: 78560-45-9) purchased from Sigma Aldrich. SU8-2000.5 (14% in thinner) negative photoresist purchased from KAYAKU Advanced Materials (Westborough, MA 01581). The SU8-2000 thinner (Cyclophentanone) was purchased from MicroCHEM (Westborough, MA 01581).

e. OrmoStamp®

Ormostamp and primer for UV-based nanoimprinting were purchased from Micro resist technology- GmbH (viscosity [Pa·s] = 0.4±0.2, Spectral sensitivity photo-curing 300 – 410 nm, refractive index of 1.51 (cured at 589 nm)).

f. PDMS molds

The hard PDMS (h-PDMS) used for the replicas of original silicon masters purchased from EULITHA (Switzerland), and was prepared by components purchased from Gelest (CymitQuimica, Spain): (7.0-8.0% vinylmethylsiloxane)-dimethylsiloxane copolymer, trimethylsiloxy terminated (CAS: 67762-94-1), 1,3,5,7-tetramethylcyclotetrasiloxane (95%, CAS: 2370-88-9), platinum-divinyltetramethyldisiloxane complex (2% in Pt in xylene, CAS: 68478-92-2), and (25-35% methylhydrosiloxane)-dimethylsiloxane copolymer, trimethylsiloxane terminated (CAS: 68037-59-2). The stamp backbone is made of soft PDMS (s-PDMS) in ratio 10:1 of monomer and cross-linker.

The s-PDMS(Sylgard 184) used for the stamps was purchased from Dow Corning (Michigan, USA), was preparate in ratio 10:1 of monomer and cross-linker.

g. Self-assembly

Glass substrates were pre-cleaned with piranha solution prepared by mixing Sulfuric acid (H_2SO_4, 95–98% w/w) and Hydrogen peroxide (H_2O_2, 30% w/w) in a 3:1 ratio.

Rhodamine B dye powder was purchased from Sigma Aldrich (RhB, CAS 81-89-9; MW 479.01 g mol^{-1}); core-shell type quantum dots (CdSe/ZnS) stabilized with octadecylamine ligand (powder) was also purchased from Sigma Aldrich; SU8-2000.5 (14% in thinner) negative photoresist was purchased from KAYAKU Advanced Materials (Westborough, MA 01581). The SU8-2000 thinner (Cyclophentanone) was purchased from MicroCHEM (Westborough, MA 01581). Polydimethylsiloxane (PDMS, Sylgard 184) used for the stamps was purchased from Dow Corning (Michigan, USA).

h. In situ growth

Hydrogen tetrachloroaurate trihydrate (HAuCl4 · 3H2O, ≥99.9%, CAS: 16961-25-4), L-Ascorbic Acid (AA, ≥99%, CAS: 50-81-7), N-dodecyl-N,N-dimethyl-3-ammonio-1-propanesulfonate (LSB, 99%, CAS: 14933-08-5), Silver nitrate ($AgNO_3$, ≥99%, CAS: 7761-88-8), Hydrochloric acid (HCl, ACS Reagent 37%, CAS: 7647-01-0), High-performance liquid chromatography (HPLC)-grade sub-micron filtered water, Milli-Q water (resistivity 18.2 MOhm).

Piranha solution for cleaning glass slides (3:1 95-98% w/w sulfuric acid, CAS: 7664-93-9, and 30% hydrogen peroxide, CAS: 7722-84-1; Fisher Scientific).

For the silanization of the masters 1H,1H,2H,2H-perfluorooctyltrichlorosilane (97%, CAS: 78560-45-9) purchased from Alfa Aesar (Thermo Fisher GmbH, Karlsruhe, Germany); Hydroxypropyl cellulose (HPC; average MW ~80,000, average MN ~10,000, powder, 20 mesh particle size (99% through; CAS: 9004-64-2) purchased from Sigma-Aldrich Quimica SL (Madrid, Spain); Polymethylhydrosiloxane (average molecular weight 1,700-3,200, CAS: 63148-57-2) used as a chemical ink was purchased from Merck in Hexane (≥99%, CAS: 110-54-3).; Polydimethylsiloxane (PDMS, Sylgard 184) purchased from Dow Corning (Michigan, USA); Hard PDMS (h-PDMS) mixture components purchased from Gelest (CymitQuimica, Spain): (7.0-8.0% vinylmethylsiloxane)-dimethylsiloxane copolymer, trimethylsiloxy terminated (CAS: 67762-94-1), 1,3,5,7 tetramethylcyclotetrasiloxane (95%, CAS: 2370-88-9), platinum-divinyltetramethyldisiloxane complex (2% in Pt in xylene, CAS: 68478-92-2), and (25-35% methylhydrosiloxane)-dimethylsiloxane copolymer, trimethylsiloxane terminated (CAS: 68037-59-2). All chemicals were used as received.

For the diluted PDMS used as soft sacrificial substrate, it was used Polydimethylsiloxane (PDMS, Sylgard 184) purchased from Dow Corning (Michigan, USA), and Toluene (≥ 99.5%, CAS: 108-88-3) in different volume ratio (30, 40, 50, 70 %w). The h-PDMS stamps were rinsed after each use with Ethanol (99.8%, CAS: 64-17-5), and acetone (99.7%, CAS: 67-64-1).

2. Methods

2.1 Synthesis

Seed-growth techniques, which entail the growth of small particles (seeds) into larger ones, were employed to produce gold nanoparticles of various sizes. Depending on the target dimension, we utilized either a one-step or a multiple-step seed-growth methods. The latter involves the overgrowth of larger particles, prepared as an intermediate stage, that are then used as seeds for the subsequent stages of particle growth.[1]

2.1.1 Seed mediated Au nanoparticles synthesis

Tetrachloroauric acid ($HAuCl_4$) finds extensive use as precursor salt for the synthesis of Au nanoparticles. A characteristic equilibrium that has to be taken into account when synthetizing gold nanoparticle involves the balance between comproportion and disproportion reactions, depending on the relative stability of each species within the mixture. It involves three distinct oxidation states: Au(III) in the precursor, Au(I) as an intermediate, and Au(0) constituting the nanoparticles.[2]

$$Au^{3+} + 2Au^{0} \rightleftarrows 3Au^{+} \qquad \textbf{(1)}$$

In the growth solution, the most stable species is Au(I), leading to the equilibrium being shifted towards comproportion between Au(III) and Au(0), implying that gold nanoparticles will undergo oxidation in the presence of Au(III).[3,4] The shift in this equilibrium to favor the growth is caused by the presence of a mild reducing agent such as AA.

In our protocol, spherical gold nanoparticles with cationic surfaces were prepared in hexadecyltrimethylammonium (CTA(+)) chloride (CTAC). To obtain uniform gold nanoparticles, seed particles (<5 nm) were first prepared in a CTAC solution in the presence of sodium borohydride ($NaBH_4$) as strong reducing agent, which led to the rapid reduction of the

gold salt precursor into Au(0). Ideally, the seeds should exhibit uniform size distribution and maintain consistent crystallographic structure. This goal is practically attained by introducing an excess of a potent reducing agent under vigorous stirring.[5] The second step of the sysnthesis is also carried out in aqueous CTAC solution. However, in this case the reduction of gold ions ($AuCl_4^-$) is realized with a weak reducing agent (ascorbic acid). This is extremely important, as ascorbic acid is not capable of inducing the nucleation of new colloids, and the final reduction to Au(0) can only be achieved on the surface of the small pre-synthetized nuclei used as seed. Ultimately, this led to the growth of gold nanoparticles with diameters ranging from 10 to 100 nm. It is also important to notice how the reactivity of the AA depends on pH, showing a lower reduction potential in acidic conditions and higher at basic pH levels, when AA is cable of reducing Au(I) into Au(0), even in the absence of seeds, compromising the seeded-growth mechanism.[6] For this reason, acidic conditions are almost always a requirement for a AA-driven nanoparticle growth.

Upon adding AA to a growth solution, the reduction of Au(III) to Au(I) occurs, evidenced by the solution becoming colorless (indicating the disappearance of the ligand-to-metal charge transfer band for a d^{10} metal center like Au(I)). This step is pivotal as it ensures that when the seeds are introduced into this growth solution, their oxidation *via* the favorable comproportion reaction is circumvented. As we mentioned before, it is possible to grow 10-100 nm gold nanoparticles in a single step. However, we chose a more complicated synthetic protocol for this thesis, as template-assisted self-assembly gives much more reliable results using colloids with a small size distribution. Specifically, our protocol interchange two growth steps with two oxidation steps, which maximize size homogeneity and sphericity of the produced colloids. The final oxidation step is carried out in the presence of sodium bromide (NaBr), which modifies the redox potentials involved in the equilibrium discussed above due to the formation of $[AuBr_4]$-CTA+ complex.

- ***Gold seeds (1-2 nm)***

Under stirring, 50 μL of a $HAuCl_4$ (0.05 M) solution were added to 5 mL of a CTAC (0.1 M) solution. Then, 200 μL of a $NaBH_4$ (0.02 M) solution freshly prepared was injected under vigorous stirring, to ensure the simultaneous formation of all nuclei dispersed uniformly throughout the solution volume. It's crucial to note that $NaBH_4$ is hygroscopic and can react with atmospheric humidity; hence, this reagent is rapidly weighted and prepared fresh for each use. The solution turns out brownish, indicating the formation of seeds > 2 nm in diameter. After 3 min the mixture was diluted 10 times in CTAC (0.1 M).

- ***10 nm Spheres***

900 μL of the seed solution was added in 10 mL of a CTAC (0.025 M) solution, followed by 40 μL of AA (0.1 M). Then, 50 uL of $HAuCl_4$ (0.05 M) solution was added under vigorous stirring, initiating the growth. The suspension turns red, signaling the growth of the NPs and the emergence of a LSPR around 520 nm. The solution was left stirring at RT for 10 min before the next step. This colloidal suspension is stable at RT for months.

- ***Seeded growth (10-100 nm)***

This synthesis requires a tight control over the temperature of the growth solution. For this reason, the preparation is carried out by submerging the reaction flask in a water bath over a hotplate equipped with a digital thermobar. The following experimental procedure is reported for the preparation of 10 mL of 50 nm NPs. However, the synthesis was typically scaled up to 600 mL.

1. In 10 mL of a CTAC (0.025 M) solution were added 65 μL of 10 nm nanospheres suspension and 25 μL of AA (0.1 M) solution. To prepare 25 nm NPs the amount of 10 nm seeds is increased 10 times.

Under vigorous stirring, 25 μL of $HAuCl_4$ (0.05 M) was added, and then the mixture is left stirring at RT for 30 min to enable the growth of the NPs. The growth time depends on the final dimension to be achieved but is typically completed in about 1 hour. The growth is followed by a significant change in the suspension color, becoming darker due to the red shift of the absorption plasmon band. If the particles are grown above 50 nm, the scattering of the nanoparticles can also be observed.

2. Following the first growth step, the temperature is increased to 40 °C and an aliquot of 25 μL of HAuCl4 (0.05 M) was added to induce the oxidation of the AuNPs, exploiting the comproportion reaction between Au(0) contained in the nanoparticles and the added Au(III). Once the oxidation is completed (45 min), the suspension is heated up to 75 °C, initiating the thermal reduction of the gold over the particle, increasing the dimension of the colloids. This second growth is completed in 20 min.
3. Finally, the suspension is cooled down again at 40 °C. In the final step, 10 mg of NaBr and 25 μL of $HAuCl_4$ were added to the mixture, inducing a second oxidative etching step in the presence of bromide that ultimately improves the spherical shape of the colloid.

Once the synthesis is completed, the particles are cleaned and concentrated by centrifugation for further characterization by Transmission Electron Microscopy (TEM) and UV-Vis spectroscopy. Specifically, AuNPs stabilized by the capping surfactant (CTAC) were centrifugated 2 times (2500 rpm/10 min for 100 nm NPs, 7000 rpm/10 min for 50 nm NPs, 10000 rpm/20 min for 25 nm NPs) and redispersed in certain amount of CTAC (>1 mM).

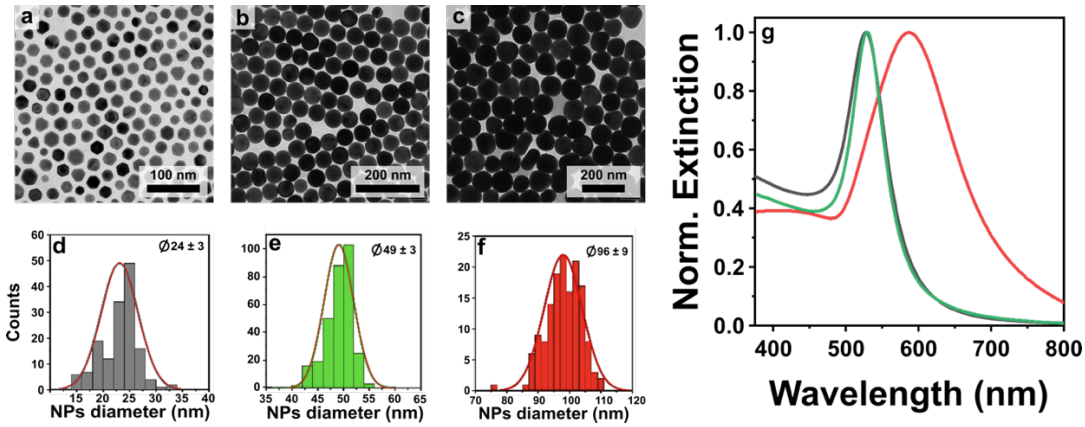

Figure ES 1 (**a**-**c**) AuNPs characterization through Transmission Electron Microscopy (TEM) and (**d**-**f**) size distribution histograms of (**d**) 24± 3 nm, (**e**) 49±3 nm, and (**f**) 96±9 nm in diameter NPs. (**g**)UV-Vis analysis: extinction maximum at 520 for 25 (**black** curve) and 50 nm (**green** curve) NPs, and 610 nm for 100 nm (**red** curve) NPs.

2.1.2 Synthesis of silver AgNPs

The synthesis of AgNPs with different sizes was carried out following the protocol of Bastus et *al.* with slight modifications.[8] The robustness of this method relay in the reproducibility of monodisperse and stable AgNPs. Although the citrate surfactant has been proved to be effective reducing agent to produce spherical noble metals NPs in water with a controlled monodispersity, efforts to achieve the control of the AgNPs morphology during the synthesis by using sodium citrate (SC) faced persistent challenges over the years. The main issue in citrate-mediated synthesis is the dual role of citrate ions as weak reducing agent and a strong complexing stabilizer.

This dual function affects the kinetics of Ag reduction, making it difficult to control the nucleation, growth and shape control. The oxidation of sodium citrate (first in dicarboxyacetone and then in acetoacetate)[9] forms stable complexes with Ag^{+} and Ag^{2+} ions, stabilizing them and slowing down their conversion into Ag_4^{2+}. The latter acts as a nucleation site for the formation of the nanoparticles, but its uncontrolled formation extendsthe heterogeneous nucleation of the AgNPs in time, promoting the formation of new nuclei during the growth process and leading large and polydisperse colloids. Over the years, other strategies to control the reduction kinetics of metal NPs have been widely investigated.

These approaches encompass, for example, incorporating chemical species that limit the reactivity of precursor molecules,[10] reduction *via* oxidative etching,[11] and regulation of the solution temperature.[12]

The synthesis used for this thesis relay on the reaction kinetic control based on the reduction of silver nitrate combining two reducing agents: sodium citrate and tannic acid (TA). The latter is a highly biocompatible mixed gallotannin composed of gallic esters of glucose, to control size and the degree of monodispersity. The rate and extent of nucleation are governed by the concentration of TA. Lower concentrations promote rapid nucleation yielding small particles, while higher concentrations of TA lead to the production of larger particles with increased size dispersity. Specifically, through the temporal evolution of UV-Vis spectra using fixed amount of the TA, it was found that the TA acts as primary reducer, and SC serves as secondary reducer and stabilizer. Additionally, certain amount of TA can be employed for nucleation, while SC takes part in the growth process once catalytic nuclei are already formed. This helps to achieve a high control over the particle's growth.

For the preparation of plasmonic metasurfaces we prepared colloids of 25, 50, and 100 nm (**Figure ES 2**). The smaller nanoparticles were applied in the preparation of lasing architecture as discussed in **Chapter 4**. This size was selected to guarantee the optimal far-field coupling within the plasmonic array units, while limiting at the same time near-field interactions. The use of bigger nanoparticles would imply a significant red shift and broadening effect of the plasmonic response, which would increase the optical losses lowering the quality factor of the lattice resonance.[13]

The following stock solutions were prepared beforehand: $AgNO_3$ (0.025 M), SC (0.025 M), and TA (0.0025 mM). In a three-neck round-bottomed flask immersed in a silicon oil bath were mixed, under vigorous stirring and in the following order, 200 mL of an aqueous solution of SC (0.005 M) and 2 mL of TA.

The solvent evaporation was prevented using a condenser, and the temperature of the system was controlled using a digital thermobar placed in the oil bath.

The temperature was increased until vigorous boiling was observed, followed by the addition of 2 mL of the $AgNO_3$ stock solution. Within 1 minute the color of the growth mixture changes from a faint yellow, due to the presence of TA, to a deep brown shade, due to the presence of Ag seeds with diameter ~ 10 nm diameter. The LSPR absorption peak maximum in this step falls at 402 nm. After the formation of the Ag seeds was completed (in about 5 min), the reaction was cooled to 90 °C to begin the nanoparticle growth.

- ***Growth of AgNPs from 10 to 25 nm***

At this point, 200 μL of SC, 500 μL of TA and 500 μL of $AgNO_3$ of the stock solutions were injected into the growth mixture, with a delay time of ≈1 min between each addition. The suspension is then left stirring for 15 min, after which an aliquot of 1 mL was extracted for UV–vis characterizations. The spectral absorbance measured with a UV–vis spectrophotometer (HITACHI U-3010) is used to estimate the AgNPs size (according to Mie theory).[14] For a size of 25 nm, the plasmon band maximum falls at 408 nm. The growth step was repeated until the desired size was reached. This procedure allows to perform highly controlled growth steps.

- ***Growth of AgNPs from 20 to 200 nm***

In this case the reaction proceeds through less fine growth step until the desired size, involving bigger amounts of reducing agents and precursor. The Ag seeds solution in the same vessel was diluted by extracting 40 mL of sample for further UV-Vis characterization and adding 33 mL of Milli-Q-water. After setting a temperature of 90°C, 1 mL of SC, 3 mL of TA were added from the stock solutions, and, after 1 min, the additions were completed by 2 mL of $AgNO_3$ stock solution. After 30 min, it is possible to proceed with another extraction of 40 mL of the Ag mixture for UV-vis characterization. Similarly to the previous

protocol, the procedure can be repeated starting from the addition of 33 mL with Milli-Q-water until the desired dimension is reached.

At the end of the growth step, in order to eliminate the excess of reagent and concentrate the particles, the colloidal suspension are centrifuged three times (rpm and time depend on the size; 15000 rpm/ 30 min for 25 nm NPs, 5000 rpm/ 15 min for 50 nm NPs, 2500 rpm/10 min for 100 nm NPs), bringing the volume from 200 mL to less than 2 mL.

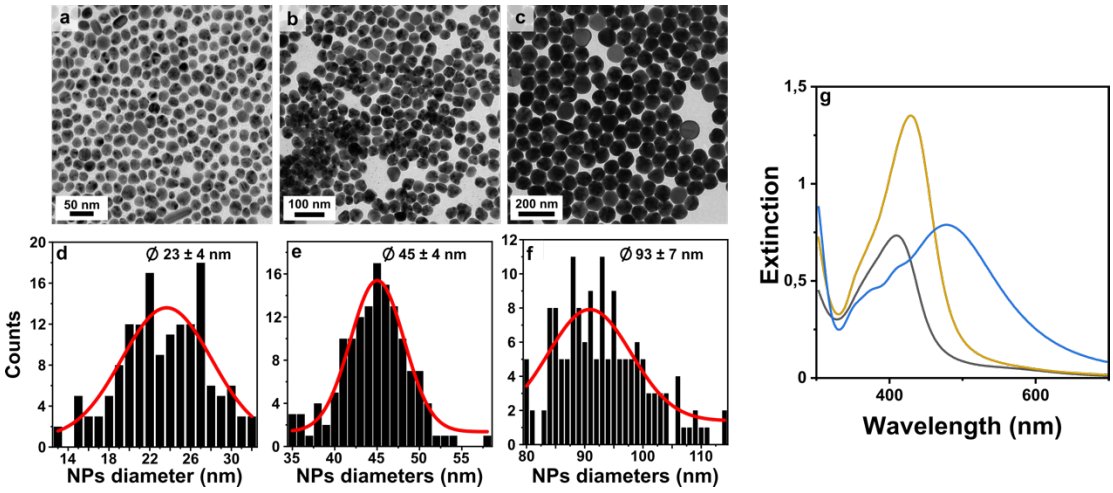

Figure ES 2 (**a**-**c**) AgNPs characterization through Transmission Electron Microscopy (TEM) and (**d**-**f**) size distribution histograms of (**d**) 23±4 nm, (**e**) 45±4 nm, and (**f**) 93±7 nm in diameter NPs. (**g**) UV-Vis analysis: extinction maximum at 408 nm for 25 nm (**black** curve), at 427nm for 50 nm (**yellow ochre** curve) NPs, and 458 nm for 100 nm (**red** curve) NPs.

2.1.3 Ligand exchange

Once concentrated, the Au and Ag NPs were functionalized *via* ligand exchange, by using thiol-terminated PEG (MW = 2000 g mol^{-1}). In addition to shape and size monodispersity, the surface chemistry of the NPs is critical for achieving uniform colloidal assembly. This protocol yields NPs stabilized by loosely bound surfactant molecules of CTAC (with a cmc ~ 1 mM). An excess of free ligand influences the suspension wetting on the substrate, leading to an accumulation of the particles on the contact line that hinders the fabrication process. Moreover, the net positive charge of CTAC-coated colloids creates a strong repulsion preventing the formation of close packing structures. To solve this issue, we

implemented a ligand exchange with the hydrophilic poly(ethylene glycol) methyl ether thiol (PEG), which enables the steric stabilization of the NPs throughout the assembly process, allowing to form densely close-packed assemblies.[15]

After two centrifugation steps, the recovered precipitated NPs were transferred into a vial and diluted in water. Subsequently, 1 mg/mL of PEG (molecular weight of 2000 g mol^{-1}) dissolved in a minimum amount of water (100 μL) was added dropwise in the suspension under vigorous stirring; the reaction was left overnight under mild stirring to promote NPs surface passivation. Finally, the NPs suspension was centrifuged two times (10000 rpm /20 min for 20 nm NPs, 5000 rpm/15 min for 50 nm NPs, 2500 rpm/10 min for 100 nm NPs) to eliminate the excess of ligand and adjust the concentration of the nanoparticles. The NPs were suspended in a final mixture of water:ethanol (6:4) with a [CTAC] = 50 μM. Here, the ethanol is used as cosolvent to improve template wetting and achieve kinetic control over NPs self-assembly by enhancing the wetting of the polydimethylsiloxane (PDMS) stamp, leading to a significant reduction in the formation of coffee rings, which had previously posed a considerable obstacle to the fabrication of well-defined colloidal arrays over areas exceeding a few hundred square micrometers.[16,17] This composition was optimized to achieve the most homogeneous assemblies.[18,19] The highest assembly quality was found for a concentration of Au^0 of 750 mM (measured monitoring the absorption at 400nm),[20] utilizing ~1 μL of suspension for each assembly. In the case of Ag, the optimal NPs suspension concentration was chosen correlating the absorption peak maximum (Absorbance at 0.5 considering a dilution 1:1000) and the quality of the final assembly, ensuring to use the same volume (1 μL) and guaranteeing the reproducibility (defect-less structures and no particles outside the cluster area) for all the samples. The quasi-stationary regime introduces complexities in relying solely on UV-Vis characterization for estimating

the nanoparticles size. Additional techniques such as TEM characterization are needed to obtain accurate and detailed information about the nanoparticle size distribution.

For the preparation of bimetallic metasurfaces (**Chapter 2**, **Paragraph 2.4.1** and **Chapter 3**, **Paragraph 3.4**), colloids of different sizes (25, 100 nm) and compositions (Au, Ag) were combined in different volume ratio (χ_{Au} = 0.75 and χ_{Au} = 0.35). An UV-Vis and EDX analysis were performed to analyze the composition of the final structures (the latter analysis was performed after drop-casting and drying the solution on a substrate, and keeping a low magnification in the SEM for the EDX spectra collection)

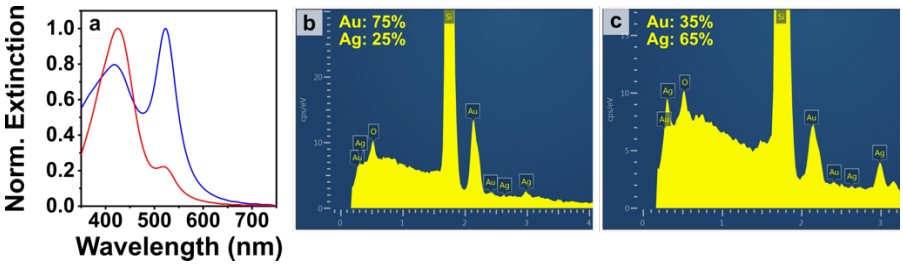

Figure ES 3 (**a**) UV-vis and (**b**, **c**) energy dispersive X-ray spectroscopy of the mixtures of gold and silver colloids: χAu = 0.75 (**b**, **blue line** in **a**), and χAu = 0.35(**c**, **red line** in **a**).

2.2 Molds and master fabrication

2.2.1 s-PDMs molds

soft-PDMS templates are employed for the self-assembly of NPs throughout the thesis, yielding molds that are notably more flexible and durable, even after multiple uses (typically 10–15 preparations). In the case of chiral-shaped assembly, we have used h-PDMS stamp as template, given its higher precision required to replicate the intricate features such as the Gammadion's arms. The polymer mixture is created by vigorously mixing a 10:1 weight ratio of monomer and curing agent, ensuring the homogeneous distribution by using a drill with a properly designed hook shaped tip. To avoid air bubble formation, the mixture is prepared into falcon tubes (PP) and then centrifugated at 3200 rpm for 5 minutes. As an

alternative, the air bubbles can be removed by preparing the s-PDMS mixture in plastic beaker (PP) and allowing to degas in a desiccator for approximately 1 h. Subsequently, the mixture was poured onto an operative masters of pillars that was previously silanized. The curing step is carried out on a hotplate with a temperature ramp of 60, 80, and 120 °C for 1 hour (1°/min). After the curing is complited, the demolding is carried out by gently separating the PDMS from the master, resulting in s-PDMS stamp patterned with cylindrical nanoholes array.

2.2.2 h-PDMs stamp for mater replicas and for HPC imprinting for in situ

These are hybrid material systems, with a thin h-PDMS patterned layer (few microns) deposited and cross-linked to a backbone composed of s-PDMS, ensuring sufficient flexibility, mechanical rigidity, small shrinkage, and UV light transmittance. Both the Ormostamp operative master and the original masters can be replicated onto h-PDMS molds, which in turn can be used to reproduce the nanoscaled features patterns several times. The h-PDMS mixture was prepared by adding the following components under vigorous stirring: 1.7g vinylmethylsiloxane, 50μL of 1,3,5,7-tetracetylcyclosilane, 4μL of Pt catalyst, 550μL of hydroxyl siloxane (co-polymer), and 2mL of toluene, decreasing its viscosity and facilitating the percolation into the nanosized features (<10nm). The addition sequence should be performed as fast as possible since the mixture will immediately start curing. Due to toluene rapid evaporation rate, the mixture remained usable for approximately 20 minutes, after which it started to solidify. After preparation, the mixture is drop-cast onto the patterned area, spread over the entire surface using a compressed air gun. This process is repeated three times for each sample, to provide a layer with thickness over few μm. The substrates are left at room Temperature (RT) for 30 min and then on a hotplate at 60 °C for 1 hour to evaporate all the toluene. After, approximately 25 mL of s-PDMS is poured onto the masters, and left curing under a temperature ramp of 60, 80, and

120 °C for 2 hours (2°/min), in order to create a flexible backbone. This process is repeatable, allowing the generation of numerous PDMS templates from a single silicon master.

2.2.3 Operative silicon masters

For this thesis, together with the Ormostamp master discussed in the next section, h-PDMS molds were used to reproduce the operative masters onto a thin SU8 layer through thermal nanoimprinting lithography. These masters are then employed to recreate the s-PDMS templates used for colloidal self-assembly, discussed in **Paragraph 2.3**. The negative epoxy-based photoresist (SU8 2000.5) is spin-coated (2000 rpm, 1000 rpm/s, 30 s) onto a cleaned glass or silica wafer. The h-PDMS mold is delicately pressed into the SU8 layer and then placed on a hotplate, where the Temperature is increased to 100 °C, causing rapid deformation of the epoxy layer. Subsequently, once the color of the pattern changes (~ 30 s), indicating the percolation of the resist into the small features of the pattern, the substrates are cooled down at RT. Finally, it is possible to perform the demolding of the stamp. The result is an SU8 operative master nanopatterned with the negative image of the h-PDMS mold. Following the demolding step, the patterned substrates undergo through 10 min direct UV-light exposure, in order to activate the monomer and start the cross-linking.[21]
The lattice period used for the masters and molds of this thesis are reported in the table below.

Table ES1 Geometrical parameters of the masters used in this work. The patterned area of each master is 49 mm^2.

Name	Lattice period (Λ)	Diameter (nm)	Depth (nm)
L400	400	230	390
L500	500	277	390
L600	600	338	390

2.2.4 OrmoStamp® for operative master replicas fabrication

Ormostamp, a photocurable polydimethylsiloxane with a Young's modulus of 650 MPa, is well-suited for replicating structures with high aspect ratio features (such as pillars and holes), effectively preventing the configuration collapse. The Ormostamp replicas (or operatives masters) were obtained from the original silicon masters purchased from *EULITHA* (Switzerland). In order to protect the original masters, avoiding the Ormostamp to stick permanently onto the silicon surface, they undergo through silanization step performed *via* chemical vapor deposition (CVD) of trichloro (1H,1H,2H,2H-perfluorooctyl) silane (97%) for 20 min under vacuum in a desiccator. Once the deposition is completed, the master is rinsed with isopropyl alcohol (IPA) to remove all the silane leftovers and heated up to 120 °C for 20 min for drying. A cleaned glass slide, pre-treated with UV-ozone (UV-O_3) for 20 min, is covered with Ormostamp primer *via* spin coating (4000 rpm, 1000 rpm/s, 60s), to ensure that the photoresist sticks well onto the glass substrate. The covered glass is then baked on hotplate at 150°C for 5 min, before proceeding with the imprinting step. A drop of liquid photoresist is placed directly on top of the silanized silicon master, and the glass slide is gently superimposed on the master, making sure that no bubbles remain trapped between the glass and the Ormostamp layer, letting it spread slowly under the effect of gravity. Finally, the photoresist is then activated under UV-light exposure for 10 min and cross-linking is favored by placing the substrates on a hotplate and applying a temperature ramp from 60 to 120 °C (6 °C min^{-1}) for 30 min. The difference in thermal expansion coefficient between the photoresist and silicon facilitates the self-detachment of Ormostamp from the silicon master. Following this process, Ormostamp patterned as a negative master can then be employed to recreate tens of defect-free replicas to be used as operative masters, safeguarding the originals.

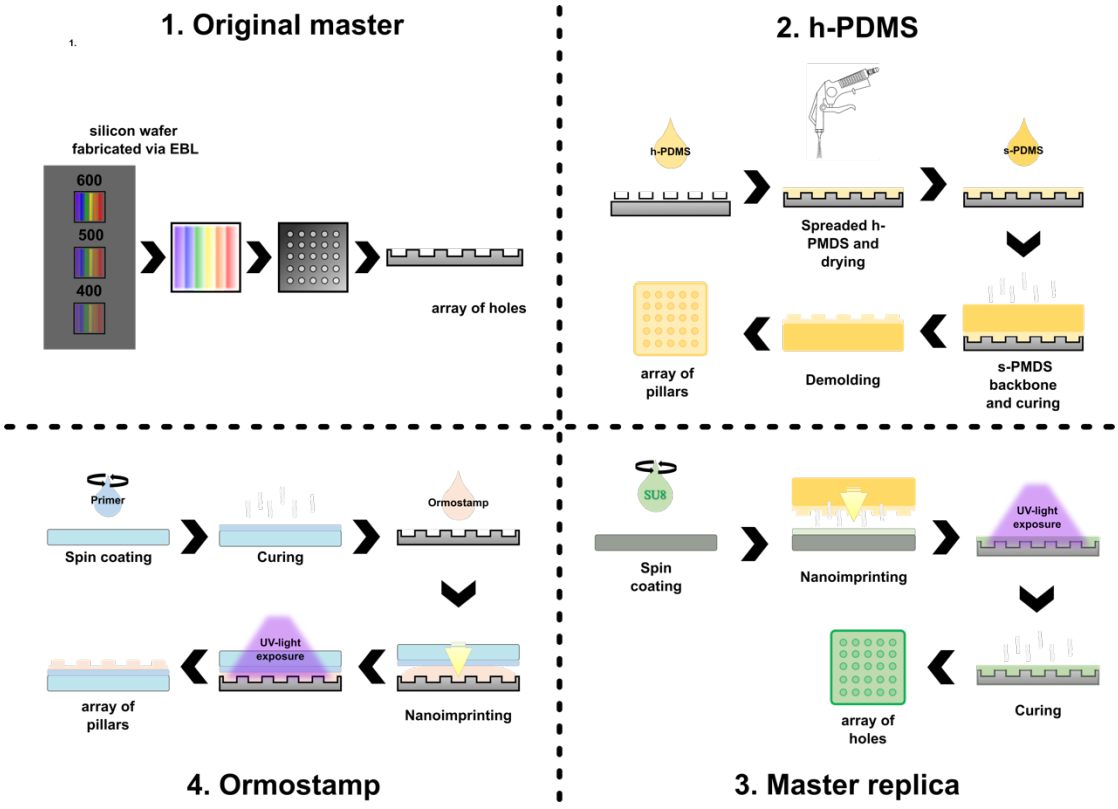

Figure ES 4 Scheme of the molds and master fabrication: **1**. Original master made via EBL. **2**. h-PDMS to replicate the original master. **3**. Replica master to generate the operative masters with SU8. **4**. Ormostamp to pass from holes to pillars and viceversa.

2.3 Sample fabrication

All glass substrates used for the preparation of all the samples used in this thesis were pre-cleaned with piranha solution prepared by mixing Sulfuric acid (H_2SO_4, 95–98% w/w) and Hydrogen peroxide (H_2O_2, 30% w/w) in a 3:1 ratio and let set for 30 min. After, they were well rinsed with Milli-Q water.

2.3.1 Glass samples preparation

A 1 μL droplet of AgNPs suspension is deposited at the center of a clean glass coverslip. Immediately after, a s-PDMS mold patterned as square array of cylindrical holes with a chosen lattice parameter (Λ) is placed over the dispersed nanoparticles. The evaporation of the solvent induces the self-assembly of the AgNPs into a plasmonic nanocluster array. The close-packing arrangement of the particles in clusters is controlled by the shape and size of

the cylindrical holes, which are influenced by the nanoparticle concentration, the solvent composition, and the CTAC concentration of the mixture. After drying overnight, the sample is ready for the demolding step. The samples were analyzed by scanning electron microscopy (SEM), using a FEI QUANTA 200 Electrons Field Emission Gun, operating between 5 and 15 kV in a low vacuum underwater atmosphere (60 Pa).

2.3.2 Lasing samples

For what concern the lasing architecture, Rhodamine B dye (RhB) was used as gain media dissolved (5.25 mg/mL in cyclopentanone and then mixed in ratio 1:1 with SU8 2000.5 epoxy-based negative photoresist (assuming the complete evaporation of the solvent at the end of the preparation, the final concentration is 2.8% w/w).[22] The SU8 was used also to replicate the operative master from which the PDMS molds are obtained. In the presence of UV light, these resists undergo a photochemical reaction, leading to the production of a photoacid, inducing the photopolymerization of SU8. Specifically, the photoacid catalyzes the cross-linking reaction in the exposed regions of the resin, making it to become less soluble in the developer solution. This selective insolubility allows for the formation of a stable and well-defined pattern in the exposed areas. A final post bake step is used to further cure and strengthen the polymerized structure, enhancing the mechanical and chemical stability and controlling the porosity of the final layer.[21]

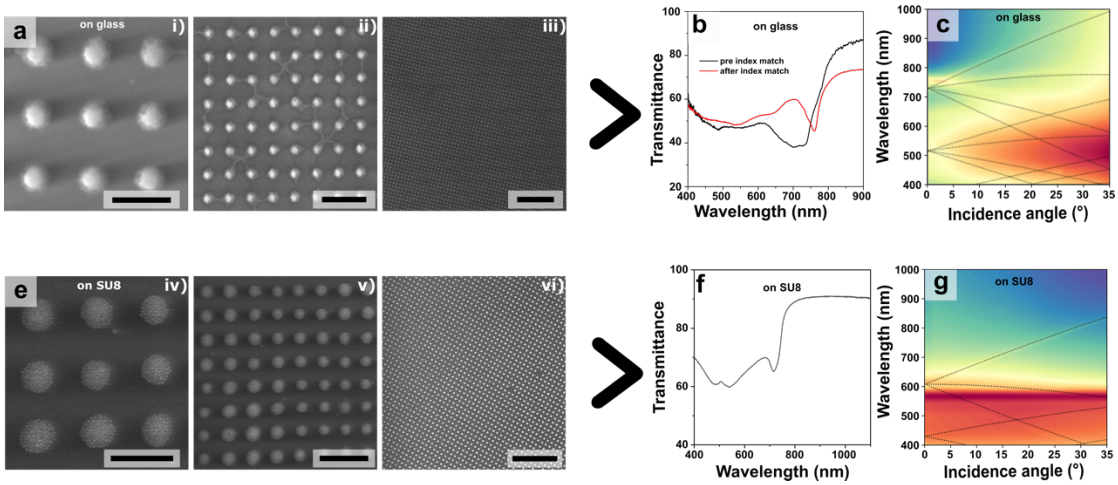

Figure ES 5 Comparison of assembly on glass and SU8 for the case of a sample with lattice period of 500 nm. (**a**, **e**): SEM images at different magnification (**a**-**i**, **ii**, **iii** and **e**-**iv**, **v**, **vi**) of the AgNPs array (**a**) on glass and (**e**) on SU8. [**Scale bars**: 500 nm (**a**-**i**, **e**-**iv**), 1 μm (**a**-**ii**, **e**-**v**), 5 μm (**a**-**iii**, **e**-**vi**)]. (**b**, **f**): Transmission spectrum of the sample (**b**) glass before (**red** curve) and after (**black** curve) index matching step, and on (**f**) SU8 index. (**c**, **g**): Intensity map (contour plots) of the transmission of the sample self-assembled on (**c**) glass and on (**g**) SU8. The degeneration of the first order of the sample on glass plotted in **panel c**, is due to the misalignment of the azimuthal respect to the illumination angle θ.

In order to facilitate the dissolution of RhB, an ultrasonic bath (Branson 2800) was used for 15 minutes. Once prepared, the mixture was spin-coated on a 20 × 20 mm cleaned glass coverslip (two steps receipt: 500 rpm, 100 rpm/s, 10 s and 2000 rpm, 300 rpm/s, 30 s). Then, samples were first pre-baked at 60 °C for 2 min and 95 °C for 5 min to ensure the solvent residues evaporation, secondly exposed for 25 min under UV light, and finally hard-baked by using a Temperature ramp 95-150 °C for 30 min.157 The final thickness (*t*) of the dye-doped SU8 layer was estimated to be 250 nm by interferometry measurements, taken with an FTIR spectrometer (Vertex 70, Bruker) connected to an optical microscope (Hyperion, Bruker). The experimental data were processed using MathLab licensed program fitting the experimental measurements by a transfer matrix model. These measurements were then confirmed by profilometry measures (**Figure 3.1**). The assembly was performed as for the glass samples, exploiting the hydrophobicity of the resin layer that facilitate the self-assembly increasing the quality of the final structure. The advantage of this strategy is

that it enables to keep the nanoparticles completely exposed to air, without using index matching layer as usually reported in literature and discussed in **Chapter 3**.

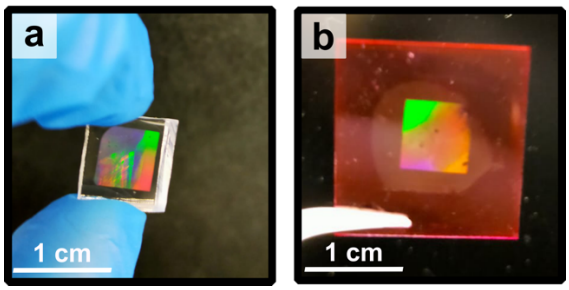

Figure ES 6 Final appearance of (**a**) s-PDMS molds and (**b**) lasing architecture sample.

2.3.3 Gammadion samples for chiral fluorescence enhancement

The fabrication of this samples involves the use of Left (L-), Right (R-), and Racemic (M-) Gammadion-shaped h-PDMS molds, replicated as mentioned in **Paragraph 2.1**.

In this case, AgNPs with different size were used for studying the optical properties to promote the modulation of the fluorescence emission. However, the 50 nm NPs displayed the best result in terms of optical response, due to the right balance between the near-field coupling among the particles within the Gammadions shaped cluster, and the far-field coupling of the scattered field from each cluster.

The architecture used for these samples, was the same of the lasing samples, namely a SU8-RhB layer was used onto a glass coverslip as gain media layer and the assembly was performed on top of this layer. The results are discussed in **Chapter 4**. The morphological characterization is discussed in **Chapter 2**, and the SEM are shown in Figure 2.6.

2.3.4 Samples for two-photon photoluminescence (2PPL)

In this case, AgNPs were assembled on top of a layer of bare core-shell quantum dots (QDs) green (CdSe/ZnO) and red (CdSe/ZnS), chosen for the high extinction coefficient and the long lifetimes. The QDs solution were prepared to maximize the concentration of the nanocrystals and at the same time have enough product to cover an entire glass coverslip. The concentration was kept at 0.1 M in toluene and the solutions were always used freshly

for the preparation of the samples, to prevent the changes in concentration induced by solvent evaporation.

The sample architecture (**Figure 2.10**) involves a layer of SU8 2000.5 spin coated on top of cleaned glass coverslip and cured through UV light exposure (10 min) and post-bake step (20 min at 120 °C). Then, the QDs were spin coated onto the SU8 layer (1000 rpm, 100 rpm/s, 30 s) reaching a thickness of about 10 nm, as estimated via atomic force microscopy (AFM).

This multilayer structure was chosen for taking advantage of the formation of SLR/wave-guiding hybrid modes which, again, support the outcoupling of the collective resonances without the need of index matching steps, as discussed in **Chapter 3**.

2.3.5 In situ samples

- **PDMS substrate**

The published protocol involves the preparation of glass supported flat PDMS substrates via sandwich method. In this approach, one of the two flat substrates needs to promote the adhesion of the PDMS. For this purpose, glass substrate cut in pieces cm-squared were treated via UV-O_3 (Jelight Model 42) treatment for 10-20 min. Instead, monocrystalline silicon wafer cut in cm-squared pieces were silanized *via* Chemical Vapor Deposition (CVD) with perfluorooctyl-trichlorosilane, by using a desiccator for 20 min. The wafers were then rinsed with IPA to remove the silane excess and dried with air compression gun. The PDMS is prepared by mixing the monomer and the curing agent in ratio 10:1 and degassed to get rid of the bubbles for 1h, if prepared in the beaker, or centrifugated for 5 min at 3200 rpm, if prepared in falcon tubes. A tiny drop of PDMS was then poured in the middle of the silanized silicon squares and degassed for 10 min to prevent that eventual bubbles remain trapped once the silicon is sandwiched with the glass. Finally, the glasses were superimposed from the UV-O_3 treated side over the PDMS drop, trying to center it and left curing on a

hotplate at 120°C for 1h. After 1h on hotplate, using a razor blade is possible to separate the glass from the silicon wafer.

While baking removes some oligomers, further cleaning steps are necessary to guarantee minimal nucleation on the PDMS surface. To extract the remaining oligomers, the PDMS is subjected to sonication in ethanol for 5 minutes, followed by sonication in acetone for 30 minutes.[23] The PDMS should swell with acetone, and then de-swell upon drying for 30 min at 60 ºC in the oven. This process should be repeated three times. The final drying step should be extended to approximately 60 minutes to ensure complete de-swelling of the PDMS before coating with HPC.

In the alternative approach, once prepared, the PDMS is diluted and before proceeding with spin-coating step, the solution is centrifuged at 3500 rpm for 2 minutes to eliminate trapped air. As part of the optimization process, the maximum revolutions per minute (rpm) were also optimized. Three different rpm settings were tested: 1000, 2500, and 5000. Although the spin-coater could reach 8000 rpm, this upper limit was not thoroughly explored. The decision was based on the observation that higher rpms led to a reduction in film thickness while compromising sample stability during spin-coating. Finally, the prepared samples underwent curing on a hotplate following a heat curve of 60-90-120°C, with temperatures increasing in 10-minute intervals. To assess the layer thickness, we utilized the generation of thin-film interference visible in the visible spectrum. This involved employing an FTIR spectrometer (Vertex 70, Bruker) in conjunction with an optical microscope (Hyperion, Bruker). By comparing the collected interference data with simulated plots, we estimated the film thickness by reflectance measurements and applying transfer matrix model. The thickness was evaluated on three different spots for all the samples, and a sample size of three was used for all the spin-coating conditions, unless otherwise specified. The average height and the standard deviation are reported in the following **Table ES2**:

Table ES2 PDMS diluted thickness measures evaluated on different substrates.

RPM	Height(mm) for 30% dilution	Height(mm) for 40% dilution	Height(mm) for 50% dilution	Height(mm) for 30% dilution
1000	4.0±0.5	7.8±0.6	12±1	-
2500	3.0±0.2	5.1±0.4	7.3±0.1	14.4±0.1
5000	2.3±0.1	3.8±0.2	5.4±0.2	10.5±0.1

- **Thermal Nanoimprint Lithography for HPC stencil**

Once prepared the polydimethylsiloxane (PDMS) substrates *via* sandwiched method, arrays of gold nanoparticles have been fabricated exploiting nanoscale chemical patterns formed *via* t-NIL. 23 g of HPC every 100 mL of water where prepared and left under stirring at RT for 5min. After ~5 min the solution will become a paste and the solution was left to dissolve over ~48 h at room Temperature until it appeared uniformly mixed. The working aqueous solution of HPC used were 21 mg/mL, 38 mg/mL, 53 mg/mL, and 66 mg/mL, prepared by adding 1.0 g, 2.0 g, 3.0 g, and 4.0 g of concentrated HPC stock solution to 10 mL of water and left under stirring for at least 1 h before using. The solution displaying the best results were the 1.0 g and 2.0 g cases. Once ready, the HPC aqueous solution was spin-coated (3000 rpm, 300 rpm/s, 60 s) onto the PDMS substrate, and the film was brought into contact with a h-PDMS mold. Under an applied pressure of ≈1 bar, the substrate was heated above the HPC Tg (140 °C), to generate holes template with the mold. This step is carried out by using a compact nanoimprinting tool (CNI v 2.0 by NIL Technology ApS, NILT, DK). After this procedure step, the imprinting confer iridescence to the patterned films easily visible at naked eye. To remove any residual in the holes of the HPC fishnet, a short 30 s UV-O_3 etching was used.

- **Chemical ink**

After the 30 sec UV–O_3 etch, the chemical ink (PMHS) solution (0.1% (v/v) in hexane), stirred for 1h before use to ensure even distribution, was spin coated (5000 rpm, 2500 rpm/s, 60 s) onto the stencil surface. The HPC fishnet integrity is entirely preserved after

the UV–O_3 treatment and ink application steps. Subsequently, the HPC stencil was dissolved in water, by using Milli-Q water dropped on top, and left swelling for The HPC fishnet integrity is entirely preserved after the UV–O_3 treatment and ink application steps. Subsequently, the HPC stencil was dissolved in water, by using Milli-Q water dropped on top, and left swelling for 30 min to facilitate the elimination. Therefore, the chemically patterned substrate was rinsed with water and dried using an air compression gun. This rinsing step is important, since the residual HPC can act as a reductant for the formation of gold nanoparticle.

The chemical ink was tested first on an unpatterned, flat soft-PDMS substrate through various techniques. The substrate was then immersed in a cuvette containing the growth solution comprising 1.5 mL 25 mM CTAB, 18 μL of 50 mM HAuCl4, and 18 μL of 100 mM ascorbic acid.

- ***In situ* growth**

The optimized growth solutionwas prepared in eppendorf using 12 μL of aqueous gold precursor ($HAuCl_4$) solution (0.05 M) added to 1 mL of cetyltrimethylammonium bromide (CTAB) surfactant, acting as capping ligand (0.025 M). Consequently, 12 μL of ascorbic acid aqueous solution (0.1 M) was added and then the solution, rapidly stirred by vortex, within 5 s changes color from orange to clear indicating the reduction of Au^{3+} to Au^{+}. As soon as the solution turns transparent, it was added to the substrates and left reacting for 1, 2, 5 or 10 min. Nanoparticle size was controlled by tuning the growth times. Then, the substrates were well-rinsed with Milli-Q water and dried by using air compression gun.

For the Au nanostars, the overgrowth solution contains 15 μL of $HAuCl_4$ solution (0.05 M), and shape-directing reagents as 1 mL of LSB surfactant aqueous solution acting as capping ligand, 6 μL $AgNO_3$ (0.01 M), and 10 μL HCl (0.1 M) added to prevent significant secondary nucleation for the 10 min growth time., the latter to prevent significant secondary nucleation

for the 10 min growth time. All the reagents are mixed; then, 50 μL of AA (0.1 M) were rapidly added and mixed (using the vortex). Immediately, 150 μL of the solution were drop casted onto the substrate and left for 5 min. Afterwards the substrates were well-rinsed with Milli-Q water and dried by using air compression gun.

2.4 Morphological characterization

Transmission electron microscopy (TEM) images were collected with a JEOL 1210 TEM instrument (Tokyo, Japan) operating at 120 kV using carbon-coated 400 square mesh copper grids.

Scanning electron microscopy (SEM) images were collected with a FEI QUANTA 200 Field Emission Gun, and a FEI Magellan 400L, operating between 5 and 30 kV. Energy Dispersive X- ray Spectroscopy maps were collected using a FEI Magellan 400L equipped with a X-Max Ultim Extreme EDX (Oxford Instruments) detector.

Atomic Force Microscopy (AFM) images were collected with a Bruker Multimode AFM equipped with Nanoscope V controller.

Thermal annealing was performed in a AS-Micro Rapid Thermal Annealing Furnace by Annealsys. Extinction spectra of the colloids were recorded using a Hitachi U-3000 spectrophotometer and customized optical bench set up.

2.5 Optical characterizations

Far-field transmission measurements the white light produced by a tungsten halogen lamp (Ocean Optics, HL-2000-HP, Florida, USA), was improved by using two filters (Edmund Optics, SCHOTT BG64, and Thorlabs, SRF11) to enhance counting in the UV and NIR regions. Two achromatic doublet lenses (f = 100.00 mm and f = 50.00 mm) were used to focus the light onto the sample and collected the signal with a fiber coupled spectrophotometer (Ocean Optics, QEPro-FL) with detection range of 380 - 1200 nm. The detection system was mounted on a rotational optical breadboard (Thorlabs, RBB12A, New

Jersey, USA), while the sample holder was secured on a rotational stage (Ø=50 mm) with resonant piezoelectric actuators (Thorlabs, ELL18/M) whose communication was controlled by interface board and software. The two-rotation system enables the concentric rotation of the sample and detector, allowing to perform the experiment by automatically rotating the illumination angle (θ) from 0° to 35° with a resolution of 0.1°. For some cases 4× objective (Olympus, RMS4X, NA: 0.10) were used to collect the data.

2.5.1 Transmittance circular dichroism

The optical measurements were carried out by using a custom-made optical set up. A white tungsten halogen lamp (Ocean Optics, HL-2000-HP, FL, USA) corrected with two filters in the UV and NIR (Edmund Optics, SCHOTT BG64, and Thorlabs, SRF11) was coupled to reflective silver collimator based on a 90° off-axis parabolic mirror with a protected silver coating, for high reflectivity in the 450 nm to 20 μm wavelength range. (RC08SMA-P01, Thorlabs) as light source injection. The light was collected by another reflective silver collimator coupled to a spectrometer (Ocean Optics, QEPro-FL) by an optical fiber. The collimated white light beam was sent through a Glan-Thompson Calcite Polarizer (GTH10M, Thorlabs) and mounted on a stepper motor rotation mount (K10CR1/M, Thorlabs). The linearly polarized light obtained was directed to a super achromatic quarter wave-plate (SAQWP05M-700, Thorlabs) mounted at ±45° compared to the polarization direction on a rotation mount (ELL14, Thorlabs) to obtain a circularly polarized light beam. All the optical elements were controlled automatically by custom software (*LabView* NXG) to ensure the reproducibility of the measurements. The illumination area was controlled by a pinhole (SM1D12). Two dual-position sliders (ELL6, Thorlabs) were used to place a shutter and the sample in the beam path. The first one was used to measure the dark current of the spectrometer, whereas the second one was used to place the sample in the light beam. The sample was placed between a pair of 4× objectives (NA = 0.1).

2.6 Lasing emission characterization

A nanoseconds-pulsed green laser (CryLaS Gmb, Ostendstrasse 25, D-12459 Berlin, Germany), peaked at 532 nm, with a repetition rate of 100 Hz, and vertically polarized was used as pumping source. By using an external trigger, the pump laser output was set at 2 pulses with a repetition rate of 100 Hz. To identify the lasing threshold, the laser power was increased from 4 μW up to 500 μW, monitored by using a power meter console (Thorlabs PM100D) coupled to a standard photodiode power sensor (Thorlabs S121C). The experimental hardware is the same used for the angular characterization, except for a 10× objective lens (NA = 0.25, WD = 12.1 mm) on the illumination path, to focalize the light in a small area on the pattern (diameter: 46.0 ± 0.4 μm, measured using a beam profiler BP209-VIS/M). The produced photoluminescence was collected by reflective silver collimator (Thorlabs, RC08SMA-P01) coupled coupled to a spectrophotometer with a fiber (Ocean Optics, QEPro-FL), and a long pass edge filter with high transmission (Semrock Edge basic BLP01-532R-25) was used to block the pump laser-line. The entire hardware was connected to a workstation and a customized (*LabView* NXG) program was used to manage the experiment.

2.6.1 Circularly emission characterization

Laser source (CryLaS Gmb, Ostendstrasse 25, D-12459 Berlin, Germany) with peak emission 532 nm were used to excite the Rhodamine B. The PL obtained from the samples was collected through a 4× objective with NA=0.1 and collimated to a super achromatic quarter-wave plate and a Glan-Thompson Calcite Polarizer (GTH10M, Thorlabs). By using a trigger controlled externally by an Arduino board (Arduino Uno), 2 laser pulses were sent onto the sample to ensure both polarizations were given the same amount of energy in the excitation process. The laser signals were optically filtered using longpass band filter (Semrock Edge basic BLP01-532R-25).

2.7 Two-photon excitated emission

The photoluminescence experiments were performed by using a spectroscopic system equipped with a 250 fs, 20W, 1030 nm NIR pulsed laser (Light Conversion, Pharos). The signals were acquired in transmission geometry with a 30 cm spectrograph (Princeton Instruments, SP300i) coupled with a thermoelectric cooled CCD (Princeton Instruments, PIXIS-BR). In the case of the 2P excitation, the laser runs with 100 Hz of repetition rate, and two short pass filters at 1 μm and 720 nm were used to cut the excitation beam from detection. For the one-photon excitation case, the 1030 nm laser was frequency doubled to 515 nm with a BBO crystal to achieve enough power in the output. Additionally, the repetition rate was decreased to 100 Hz and a long pass filter (515 nm) was used to cut off the excitation from detection.

2.8 Computational methods

Simulations were performed using finite differences in the time domain (FDTD) implemented in the 3D Electromagnetic Simulator of Lumerical (FDTD solutions, Ansys). The calculations solve Maxwell's equations on a non-uniform mesh grid, with a minimum step size of 1 nm close to each NPs and diminishing the step up to 0.3 nm in the inter-particle hot spots regions. In addition, a conformational variant refinement was used considering the presence of the dielectric/metal interface. The band structure simulation in **Chapter 3** was calculated from the excitation of our system, by placing a random cloud of broadband dipolar sources in a cell. Bloch periodic boundary conditions were used at each boundary (x- and y- direction), to acquire the band frequencies for each k- wavevector simulated. The sum of electric field amplitudes was recorded across 20 specific monitors positioned throughout the simulation volume in order to set the color scale bar. Frequencies corresponding to the appearance of the band (*i.e.*, the mode) exhibit longer lifetimes of electromagnetic fields due to constructive interference conditions. At all other frequencies,

the electromagnetic field distribution remains related. At the frequencies where the band (i.e. the mode) appears, the EM fields exists for longer times due to constructive interference condition. All the other frequencies correspond to electromagnetic field distributions that quickly vanish due to destructive interference; hence they do not contribute to mode evaluation.

ES References

(1) Jana, N. R.; Gearheart, L.; Murphy, C. J. Seeding Growth for Size Control of 5−40 Nm Diameter Gold Nanoparticles. *Langmuir* **2001**, *17* (22), 6782–6786. https://doi.org/10.1021/la0104323.

(2) Vigderman, L.; Zubarev, E. R. High-Yield Synthesis of Gold Nanorods with Longitudinal SPR Peak Greater than 1200 Nm Using Hydroquinone as a Reducing Agent. *Chem. Mater.* **2013**, *25* (8), 1450–1457. https://doi.org/10.1021/cm303661d.

(3) Scarabelli, L.; Grzelczak, M.; Liz-Marzán, L. M. Tuning Gold Nanorod Synthesis through Prereduction with Salicylic Acid. *Chem. Mater.* **2013**, *25* (21), 4232–4238. https://doi.org/10.1021/cm402177b.

(4) Rodríguez-Fernández, J.; Pérez-Juste, J.; Mulvaney, P.; Liz-Marzán, L. M. Spatially-Directed Oxidation of Gold Nanoparticles by Au(III)−CTAB Complexes. *J. Phys. Chem. B* **2005**, *109* (30), 14257–14261. https://doi.org/10.1021/jp052516g.

(5) Carregal-Romero, S.; Pérez-Juste, J.; Hervés, P.; Liz-Marzán, L. M.; Mulvaney, P. Colloidal Gold-Catalyzed Reduction of Ferrocyanate (III) by Borohydride Ions: A Model System for Redox Catalysis. *Langmuir* **2010**, *26* (2), 1271–1277. https://doi.org/10.1021/la902442p.

(6) Gramlich, G.; Zhang, J.; Nau, W. M. Increased Antioxidant Reactivity of Vitamin C at Low pH in Model Membranes. *J. Am. Chem. Soc.* **2002**, *124* (38), 11252–11253. https://doi.org/10.1021/ja026927b.

(7) Khan, Z.; Singh, T.; Hussain, J. I.; Hashmi, A. A. Au(III)–CTAB Reduction by Ascorbic Acid: Preparation and Characterization of Gold Nanoparticles. *Colloids Surf. B Biointerfaces* **2013**, *104*, 11–17. https://doi.org/10.1016/j.colsurfb.2012.11.017.

(8) Bastús, N. G.; Merkoçi, F.; Piella, J.; Puntes, V. Synthesis of Highly Monodisperse Citrate-Stabilized Silver Nanoparticles of up to 200 Nm: Kinetic Control and Catalytic Properties. *Chem. Mater.* **2014**, *26* (9), 2836–2846. https://doi.org/10.1021/cm500316k.

(9) Ojea-Jiménez, I.; Bastús, N. G.; Puntes, V. Influence of the Sequence of the Reagents Addition in the Citrate-Mediated Synthesis of Gold Nanoparticles. *J. Phys. Chem. C* **2011**, *115* (32), 15752–15757. https://doi.org/10.1021/jp2017242.

(10) Xiong, Y.; Siekkinen, A. R.; Wang, J.; Yin, Y.; Kim, M. J.; Xia, Y. Synthesis of Silver Nanoplates at High Yields by Slowing down the Polyol Reduction of Silver Nitrate with Polyacrylamide. *J. Mater. Chem.* **2007**, *17* (25), 2600–2602. https://doi.org/10.1039/B705253G.

(11) Wiley, B.; Herricks, T.; Sun, Y.; Xia, Y. Polyol Synthesis of Silver Nanoparticles: Use of

Chloride and Oxygen to Promote the Formation of Single-Crystal, Truncated Cubes and Tetrahedrons. *Nano Lett.* **2004**, *4* (9), 1733–1739. https://doi.org/10.1021/nl048912c.

(12) Bastús, N. G.; Comenge, J.; Puntes, V. Kinetically Controlled Seeded Growth Synthesis of Citrate-Stabilized Gold Nanoparticles of up to 200 Nm: Size Focusing versus Ostwald Ripening. *Langmuir* **2011**, *27* (17), 11098–11105. https://doi.org/10.1021/la201938u.

(13) Conti, Y.; Passarelli, N.; Mendoza-Carreño, J.; Scarabelli, L.; Mihi, A. Colloidal Silver Nanoparticle Plasmonic Arrays for Versatile Lasing Architectures via Template-Assisted Self-Assembly. *Adv. Opt. Mater.* **2023**, *n/a* (n/a), 2300983. https://doi.org/10.1002/adom.202300983.

(14) Amendola, V.; Meneghetti, M. Size Evaluation of Gold Nanoparticles by UV−vis Spectroscopy. *J. Phys. Chem. C* **2009**, *113* (11), 4277–4285. https://doi.org/10.1021/jp8082425.

(15) Hanske, C.; González-Rubio, G.; Hamon, C.; Formentín, P.; Modin, E.; Chuvilin, A.; Guerrero-Martínez, A.; Marsal, L. F.; Liz-Marzán, L. M. Large-Scale Plasmonic Pyramidal Supercrystals via Templated Self-Assembly of Monodisperse Gold Nanospheres. *J. Phys. Chem. C* **2017**, *121* (20), 10899–10906. https://doi.org/10.1021/acs.jpcc.6b12161.

(16) Hanske, C.; Hill, E. H.; Vila-Liarte, D.; González-Rubio, G.; Matricardi, C.; Mihi, A.; Liz-Marzán, L. M. Solvent-Assisted Self-Assembly of Gold Nanorods into Hierarchically Organized Plasmonic Mesostructures. *ACS Appl. Mater. Interfaces* **2019**, *11* (12), 11763–11771. https://doi.org/10.1021/acsami.9b00334.

(17) Hamon, C.; Sanz-Ortiz, M. N.; Modin, E.; Hill, E. H.; Scarabelli, L.; Chuvilin, A.; Liz-Marzán, L. M. Hierarchical Organization and Molecular Diffusion in Gold Nanorod/Silica Supercrystal Nanocomposites. *Nanoscale* **2016**, *8* (15), 7914–7922. https://doi.org/10.1039/C6NR00712K.

(18) Molet, P.; Passarelli, N.; Pérez, L. A.; Scarabelli, L.; Mihi, A. Engineering Plasmonic Colloidal Meta-Molecules for Tunable Photonic Supercrystals. *Adv. Opt. Mater.* **2021**, *9* (20), 2100761. https://doi.org/10.1002/adom.202100761.

(19) Scarabelli, L.; Vila-Liarte, D.; Mihi, A.; Liz-Marzán, L. M. Templated Colloidal Self-Assembly for Lattice Plasmon Engineering. *Acc. Mater. Res.* **2021**, *2* (9), 816–827. https://doi.org/10.1021/accountsmr.1c00106.

(20) Scarabelli, L.; Sánchez-Iglesias, A.; Pérez-Juste, J.; Liz-Marzán, L. M. A "Tips and Tricks" Practical Guide to the Synthesis of Gold Nanorods. *J. Phys. Chem. Lett.* **2015**, *6* (21), 4270–4279. https://doi.org/10.1021/acs.jpclett.5b02123.

(21) Matarèse, B. F. E.; Feyen, P. L. C.; Falco, A.; Benfenati, F.; Lugli, P.; deMello, J. C. Use of SU8 as a Stable and Biocompatible Adhesion Layer for Gold Bioelectrodes. *Sci. Rep.* **2018**, *8*

(1), 5560. https://doi.org/10.1038/s41598-018-21755-6.

(22) Schokker, A. H.; Koenderink, A. F. Lasing at the Band Edges of Plasmonic Lattices. *Phys. Rev. B* **2014**, *90* (15), 155452. https://doi.org/10.1103/PhysRevB.90.155452.

(23) Odom, T. W.; Love, J. C.; Wolfe, D. B.; Paul, K. E.; Whitesides, G. M. Improved Pattern Transfer in Soft Lithography Using Composite Stamps. *Langmuir* **2002**, *18* (13), 5314–5320. https://doi.org/10.1021/la020169l.

APPENDIX A

A.1 LIST OF PUBLICATIONS

1. **Surface Lattice Plasmon Resonances by Direct in Situ Substrate Growth of Gold Nanoparticles in Ordered Arrays**

- Gail A Vinnacombe-Willson, Ylli Conti, Steven J Jonas, Paul S Weiss, Agustín Mihi, Leonardo Scarabelli Advanced Materials 2022, 34, 2205330 DOI: 10.1002/adma.202205330

2. **Pre-and Post-assembly Modifications of Colloidal Plasmonic Arrays: the Effect of Size Distribution, Composition, and Annealing**

- Oriol Colomer-Ferrer, Serni Toda Cosi, Ylli Conti, David E Medina-Quiroz, Leonardo Scarabelli, Agustin Mihi Journal of Material Chemistry C, 2022,10, 13913-13921 DOI: 10.1039/D2TC01148D

3. **Direct Bottom-Up in Situ Growth: A Paradigm Shift for Studies in Wet-Chemical Synthesis of Gold Nanoparticles**

- Gail Vinnacombe-Willson, Ylli Conti, Andrei Stefancu, Paul Weiss, Emiliano Cortés, Leonardo Scarabelli Chemical Reviews 2023, DOI: 10.1021/acs.chemrev.2c00914

4. **Colloidal Silver Nanoparticle Plasmonic Arrays for Versatile Lasing Architectures via Template-Assisted Self-Assembly**

- Ylli Conti, Nicolas Passarelli, Jose Mendoza-Carreño, Leonardo Scarabelli, Agustin Mihi Advanced Optical Materials 2023, 2300983 DOI: 10.1002/adom.202300983

5. **Colloidal Plasmonic Metasurfaces for the Enhancement of Non-Linear Optical Processes and Molecular Spectroscopies**

- Ylli Conti, Naihao Chiang, Leonardo Scarabelli, ChemNanoMat 2024,10, e202300566, DOI: 10.1002/cnma.202300566 (**corresponding author**)

6. **Template-Assisted Self-Assembly of Chiral Plasmonic from Non-chiral Building Blocks for Enhanced Chiral Photoluminescence**

-Ylli Conti, Jose Mendoza-Carreño, Agustin Mihi, Leonardo Scarabelli (**manuscript in preparation**)

7. **Enhanced Two-photon Emission of QDs through Lattice Plasmon Resonance Coupling**

- Ylli Conti, Yen-Chen Chen, Xing He, Naihao Chiang, Leonardo Scarabelli (**manuscript in preparation**)

A.2 CONTRIBUTION TO SCIENTIFIC EVENTS

1. Presenting author of an oral presentation entitled "**Ordered arrays of silver nanoparticles for narrow bandwith lattice plasmon resonances**" at Spanish Conference on Nanophotonics - *CEN2021* – Vigo, September 20-22, 2021
2. Poster presentation entitled "**Narrow-bandwidth surface plasmon resonances from colloidal silver nanoparticles and their integration into lasing architecture**" at *Nanolight* – Benasque Pedro Pascual Science Centre, Benasque, Huesca, March 06-12, 2022.
3. Poster presentation entitled **"Engineering of plasmonic nanoparticles substrates for narrow bandwith lattice plasmon resonance**" at *Plasmonics and Nanophotonic*- Gordon Research Seminar (GRS) - Newry, ME, United States, July 09-10, 2022.
4. Poster presentation entitled "**Engineering of plasmonic nanoparticles substrates for narrow bandwith lattice plasmon resonance**" at *Plasmonics and Nanophotonic*-Gordon Research Conference (GRC) - Newry, ME, United States, July 10-15, 2022.
5. Presenting author of an oral presentation entitled "**Silver Nanoparticle Plasmonic Arrays for Versatile Lasing Architectures via Template-Assisted Self-Assembly**" at workshop ACTIVE 2022- Institute of Materials Science of Barcelona (ICMAB-CSIC), October 06-07, 2022.
6. Poster presentation entitled "**Colloidal based plasmonic metasurfaces as optical cavities to promote non-linear optical phenomena**" at *Plasmonically Powered Processes*- Gordon Research Seminar (GRS) - Ventura, CA, United States, June 03-04, 2023.

7. Poster presentation entitled "**Colloidal based plasmonic metasurfaces as optical cavities to promote non-linear optical phenomena**" at *Plasmonically Powered Processes*- Gordon Research Seminar (GRC) - Ventura, CA, United States, June 04-09, 2023.
8. Scientific Equipment Platforms ICMAB- Institute of Materials Science of Barcelona (ICMAB-CSIC), June 29, 2022.
9. Presenting author for invited seminar entitled "**Plasmonic metasurfaces for non-linear optical phenomena**" at University of Houston - Houston, TX, United States, July 14, 2023.
10. Presenting author of a seminar entitled "**Colloidal based plasmonic metasurfaces for advanced light-matter interactions**" at Rice University - Houston, TX, United States, July 24, 2023

A.3 HONOURS AND AWARDS

- VII call for JIQ Mobility Grants (2023)

ALANCE DE LA TESIS Y PREFACIO

El trabajo de esta tesis de doctorado se realizó en el marco de la beca Postdoctoral Junior Leader-Incoming financiada por la Fundación "La Caixa" (ID 100010434, código de beca LCF/BQ/PI20/11760028) que tuvo como objetivo el desarrollo de estrategias alternativas para la construcción de materiales plasmónicos nanoestructurados para el estudio de la dinámica de moléculas de plasmón, procesos mediados por plasmones y química mejorada en superficie.

Específicamente, mi trabajo se centró en la fabricación de arquitecturas plasmónicas/fotónicas, sus acoplamiento a especies moleculares, la caracterización de sus propiedades ópticas utilizando diversas técnicas experimentales y la aplicación práctica de las cavidades plasmónicas obtenidasen el ámbito de la óptica no lineal.

Las metasuperficies fotónicas son estructuras artificiales 2D construida con componentes que presentan dimensiones inferiores a la longitud de onda de la radiación electromagnetica incidente. Estos componentes pueden ser dispuestos periódicamente o no periódicamente, con el fin de producir una respuestas electromagnéticas especifica. Esta flexibilidad de diseño permite la creación de materiales con propiedades macroscópicas excepcionales que no se pueden encontrar en la naturaleza.

Las nanopartículas plasmónicas también bueden actuar como componentes para la fabricación estructuras fotónicas, p. ej. En matrices ordenadas, donde el acoplamiento entre plasmones y estados difractivos conduce a la aparición de resonancias de plasmones de red superficiales, espectralmente sintonizables desde el ultravioleta (UV) al infrarrojo (IR) variando el parámetro de la matriz (Λ), el índice de refracción del medio y el ángulo de iluminación.

Las resonancias reticulares conservan las propiedades de los dos componentes individuales, como una sección transversal de dispersión mejorada típica de las resonancias plasmónicas, y por el otro lado largos tiempos de vida y un perfil espectral muy fino, con factores de calidad altos y deslocalización espacial típica de los fenómenos difractivos. Como resultado, las

resonancias reticulares superficiales son candidatos ideales para promover fenómenos ópticos no lineales como el láser, el acoplamiento fuerte o la generación de segundos armónicos.

La creación de matrices plasmónicas finamente sintonizadas requiere técnicas de fabricación escalables que combinen las ventajas de las fabricaciones *top-down* y *bottom-up*. Las técnicas de autoensamblaje coloidales ofrecen alternativas de bajo costo a las técnicas de litografia *top-down*, proporcionando un enfoque integral de alto rendimiento para implementar metasuperficies plasmónicas coloidales en una variedad de materiales diferentes. Los resultados obtenidos sugieren que el autoensamblaje se establece como alternativa viable para la fabricación de cavidades ópticas de alta calidad para aplicaciones ópticas avanzadas como el láser y la fluorescencia excitada de dos fotones mejorada.

Además de optimizar la técnica de autoensamblaje asistido por molde, hemos desarrollado una nueva estrategia para superar algunas de las limitaciones de esta tecninca , como el exceso de reactivos y la necesidad de ligandos estabilizantes. El crecimiento *in situ*, donde las estructuras plasmónicas se forman directamente sobre los sustratos, evitndo la síntesis en disolución y los pasos de autoensamblaje, se desarrolló como una alternativa interesante para lograr patrones nanométricos sintonizables. La prueba de concepto presentada en esta tesis demuestra la posibilidad de hacer crecer matrices plasmónicas que se comporten como cavidades ópticas mediante crecimiento directo *in situ*, un resultado que nunca antes se había logrado. A pesar de estos interesantes resultados, es necesaria más investigación para comprender los aspectos mecanicistas del crecimiento *in situ* y controlar la morfología y orientación de las partículas, lo que en última instancia mejorará la escalabilidad y versatilidad de esta tecnica emergente.

El trabajo experimental de la tesis se realizó principalmente en el Instituto de Ciencia de Materiales de Barcelona (ICMAB-CSIC), complementado con una estancia de investigación de cuatro meses en la Universidad de Houston (Texas, EE.UU.).

A continuación se presenta un breve resumen de cada capítulo.

El **Capítulo 1** proporciona el contexto esencial sobre plasmónica y óptica no lineal (NL) en el marco de esta tesis, con un enfoque específico en dilucidar las características de las nanopartículas metálicas, los conjuntos de nanopartículas metálicas y las interacciones nanopartículas-moleculares para promover fenómenos ópticos no lineales.

El propósito del **Capítulo 2** es resumir y categorizar los principios del ensamblaje coloidal plasmónico, comparando diferentes métodos de fabricación y destacando los emergentes. En particular, la atención se centra en enfoques alternativos que utilizan litografía blanda, incluido el autoensamblaje asistido por molde, y la estrategia más reciente de crecimiento *in situ* para construir nanoestructuras funcionales mediante la integración de litografía de nanoimpresión y técnicas de contraste químico. La discusión se centra en el uso de nanopartículas metálicas para crear metasuperficies plasmónicas de base coloidal.

El **Capítulo 3** presenta los resultados de la caracterización óptica obtenidos en el contexto de esta tesis. Se presentan varias estrategias para optimizar el diseño de una metasuperficie plasmónica coloidal. Estos incluyen cambiar el índice de refracción del entorno, la morfología de las unidades plasmónicas o el material del sustrato, en fases previas y posteriores al ensamblaje. Este estudio muestra la adaptabilidad del autoensamblaje con molde al utilizar varios componentes para fabricar matrices plasmónicas de mayor complejidad que permitan diseñar la respuesta óptica colectiva.

En el **Capítulo 4**, nuestra investigación profundizó en las características de las metasuperficies plasmónicas coloidales para mejorar diversos fenómenos ópticos. Estos incluyeron la estimulación de la emisión láser en moléculas de colarante comunes (Rodamina B), la emisión excitada de dos fotones mejorada en puntos cuánticos y la emisión quiral inducida en moléculas emisoras aquirales mediante acoplamiento resonante con coloides dispuestos en matrices con forma quiral.

ACKNOWLEDGEMENTS

I would like to start this section by thanking my boss and mentor Dr. Leonardo Scarabelli, for having the audacity to hire me as his first PhD student. Thank you for believing in me from day one, for respecting my opinions and pushing me to do my best, always. Thank you for sharing your incredible strength of spirit, and all your passion for science that has led you to get exceptional goals in your career, and I wish you the best for that. Thanks for sharing with me the passion for black humor, that relieved us of the stress of long working days!! And I also thank Odissea, who changed your life but also a bit of mine. :)

I sincerely thank Prof. Naihao Chiang and his group for welcoming me as I was part of the group; thanks for all the fantastic BBQs and spicy food, the inspiring scientific discussions, and trolls, all the experiences and drinks we shared in the months I spent there. I sincerely thank you.

Another thank you is directed to the Vinnacombe-Willson (Gail and Jake), the american/philipino/mexican alter ego! Thank you for the very good time (and drinks) spent together and for being very friendly people. Thanks to Gail for involving me in her projects during my first PhD months, making me always feel less inadequate because of my huge impostor syndrome.

I would like to thank the Nanoopto's group, evolved and changed over the years, where I have found a good environment in which doing science, despite everything.
In particular, I would thank Prof. Alejandro Goñi, and Dr. Sebas always ready to help and get involved in our experiments.
I thank Jose my "hermano de PhD", with which I started my adventure in 2021, for all the help and support as friend and colleague, with who I could share all the struggle of being PhD students. I thank Miquel Casademont for being always ready to help and available for everyone, and for his "panellets" (the best I tasted in Catalunya).
I thank also Martì for making life a little easier for everyone with his "creations", and for his peculiar and lovely way to speak Italian…e se non è vero è ben trovato!!

Thanks to Reyda, that friend with whom I immediately had a good feeling that hopefully will bind us for the future.

I thank Osnat and Fendy because their friendship makes them for sure my favorite Mexican people! <3

Thanks to all the Italian/Spanish group met here in Barcelona (Camilla, Cristiano, Cristineto, Bego, etc.) who made me feel immediately integrated and less homesick.

Of course, a big thank you is for ALL friends I left in Italy, especially for Biagio, always ready to support me, and Simone ilNegro, always in my thoughts. But most of all I must thank Antonio, for being my "Ama" always by my side, who supports my daily breakdowns and my trashy side.

A special thank you to my family, to my father and my mother now starting an exciting new chapter of their life. Thank you for all the sacrifices and support over the years, for standing by me in every decision I take, and thank you for your unconditional love that constantly relieves my homesickness. Thank you to my siblings Vale and Nicola, and Mario who I consider to be a brother, for taking care of me and because being part of a family means having someone you can rely on like you.

Thanks to ilMatto, my love and family. Always with me and by my side with all his sweetness, and kindness. Thank you for being here for me even though I am often a difficult person to deal with. *"Per due che come noi non si son persi mai, e che se guardi indietro non ci crederai, perché ci vuole passione."*
Thanks to your family for all the love and support of these years, and thanks to Tommaso who has changed our lives forever and makes me appreciate being "just" the aunt!

Last but not least, thanks to my little sweet beast Jambo. Despite all, I couldn't see my life without his snarling face.

Brindo a me e a tutti voi.